Electrical Detection of Spin-Dependent Transport in Silicon

Cheuk Chi Lo

Electrical Engineering and Computer Sciences
University of California at Berkeley

Technical Report No. UCB/EECS-2011-54
http://www.eecs.berkeley.edu/Pubs/TechRpts/2011/EECS-2011-54.html

May 13, 2011

Electrical Detection of Spin-Dependent Transport in Silicon

by

Cheuk Chi Lo

A dissertation submitted in partial satisfaction of the
requirements for the degree of
Doctor of Philosophy

in

Engineering – Electrical Engineering and Computer Sciences

in the

Graduate Division

of the

University of California, Berkeley

Committee in charge:

Professor Jeffrey Bokor, Chair
Professor Eli Yablonovitch
Professor K. Birgitta Whaley

Spring 2011

The dissertation of Cheuk Chi Lo, titled Electrical Detection of Spin-Dependent Transport in Silicon, is approved:

Chair _____ Date _____

_____ Date _____

_____ Date _____

University of California, Berkeley

Electrical Detection of Spin-Dependent Transport in Silicon

Abstract

Electrical Detection of Spin-Dependent Transport in Silicon

by

Cheuk Chi Lo

Doctor of Philosophy in Engineering – Electrical Engineering and Computer Sciences

University of California, Berkeley

Professor Jeffrey Bokor, Chair

Information, be it classical or quantum mechanical, requires representation in physical reality for processing and storage. Conventional classical computation utilizes the charge degree of freedom of carriers in semiconductors for encoding information; however, fundamental physical limitations will be reached within the next two decades preventing further improvements in computational capacity with charged-based devices. In recent years, the utilization of the spin states of charged carriers has shown remarkable promise for both enhancing the functionalities of classical computation devices and achieving quantum information processing. In this work, I explore this spin degree of freedom in donor-doped silicon metal-oxide-semiconductor (MOS) devices, which are promising architectures for the implementation of spin-based qubits in silicon for quantum information processing. The spin-dependent transport phenomena in such systems are studied systemically by electrically detected magnetic resonance (EDMR) techniques at X-band ($\approx 9.5\,\mathrm{GHz}$) and W-band ($\approx 95\,\mathrm{GHz}$), with corresponding Zeeman fields of 0.35 T and 3.5 T, respectively. It is found that direct spin-dependent scattering amongst conduction electrons and neutral donors gives rise to a much weaker contribution to spin-dependent transport than previously reported. Instead, the dominant spin-dependent processes in these systems are due to the polarization-dependent conduction electron mobility and subsequent polarization transfer from donor electrons. The technique of EDMR also allows us to perform *in situ* electron polarization detection, which is used to demonstrate spin drift and spin diffusion effects in silicon MOSFET devices. Towards the realization of donor spin-state readout, few-donor doped finFETs are also developed and the transport spectroscopy of such devices explored. These measurements provide invaluable insight into these interesting quantum devices and pave the way for the realization of spin-based computation.

Contents

List of Figures

List of Tables

Acknowledgments

First and foremost, I would like to thank my advisors, Professor Jeffrey Bokor and Dr. Thomas Schenkel (in alphabetical order!), for giving me the opportunity to work on this fascinating project. I thank Jeff for giving me the freedom to explore, sharing his critical insights in research and mentoring me throughout the years. I thank Thomas for his encouragements and inspirations, unyielding support and vision that drives this research program forward. Both have shaped me profoundly on both professional and personal levels, and I am grateful for the opportunity to work with them.

This work would not have been possible without the help and support of fellow students and collaborators who have generously given me the opportunities to work and learn in their laboratories. In an attempt of fairness, I'll try to acknowledge them in order of geographical proximity:

First, students in the Berkeley EECS Device Group, whom I've shared offices with over the years and more importantly, chitchatted with in the cleanroom while we waited for our wafers to dry/clean/anneal/etch/pattern/*etc.* during odd hours of the day, sharing fabrication tips, complaining about equipments (and/or advisors), and as a result keeping us all sane. I thank especially Anu Bowonder, Hei Kam, Pratik Patel and Kinyip Phoa. I also thank Joanna Lai, Jason Shangkuan, Yu-Chih Tseng and Hiu Yung Wong for training me when I began my endeavors in the cleanroom. I thank Sung Hwan Kim, Donovan Lee, Jaeseok Jeon and Vinent Pott for keeping the device group clusters running and the DCL in good shape. The initial transport spectroscopy measurements were done together with Enrico Hermann, who was visiting our group from the University of Würzburg for one year. Together we experimented with cryostats, took turns to rotate the needle valve of the He-3 system overnight, and enjoyed raman noodles in the ALS snack room. His cheerfulness and curiosity have been greatly missed. The QUEST project brought more people to our Berkeley silicon QC community: Thorsten Last, with whom I travelled to Tallahassee with to perform high magnetic field magnetotransport studies and enjoyed beer at Miller's. His knowledge of spin physics, transport measurements and frank opinions are always appreciated. I am also expecting a case of cold Canadian Molson beer from Thorsten when semiconductor qubits prove superior. The help from the UC Berkeley Microlab/Nanolab staff: Jimmy Chang, Joe Donnelly, Marilyn Kushner, Jay Morford, Sia Parsa and Danny Pestal, and Charlotte Jone's assistance on everything administrative, are also much appreciated. I thank Jason Lee, Richard Su and Chuohao Yeo for their friendship and support as we began our journeys in graduate school. I would also like to thank Professor Eli Yablonovitch and Professor Brigitta Whaley for agreeing to serve in my dissertation committee, Professor T. Kenneth Gustafson for serving as chair of my qualifying exam committee, and Professors Chenming Hu, Nathan Cheung, and Vivek Subramanian for serving in my preliminary examination committee.

Up the hill at LBNL, I would like to thank BIERLab co-founder Christoph Weis. Together we modified the old Bruker ESP300E which made routine EDMR measurements possible, and

established *the magnificent BIERLab*. Christoph's incredible quartz-filing skill was critical in getting EDMR to work, and his let's do/get/fabricate/finish it attitude is much appreciated and pushes progress forward. He also holds the distinctions for (i) operating the He flow cryostat continuously for the longest duration at *elevated temperatures*, (ii) scoring the *second* highest points in *Filler* in BIERLab history, and (iii) being the only person to have read through Appendix B. I also thank him for the constant updates on the greatest and newest in hockey news, including frequent reminders of how Gretzky is the best hockey player ever[1]. I would also like to thank Arun Persaud, whom I've travelled together with to many QC reviews. Arun's resourcefulness and wizardry with LabView have been instrumental in getting the Helium-3 measurements running, and I also thank him for organizing the SiQC journal clubs. I also thank Michael Dickinson, Tom McVeigh, Wes Tabler and Steve Wilde from the IBT group for their assistances throughout the years. The Helium-3 system we used is located at beamline 1.4 of the ALS. I thank Ferenc Borondics for showing us how to operate the system, and beamline scientists Hans Bechtel and Michael Martin for their support. I also thank Simon George at the ALS for allowing Christoph and me to hijack his Bruker ESP300E system for prolonged periods of times, and also his helpful advices on improving the setup. The Molecular Foundry at LBNL is an invaluable resource for nano-scale science research. In particular I would like to thank Scott Dhuey for his amazing e-beam lithography work and quick turn-around times with our samples, Deirdre Olynick, for her insights and fabrication tips on all things nano, and Stefano Caribi for keeping the Foundry cleanroom running and as hassle-free to users as possible. I would also like to express my sincere gratitude to Jeffrey Neaton for patiently helping me with *ab inito* calculations early on.

Away from Berkeley, I would like to thank Rogerio de Sousa (now at the University of Victoria, B.C., Canada). His encouragements and insights into the theoretical aspects of this work are always much valued. Professor T.-C. Shen (Utah State University), who — during my very first days in the cleanroom — patiently spent two hours training me to re-thread the wirebonder during his sabbatical at Berkeley, and also for measuring devices we have sent to his lab over the years.

Towards the East Coast, in the duration of my graduate work I have been extremely lucky to have been able to visit Professor Steve Lyon's group at Princeton University on more than several occasions. It is in his lab that I first learnt the art of cryogenics, EPR, EDMR, and simply doing experiments properly. Steve's enthusiasm and insights were always helpful, and discussions during morning coffee and Friday chowder always stimulating. I thank Alexei Tyryshkin in particular, for patiently training me, answering my silly questions, sharing his encyclopedic knowledge of EPR and sharp intuitions, and driving me back and forth to my hotel during my visits. It is from Alexei that I learnt the basic skills as an experimentalist (including the habit of not wearing cryo-gloves), and I would always treasure our time working together in that dark, noisy and often humid basement of the Chemistry

[1]Christoph: you'll get your chance to defend this statement in your thesis.

building, known as the EPR lab. The students in Lyon Group: Shyam Shanker, Jianhua He and Forrest Bradburry were always welcoming and helpful, and I thank them all for their hospitality.

Across the Atlantic, I would need to thank John Moron and the Quantum Spin Dynamics group at the University of Oxford for giving me the opportunity to attempt W-band EDMR measurements. John's invitation to formal dinner at St. John's was eye-opening, and I learnt the important lesson of licking my fingers first before putting out candles. Special thanks go to Volker Lang, who designed and fabricated the elegant W-band probe. We have spent countless hours in CAESR trying to get W-band EDMR to work, and discovered the difficulty in getting a good-old compass in this day and age (which turned out to be crucial in getting W-band EDMR to work!). Together we have made it a tradition to *Maison Blanc* for afternoon break and *Wagamama* for dinner, which I very much look forward to every time I visit. It was always a pleasure doing experiments with Volker, and his pursuit for details and excellence is always inspiring. I would also like to thank Richard George for his help with the measurements and insights into the physics of our experiments. Across the English Channel I would like to thank Sergi Zvyagin (Dresden High Magnetic Field Laboratory) for letting us attempt high-field EDMR in his lab. Sergi's hospitality (and cold medicine) are very much appreciated.

Last but not least, I would need to express my profound gratitude for my family: dad, mom, Cheuk Ming, Madeline, little Andrew and Pervina, for their love and unwavering support throughout the years.

Chapter 1

Introduction

Modern computational technology is based on the charge degree of freedom of carriers to convey information, while another intrinsic property of carriers — their spin degree of freedom — has been largely neglected. The steady advances in computational capacities of charge-based devices over the last few decades have been made possible by our ability to shrink electronic components smaller and smaller to enhance their operational speed. However, as devices are scaled down to the nano-scale, fundamental physical limitations will hinder further improvements in device performances within two decades [1]. Therefore, alternative physical resources need to be explored for the sustained improvements in computational capacities. The intrinsic spin degree of freedom of charged carriers is one such physical resource that can be exploited. The utilization of this extra spin degree of freedom for improving the performance of *classical* computational tasks forms the basis of the burgeoning field of spintronics [2]. One can also exploit the inherently quantum mechanical nature of spin to construct *quantum computers* for quantum information processing and efficient quantum mechanical simulations [3].

1.1 Spintronics

The field of spintronics explores the utilization of the spin degree of freedom of charged carriers to perform classical computational tasks. The spin of a charged carrier (e.g. electron) can be thought of as a small magnetic moment that can point upwards (spin up) or downwards (spin down), in analogy to the needle of a compass. One simple illustration of constructing a spin-based classical computer involves the utilization of individual electronic spin states to represent the binary logic levels for information processing [4]. However, such a scheme seems technologically prohibitive to realize due to the small magnetic moment of individual spin states. More realistic spin-based schemes involve information represented by ensembles of spins, such as the magnetization of single-domain nano-magnets [5] and *spin currents* — in analogy to charged currents — for information processing [6]. Early spintronic devices

include metallic ferromagnetic systems such as spin-valves and magnetic tunnel junctions. These technologies have contributed immensely to the improvement of magnetic storage medium [2]. A broader goal is to achieve spin-based logic devices that would complement or even replace CMOS technology. Complementary technologies would combine spin-enabled functionalities with more traditional semiconductor devices, for instance the incorporation of ferromagnetic contacts to silicon MOSFET to implement efficient field-programmable logic devices. A famous example of a proposed replacement technology to CMOS is the Datta-Das spin transistor [7]; however, its implementation has been elusive and its competitiveness as a logic device is still under debate [8, 9]. Nevertheless, many other schemes exploring the spin degree of freedom in semiconductors have been pursued in recent years [10].

The behavior of the spin degree of freedom of charged carriers in a given material system has to be well understood in order to realize these novel computational devices. The biggest challenge in studying spin effects in semiconductors is the difficulty in injecting non-equilibrium spin populations into semiconductors using ferromagnetic contacts. This effect is called the *conductivity mismatch* problem [11], and has been circumvented by the utilization of tunnel barriers at the ferromagnet injector-semiconductor interface [12, 13]. A second challenge, more specific to studying spin effects in silicon, is the difficulty in detecting spin polarization in the material. Optical techniques are often used for the detection of spin population of charged carriers in semiconductors. However, the optically inactive silicon substrates render this technique difficult to apply. This thesis contributes to the study of carrier spin effects in silicon by exploiting the technique of electrically detected magnetic resonance to detect polarization changes in silicon devices without the elaborate detector technology.

1.2 Quantum computation

Our ability to manipulate information and perform computational tasks depends on how the information is represented. In a classical computer, information is stored in binary logic *bits* of 1's and 0's. However, information can also be represented by quantum mechanical states as well. The simplest example is a quantum mechanical two-level system, represented by the state $\psi = \alpha|1\rangle + \beta|0\rangle$. In this case, this basic unit for information processing is referred to as a quantum mechanical bit, or *qubit*. Information processing with quantum mechanical qubits allows additional resources, namely the quantum mechanical effects of superposition (the state can simultaneously be in a $|1\rangle$ state and a $|0\rangle$ state) and entanglement (different quantum mechanical states interact and evolve simultaneously), to be exploited when designing algorithms for solving computational tasks [14, 15]. In 1982, Richard Feynmann proposed the use of quantum mechanical systems to perform quantum mechanical simulations, a task which is inherently difficult to perform on a classical computer [16]. In 1994, Peter Shor published an algorithm — now known as Shor's algorithm — which shows that finding the prime factors of integers can be efficiently solved using a quantum computer [17].

The factoring problem has no efficient classical solution and is at the heart of modern day encryption techniques such as the Rivest-Shamir-Adleman (RSA) algorithm. The discovery of Shor's algorithm has propelled the entire field of quantum computation as it has become clear that a quantum information processor can be used to perform certain tasks much more efficiently than its classical counterparts.

Given the potential benefits of a quantum computer, what does it actually take to construct one? David DiVincenzo summarized the requirements for the physical realization of a quantum computer as follows [18]:

C-1. A scalable physical system with well characterized qubits

C-2. The ability to initialize the state of the qubits to a simple fiducial state

C-3. Long relevant decoherence times, much longer than the gate operation time

C-4. A universal set of quantum gates

C-5. A qubit-specific measurement capability

Two additional criterion were added for quantum communication, which is essential for building a large scale quantum computer:

C-6. The ability to interconvert stationary and flying qubits

C-7. The ability to faithfully transmit flying qubits between specific locations

Loss and DiVincenzo [3] and Kane [19] proposed two different types of spin qubits in the solid-state in 1998. Both proposals received tremendous attention due to the promises of scalabilities with solid-state implementations of quantum computers. While Loss and DiVincenzo proposed the utilization of confined electron spins for quantum information processing, Kane proposed using the nuclear spin states of shallow donors in silicon (electron spins still play an important role in this quantum computer as we will discuss in the next section). The realization of the Kane quantum computer is the underlying motivation for this work. In the next section, we will illustrate DiVincenzo's criterion using the original Kane architecture as an example.

1.2.1 The Kane quantum computer

Kane proposed the use of shallow donors in silicon for achieving spin-qubits in the solid state [19]. Silicon is an attractive host material for spin-based quantum computation due to the long spin relaxation and spin coherence times (we will define these terms more rigorously in Chapter 2). In addition, the spectacular success of the modern silicon microelectronics

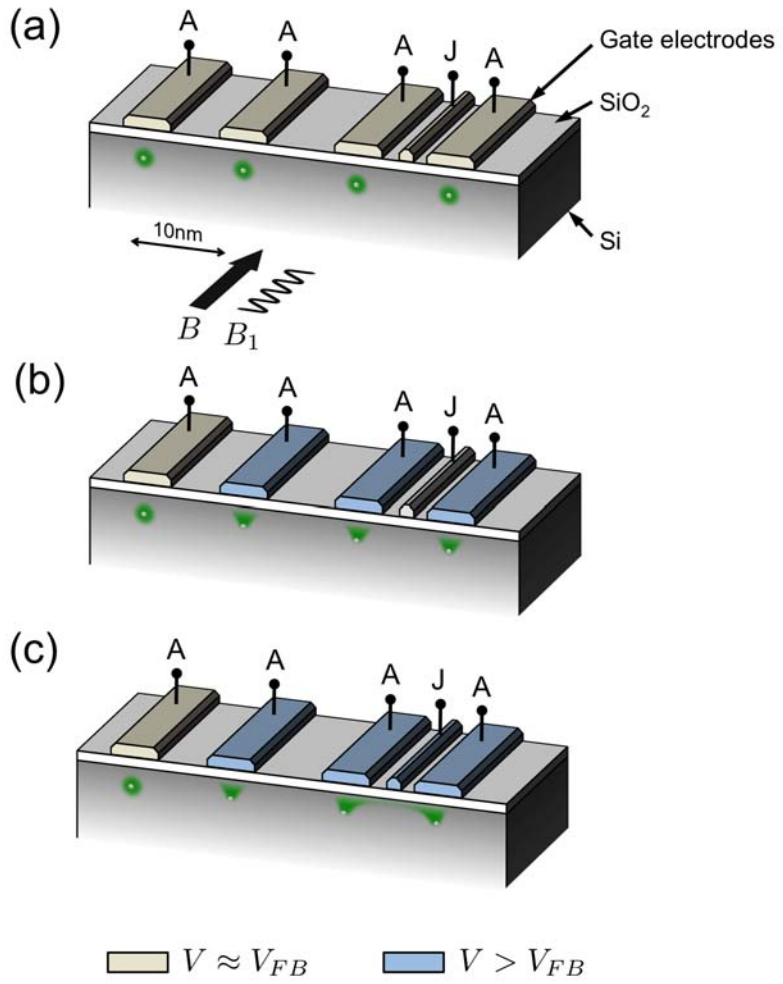

Figure 1.1: Schematics of the Kane quantum computer. (a) Array of donor qubits placed under surface gates. Green regions represent the donor electron wave functions. The globally applied static B and oscillating B_1 magnetic fields are also shown. (b) When the A-gates are set to above the flat-band voltage V_{FB}, the hyperfine couplings of the donor electrons are shifted, allowing qubit-selectivity for spin manipulation. (c) Inter-qubit J-gates allow adjacent donor electrons to interact by drawing the electronic wave functions to overlap with each other.

industry promises an easier path towards large-scale fabrication and integration of silicon-based quantum devices.

The essence of the Kane quantum computer is illustrated in Fig. 1.1(a). The proposed computer consists of ordered arrays of shallow donors (e.g. ^{31}P) approximately 10 nm apart embedded in a silicon, placed close to the Si-SiO_2 interface and under nano-scale gate electrodes. At low temperature the donors are neutral with one electron residing at each donor site. The spin states of the donor nuclei form the qubit states for the quantum computer (DiVincenzo's first criteria, see C-1 in the previous section). The donor electron and nuclear spins are initialized with the application of a large dc magnetic field B (C-2). The shallow donor nuclear spin states in silicon are known to have extremely long spin relaxation times (seconds to hours) at cryogenic temperatures, and can be further prolonged with the use of isotopically enriched silicon-28 material (C-3).

Single qubit operations are carried out by applying an ac magnetic field B_1 to achieve nuclear spin resonance. As the ac field is applied globally, individual qubits can be tuned in and out of the resonance field by changing the hyperfine coupling between the donor electron and nuclear spins. The shift in hyperfine coupling is accomplished by applying appropriate voltages to the A-gates located directly above the dopants, which in turn perturbs the electron wave function as shown in Fig. 1.1(b). Multi-qubit interaction between adjacent nuclear spins is performed by electron-mediated exchange interaction. The strength of this interaction is determined by the overlap between neighboring electron wave functions, which can be controlled by the inter-qubit J-gates as shown in Fig. 1.1(c). The availability of both single and multi-qubit control forms the basis of a universal set of quantum gates (C-4).

In order to read out the spin-states of selected qubit sites, a spin-dependent charge transfer process between two adjacent neutral donors is proposed. The charge transfer process is then monitored by a sensitive charge detector nearby (C-5). This readout problem will be discussed in more detail in the next chapter. The issues of quantum communication were not specifically addressed in the original proposal; however, subsequent modifications of the original scheme have proposed the use of shuttling electrons to perform long range communication beyond nearest neighbor interaction (C-6 and C-7) [20].

1.2.2 Recent progress in silicon-based quantum computation research

It is evident from the discussion above that the realization of the Kane quantum computer is a formidable task, requiring both innovative advances in nano-fabrication technologies and enhanced understanding of the physics behind the control, interaction and limitations of donors in silicon. In this section we will summarize some of the key advances which have been made towards the realization of such a computer since the original proposal.

Donor placement in silicon Ion implantation has long been the method of choice for dopant placement in the semiconductor industry. There are two major challenges for the creation of donor arrays with ion implantation. First, a method needs to be implemented to verify the occurrences of single-ion implantation events. A few approaches have been developed to address this issue, including the detection of secondary electrons from highly charged ions [21, 22, 23, 24], charge collection from photodiode-like detectors [25, 26, 27, 28, 29] and the direct measurement of changes to electrical transport characteristics in nano-scale devices [30, 31, 32, 33]. The second challenge is the placement of single ions at desired locations with near-atomic precision. Groups have demonstrated the use of nano-meter scale apertures with photoresist [34, 35, 36, 31, 37], or implantation windows close to the tips of scanning probes for dynamic ion placements [38, 39]. With such techniques, single-ion implants of approximately 5 nm precision have been demonstrated. An alternative approach for donor placement with near-atomic precision on the surface of silicon has also been developed using hydrogen lithography with scanning probe microscopy [40, 41, 42, 43]. The creation of nano-scale device structures with ^{31}P donors has been achieved using this technique [44], paving the way towards the creation of large-scale donor arrays. However, the ability to place different donor species with this technique remains unclear.

Single-spin addressability The tuning of the dopant spin resonance conditions with A-gates requires a measurable *Stark shift* controlled by the gate-induced electric field. Such tuning with electric fields was first demonstrated by Bradbury *et al* using an in-plane capacitor geometry on a large ensemble of donors [45]. However, the demonstrated Stark effect was much smaller than originally anticipated from effective mass theory calculations. More recently, measurements of donor-mediated transport in nano-scale devices under large electric fields have shown Stark effects that agree well with more sophisticated tight-binding calculations [46, 47]. An alternative strategy for adjusting the hyperfine interaction of donors is by inducing strain into the device [48]. The electrostatic tuning of the strain in donor doped silicon and its subsequent Stark shift have been recently reported [49].

Multi-gate operation The six-fold degenerate conduction band minima of silicon causes interferences in the donor electron wave functions [50], and this results in oscillatory behavior in the exchange coupling strength with donor-donor position [51]. To avoid the oscillatory behavior of exchange coupling, the evolution under magnetic dipolar interaction has been proposed to be used to achieve qubit-qubit interaction instead of relying on exchange interaction [52]. Another proposal is to use the Hilbert space of electron-nuclear spin pairs instead of donor nuclear spins alone [20]. Electron shuttling is proposed to guide donor electrons to other donor sites to enable multi-qubit interaction. Coherent transfer by adiabatic passage has been proposed to achieve electron shuttling [53]. However, experimental demonstration of such schemes remains elusive.

Spin-state readout In the original Kane proposal, a spin-dependent charge transfer process from adjacent neutral donors was proposed to achieve single donor spin-state readout. However, subsequent calculations have shown that this process is unlikely to succeed due to the weak binding energy of the doubly-occupied donor state [54]. A variety of different spin-to-charge conversion mechanisms have since been proposed [55, 56, 57, 58, 59, 60]. Indeed, the utilization of a silicon MOS device to perform donor spin-state readout is one of the major motivations for this work. We will address these different spin-state readout schemes in more detail in Chapter 2.

Silicon quantum dots In addition to shallow donors, confined electrons in artificial quantum dots can also be used for spin-based quantum information processing [3]. Quantum dot formation can be achieved by electrostatic confinement induced by gate electrodes on the surface of the substrate. While great progress has been made in creating electrostatically defined quantum dots in III-V semiconductors such as GaAs systems [61, 62, 63], experiments in silicon has lagged due to the difficulty in achieving few-electron quantum dots as the effective mass is much larger in silicon. Early efforts for achieving electrostatically defined quantum dots in silicon have focused on silicon-germanium (SiGe) modulation-doped heterostructures [64, 65, 66]. These heterostructures offer much lower interface defect densities compared to the Si-SiO_2 interface. Rapid progress has been made in the past few years in which few-electron quantum dots in SiGe have been created successfully, and the spin-relaxation times measured [67, 68]. More recently, several groups have begun investigating silicon Si-SiO_2 MOS quantum dots [69, 70, 71], and high quality devices have been achieved with improved material processing and fabrication methods.

Electron or nuclear spin? In Kane's original proposal, the nuclear spins of shallow donors form the basis of the qubits. However, it was also recognized that the electron spin is much easier to address. Since the nuclear spins have much longer spin relaxation times than electron spins [72], electrons are better suited for communication and readout, while the nuclear spins can serve as quantum memory storage. The coherent transfer of quantum information between the electron and nuclear spin states of donors has recently been demonstrated in ensembles of neutral donors [73]. Much progress has been made towards the measurement and understanding of the spin relaxation times of donor electrons and electrostatically confined electrons in silicon. Some of these results are summarized in Fig. 1.2 [72, 24, 74, 60, 59, 75, 76, 69, 77, 68]. The goal of this work is to address the donor *nuclear* spin-state readout problem using *electron* spin resonance techniques, as we will explore in detail in subsequent chapters. However, we should note that quantum information processing can still be carried out with the electron spin, as an electron-nuclear spin-swap can be used to convert the electron spin-state to the nuclear spin-state for readout [73].

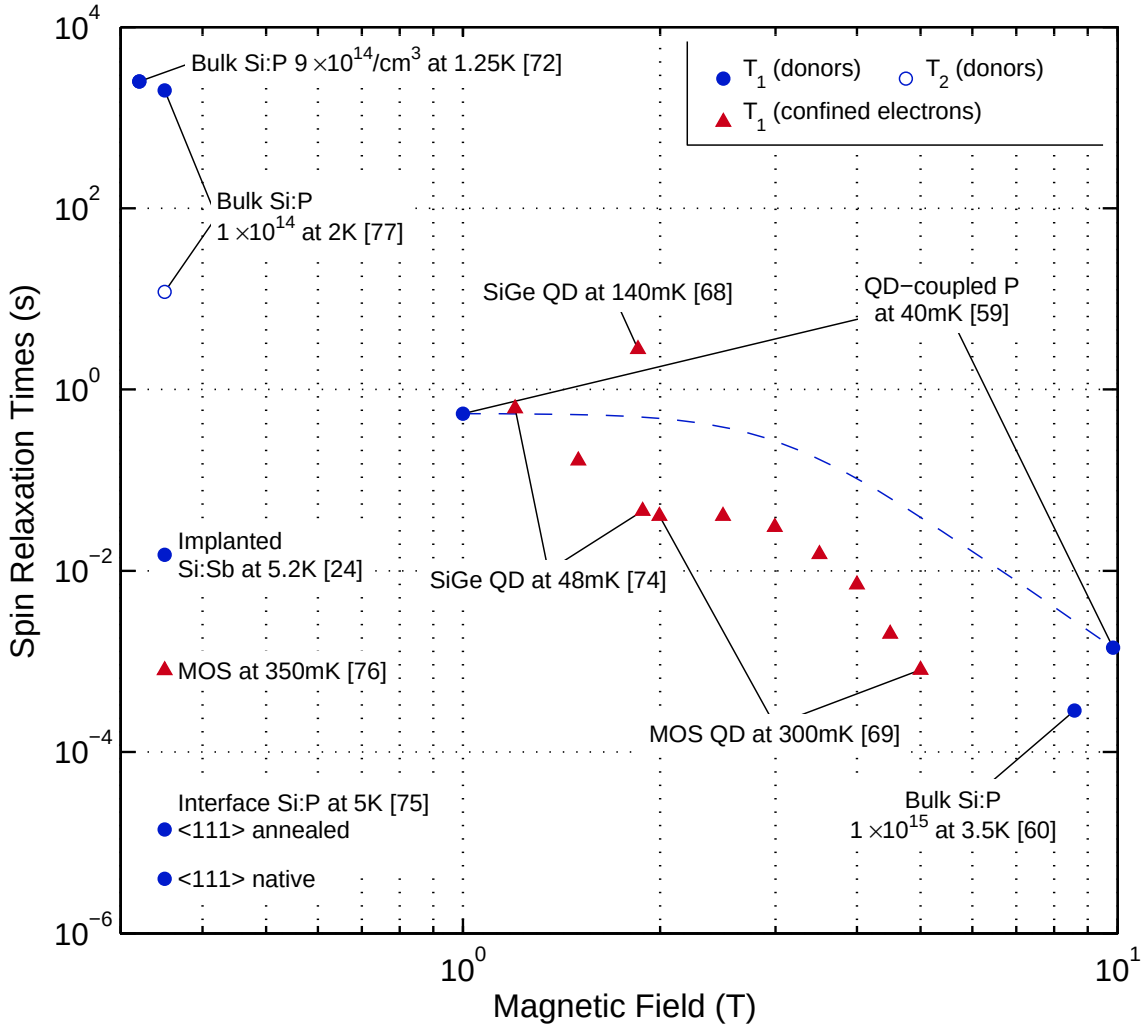

Figure 1.2: Spin relaxation times in silicon reported in literature for both donor electrons and naturally or electrostatically confined conduction electrons, such as in quantum dots (QD).

1.3 Overview of thesis

Addressing the donor spin-state readout problem is a main motivator for this work. The spin-to-charge conversion mechanism, i.e. the spin-dependent transport mechanism in silicon, must be well understood in order to harness it for quantum readout. This thesis contributes to the understanding of spin-dependent transport in silicon MOSFETs and the donor-conduction electron interaction in such systems. It encompasses device fabrication of specially designed donor-doped MOSFETs and also other silicon-based devices useful for gaining insights towards donor based qubits in silicon. Much effort is also devoted towards the development of the experimental capabilities required for probing spin-dependent transport in these devices.

Chapter 2 provides the theoretical background on various aspects of the work reported in later chapters. The spin angular momentum of electrons, theoretical description of spin resonance and the spin Hamiltonian are introduced. Various spin-dependent transport mechanisms are reviewed, and the basic physics of MOSFETs operating in the quantum limit is also discussed.

Chapter 3 covers the experimental techniques used in this work. Electron paramagnetic resonance (EPR) is first introduced. The technique used to study spin-dependent transport in microscopic devices — electrically detected magnetic resonance (EDMR) — in both low field (X-band) and high field (W-band) are both described in this chapter. The setup for transport spectroscopy of nanoscopic devices is also discussed.

Chapter 4 examines the spin-dependent transport mechanism in silicon MOSFETs. It is found that the conventional spin-dependent scattering picture is insufficient in explaining our observations; and instead, a polarization-dependent resistivity model seems to be more valid.

With the spin-dependent transport mechanism better understood, more systematic study of the spin-dependent transport of various types of MOSFETs is detailed in Chapter 5, and the spin relaxation and spin coherence times of conduction and donor electrons are extracted. Chapter 6 then examines the effects of spatial inhomogeneity in carrier polarization and its effects on spin-dependent transport measured in MOSFETs with EDMR.

Chapter 7 discusses the designs and fabrications of single-ion implantation compatible nano-scale MOS device architectures: the 28SOI-finFETs and triple-gate TG-finFETs. The EDMR results and transport spectroscopy of these devices are also examined.

Finally, Chapter 8 concludes by summarizing the main results obtained in this work and discusses potential future experiments towards the realization of donor spin-state readout MOS devices.

Chapter 2

Theoretical Background

In this chapter, we will review the theoretical foundations behind our experiments. We begin with a description of spin resonance with the phenomenological Bloch equations. The energy levels of the spin states and allowed transitions are then described by the introduction of the spin Hamiltonian. We then examine the known spin-dependent transport mechanisms in silicon. The theoretical description of silicon MOSFETs operating at low temperature is then discussed.

2.1 Electron spin in solid-state

There are three different approaches to formulate a mathematical description of spins. The first, the Bloch equations, relies on a phenomenological description of the spin system in terms of the (bulk) magnetization of the system [78]. This framework provides an intuitive picture to visualize the evolution of the spin system; as such, spin manipulation is also conveniently introduced in this formalism. The second, the spin Hamiltonian, concerns more specifically the energy levels of the spin system, which is essential for understanding the excitation spectra in spin resonance experiments. The last approach uses density matrices to describe the quantum mechanical state of the ensemble of spins, and is useful for understanding the relaxation mechanisms in the spin systems. We will review the first two frameworks in this chapter as they will be sufficient for understanding the bulk of the results obtained in this thesis. The reader is referred to Schweiger and Jeschke [79] and Slitcher [80] for a complete treatment with the density matrix approach.

2.1.1 Bloch equations and spin resonance

We begin with a description of the relationship between the electron spin and magnetic moment. Once this relationship is established, the equation of motion for the magnetic moment can be described in the semi-classical framework of the Bloch equations, which

forms for basis for the understanding of basic electron paramagnetic resonance (EPR).

The magnetic moment associated with an electron with angular momentum $\mathbf{S}$ — the intrinsic spin angular momentum — is given by [78, 80, 79][1]:

$$\mu = -g\frac{q\hbar}{2m_0}\mathbf{S} = -g\mu_B\mathbf{S} \tag{2.1}$$

where $q = 1.6 \times 10^{-19}$ C is the electron charge, $m_0 = 9.1 \times 10^{-31}$ kg the electron mass, $\hbar = 1.0546 \times 10^{-34}$ J-s the reduced Plank constant and $\mu_B = 9.27 \times 10^{-24}$ J/T the Bohr magneton. The Landé g-factor is a purely quantum mechanical effect, and has a value of $g \approx 2$ ($g = -1$ in the classical picture). We will describe this g-factor in more detail later in the next section. In a sample with many spins, i.e. paramagnetic electrons, the net magnetization of the sample is given by the summation of individual magnetic moments:

$$\mathbf{M_0} = \sum_i \mu_i \tag{2.2}$$

When a magnetic field $\mathbf{B} = (0, 0, B_0)$ is applied[2], the time-evolution of the magnetization is given by the classical equation of motion:

$$\frac{\partial \mathbf{M}}{\partial t} = \gamma \mathbf{M} \times \mathbf{B} = (-\omega_0 M_y, -\omega_0 M_x, 0) \tag{2.3}$$

where $\gamma = \frac{g\mu_B}{\hbar}$ is known as the gyroscopic factor and $\omega_0 = \gamma B_0$ the *Larmor frequency*, which is the frequency at which the magnetization vector precesses about the $\hat{z}$ axis. Felix Bloch introduced a phenomenological set of equations for describing the time evolution of magnetization in the presence of the quantum mechanical effects of spin relaxation. The Bloch equations read:

$$\frac{\partial \mathbf{M}}{\partial t} = (-\omega_0 M_y, -\omega_0 M_x, 0) + \left(\frac{M_x}{T_2}, \frac{M_y}{T_2}, \frac{M_0 - M_z}{T_1}\right) \tag{2.4}$$

where M_0 is the thermal equilibrium magnetization of the sample. T_1 describes the characteristic timescale in which the magnetization along the principle axis relaxes, and is called the longitudinal spin-lattice relaxation time. This process involves energy exchange from the spin system to the lattice. T_2 describes the timescale in which the transverse magnetization changes, and is called the transverse spin relaxation time. This relaxation process does not involve energy transfer from the spin system to the lattice. Although the Bloch equations are developed for the classical observable of magnetization, it can be shown to be formally exact to the treatment of quantum mechanical two-level systems using density operators to describe the spin ensemble [80].

[1] Here we assume the orbital angular momentum $\mathbf{L}$ to be zero, an assumption valid for ground-state donor electrons and conduction electrons in silicon.

[2] We will refer to the magnetic induction B as the magnetic field in this thesis, a practice which is common in modern EPR literature.

Spin resonance occurs when an oscillating magnetic field is introduced to the system. In the following we assume the magnetic field $\mathbf{B}$ is static and the oscillating field $\mathbf{B_1}$ is circularly polarized in the x-y plane with angular frequency ω_{ac} [3]:

$$\mathbf{B_1}(t) = B_1 \left(\cos(\omega_{ac}t), \sin(\omega_{ac}t), 0\right) \tag{2.5}$$

To understand the effect of the oscillation field, it is convenient to introduce the rotating coordinate system, where the observer rotates about the $\hat{z}$ axis at angular frequency ω_{ac}. In this rotating frame, the x-component of $\mathbf{B_1}(t)$ becomes stationary with amplitude B_1. The Bloch equations in the rotating frame then read:

$$\frac{\partial \mathbf{M}}{\partial t}^R = \left(-\Omega M_y + \frac{M_x}{T_2}, -\Omega M_x - \omega_1 M_z + \frac{M_y}{T_2}, \omega_1 M_y + \frac{M_0 - M_z}{T_1}\right) \tag{2.6}$$

where $\Omega = \omega_0 - \omega_{ac}$ and $\omega_1 = \gamma B_1$ is the *Rabi frequency* describing the precession of the magnetization about the oscillating field component in the rotating frame. The components of magnetization can be solved easily in the rotating frame:

$$\begin{aligned} M_x^R &= \frac{\omega_1(\omega_0 - \omega_{ac})T_2^2}{1 + (\omega_0 - \omega_{ac})^2 T_2^2 + \omega_1^2 T_1 T_2} M_0 \\ M_y^R &= \frac{-\omega_1 T_2}{1 + (\omega_0 - \omega_{ac})^2 T_2^2 + \omega_1^2 T_1 T_2} M_0 \\ M_z^R &= \frac{1 + (\omega_0 - \omega_{ac})T_2^2}{1 + (\omega_0 - \omega_{ac})^2 T_2^2 + \omega_1^2 T_1 T_2} M_0 \end{aligned} \tag{2.7}$$

and they are related to the complex susceptibility:

$$\chi = \chi' + i\chi'' = \frac{M_x^R}{B_1} - i\frac{M_y^R}{B_1} \tag{2.8}$$

where the in-phase component χ' corresponds to dispersion, and the out-of-phase component χ'' corresponds to absorption. This is related to the power absorbed by the sample P [78]:

$$P = \frac{\partial}{\partial t}(-\mathbf{M} \cdot \mathbf{B}) = \omega_{ac}\chi'' B_1^2 \tag{2.9}$$

Thus, the power absorbed by the sample can be computed once the imaginary (absorption) component of the susceptibility is known. In the limiting case of weak oscillating fields, $\omega_1^2 T_1 T_2 << 1$:

[3] The assumption of circularly polarized oscillating fields is merely for mathematical simplicity. The commonly used linearly polarized oscillating fields in experiments can be thought of as two circularly polarized fields with the angular components rotating in opposite directions.

$$\chi'' = \frac{\gamma T_2}{1 + (\omega_0 - \omega_{ac})^2 T_2^2} M_0 \tag{2.10}$$

and in the opposite limit of strong saturation, $\omega_1^2 T_1 T_2 >> 1$:

$$\chi'' = \frac{1}{1 + (\omega_0 - \omega_{ac})^2 \left(\frac{T_2}{\sqrt{1+\omega_1^2 T_1 T_2}} \right)^2} \tag{2.11}$$

The absorbed power strongly peaks when $\omega_{ac} = \omega_0$, and this is the resonance condition in EPR. The absorption linewidths of the EPR signals are related to the transverse relaxation time T_2. However, if the sample is strongly inhomogeneous, the absorption lines will be artificially broadened by a distribution, usually Gaussian in nature. If this is the case, the measured linewidth does not represent the transverse relaxation time and we denote the measured linewidth as T_2^*. It is related to the transverse relaxation time by the *phase memory time* T_m of a single spin by:

$$\frac{1}{T_2} = \frac{1}{T_2^*} + \frac{1}{T_m}. \tag{2.12}$$

On the other hand, if the sample is homogeneous and the linewidth is limited by the intrinsic T_2, the spectral absorption line has a Lorentzian lineshape.

In EPR, it is the power absorbed by the sample that is monitored in the experiment (Chapter 3). We have seen that the power absorbed is sensitive to the transverse components of magnetization only (Eqs. 2.8 and 2.9). An important difference between conventional EPR and electrically detected EPR (also known as electrically detected magnetic resonance — EDMR) is that in the latter case, it is changes to the longitudinal component M_z that are measured instead. This will be addressed briefly in the following sections, and discussed more thoroughly in Chapters 4 and 5 for the case of EDMR of MOSFETs.

2.1.2 Spin Hamiltonian

The Hamiltonian for describing the spin of electrons (the spin Hamiltonian) is given by [78, 81, 79]:

$$\mathcal{H}_{\mathcal{S}} = \mathcal{H}_{\mathcal{ZE}} + \mathcal{H}_{\mathcal{HF}} + \mathcal{H}_{\mathcal{SS}} + \mathcal{H}_{\mathcal{SO}} \tag{2.13}$$

where the terms on the right hand side correspond to the Zeeman, hyperfine, spin-spin interaction, and spin-orbit interaction contributions, respectively.

The Zeeman term describes the interaction of spin with a magnetic field, and is given by:

$$\mathcal{H}_{\mathcal{ZE}} = \left(\frac{\mu_B}{\hbar} \right) \mathbf{S} \cdot \mathbf{g} \cdot \mathbf{B} \tag{2.14}$$

where $\mathbf{S}$ is the spin angular momentum operator for electrons in units of $\hbar$, and $\mathbf{B}$ the applied magnetic field. The Landé g-tensor, $\mathbf{g}$, is a consequence of spin-orbit coupling and can be accurately calculated for a given bandstructure. It is generally anisotropic in crystals, and hence a tensor. Since silicon has very weak spin-orbit coupling, the g-factor of electrons in silicon generally has $g \approx 2$. Both the value of g and its anisotropy for conduction electrons in silicon MOSFETs will be discussed in Chaper 5.

The hyperfine interaction results from the interaction between the electronic spin and a nearby nuclear spin $\mathbf{I}$. If only one such nuclear spin is present, such as the case of singly occupied neutral donors, it is given by:

$$\mathcal{H}_{\mathcal{HF}} = \mathbf{S} \cdot \mathbf{A} \cdot \mathbf{I} \tag{2.15}$$

where $\mathbf{A}$ is the hyperfine interaction tensor, and $\mathbf{I}$ the nuclear spin. For shallow donors in silicon, $\mathbf{A}$ is mostly isotropic due to the symmetry of the donor electron wave function, and this contribution is proportional to the wave function at the nuclear site: $A = \frac{2}{3}\frac{\mu_0}{\hbar} g\mu_B g_n \mu_n |\psi(\mathbf{r_i})|^2$, where μ_0 is the vacuum permeability, g_n and μ_n the nuclear g-factor and the nuclear magneton, respectively [50, 72]. This contribution is also known as the Fermi contact hyperfine interaction. It is the tunability of $\mathbf{A}$ via ψ that forms of basis of the hyperfine A-gate of the Kane quantum computer [19]. Different donor species have different hyperfine coupling strengths due to changes in the electronic wave function. This will be discussed in more detail when we examine the EDMR spectra in Chapter 4.

The spin-spin interaction results from the influence of nearby (electron) spins. There are two types of spin-spin interactions that are of particular importance to donor qubits: the dipole-dipole coupling and exchange interaction. For two electrons 1 and 2, the dipolar term can be expressed as:

$$\begin{aligned} \mathcal{H}_{\mathcal{SS},\mathcal{D}} &= \mathbf{S_1} \cdot \mathbf{D} \cdot \mathbf{S_2} && (2.16) \\ &= \frac{1}{r_{12}^2}\frac{\mu_0}{4\pi\hbar} g^2 \mu_B^2 \left[\mathbf{S_1}\mathbf{S_2} - \frac{3}{r_{12}^2}(\mathbf{S_1}\mathbf{r_{12}})(\mathbf{S_2}\mathbf{r_{12}}) \right] && (2.17) \end{aligned}$$

where $\mathbf{r_{12}}$ is the spatial separation of the two electrons with distance r_{12}. The exchange interaction is given by:

$$\mathcal{H}_{\mathcal{SS},\mathcal{J}} = \mathbf{S_1} \cdot \mathbf{J} \cdot \mathbf{S_2} \tag{2.18}$$

where $\mathbf{J}$ is the exchange integral given by the overlap of the spatial wave functions. While spin-spin interactions are dominant sources of decoherence, they can be exploited for multi-qubit interaction as originally proposed by Kane (J-coupling) [19] and de Sousa, Delgado and Sarma (D-coupling) [82].

Lastly, the spin-orbit coupling is given by:

$$\mathcal{H}_{\mathcal{SO}} = \lambda \mathbf{L} \cdot \mathbf{S} \tag{2.19}$$

where λ characterizes the strength of this interaction. There are two forms of contributions to this term [83]: (i) the Dresselhaus spin-orbint coupling (also called bulk-induced anisotropy), resulting from anisotropy in the crystal lattice [84] and (ii) Rashba spin-orbit coupling (also called surface-induced anisotropy), resulting from spatial inhomogenties of the potential landscape [85]. The Dresselhaus term does not contribute in silicon, as silicon has inversion symmetry in the crystal lattice. On the other hand, the Rashba term might be important for conduction electrons at the Si-SiO_2 interface in a MOSFET, due to the large electric fields present.

For shallow donors in silicon, the most important contributions are the Zeeman and hyperfine interactions. For the $S = 1/2$ electron and $I = 1/2$ donor nucleus with isotropic interactions and under an applied magnetic field of $\mathbf{B} = B\hat{z}$, the first-order spin Hamiltonian is given by:

$$\begin{aligned} \mathcal{H}_d &= \mathcal{H}_{\mathcal{Z}\mathcal{E}} + \mathcal{H}_{\mathcal{H}\mathcal{F}} \\ &= \frac{g\mu_B}{2} B\sigma_{\mathbf{S}} + \frac{A}{4}\sigma_{\mathbf{S}} \cdot \sigma_{\mathbf{I}} \end{aligned} \tag{2.20}$$

where the Zeeman interaction of the nucleus is omitted as it is three orders of magnitude smaller than the electron Zeeman term. We have also expressed the spin operators in terms of the Pauli matrices:

$$\sigma_x = \begin{pmatrix} 0 & 1 \\ 1 & 0 \end{pmatrix} \quad \sigma_y = \begin{pmatrix} 0 & -i \\ i & 0 \end{pmatrix} \quad \sigma_z = \begin{pmatrix} 1 & 0 \\ 0 & -1 \end{pmatrix} \tag{2.21}$$

as $\mathbf{S} = \frac{\hbar}{2}\sigma_{\mathbf{S}}$ and $\mathbf{I} = \frac{\hbar}{2}\sigma_{\mathbf{I}}$. This Hamiltonian can be expressed in terms of the basis set $|m_s\rangle \otimes |m_I\rangle = |m_S m_I\rangle$. Using $\uparrow$ and $\downarrow$ to represent the $m_S = +\frac{1}{2}$ and $-\frac{1}{2}$ states, respectively, the eigenequation becomes:

$$\begin{bmatrix} \frac{g\mu_B}{2}B + \frac{1}{4}A & 0 & 0 & 0 \\ 0 & \frac{g\mu_B}{2}B - \frac{1}{4}A & \frac{1}{2}A & 0 \\ 0 & \frac{1}{2}A & -\frac{g\mu_B}{2}B - \frac{1}{4}A & 0 \\ 0 & 0 & 0 & -\frac{g\mu_B}{2}B + \frac{1}{4}A \end{bmatrix} \begin{bmatrix} |\uparrow\uparrow\rangle \\ |\uparrow\downarrow\rangle \\ |\downarrow\uparrow\rangle \\ |\downarrow\downarrow\rangle \end{bmatrix} = E \begin{bmatrix} |\uparrow\uparrow\rangle \\ |\uparrow\downarrow\rangle \\ |\downarrow\uparrow\rangle \\ |\downarrow\downarrow\rangle \end{bmatrix} \tag{2.22}$$

The eigenenergies of the system are found to be:

$$E = \begin{cases} \frac{g\mu_B}{2}B + \frac{1}{4}A \\ -\frac{1}{4}A + \sqrt{1 + (\frac{g\mu_B B}{A})^2} \\ -\frac{1}{4}A - \sqrt{1 + (\frac{g\mu_B B}{A})^2} \\ -\frac{g\mu_B}{2}B + \frac{1}{4}A \end{cases} \tag{2.23}$$

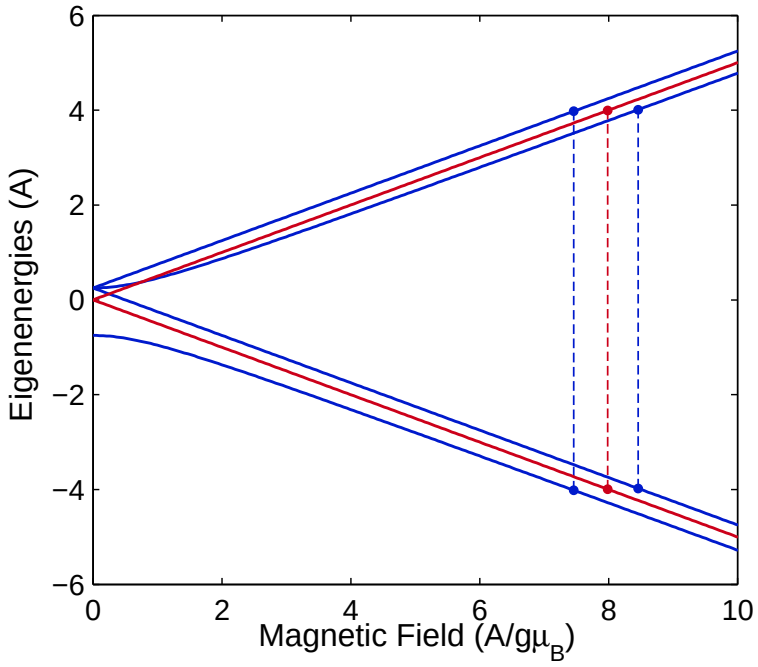

Figure 2.1: Energy levels and spin transitions for a $S = 1/2$ system. Zeeman field splitting in the absence of hyperfine interaction (red). Finite hyperfine interaction with strength A and nuclear spin $I = 1/2$ (blue). The allowed EPR transitions under high field conditions are indicated by dashed lines.

Fig. 2.1 shows the eigenenergies of the system as a function of magnetic field. Under the high field approximation ($g\mu_B B >> A$), the eigenstates are well described by the basis states.

The allowed transitions under ac field excitation can be calculated by the inclusion of the time-varying field to the Zeeman interaction term [78, 80]:

$$\begin{aligned} \mathcal{H}_{\mathcal{ZE}} &= \left(\frac{\mu_B}{\hbar}\right) g\mathbf{S}\cdot\mathbf{B_0} + \left(\frac{\mu_B}{\hbar}\right) g\mathbf{S}\cdot\mathbf{B_1}(t) \\ &= \mathcal{H}_0 + \mathcal{H}_1 \end{aligned} \tag{2.24}$$

where the transitions due to the second term can be computed using time-dependent perturbation theory. The transition rate per unit time from the unperturbed eigenstates due to the ac field is given by:

$$\Gamma_{m_S m'_S} = \frac{1}{t}\omega_1^2 |\langle m'_S|S_x|m_S\rangle|^2 \delta(E_{m'_S} - E_{m_S} - \hbar\omega_{ac}) \tag{2.25}$$

where $E_{m'_S} - E_{m_S}$ is the energy separation of the Zeeman-split levels. Since $S_x = \frac{1}{2}(S_+ + S_-)$,

the allowed EPR transitions are given by $\Delta m_S = \pm 1$ and $\Delta m_I = 0$. These transitions are shown as dashed lines in Fig. 2.1.

2.2 Spin-dependent transport in silicon

The study of the spin-dependence of charged carrier transport (i.e. spin-dependent transport) in silicon was first demonstrated by Maxwell and Honig [86]. They observed a spin-dependent photoconductivity in silicon at low temperatures and high magnetic fields [4]. These early measurements relied on studying the sample resistivity as the external magnetic field was varied. A leap from these early studies in gaining insights into the spin-dependent transport mechanisms came when the resistivity measurements were combined with the powerful spectroscopic technique of electron paramagnetic resonance (EPR), where spin transitions can be induced by microwave fields. Such electrical detection of electron spin resonance in silicon was first demonstrated by Lepine in 1972 [89], laying the foundations for the field of electrically detected magnetic resonance (EDMR). Since then, spin-dependent transport in numerous silicon systems and devices have been studied, including photoconductivity of crystalline silicon [90, 91, 92, 56, 75], irradiated silicon [93], amorphous silicon [94, 95], p-n junctions [96, 97, 98] and field-effect transistors [99, 100, 101, 102, 103].

Most EDMR measurements in silicon focus on the spin-dependent transport mechanism of spin-dependent recombination (SDR), where paramagnetic defects mediate the electron-hole pair recombination process. Therefore, the term EDMR is almost synonymous with SDR in the literature. However, all charge transport processes — scattering, tunneling, trapping and recombination — have some spin dependencies associated with them. Before we discuss these spin-dependent mechanisms in more detail, we will first review two general frameworks that are used to understand and interpret spin-depedent transport phenomena measured by EDMR.

2.2.1 Polarization models

The first type of spin-dependent transport models are called polarization models as they predict that the change in sample resistivity upon spin resonance is proportional to the polarization of the carriers (i.e. the fractional difference in the spin up and spin down populations):

$$p = \frac{n_\uparrow - n_\downarrow}{n_\uparrow + n_\downarrow} \tag{2.26}$$

In Lepine's original paper on spin-dependent recombination in silicon, he used such a model to explain his EDMR measurements [89]: under the applied magnetic field B, param-

[4] The change in photoconductivity was originally attributed to neutral impurity scattering [87]. It was later found to be due to spin-dependent trapping of doubly occupied donor states instead [88].

agnetic defects (which act as recombination centers) and photo-induced carriers will achieve thermal equilibrium polarizations p_{d0} and p_{c0}, respectively, resulting in a steady-state photocurrent. Assuming that carriers can only be captured by the recombination centers if the carrier-defect is in a *singlet* spin state, upon the resonance condition for either spin species, the thermal equilibrium polarization will be destroyed, i.e. $p \rightarrow 0$. Hence, the singlet content of the system increases, resulting in enhanced recombination and thus a lower steady-state photocurrent. In such a model, the fractional change in photoconductivity of the sample upon full saturation at resonance is given by:

$$\frac{\Delta\sigma}{\sigma} \approx p_{d0}p_{c0} \tag{2.27}$$

With the experimental conditions used by Lepine (room temperature and $B = 0.3$ T), $p_0 \approx g\mu_B B/k_B T \approx 10^{-3}$, and the expected change in photocurrent is thus $\approx 10^{-6}$. However, subsequent studies found SDR-EDMR signal amplitudes in the order of $\Delta\sigma/\sigma \approx 10^{-2} - 10^{-4}$ [96, 94, 90, 91, 92, 97], and it became clear that polarization models cannot explain the experimental observations in SDR-EDMR experiments. However, the polarization framework provides a good picture for understanding spin-dependent scattering (SDS) and spin-dependent tunneling (SDT) processes, as we will examine later in this chapter.

2.2.2 Spin-pair models

Kaplan, Solomon and Mott (KSM) proposed an alternative model to explain the SDR-EDMR signal amplitudes in 1978 [104]. The KSM model introduced the concept of local pairs such as donor-defect or donor-acceptor pairs. It is assumed that electron and holes are first captured by the defect pairs (e.g. electrons by donors and holes by acceptors), the pairs have to be in close proximity of each other allowing a weak exchange interaction and hence finite recombination. As before, singlet pairs are assumed to recombine much faster than triplet pairs. In this model the global carrier polarizations do not affect the recombination rates directly, as only the singlet and triplet populations of the local pairs do. Under thermal equilibrium conditions the singlet pairs are depleted as they recombine quickly after formation. Hence the triplet population is much higher than anticipated from simple thermal equilibrium polarization considerations. Upon resonance, triplet pairs can be converted to singlet pairs, and hence the steady-state current will decrease, as in Lepine's model. In the KSM picture, $\Delta\sigma/\sigma \approx 10^{-2} - 10^{-4}$ is easily obtainable and no magnetic field dependence has been found, in agreement with this model [96]. The KSM model has become central to the interpretation of SDR-EDMR experiments, especially in ^{31}P-P_b center recombination studies.

2.3 Spin-dependent transport mechanisms

As mentioned in the previous section, virtually all charge transport processes have associated spin dependences. We will briefly discuss these mechanisms in this section, keeping in mind that any one of them can potentially be used as a spin-readout mechanism if suitably implemented. As such, our discussion will focus on processes that pertain to shallow donors in particular. Some of these processes are shown schematically in Fig. 2.2.

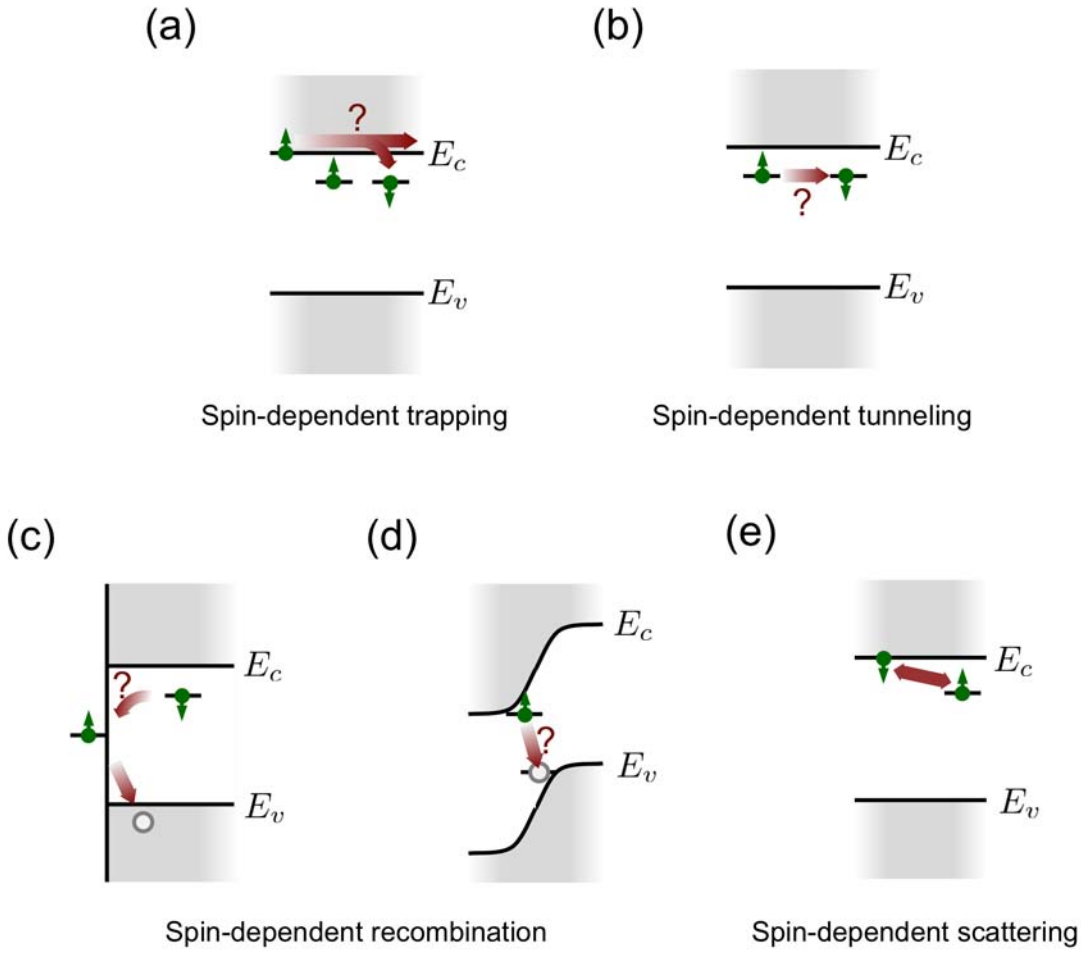

Figure 2.2: Spin-dependent transport mechanisms involving shallow donors in silicon.

2.3.1 Spin-dependent trapping

Spin-dependent charge trapping (Fig. 2.2(a)) was in fact one of the first spin-dependent transport phenomena studied in donor-doped silicon [86, 87, 88]. The essential element is the presence of paramagnetic trap centers, for instance shallow donors at low temperature. Shallow donors at low temperature have two charged states: the neutral D^0 state with one bound electron and the doubly occupied D^- state. The D^0 ground state has a binding energy of $E_b \approx 50$meV in silicon, while the D^- state only has a binding energy of $E_b \approx$ 1-2meV. This shallow D^- state only exists when the two bounded electrons are in a singlet configuration, while no bound triplet states exist (unless the magnetic field is very large). At sufficiently low temperatures, a D^0 state can capture a nearby conduction electron if the latter forms a singlet with the donor-bound electron. If the conduction electrons are completely polarized, e.g. under strong magnetic fields, this trapping mechanism by the D^0 state can be exploited for determining the original donor electron spin-state [60]. The formation of the D^- state can then be detected electrically due to increased Coulombic scattering centers in the system.

2.3.2 Spin-dependent tunneling

Spin-dependent tunneling (Fig. 2.2(b)) occurs under similar principles as spin-dependent trapping, but the electrons tunnel to localized paramagnetic states spin-dependently. The spin dependence of the tunneling probability is a result of spin Coulomb blockade. This was the central idea behind Kane's original spin-state readout proposal [19], where a spin-dependent tunneling process between a control donor D^0 state can be used to read out a nearby target qubit D^0 state, again relying on the formation of D^- state at the control site. This D^- state can then be detected by a nearby charge-sensitive single electron transistor. Similar donor spin-state readout schemes involve the spin-dependent tunneling from donors to adjacent quantum dots [59], or in principle paramagnetic trap states [105]. Spin-dependent tunneling has been very successfully used to perform spin-state readout in double quantum dot structures [61, 106, 63, 59].

2.3.3 Spin-dependent recombination

Spin-dependent recombination (Fig. 2.2(c)-(d)) occurs when both electron and holes are present in the system, either photoexcited or in a p-n junction. The recombination between electrons and holes pairs are greatly enhanced in the presence of mid-gap trap states, as shown by the Shockley-Read-Hall recombination theory [107]. If these states are paramagnetic, then a spin-dependence will result as the capture rate is spin-dependent as in spin-dependent trapping [108]. The SDR process is easily detectable in changes in the photoconductivity of the sample or the bias current of the p-n junction, as the number of charged carriers collected by the contacts changes upon the resonance condition in an EDMR experiment [96, 90, 91, 92, 97, 98]. For shallow donors, great progress has been made towards

detecting the donor spin-state when defect centers such as P_b centers are nearby [56, 75, 109]. In this case, the photoexcited electrons are first captured by the donor to form a D^0 state. The D^0 electron-hole recombination is enhanced if the electron can first travel to a mid-gap defect state, such as the paramagnetic P_b states. Again, the paramagnetic defect states will only accept donor electrons if they form a singlet pair. If this is the case, the recombination rate in the sample will be greatly enhanced. The KSM model is found to provide an exceptionally accurate description of the SDR processes.

2.3.4 Spin-dependent scattering

The above spin-dependent transport processes all rely on the spin-dependence of localized charge transfer. However, scattering events with paramagnetic centers by mobile carriers also have a spin-dependence, as the scattering rates Γ depend on their relative spin states (Fig. 2.2(e)) [99, 110]. This can be understood intuitively if we consider the two-electron real-space wave function for the scattering pair:

$$\Psi_{s/t}(\mathbf{r_1}, \mathbf{r_2}) = \frac{1}{\sqrt{2}} \left[\psi_a(\mathbf{r_1})\psi_b(\mathbf{r_2}) \pm \psi_a(\mathbf{r_2})\psi_b(\mathbf{r_1})\right] \chi_{s/t} \tag{2.28}$$

where the upper sign is for the singlet spin state χ_s and the lower sign for the triplet spin state χ_t. $\psi_{a/b}$ are the individual real-space wave functions of the scattering pair, and $\mathbf{r_{1,2}}$ the coordinates of the two electrons. The matrix element for the interaction between the two electrons depends strongly on the spatial overlap of the two-body wave function. For the case of Ψ_s, the real-space overlap is larger than Ψ_t from symmetry considerations of Eq. 2.28, hence one would expect the singlet scattering cross section to be greater than the triplet scattering cross section, i.e. $\Sigma_s > \Sigma_t$. Therefore, if the singlet versus triplet content in the system is altered, a change in sample resistivity will result. A detailed calculation of the scattering cross sections between 2DEG electrons and neutral donors in a MOSFET can be found in Ref. [110].

Now we will show that the probability of singlet versus triplet scattering for the system can be expressed in terms of the spin density polarizations in the system, i.e. the mechanism is described by the polarization model. We will assume the paramagnetic scattering pair involved are neutral donors. The probabilities of conduction electrons of given spin states ($\uparrow$ or $\downarrow$) to undergo singlet or triplet scattering events with donors are:

$$P_s^{\uparrow/\downarrow} = \frac{1 \mp p_d}{4} \tag{2.29}$$

$$P_t^{\uparrow/\downarrow} = \frac{3 \pm p_d}{4} \tag{2.30}$$

where the upper sign is for spin up conduction electrons, and the lower sign for spin down conduction electrons. The conductivity of the sample can be decomposed into contributions from the spin up and spin down electrons, with momentum scattering times $\tau_{f\uparrow/\downarrow}$:

$$\begin{aligned}\sigma &= \sigma_\uparrow + \sigma_\downarrow = \frac{q^2}{m}\left(\tau_{f\uparrow} n_{c\uparrow} + \tau_{f\downarrow} n_{c\downarrow}\right) \\ &= \frac{q^2}{m}\left[(P_s^\uparrow \tau_s + P_t^\uparrow \tau_t) n_{c\uparrow} + (P_s^\downarrow \tau_s + P_t^\downarrow \tau_t) n_{c\downarrow}\right] \\ &= \frac{q^2}{m}\left(\frac{\tau_s + 3\tau_t}{4}\right)\left[1 + \left(\frac{\tau_t - \tau_s}{\tau_s + 3\tau_t}\right) p_c p_d\right] n_c\end{aligned} \tag{2.31}$$

therefore $\Delta\sigma \propto p_c p_d$, and has the form of Lepine's original polarization model. The scattering times τ_s and τ_t contain contributions from other scattering mechanisms as well, which are not necessarily spin-dependent. When this is the case, the conductivity change upon resonance will be less than that predicted by the above expression. While we use the scattering off neutral donors as an example, this process can occur for other paramagnetic species as well, such as P_b defects, or even electron-electron scattering within the 2DEG itself [111]. Since the electron polarizations are proportional to the magnitude of the magnetic fields, enhanced signals are expected at higher magnetic fields.

2.4 Silicon MOS systems at cryogenic temperatures

Since most of the work described in this thesis are measured with silicon MOSFETs, we will review some of the relevant physics related to these devices at cryogenic temperatures. The reader is referred to Ref. [112] for a comprehensive review. Applying a gate voltage V_g above the flat-band voltage V_{FB} to the gate electrode of the MOS device results in the lowering of the silicon surface potential at the Si-SiO_2 interface. This creates a confinement potential for electrons in the direction normal to the surface (the $\hat{z}$ direction) as shown in Fig. 2.3, and electrons accumulate close to the interface. The populations of the ($\hat{z}$-) quantized energy levels depend on the position of the Fermi level ϵ_f and the Fermi-Dirac distribution. At room temperature, a large number of states have non-vanishing occupancy probabilities due to the relatively large thermal energy $k_B T$ compared with the energy level splittings. At cryogenic temperatures when $k_B T$ is much smaller than the energy splitting of the first excited state ϵ_1 and ground state ϵ_0, only the ϵ_0 state will be occupied for low carrier concentrations (compared to the density-of-states). This situation is sometimes referred to as the quantum limit for the MOS system. The lowest-subband electron envelope wave function is well approximated by a variational wavefunction of the form [113]:

$$\psi_0 = \sqrt{\frac{1}{2}\left(\frac{3}{z_0}\right)^3} z e^{-\frac{3}{2}\frac{z}{z_0}} \tag{2.32}$$

where z_0 is the variational parameter which describes the average depth of the wave function, and z is the position into the substrate along the $\hat{z}$ direction. z_0 is found by minimizing

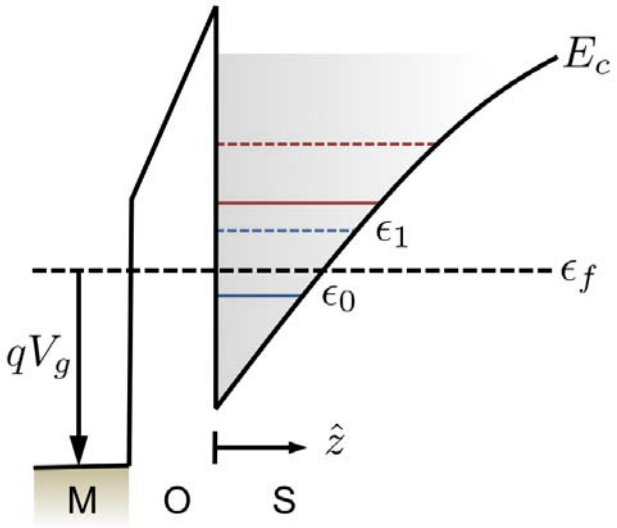

Figure 2.3: Energy-band diagram of the MOS system. In the quantum limit, only the lowest subband with energy ϵ_0 is occupied. The lowest subband is two-fold spin degenerate in the absence of magnetic fields, and also two-fold valley degenerate when valley splitting is negligible. Solid lines of energy levels indicate the ground (blue) and first excited (red) energy levels of the z-valley states. Dashed lines correspond to that of the x- and y-valley states.

the energy of electrons with respect to the kinetic energy, the potential energies due to interaction with other accumulated electrons and with depletion charges in the substrate, the image potential (due to the presence of the Si-SiO_2 interface) and exchange interaction. When substrate depletion charges, image potential and exchange interaction are ignored, an analytical expression for z_0 can be obtained [114]:

$$z_0 = \left(\frac{9\epsilon_S \hbar^2}{4m^* q^2 n_c} \right)^{\frac{1}{3}} \tag{2.33}$$

where $\epsilon_S = 11.9\,\epsilon_0$ is the dielectric constant of silicon, n_c the electron density, and m^* the effective mass. This is a reasonable approximation for the devices we will study in the following chapters as the devices are accumulation-mode devices (no depletion charge), and we generally operate them with relatively low carrier concentrations. The wave function probability amplitudes and average positions for two different electron densities are shown in Fig. 2.4. It is clear that the charge centroid moves towards to the Si-SiO_2 interface for higher carrier densities as expected.

A more detailed description of the energy levels of the MOS system needs to take the

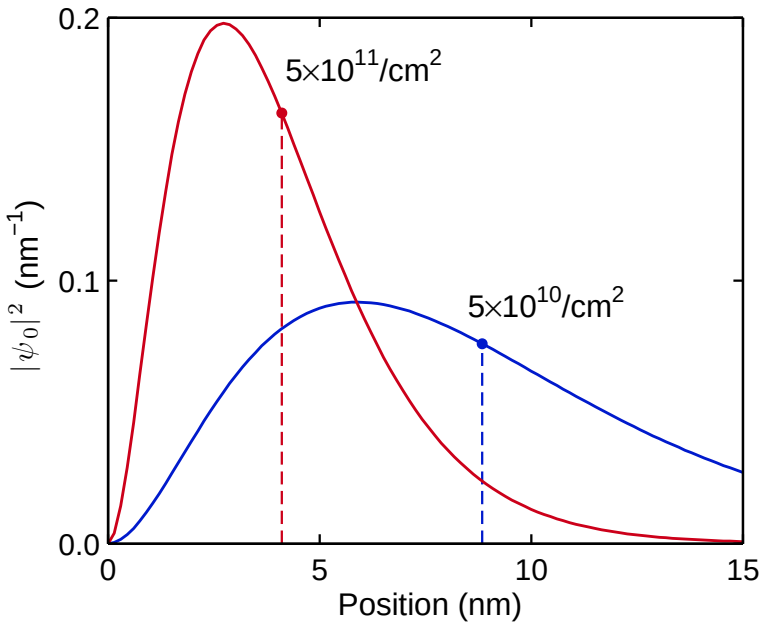

Figure 2.4: 2DEG electron envelope wave functions for two different electron densities: $n_c = 5 \times 10^{10}/\text{cm}^2$ (blue) and $n_c = 5 \times 10^{11}/\text{cm}^2$ (red), in a MOS device. The average positions of the charge distributions are indicated by the dashed lines.

silicon band structure into account [115]. The six-fold degenerate conduction bands valleys are split for a gate-induced 2DEG system at the silicon $\langle 001 \rangle$ surface [112]. Electrons in the $\pm z$-valleys along the principal axis have energy levels determined by the longitudinal effective mass $m_l = 0.916\, m_0$. States corresponding to the four in-plane $\pm x$- and y-valleys have their energy levels determined by the transverse effective masses $m_t = 0.19\, m_0$. It is usually the difference in energy between these two set of valleys that correspond to ϵ_1 and ϵ_0 states, with the ϵ_0 state corresponding to the $\pm z$-valley states. An additional complication is called valley splitting [112]. The valley splitting Δ_v corresponds to the energy difference between the principal $\pm z$-valley states. This splitting aries from the abrupt Si-SiO_2 interface, which admixes these two valley states and creates the splitting. Δ_v can range from $\approx 10^{-5} - 10^{-3}$eV, and is known to be very sensitive to the quality of the oxide interface. In our discussion of the results in the remainder of the thesis, we will assume no valley splitting is present.

With the assumption of $\epsilon_1 - \epsilon_0 \gg kT \gg \Delta_v$, the conduction electrons behave as a two dimensional electron gas (2DEG). Two dimensional systems have a constant density of states given by:

$$\rho_{2DEG} = n_v n_s \left(\frac{\pi}{2\hbar^2} m^* \right) \tag{2.34}$$

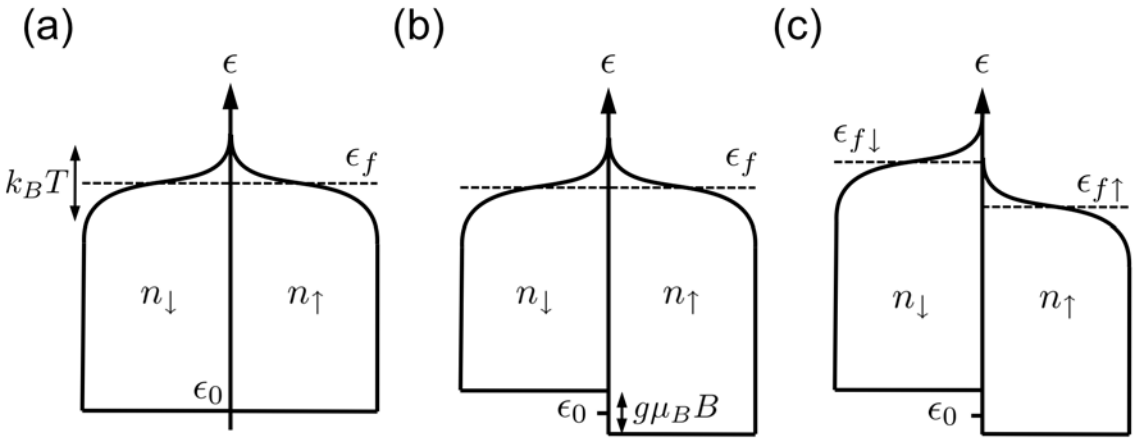

Figure 2.5: Schematics of electron distributions for ideal 2DEGs. (a) The constant density of states and Fermi distribution in thermal equilibrium for a 2DEG. (b) Lifting of the subband spin degeneracy by applying a magnetic field. (c) Non-thermal equilibrium distribution of electrons when the 2DEG is under spin excitation. Under full spin saturation, the difference in up and down Fermi energies is equal to the Zeeman splitting. The total electron concentration $n_c = n_\uparrow + n_\downarrow$ is constant in all three cases.

where n_v and n_s are the valley and spin degeneracies, respectively. Since we assume the valley splitting to be insignificant, we use $n_v = 2$ for the $\langle 001 \rangle$ surface [112]. In the absence of a magnetic field, each valley is spin-degenerate and $n_s = 2$. The energy distribution of electrons obeys the Fermi-Dirac distribution, and this is illustrated in Fig. 2.5(a) under thermal equilibrium conditions. The spin-degenerate levels split under the application of a magnetic field due to the Zeeman interaction: then $n_s = 1$ and this situation is shown in Fig. 2.5(b). The spin-resolved density of states of the silicon $\langle 001 \rangle$ 2DEG is then equal to:

$$\rho_{2DEG} \approx 1.6 \times 10^{13}/\text{cm}^3/\text{meV}. \tag{2.35}$$

When the electrons are subject to spin excitation or spin injection, the Fermi energies of the spin up and down electrons split as shown in Fig. 2.5(c). When the spin excitation is fully saturated, the splitting of Fermi levels will correspond to the Zeeman energy.

If the applied magnetic field is perpendicular to the plane of the 2DEG, additional complications due to Subnikov-de Hass (SdH) oscillations at low fields and Quantum Hall Effect (QHE) at high magnetic fields complicate the transport characteristics of the MOSFET [112, 115]. These effects originate from the quantization of the in-plane orbital motion of the conduction electrons into Landau levels. In this work, we restrict all measurements to an in-plane configuration, so that only the electron polarizations and not their orbital motions

are affected.

The main contributions to the 2DEG electron scattering rate τ_f^{-1} at cryogenic temperatures can be conveniently expressed in terms of Matthiessen's rule [116]:

$$\frac{1}{\tau_f} = \frac{1}{\tau_{SR}} + \frac{1}{\tau_{DF}} + \frac{1}{\tau_{ND}} + \frac{1}{\tau_{ee}} \tag{2.36}$$

Where the terms on the right hand side are surface roughness, defects, neutral donors, and electron-electron scattering. At first it might seem surprising that 2DEG electron-electron scattering can affect the 2DEG transport as momentum is conserved. However, an alteration of the momentum distribution due to electron-electron scattering can indirectly affect other inelastic scattering mechanisms as well, resulting in a change in sample conductivity. The dominant scattering mechanism at room temperature — phonon scattering — is negligible for $T < 20\,\mathrm{K}$.

The expression for the conductivity of a 2DEG is the same as the one obtained from the Drude model with the scattering time computed at the Fermi energy $\tau_f = \tau(\epsilon = \epsilon_f)$ [117]:

$$\sigma = \frac{q^2 \tau_f}{m^*} n_c \tag{2.37}$$

We note that while only electrons close to the Fermi surface can scatter, the *total* carrier concentration n_c also appears in the expression. We can express this in a more intuitive way by taking the constant density-of-states into account [118]: $n_c = \rho_{2D}\epsilon_f = \rho_{2D}(\frac{1}{2}m^* v_f^2)$, and the 2DEG conductivity becomes:

$$\sigma = \frac{q^2 \tau_f}{2} v_f^2 \rho_{2DEG}. \tag{2.38}$$

Now we see that a higher carrier concentration contributes to a higher Fermi velocity and hence higher conductivity. The fact that the total carrier concentration n_c appears in the conductivity justifies the use of spin density polarizations in the polarization models of spin-dependent transport for the 2DEG system.

Chapter 3

Experimental Techniques

The main experimental techniques used will be described in this chapter. First, we review the experimental apparatus needed for performing conventional electron paramagnetic resonance (EPR) experiments. We will then describe the modification of standard EPR for measuring spin-dependent transport in microscopic devices: the technique of electrically detected magnet resonance (EDMR). Such measurements were performed at X-band ($\approx 10\,\mathrm{GHz}$) and W-band ($\approx 100\,\mathrm{GHz}$). We will also discuss an effective way to suppress microwave rectification effects in EDMR by the implementation of a capacitive shunt. Lastly, the experimental setup for measuring transport spectroscopy of nano-scale devices at cryogenic temperatures will be described.

3.1 Electron Paramagnetic Resonance (EPR)

The spin degree of freedom of electrons can be accessed with EPR measurements. The theoretical basis of such measurements was covered in Chapter 2, and here we will sketch out the experimental apparatus needed to perform such experiments [81]. For a given magnetic (Zeeman) field B_0, the spin resonance condition is given by (neglecting hyperfine coupling and higher order terms):

$$hv = g\mu_B B_0 \tag{3.1}$$

For electrons with Landé g-factors of $g \approx 2$ and B_0 within 1-6 T, the photon frequency v lies within the microwave frequency range. Hence, the oscillatory magnetic field component in spin resonance experiments is generally referred to as a microwave field B_1, and we will refer to its frequency as $v = f_{\mu w}$ for clarity. The basic elements for conventional continuous wave EPR (cw-EPR) spectroscopy is shown in Fig. 3.1 [119]. The sample is placed in a single-mode resonant microwave cavity, which in turn is located between the Helmholtz coils of an electromagnet. The microwave bridge sends the microwave down to the cavity, and the reflected microwave is detected by a Schottky diode. The signal is then fed into the

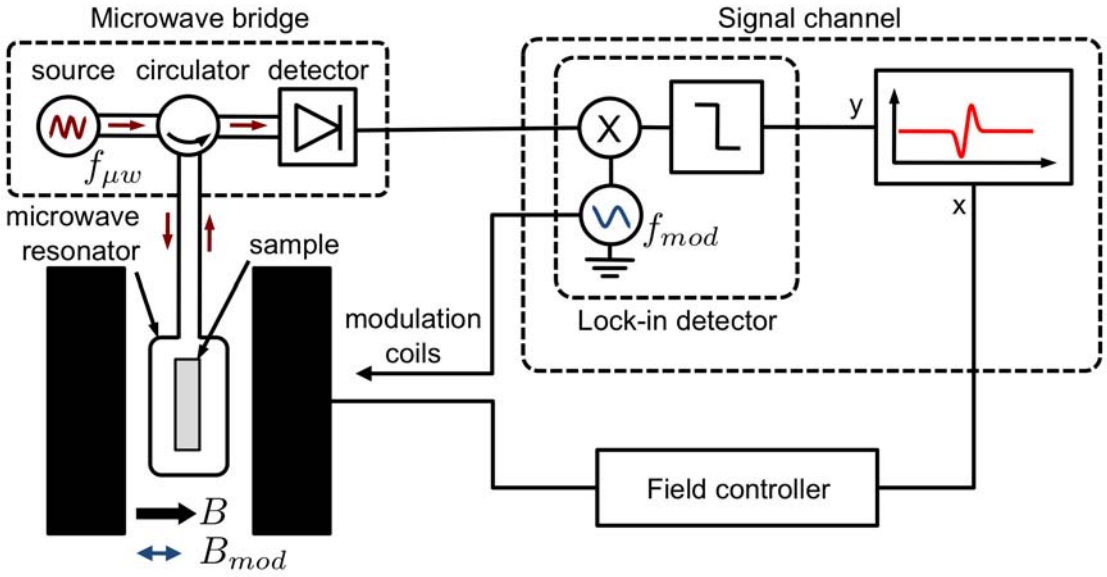

Figure 3.1: Schematics of the cw-EPR setup. The two solid black blocks on the lower left represent the electromagnets for generating the Zeeman field.

signal channel of the spectrometer for amplification and processing. The use of single-mode microwave cavities enhance B_1 by the loaded resonator Q-factors. For low temperature measurements, the microwave cavity and the sample are connected to a helium flow cryostat for cooling.

In cw-EPR measurements, the microwave power and frequency are fixed in each measurement. The microwave intensity reflected from the microwave cavity is monitored as the magnetic field is stepped, controlled by a field controller. The sample absorbs microwave when the condition given by Eq. 3.1 is satisfied, and this results in a resonance signal on the spectrometer. In order to improve the signal-to-noise ratio, a modulation technique is used during measurements. The magnetic field B is superimposed with a small ac magnetic field B_{mod}, typically with modulation frequencies f_{mod} in the 10-100 kHz range. The signal channel then only detects signals at f_{mod}. By carefully selecting the amplitude of B_{mod} to be smaller than the linewidths of the resonance lines, the resultant spectra are the first derivative absorption spectra with respect to magnetic field.

Commercial EPR systems are classified into different frequency bands, and each frequency requires different resonators. X-band systems operate at ≈ 10 GHz and have Zeeman fields of ≈ 0.35 T for $g = 2$ electrons. The corresponding resonant microwave cavities are about 3 cm long, and have transverse dimensions of the order of $\approx$ 3-5 mm, depending on the specific resonator type used. On the other hand, W-band systems operate at ≈ 100 GHz and have Zeeman fields of ≈ 3.5 T for $g = 2$ electrons. The smaller wavelength implies smaller

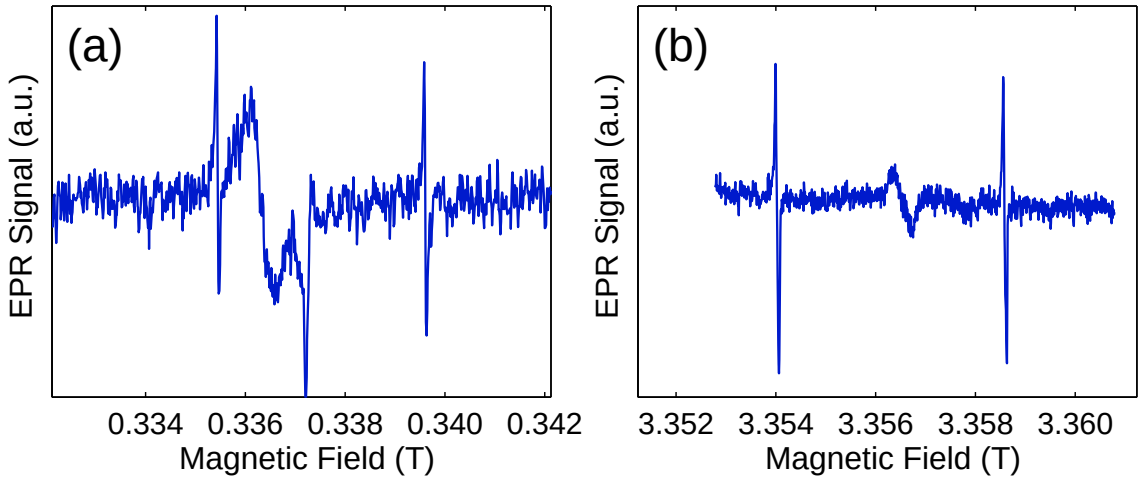

Figure 3.2: EPR spectra of Si:P measured in (a) X-band (9.44 GHz) and (b) W-band (94 GHz) at $T = 15$ K. The two sharp resonance signals separated by 4.2 mT are the hyperfine-split ^{31}P donor signals. The signals around the center are due to clusters of ^{31}P donors and paramagnetic defects at the silicon surface.

microwave resonators, as will be discussed in the following section. Our measurements were carried out in these two frequency bands. The EPR spectra for phosphorus-doped silicon (Si:P) measured in X- and W-bands are shown in Fig. 3.2, showing the large hyerpfine-split resonance peaks and defects at the surface of the silicon crystal. A more detailed discussion of the resonance peaks will be discussed in Chapters 4 and 5.

Three different EPR systems were used in this work:

1. **Berkeley Innovative Electron Resonance Laboratory (BIERLab), LBNL**
   Bruker ESP300E (X-band) with rectangular TE_{102} resonator.

2. **Lyon Lab, Princeton University**
   Bruker ElexSys E580l with MD5 cylindrical TE_{011} resonator (X-band).

3. **Centre for Advanced Electron Resonance (CAESR), University of Oxford**
   Bruker ElexSys E680 ERP spectrometer (X- and W-band) with MD5 cylindrical TE_{011} resonator for X-band, and EN 600-1021H TE_{011} pulsed ENDOR resonator for W-band.

These three systems are shown in Fig. 3.3. The initial X-band measurements were carried out at Princeton, while the data presented in the bulk of this thesis were obtained at LBNL. All W-band measurements were obtained at Oxford.

While EPR techniques are well-established and relatively easy to perform, there are severe limitations to the detection sensitivity due to the small Zeeman energy associated

Figure 3.3: EPR spectrometers used in this work: (a) Bruker ESP300E X-band cw-EPR set-up at BIERLab, LBNL. (b) Bruker ElexSys E580l X-band EPR spectrometer at Princeton. Bruker ElexSys E680 with (c) X-band electromagnet (right unit), and (d) W-band superconducting magnet at Oxford.

with individual electronic spin states. For paramagnetic systems with $g \approx 2$ approximately 10^{10} spins are needed for Zeeman fields of ≈ 0.35 T (X-band) even with the best detection diodes available. The detection sensitivity is improved at W-band due to the larger Zeeman field; however, a large ensemble of approximately 10^9 spins is still required.

Before proceeding to the next section, it is helpful to remind ourselves of the relevant energy scales involved in the X- and W-band experiments; this is shown in Fig. 3.4.

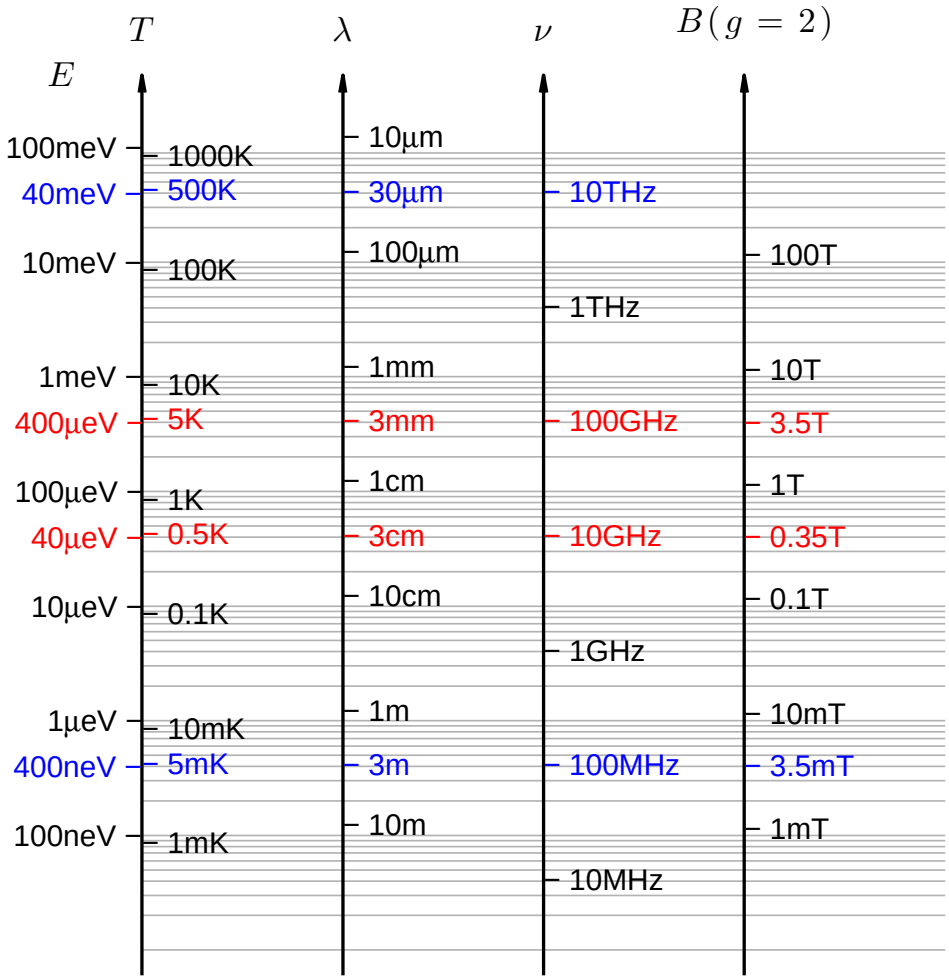

Figure 3.4: Equivalent energy (E) of relevant physical parameters for the experiments described in this thesis: temperature ($T = E/k_B$), wavelength ($\lambda(\mu\text{m}) = E(\text{eV})/1.24$), frequency ($\nu = E/h$) and Zeeman field ($B = E/g\mu_B$, with $g = 2$). Conditions for X-band (≈ 10 GHz) and W-band (≈ 100 GHz) experiments performed in this work are shown in red. Energies relevant to shallow donors in silicon, with binding energies $E \approx 40$ meV and hyperfine interaction $E \approx 400$ neV are shown in blue.

3.2 Electrically detected magnetic resonance (EDMR) with resonant microwave cavities[1]

Electrically detected magnetic resonance (EDMR) is a modification of conventional EPR for enhanced detection sensitivity. It is also a versatile technique for studying the spin-dependent transport properties of electronic devices, as discussed in Chapter 2. Understanding these properties, such as the spin-to-charge conversion mechanisms and Landé g-factor, allows the elucidation of the microscopic environments seen by charged carriers [120, 108] and accessing the spin dynamics useful for spin-based quantum information processing [56, 121, 75]. The fundamental operational principle of EDMR is that instead of monitoring the microwave absorbed by the sample on resonance as in conventional EPR, the change in the electrical transport characteristics of the device is measured. Since we are no longer limited by the small Zeeman energy and detection diode sensitivity, EDMR can achieve orders of magnitude higher sensitivity than conventional EPR [122], enabling the investigation of the spin dynamics in microscopic devices.

3.2.1 cw-EDMR experimental setup

The cw-EDMR experiments are performed under similar conditions as EPR, with the microwave power held constant and Zeeman field scanned. The sample is loaded into a microwave cavity and electrically connected by co-axial cables to the bias and detection circuitries to avoid cross-talks between the signal-carrying wires. Both constant voltage and constant current schemes can be used for biasing the device during the EDMR experiments. However, it was found that the constant current measurements provided slightly better signal-to-noise ratio in our setup, and is therefore used for most of the experiments.

A schematic of the basic EDMR setup used for the measurements at BIERLab is shown in Fig. 3.5. For the constant current bias scheme, the current source is built with resistor networks powered by 9 V batteries. Voltage sources for biasing the gate electrodes are also built with similar resistor networks and 9 V battery sources. Care is taken to ensure proper shielding of the bias network to minimize noise in the detection circuitry. The voltage drop across the device is then amplified by a low noise differential amplifier (FEMTO DLPVA-100FD). The amplified signal is then fed through a band pass filter (we use the pre-amplifier stage of a Princeton Applied Research 5210 dual-channel lock-in amplifier), set to the modulation frequency to reduce extraneous noise. A final low noise amplifier (FEMTO DLPVA-100FS) is used for impedance matching the output from the band-pass filter and the spectrometers signal channel input. The EDMR setups at Princeton and Oxford were similar, although different amplifiers were used at times.

[1] The author is deeply indebted to Professor Steve Lyon and his group at Princeton University, in particular Dr. Alexei Tyryshkin's patient training and guidance, for the experimental techniques described in this section.

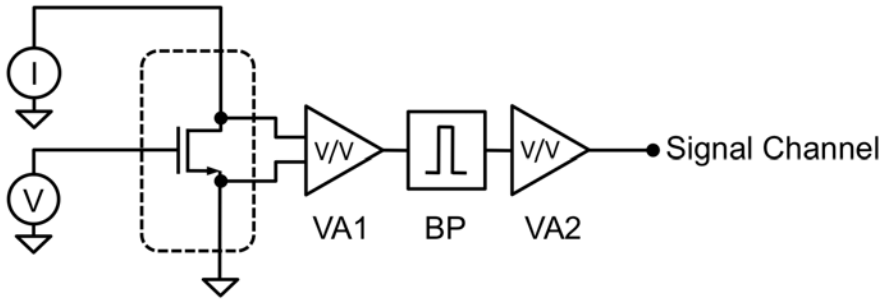

Figure 3.5: Schematics of the cw-EDMR setup. The sample (illustrated as MOSFET) is under DC bias with constant current. The differential source-drain voltage is first amplified by a low-noise amplifier (VA1), then band-pass filtered at the modulation frequency (BP), and a third amplifier (VA2) is used for impedance matching the signal to the EPR spectrometer's signal channel for demodulation.

The modulation frequency f_{mod} used in EDMR experiments are typically in the low kHz range. These relatively low frequencies are used to ensure that the measured signals are not attenuated by the parasitic RC delay in the measurement set-up, where the wire capacitance is approximately 500 pF.

3.2.2 X- and W-band microwave resonators and EDMR chip layouts

Since EDMR measurements are performed with resonant microwave cavities, the metallic content present in the cavity needs to be minimized to avoid excessive degradation of the cavity Q-factor. Therefore, EDMR devices are designed to have elongated layouts with large-area contact pads located far away from the microwave cavity. Electrical contacts are established from the active area to the large contact pads by patterned thin-film metallic electrodes, with thicknesses less than the microwave skin depths. Figs. 3.6(a)-(b) illustrate the placement of the EDMR devices in rectangular (BIERLab) and cylindrical (Princeton and Oxford) X-band resonators. These X-band microwave resonators have lengths of ≈ 3 cm and allow maximum sample widths of ≈ 5mm. The center of the cavity is where the magnetic component of the microwave field B_1 is the largest (and the electric field E_1 smallest), and hence the ideal position for the devices to be positioned at. Therefore, X-band EDMR chips are designed to have a width of 2 mm and length 25 mm, with the device located 1 mm away from one edge of the chip, as shown in Figs. 3.7(a) and (b). The loaded Q-factors of the resonators at 5 K are approximately 1000 for the rectangular resonator, and 6000 for the

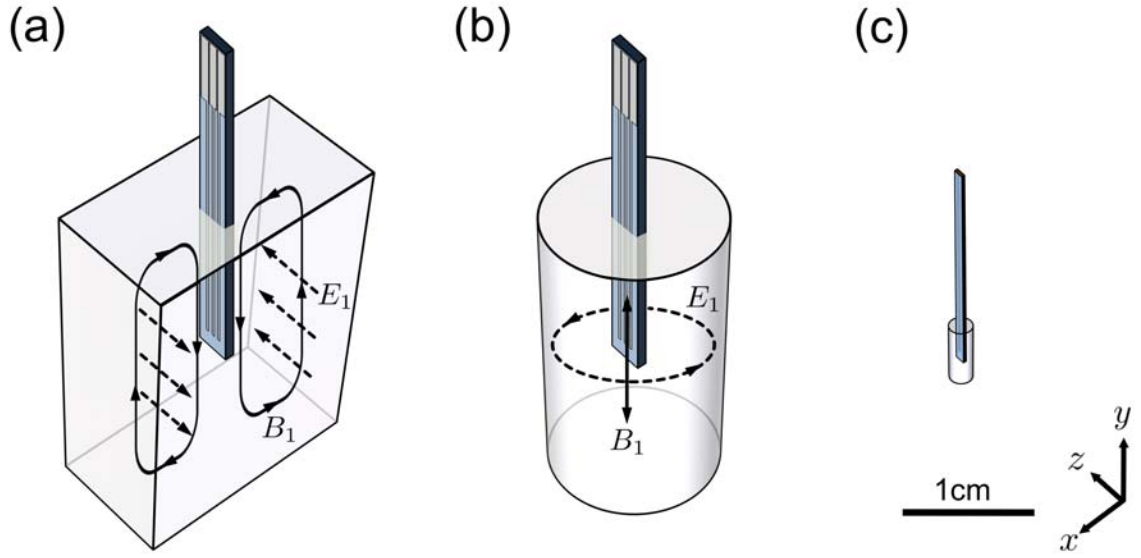

Figure 3.6: Placement of EDMR chips into X-band (a) rectangular TE_{102}, (b) cylindrical TE_{011}, and (c) W-band cylindrical TE_{011} microwave resonators. The electric E_1 and magnetic B_1 components of the microwave fields are also illustrated.

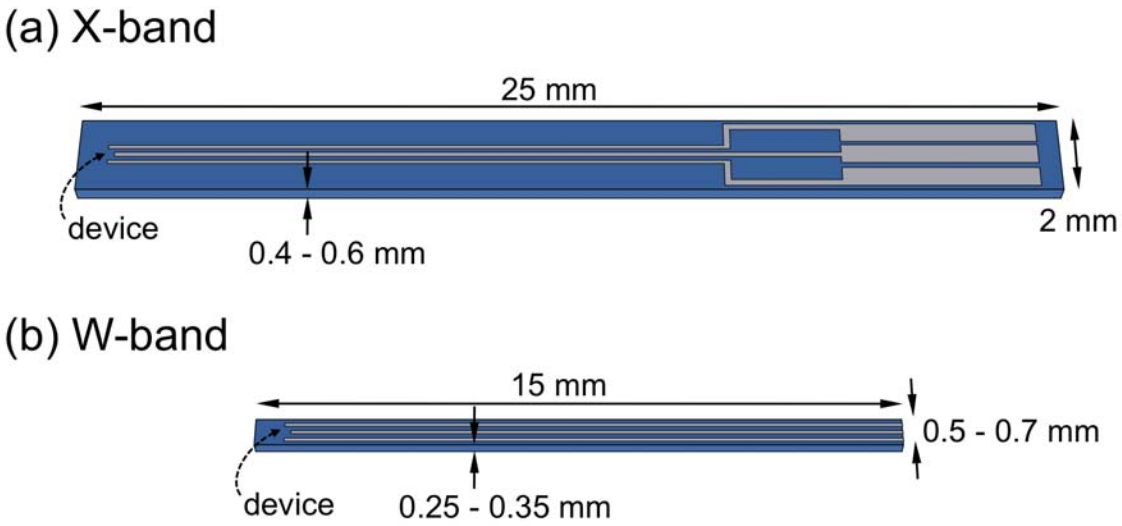

Figure 3.7: EDMR chip dimensions and layouts for (a) X- and (b) W-band microwave cavities. The bonding pads on the right hand side of the chips are either wirebonded or put into direct contact with printed circuit boards for electrical connection to the bias network.

cylindrical resonators.

W-band measurements[2] were carried out with a cylindrical TE_{011} dielectric microwave resonator. This resonator has length $\approx$ 1 mm and diameter 0.8 mm. The EDMR chip placement in this small cavity is schematically illustrated in Fig. 3.6(c). The W-band EDMR chips are diced to widths of $0.5 - 0.7$ mm and 15 mm in length, with the device again located 1 mm away from one edge of the chip, shown schematically in Fig. 3.7(b). In order to fit the small chips into the W-band microwave cavity, the chips are back-etched to reduce the substrate thickness to $\approx 300\ \mu$m. The loaded Q-factor of the W-band resonators with our devices at 5 K is typically around 600. More information regarding W-band EDMR sample preparation can be found in Appendix C.

3.2.3 EDMR signal intensity

In order to compare the EDMR signals of different devices and bias conditions, an appropriate figure-of-merit needs to be defined. The natural choice would be the fractional change in sample resistivity on- and off-resonance:

$$\text{EDMR signal intensity} \equiv \frac{\rho - \rho_0}{\rho_0} = \frac{\Delta\rho}{\rho_0} \tag{3.2}$$

where ρ_0 is the thermal equilibrium resistivity (off-resonance). When the sample is biased under constant current with a corresponding off-resonance voltage drop V_0 across the device, then $\Delta V/V_0 \approx \Delta\rho/\rho_0$. Since magnetic field modulation is used, the recorded (raw) EDMR signal is actually:

$$\text{Raw EDMR signal} \propto \frac{\partial}{\partial B}\left(\frac{\Delta\rho}{\rho_0}\right) B_{mod} \tag{3.3}$$

with B_{mod} being the modulation amplitude. The modulation amplitude is chosen to be smaller than the linewidth of the resonance signals for this definition of the EDMR signal to be meaningful. The recorded EDMR signal is integrated with respect to B to obtain the EDMR signal intensity $\Delta\rho/\rho_0$, analogous to total absorption in conventional EPR:

$$\frac{\Delta\rho}{\rho_0} = \int \frac{\partial}{\partial B}\left(\frac{\Delta\rho}{\rho_0}\right) dB \tag{3.4}$$

When measuring MOSFET samples, the drain current (and hence drain voltage) is usually kept sufficiently low to ensure (i) the device is operating in the triode regime for a uniform 2DEG density, and (ii) no significant Joule heating of carriers will result. On the other hand, a larger bias voltage is desired as the detected signal amplitude is directly proportional to it. We typically use an electric field of $1.2 - 2.5$ V/cm, which is a compromise taking the above considerations into account.

[2]The W-band EDMR technique was developed in close collaboration with Volker Lang of the Quantum Spin Dynamics Group at the University of Oxford.

3.2.4 Microwave rectification effects

One problem often encountered with EDMR measurements are microwave-induced rectification effects, which can both adversely affect the bias conditions of the device and generate excessive noise in the EDMR measurements. These microwave-induced rectification effects are due to non-linear current-voltage I-V characteristics of the devices. We will show that such rectification effects can be effectively suppressed by the incorporation of capacitive shunts to the devices, and results in over ten times improvement in signal-to-noise ratio in EDMR measurements.

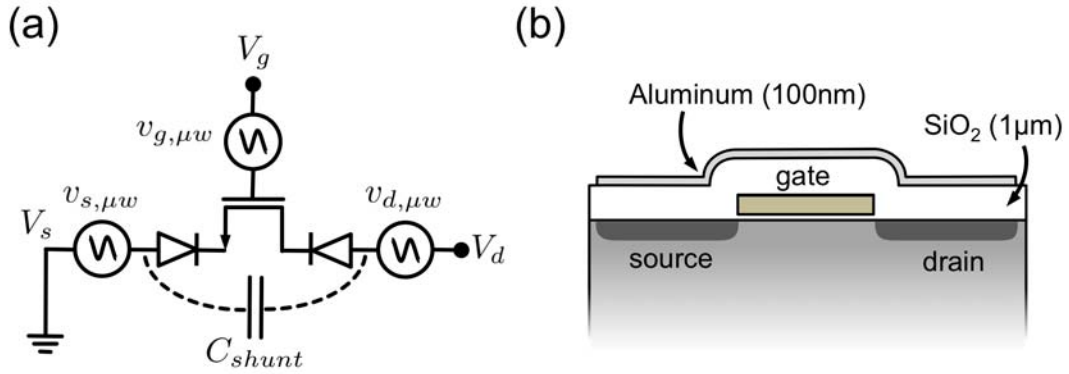

Figure 3.8: (a) Circuit diagram representation of the high frequency voltage fluctuations induced on the MOSFET, where the non-ideal metal-silicon contacts are represented by diodes. A shunt capacitor C_{shunt} across the device can suppress the high frequency voltage fluctuations and subsequent rectification effects. (b) Schematic of the implementation of the shunt capacitor with the MOSFETs. 1 μm thick silicon dioxide (SiO_2) and 100 nm aluminium layers were used to cover the device and metallic lines and contacts.

As described in the previous section, the active region of the device is placed in the microwave resonator where the magnetic component B_1 of the microwave field is at a maximum and electric component E_1 at a minimum (Fig. 3.6). However, voltage fluctuations can be inadvertently induced on the sample and the metallic wires inside the resonator. In the case of a MOSFET, these microwave-induced voltage fluctuations $v_{i,\mu w}$ ($i = \{s\text{ (source)}, d\text{ (drain)}, g\text{ (gate)}\}$) will be superimposed to the external bias V_i of the device, as shown in Fig. 3.8(a). $v_{i,\mu w}$ can arise from magnetic induction of the current-loop consisting of the device and the biasing circuitry from the oscillatory B_1 field [123, 124], or the absorption of the E_1 field by the metallic electrodes in the resonant microwave cavity. The latter effect can be substantially larger than one might expect when considering the elec-

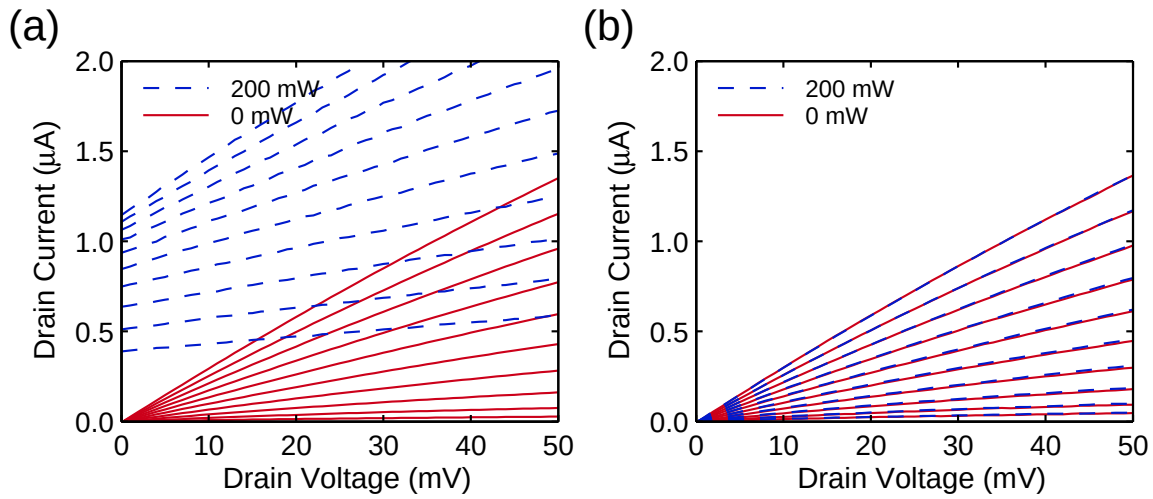

Figure 3.9: (a) Measured I-V characteristics of a MOSFET in the TE_{102} microwave resonator with the microwave off (solid, red traces) and set to the maximum of 200 mW (dashed, blue traces) without the capacitive shunt. (b) Measured I-V characteristics of an identical MOSFET but with the shunt capacitor added, with identical bias conditions to (a). The gate voltage V_g is adjusted from 350 mV to 750 mV, in increments of 50 mV for both plots. All measurements were performed at $T = 4.8\ K$.

tric field distribution in an ideal cavity, as the tangential fields on the surface of a dielectric sample (e.g. the silicon chip) can be enhanced substantially when loaded into a microwave resonator [125]. In addition, the long metallic lines can also form a microstrip-like resonator and enhance the local field strengths at the device [102]. If the sample has perfectly linear (ohmic) current-voltage I-V characteristics, these high frequency voltage fluctuations will be canceled out in subsequent time averaged measurements. On the other hand, if the sample exhibits non-linear I-V characteristics, the voltage fluctuations will be rectified and result in offsets in time-averaged measurements. In the case of MOSFETs, in addition to the inherent non-linearity in the I-V behavior, non ideal metal-semiconductor contacts (especially at cryogenic temperatures) will also contribute to the overall non-linear behavior. However, if a large capitative shunt can be implemented close to the active region of the device as shown in Fig. 3.8(b), the high frequency voltage fluctuations and hence the rectification effects should be suppressed.

To implement devices with shunt capacitors, 1 μm thick SiO_2 and 100 nm thick aluminum were deposited over the metal lines and covering the MOSFETs themselves, as shown in Fig. 3.8(b). The data presented here are from devices with channel lengths of 80 μm and widths 5 μm, and measured at $\theta = 90°$, where θ is the angle between the normal of the silicon

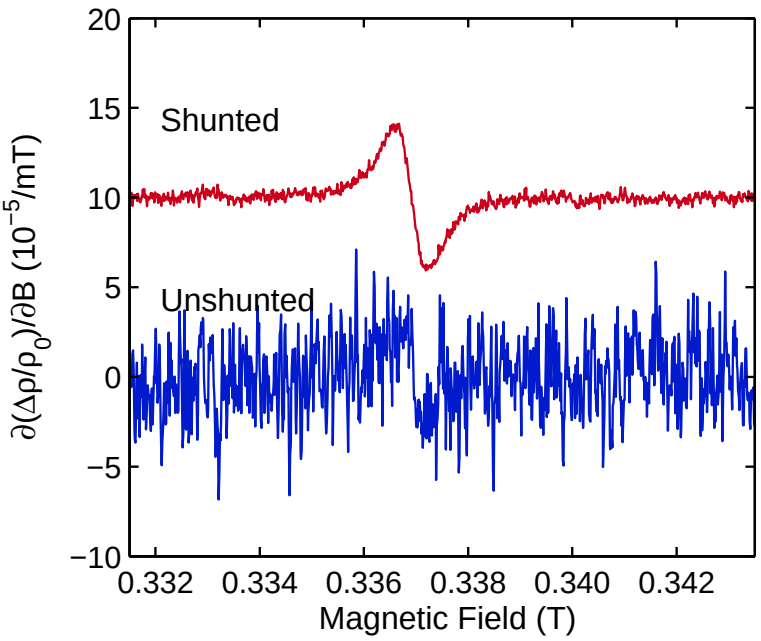

Figure 3.10: EDMR signal of unshunted (lower trace, blue) and shunted (upper trace, red) devices measured in a X-band rectangular TE_{102} resonant microwave cavity (offset for clarity). Both measurements were recorded with identical data acquisition times and under a microwave power of 200 mW. Magnetic field modulation at 1.56 kHz with 0.4 mT modulation amplitude were used.

chip and the applied magnetic field B. Fig.3.9(a) shows the I-V characteristics of a MOSFET *without* the shunt capacitor. The I-V traces were first recorded with the microwave turned off and then recorded again with the microwave power set to the maximum of 200 mW. Under maximum microwave power, significant microwave-induced rectification is observed as evident by the large offset currents. The same I-V measurement was performed on an identical device but *with* a capacitive shunt, and the results are shown in Fig. 3.9(b). The I-V characteristics of the shunted device look essentially identical regardless of the microwave power applied, proving the effectiveness of the shunt capacitor. We have checked that the inclusion of the thin shunt layer has no effect on the cavity $Q-$factor ($\approx$ 1300), ensuring that the same microwave power is delivered to the device.

The use of the shunt capacitor is only beneficial for EDMR experiments if the additional metallic layer does not block the microwave coupled to the active area of the device. In Fig. 3.10 we show the measured EDMR signal from the shunted and unshunted devices under identical data acquisition and measurement conditions. The resonance signals observed originate from the conduction electrons in the channel of the MOSFETs, and details of the EDMR mechanisms in MOSFETs are discussed in Chapter 4. The shunted device exhibits

a 15 times enhancement in signal-to-noise ratio over the unshunted device, and proves that the the microwave B_1 field is still effectively coupled into the device.

We have also measured the rectification effects with $\theta = 0°$, where the normal of the silicon chip is aligned with the applied magnetic field. A more pronounced microwave rectification behavior with $\approx 10\%$ increase in offset currents was observed for the unshunted device in this configuration. However, for the shunted device, the I-V and EDMR characteristics remain similar to the $\theta = 90°$ case. The shunts were also tested in the W-band setup, and they exhibit similar effectiveness in suppressing rectification and EDMR noise [126].

While we demonstrated the suppression of the microwave rectification effects with a MOSFET, the use of the shunt capacitor is generally applicable to other EDMR measurements if the device exhibit non-linear I-V characteristics. One of the most common EDMR experiments involves spin-dependent recombination of photo-excited carriers, and in this case having a metallic shunt layer over the device will obstruct the illumination needed for photo-carrier generation. We have tested MOSFET EDMR samples with the metallic shunt layer covering the metal lines only and terminating $\approx 10\,\mu$m away from the active region of the MOSFET, and have found this design to be equally effective in suppressing microwave-induced rectification in X-band systems. All EDMR measurements presented in the rest of this thesis are from devices with the microwave shunt implemented.

3.3 Transport spectroscopy

The EDMR measurements of micron-scale MOSFETs (Chapters 4, 5, 6) were performed with the devices biased above threshold in the drift-diffusion regime. However, quantum transport phenomena such as Coulomb blockade, resonant tunneling and quantized conductance can occur for nanoscopic devices with few donors in the active channel when biased in the subthreshold regime. A sensitive transport measurement scheme must thus be setup to properly characterize these devices and understand the microscopic environment and conduction pathways. Such measurements are called transport spectroscopy measurements due to the occurrence of resonance features in the transport measurements. In the transport spectroscopy experiment of MOSFETs, the gate and drain voltages are carefully scanned and the small-signal conductance $g_d = \partial I_d / \partial V_d$ through the device measured. The conductance is usually measured with a lock-in technique to improve signal-to-noise ratio. Since the co-axial cables used for such measurements typically have capacitances of $C_{wire} \approx 200\,\mathrm{pF/m}$ (RG-174 co-axial cable or Lakeshore CC-SS low thermal conductivity co-axial cables), the lock-in measurements are performed at a low frequency $f_{mod} \lesssim 100\,\mathrm{Hz}$ as the resistances associated with the devices are typically in the MΩ range or higher.

The basic setup for our transport spectroscopy measurements is shown in Fig. 3.11. The voltage sources were taken from the auxiliary outputs of a Stanford Research 830 lock-in amplifier. The modulation signal reference is added to the dc bias to the drain terminal of the device with a voltage adder (battery powered with National Semiconductor LM741 oper-

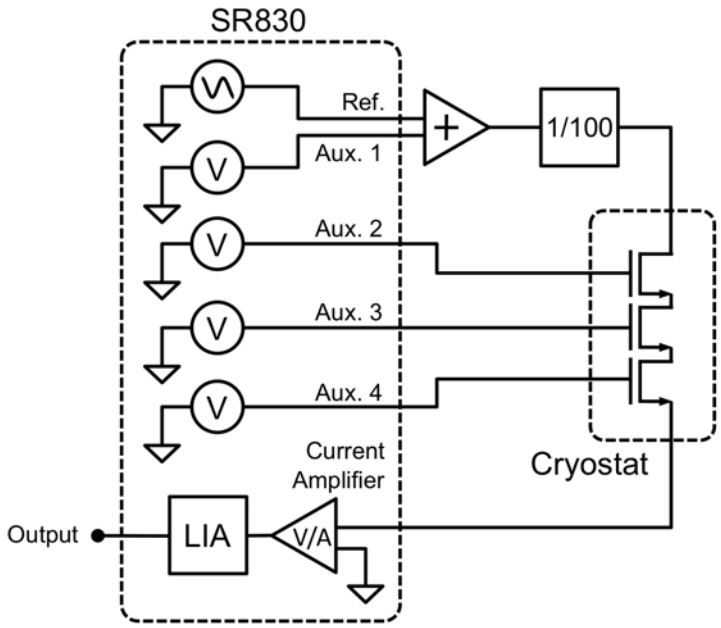

Figure 3.11: Experimental setup for transport spectroscopy measurements. The device illustrated is a triple-gate finFET, which will be described in more detail in Chapter 7.

ational amplifier). The source terminal of the device is connected to the current preamplifier of the lock-in amplifier. The measured current through the device is then demodulated to give the conductance of the device. Since the auxiliary outputs typically have offset voltages of a few mV, which becomes particularly problematic for sensitive measurements for the drain biases, a 100:1 voltage divider is inserted in series to the drain terminal. The voltage divider also helps to reduce the ac excitation amplitude to $< 100\,\mu$V, which is needed for resolving fine resonance features and to avoid heating of the carriers.

The devices were mounted on 24-pin ceramic chip carriers with an adhesive that provided good stability with thermal cycles (Dow Chemical Cyclotene electronics resin), and at the same time can be easily removed in a solvent. Aluminium wirebonds were used for connecting the device to the pads of the chip carriers. 4.2 K measurements were performed with a home-built dip-stick. The chip carriers were mounted on the dip-stick and submerged in liquid helium with standard liquid helium dewars. Lower temperature measurements were performed with a Janis Research Helium-3 cryostat at ALS beamline 1.4, LBNL. This cryostat was originally designed for infra-red measurements at the beamline. The optical access windows were closed for the transport measurements in order to lower the operational base temperature and increase hold time. This cryostat is shown in Fig. 3.12.

Helium-3 cryostats operate on the principle of thermal cooling induced by evaporation

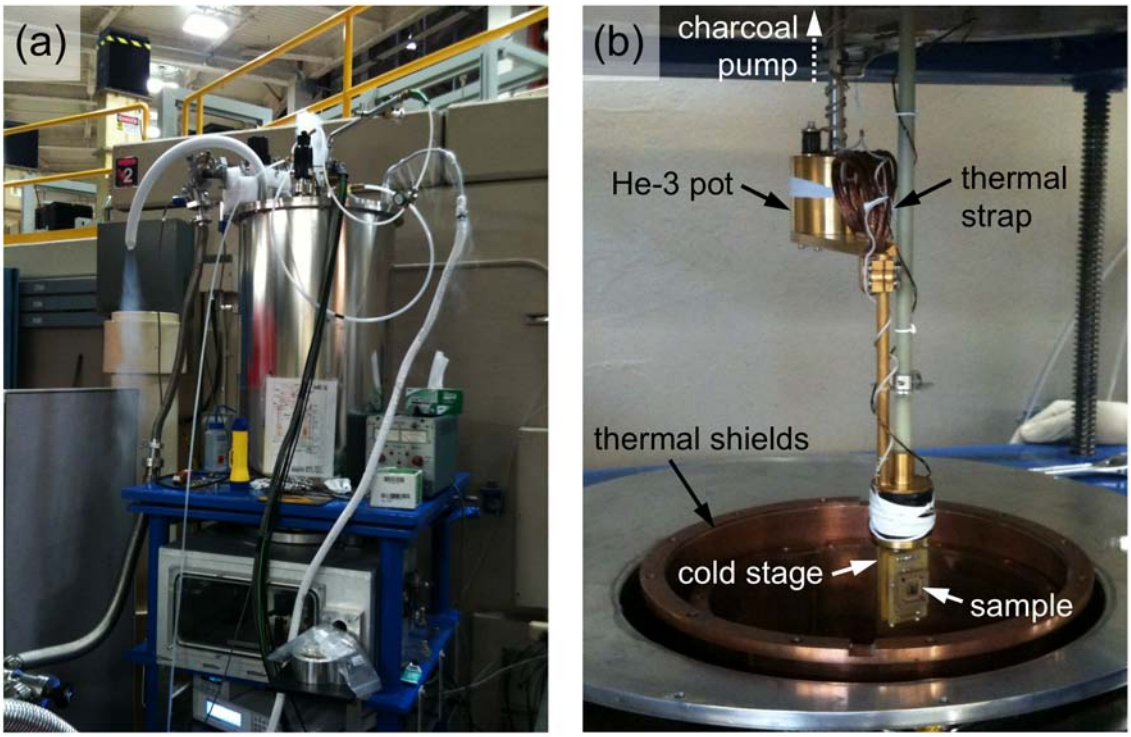

Figure 3.12: The Helium-3 cryostat used for transport spectroscopy measurements at beamline 1.4, ALS (LBNL). (a) The cryostat after refilling the liquid nitrogen reservoir. The cold sample insert is located inside the rectangular compartment near the bottom of the picture. (b) Sample insert with thermal shields removed.

of condensed ^{3}He. The sample stage (cold stage) is thermally anchored to the He-3 pot, a compartment where condensed ^{3}He resides. The He-3 pot is in turn connected to a charcoal pump, where gaseous ^{3}He can be absorbed into the charcoal. The He-3 pot and the charcoal pump forms the closed system of the ^{3}He insert. The charcoal pump is in thermal contact to a small reservoir of ^{4}He (the 1K pot) on top, and the ^{3}He in the closed system remains in a gas phase when warm. When liquid ^{4}He is filled into the 1K pot, reducing the vapor pressure by pumping on the 1K pot can super cool the ^{4}He from 4.2 K (atmospheric pressure) to ≈ 1.3 K. This lower temperature in turn condenses the gaseous ^{3}He in the charcoal pump, and liquid ^{3}He accumulates in the He-3 pot ($T = 3.2$ K at atmospheric pressure). The condensed liquid ^{3}He can then be pumped by means of heating the charcoal pump to $4 - 40$ K, which brings the ^{3}He liquid to its base temperature of about 300 mK. The cold stage is then cooled to the base temperature through the thermal anchors. The He-3 pot and cold stage will warm up when all the liquid ^{3}He has evaporated into the charcoal pump, and then the charcoal pump

needs to be turned off and the cooling cycle is repeated.

To ensure the sample reaches the base temperature, care must be taken when thermally anchoring the sample to the cold stage, and the stage must be very well thermally isolated otherwise. Phosphor bronze wires with low thermal conductivity are used to electrically connect the sample to room-temperature electronics. The phosphor bronze wires are thermally anchored to the liquid helium reservoirs to reduce heat transfer from room temperature to the cold stage. Typical hold-time at base temperature is about 8 hours for this system. The cool-down cycle from room temperature to condensing the ^{3}He in the He-3 pot takes three to four days, with constant adjustment to the 1K pot needle valve to avoid mechanical freeze up. The outer liquid nitrogen and helium shields for thermal isolation also need to be refilled daily while operating, and it typically consumes about ≈ 50 L of liquid helium a day. As opposed to top-loaded cryostats, the Helium-3 system used in this work requires warming up of the entire cryostat before the sample can be removed and replaced. Hence, only selected samples showing promising transport characteristics when screened with the liquid helium dip-stick are measured in the Helium-3 system.

Chapter 4

Spin-dependent Transport in Silicon MOSFETs

In principle, the interaction between conduction electrons and embedded donor atoms in the channel of a silicon MOSFET can be exploited for constructing a donor spin-state readout device, thus fulfilling one of the DiVincenzo criterion towards a donor-based quantum computer architecture [57]. In this chapter, we will investigate the nature of this interaction in detail. The central question we would like to address is: what causes the change in the MOSFET resistivity when the donor electron spins are flipped? We address this question by examining such interactions in micron-scale donor-doped MOSFETs using EDMR[1]. These MOSFETs were specifically designed to have a low donor concentration in the channel which enables clear identification of the 2DEG and donor contributions to the resonance signals. Zeeman field scaling of the EDMR signals provides additional clues to the underlying spin-dependent transport mechanism. We discuss our results in terms of bolometric heating, spin-dependent scattering, and a polarization transfer from the donor to the 2DEG spin systems.

4.1 Silicon MOSFETs for EDMR

The silicon MOSFETs used for spin-dependent transport studies require some special consideration. While issues such as microwave rectification effects in resonant microwave cavities and EDMR-compatible chip layouts were discussed in Chapter 3, we will discuss additional device design constraints in this section. We will also outline the device fabrication process flow and typical current-voltage (I-V) characteristics of these MOSFETs operating at cryogenic temperatures.

[1]The potential and strategies for miniaturization of similar MOSFETs to the single dopant regime will be addressed in Chapter 7.

4.1.1 Sample design considerations

Channel dopants Heavy p-type substrates, such as those used for building conventional NMOS devices are not desirable for our measurements as the high acceptor concentration may ionize the donors residing in the channels of the MOSFETs. On the other hand, while bulk-doped n-type substrates provide neutral donors in the channel, the excessive background dopants also create dubious signals in resonant microwave cavity based EDMR measurements (see Appendix A(aFET1)). Instead, low dosage donor implantations ($\approx 2 \times 10^{11}/\mathrm{cm}^2$) were used for donor placement into the MOSFET channels. The effect of donor distribution on the EDMR signals will be discussed in Chapter 5.

Substrates One of most the attractive aspects of using silicon as a host material for spin-based computation schemes is the availability of nuclear spin-free substrates via isotope purification. It is well known that donors in isotopically purified ^{28}Si substrates have much longer spin coherence times than their natural silicon counterparts from bulk-based EPR measurements. However, it is not clear whether these advantages remain for donors interacting with a 2DEG in MOSFETs, as decoherence originating from this interaction or other near-surface noise sources play a much larger role. Therefore, both types of substrates were used in this work: natural silicon and 99.95% isotopically purified ^{28}Si.

The natural Si wafers (FZ-Si) used were grown by the float zone technique and typically had room temperature resistivities exceeding $10,000\,\Omega\,\mathrm{cm}$, corresponding to residual impurities less than $10^{13}\,\mathrm{cm}^{-3}$. Both n-type and p-type substrates were used in this work, but due to the low background concentration, these substrates are essentially considered to be intrinsic.

The ^{28}Si substrates (28-Si) consisted of $\approx 1\mu$m thick ^{28}Si grown epitaxially on top of high resistivity natural silicon handle wafers. While the handle wafers were nominally undoped, the epitaxially ^{28}Si layers were background doped with $3 \times 10^{16}\,\mathrm{cm}^{-3}$ of ^{31}P donors. High thermal budget steps in the fabrication process caused the ^{31}P donors to redistribute close to the surface. Since conduction electrons only flow within $\approx 10\,\mathrm{nm}$ from the Si-SiO_2 interface of the MOSFETs, the natural silicon handle wafer does not affect the behavior of the device.

$n+$ doping The source-drain regions of a MOSFET are formed by degenerately doping the silicon above the metal-insulator transition. A high doping concentration is critical for the formation of reliable and low resistivity ohmic contacts to the metal layers. We found that a drive-in diffusion process using phosphosilicate glass (PSG) provided reliable ohmic contacts for the cryogenic measurements. The peak ^{31}P concentration from this process was about $5 \times 10^{19}/\mathrm{cm}^3$ at the silicon surface as determined by secondary ion mass spectroscopy.

4.1.2 Device fabrication

An outline of the process flow used for fabricating the micron-scale silicon MOSFETs is described in this section. A detailed step-by-step process flow can be found in Appendix B (aFET6).

1. **Field oxide growth and active area definition**
   The field oxide was first grown on 4" wafers with a wet oxidation process. The active regions (MOSFET channel and source-drain regions) were subsequently defined by optical lithography and patterned by wet etch in diluted HF solution.

2. **Donor implantation and gate stack**
   5 nm screening oxide was grown over the exposed active regions. The wafers then received a shallow donor implantation (either ^{75}As or ^{121}Sb) to dope the channel regions. The screening oxide was then removed by a dilute HF etch, and dry oxidation was carried out to grow the 20 nm thick gate oxide. 300 nm *in situ* phosphorus doped polycrystalline silicon was then deposited and patterned to form the gate electrode.

3. **Source-drain dopant diffusion**
   Another HF dip was used to remove the oxide over the source-drain regions. PSG was then deposited over the wafers. A high temperature anneal step was then carried out to drive-in the phosphorous from the PSG layer into the silicon substrates to form the heavily doped $n+$ regions.

4. **Metallization and shunt layers**
   After opening of contact windows through the PSG layer, aluminum was sputter deposited and subsequently patterned. Forming gas anneal was then carried out to form ohmic contacts to the $n+$ source-drain regions and passivate dangling bonds at the Si-SiO_2 interface. Silicon dioxide was then deposited by plasma-enhanced chemical vapor deposition, then followed by the sputter deposition of aluminum to form the capacitive shunt. The wafers were then diced into elongated chips for EDMR measurements as described in Chapter 3.

4.1.3 Device *I-V* characteristics

The completed devices were first tested at room temperature on a probe station for screening. Significant source-to-drain leakage through the substrate is usually found at room temperature due to the lack of junction isolation. However, once the devices were cooled below the freeze-out temperature, the leakage was eliminated. Figs. 4.1 and 4.2 show representative *I-V* characteristics of these donor-doped MOSFETs operating at $T = 4.6\,\mathrm{K}$. This device was channel implanted with ^{121}Sb at 60 keV and at a dose of $2 \times 10^{11}\mathrm{cm}^{-2}$ (FZ-Si:^{121}Sb).

The devices typically have threshold voltages of $V_t = 0.25 - 0.30\,\mathrm{V}$ at $T = 4 - 5\,\mathrm{K}$, and the field-effect mobility μ varies from $5,000\ \mathrm{cm}^2/\mathrm{V\text{-}s}$ to $20,000\ \mathrm{cm}^2/\mathrm{V\text{-}s}$, depending on the

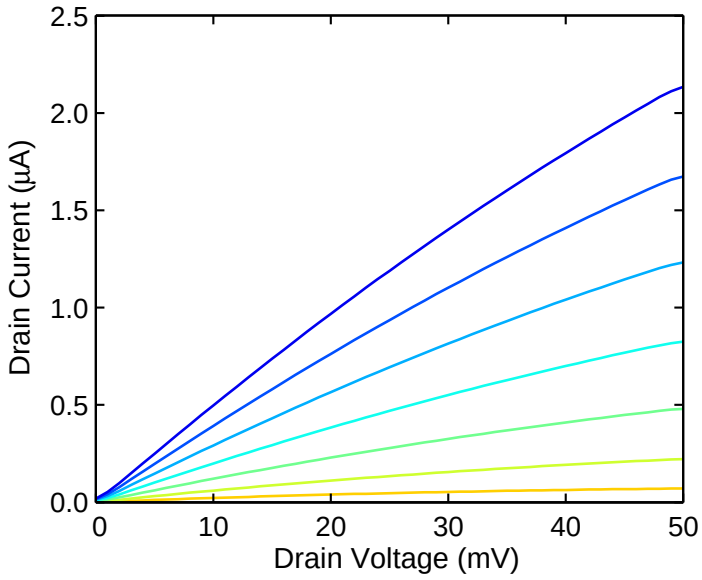

Figure 4.1: I-V characteristics for a MOSFET with $l = 160\,\mu$m and $w = 10\,\mu$m measured at $T = 4.6\,$K. $V_g = 500\,$mV to $200\,$mV from top to bottom, in $-50\,$mV steps.

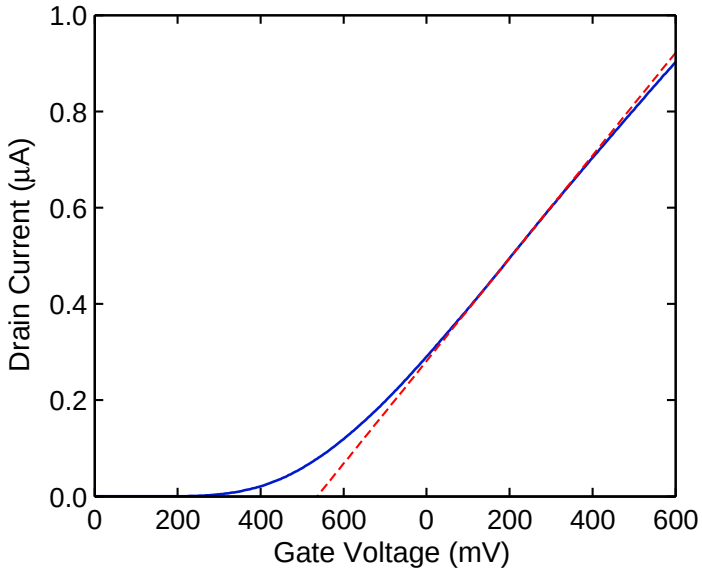

Figure 4.2: Gate transfer characteristics of a MOSFET with $l = 160\,\mu$m and $w = 10\,\mu$m with $V_d = 10\,$mV and measured at $T = 4.6\,$K. The extracted threshold voltage is $V_t = 0.26\,$V.

donor concentrations under the channel. All EDMR measurements were carried out with an in-plane magnetic field ($\theta = 90°$, $\hat{n} \perp B$), and no change in device I-V characteristics were found up to ≈ 3.5 T, where the W-band EDMR experiments were made.

4.2 EDMR of donor-doped MOSFETs at X- and W-band

We performd EDMR experiments with the MOSFETs as described in Chapter 3 to study the spin-dependent transport process in such devices. We will first examine the EDMR spectra obtained at X-band in detail in order to understand the spectroscopic features and power saturation. These X-band data are then compared to the higher magnetic field measurements performed at W-band, which gives us clues regarding the mechanism behind such spin-dependent transport phenomena observed in silicon MOSFETs.

4.2.1 EDMR spectra

Fig. 4.3 shows the X-band EDMR spectra of three different MOSFETs, each doped with a different shallow donor species in the channel. The raw signals are normalized for easy comparison of the spectroscopic features. The top (green) trace in Fig. 4.3 is from a device built on 28-Si substrate, with neutral ^{31}P donors coming from the background doped epitaxial layer (28-Si:^{31}P). The middle (red) trace is from a device built on FZ-Si that received a channel implantation of ^{75}As donors at an energy of 50 keV with a dose of $2 \times 10^{11}/\text{cm}^2$ (FZ-Si:^{75}As). The bottom (blue) trace is from a device also built on FZ-Si but received a channel implantation of ^{121}Sb donors at an energy of 60 keV with a dose of $2 \times 10^{11}/\text{cm}^2$ (FZ-Si:^{121}Sb).

In all three traces, the large center line has a g-factor of $g_{2DEG} = 1.9999$ and is assigned to the 2DEG, in agreement to EPR measurements of large-area MOSFETs [127, 76]. The satellite peaks on both sides around the 2DEG signal corresponds to neutral donor electron resonances. These donor peaks have a center-of-gravity g-factor of $g_d = 1.9987$ [72]. The number of peaks are determined by the nuclear spin of the donor species, and their spacing is determined by the hyperfine coupling strength between the donor electron and the donor nucleus. Table 4.1 lists the nuclear spins and isotropic contact hyperfine coupling strengths for the common donors in silicon [72].

The spectra shown in Fig. 4.3 clearly demonstrate that EDMR of silicon MOSFETs is a sensitive technique for detecting and identifying dopant species in microscopic devices. In earlier generations of devices where the oxide quality was poor, the EDMR measurements also revealed the presence of paramagnetic defects such as P_b centers (Appendix A(aFET2)). These defect signals were not observed in the devices upon which our discussions in the next sections are based.

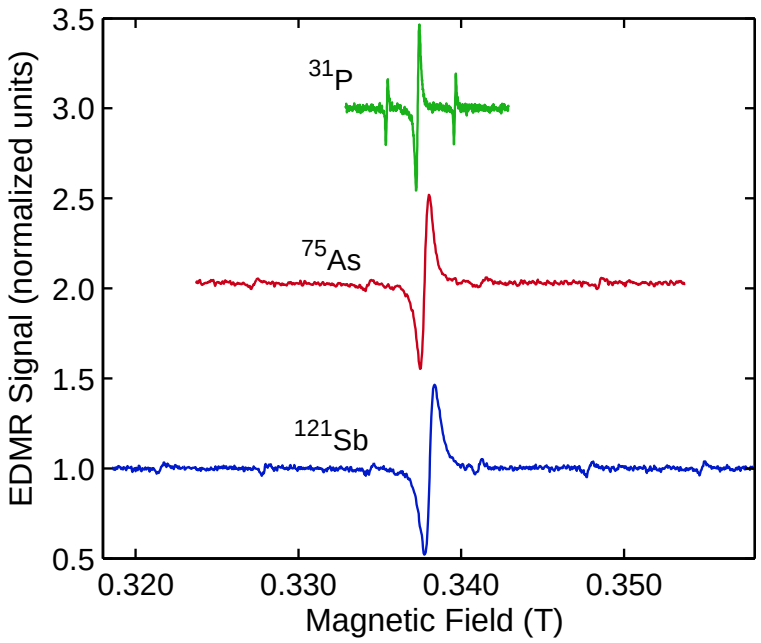

Figure 4.3: X-band EDMR spectra with different channel implants: ^{31}P, ^{75}As, and ^{121}Sb. All devices have dimensions $l = 160\,\mu$m and $w = 10\,\mu$m. The measurements were performed at $T = 5$ K with $f_{\mu w} = 9.44$ GHz and $P_{\mu w} = 200$ mW.

Donor	I	A (mT)
^{31}P	1/2	4.2
^{75}As	3/2	7.1
^{121}Sb	5/2	6.7
^{123}Sb	7/2	3.6

Table 4.1: Nuclear spin I and hyperfine coupling constants A of shallow donors in silicon.

4.2.2 Saturation of spin transition

In an EDMR experiment, spin transitions are induced when the resonance condition for the particular electron species is met. As described in Chapter 3, the metric we use to evaluate the strength of a given resonance signals is:

$$\text{EDMR signal intensity} \equiv \frac{\Delta\rho}{\rho_0} = \int \frac{\partial}{\partial B}\left(\frac{\Delta\rho}{\rho_0}\right) dB \tag{4.1}$$

where ρ_0 is the off-resonance sample resistivity, and $\Delta\rho = \rho(p) - \rho_0(p_0)$: the change in sample resistivity when the polarization is perturbed from its equilibrium value p_0 to p on resonance. The magnitude of $\Delta\rho$ depends on the level of saturation of the spin transition. The expected polarization due to resonance absorption can be deduced from the Bloch equations (Chapter 2) as $p \propto M_z$:

$$\begin{aligned} p = \frac{n_\uparrow - n_\downarrow}{n_\uparrow + n_\downarrow} &= p_0 \left[\frac{1 + \gamma^2 T_2^2 (B_0 - B)^2}{1 + \gamma^2 T_2^2 (B_0 - B)^2 + \gamma^2 B_1^2 T_1 T_2} \right] \\ &= p_0 \left[\frac{1 + \gamma^2 T_2^2 (B_0 - B)^2}{1 + \gamma^2 T_2^2 (B_0 - B)^2 + \alpha P_{\mu w} \gamma^2 T_1 T_2} \right] \end{aligned} \tag{4.2}$$

where the microwave power is $P_{\mu w} = \alpha B_1^2$ and α is a proportionality constant. A meaningful comparison of different EDMR signal intensities can only be made if the polarizations are equal. This is most easily achieved by ensuring the measurements are performed in full saturation, i.e. $\alpha P_{\mu w} \gg \gamma^2 T_1 T_2$ and $p \to 0$. When the microwave power is low, the induced spin-flip rate is small compared with the natural relaxation rates, and hence only a small perturbation to the electron polarization is expected. When the microwave power is sufficiently high such that induced spin state transitions occur at a much faster rate then

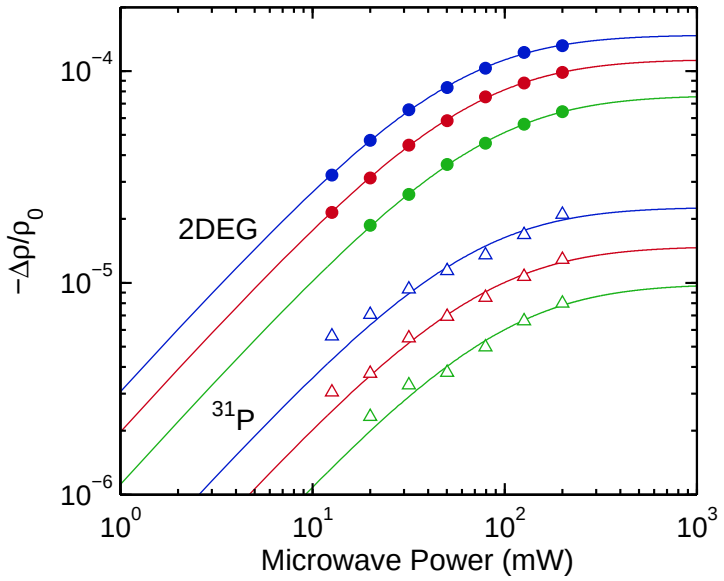

Figure 4.4: X-band power dependence of the 2DEG (solid circles) and ^{31}P (open triangles) EDMR signal intensities from a 28-Si:^{31}P device with $l = 160\,\mu$m and $w = 10\,\mu$m at $T = 4.6$K. $V_g = 275$ (blue), 375(red) and 475(green)mV. $V_d = 20$mV for all measurements.

the natural relaxation rates, the spin up and spin down populations will become equal and saturation will be reached.

Fig. 4.4 shows the microwave power dependence of the EDMR signal intensity for a 28-Si:^{31}P device, under three different gate bias conditions. The maximum microwave power available in this system is 200 mW (Bruker ESP300E with rectangular microwave cavity and loaded Q-factor of $\approx$ 1300). In all cases, the resonance signals are nearly completely saturated at the highest available microwave power. The lines represent best-fits to the data assuming a polarization transfer model with $\Delta\rho \propto p_c^2$, as will be discussed in more detail later. In summary, comparison of EDMR signal intensities are only made when the spin transitions are fully saturated ($p \to 0$) and the EDMR signal intensities maximized.

4.2.3 Calibrated X-band EDMR spectrum

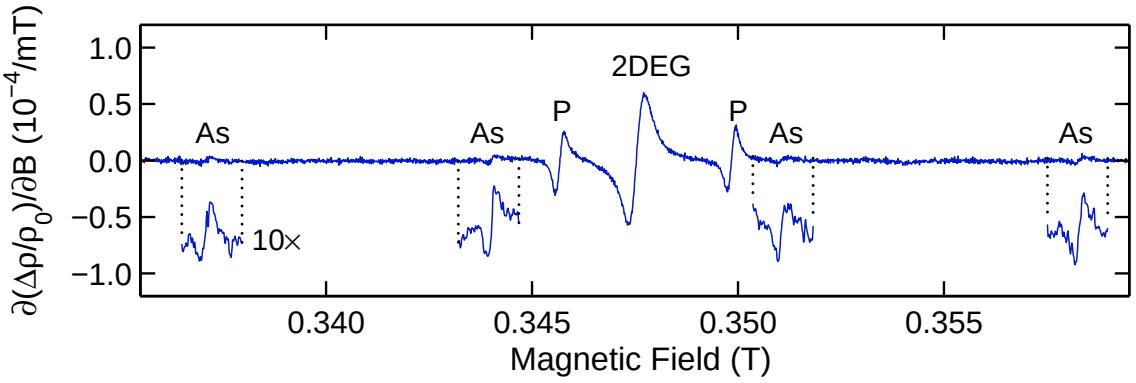

Figure 4.5: EDMR spectra obtained in X-band with $f_{\mu w} = 9.7\,\text{GHz}$ and $T = 5\,\text{K}$. The 2DEG, phosphorus (P) and arsenic (As) resonances are indicated along the trace. Sections of the EDMR spectrum containing the ^{75}As signals are magnified by 10$\times$ and offset for clarity. $V_g = 0.3\,\text{V}$ and $V_d = 40\,\text{mV}$.

Keeping the basic interpretation of the EDMR measurements discussed in the previous sections in mind, we can now examine the spectra in greater detail. Fig. 4.5 shows the EDMR spectrum of a device built on a 28-Si substrate, again background doped with ^{31}P but in addition received a channel implant of ^{75}As (28-Si:^{31}P+^{75}As). The device actually has a triple-gate geometry, which we will discuss in detail in Chapter 6. For these measurements, all three gates are biased together and the device can be considered as a simple three-terminal MOSFET. The spectra clearly shows the large 2DEG signal at the center, the two ^{31}P donor signals separated by 4.2 mT centered around the 2DEG signal, and the four hyperfine-split ^{75}As peaks further out. The relative ratio between the ^{31}P and ^{75}As signal intensities is consistent with the number of hyperfine-split resonance lines and the total number of dopants

under the channel, as confirmed by secondary ion mass spectroscopy (SIMS). More details of dopant distribution in the channel will be discussed in Chapter 5.

We should pay attention to two additional details. First, the 2DEG signal intensity is considerably larger than the donor signal intensities, even when combined. Second, the resistivity decreases on resonance[2], i.e. $\Delta\rho < 0$. These observations will be important in understanding the underlying spin-dependent transport mechanism and will be addressed in the next few sections. However, we will first examine the effect on the EDMR signals with Zeeman field scaling to W-band.

4.2.4 Calibrated W-band EDMR spectrum

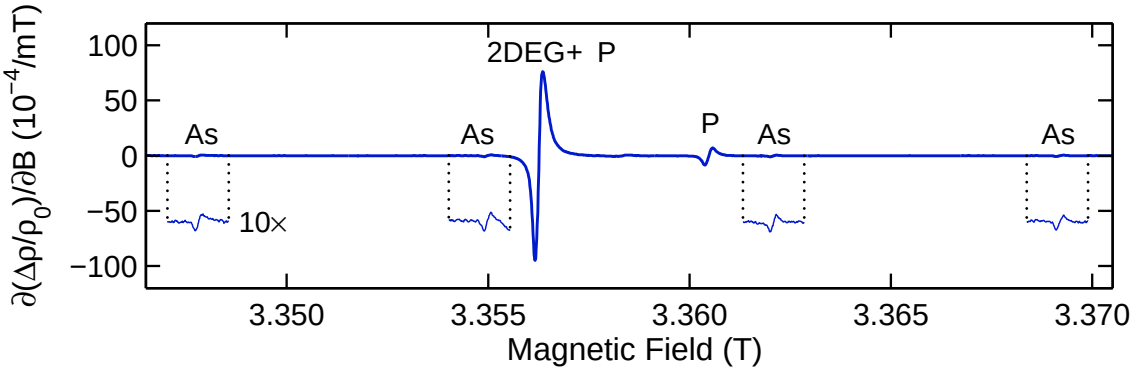

Figure 4.6: EDMR spectra obtained in W-band with $f_{\mu w} = 94\,\text{GHz}$ and $T = 5\,\text{K}$. The 2DEG, phosphorus (P) and arsenic (As) resonances are indicated along the trace. Sections of the EDMR spectra are magnified by 10× and offset for clarity. $V_g = 0.3\,\text{V}$ and $V_d = 40\,\text{mV}$.

The donor EDMR signal intensities observed in X-band were typically in the order of $\Delta\rho/\rho_0 \sim 10^{-6} - 10^{-5}$. An increase in these signal intensities are highly desired in terms of the practicality of constructing a spin-state readout device using such a measurement scheme. One approach to enhance the resonance signals is to increase the Zeeman field: as the magnetic field is increased, so will the polarization of electrons in the system. Hence, a larger contrast on and off the resonance condition is expected. We note that this argument holds true only for mechanisms where the polarization models are valid. If spin-pair based mechanisms are the dominating spin-dependent transport processes, the resonance signals should have no magnetic field dependence to first order.

[2]This was done by checking the phase of the lock-in signal carefully by Alexei Tyryshkin with the setup at Princeton University.

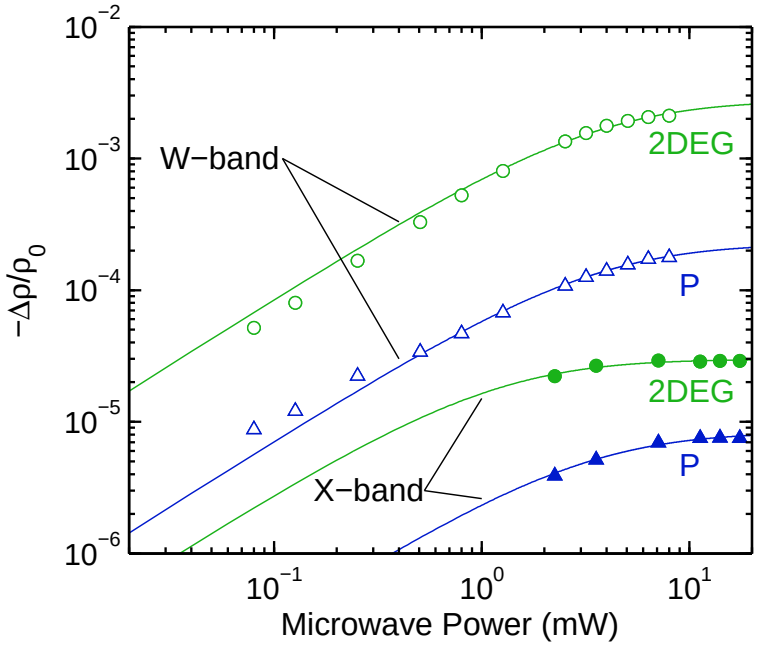

Figure 4.7: Microwave power dependence of the 2DEG (green circles) and ^{31}P (blue triangles) EDMR signal intensities measured in X- and W-band. ^{75}As signals have similar power dependences and are not shown. $V_g = 0.3$ V in all measurements.

Fig. 4.6 shows a representative EDMR spectrum measured in W-band ($f_{\mu w} = 94$ GHz, $B \approx 3.4$ T) with the same device whose X-band EDMR spectrum was discussed in the previous section (Fig. 4.5). The measurements were made under identical bias conditions. The same three groups of resonance lines are seen in the W-band spectrum centered now at the high field of 3.358 T. The field position of the 2DEG relative to the phosphorus center-of-gravity amounts to

$$\Delta B = \frac{h f_{\mu w}}{\mu_B} \left(\frac{1}{g_{2DEG}} - \frac{1}{g_P} \right) = -2.1\,\mathrm{mT} \tag{4.3}$$

hence the 2DEG coincides with the low-field ^{31}P line. This results in the two large resonance lines with different amplitudes around the center, while the four smaller hyperfine-split ^{75}As lines have equal amplitude. The sign of the EDMR signal can be checked directly with an accurate voltmeter on and off resonance with the large 2DEG signal intensity in W-band. The dc measurement confirms that that the sign of the EDMR signal is negative (i.e. $\Delta\rho < 0$), in agreement with phase shift measurements carried out at X-band. With the spin transitions being saturated, as shown in Fig. 4.7, the signal intensities increase from X- to W-band by ≈ 100 and ≈ 20 for the 2DEG and donors, respectively.

4.3 The spin-dependent transport mechanism in MOSFETs

The dominant spin-dependent transport mechanism in donor-doped silicon MOSFETs is discussed in this section. Due to the lack of photocarriers and the fact the MOSFETs are operated in the drift-diffusion regime, spin-depenedent recombination and spin-dependent tunneling are not expected to contribute at all (Chapter 2). Instead, we will focus on (i) bolometric heating, (ii) spin-dependent scattering, and (iii) polarization transfer from the donor to the 2DEG spin system. We begin our discussion with a brief review of the underlying physics of these three mechanisms.

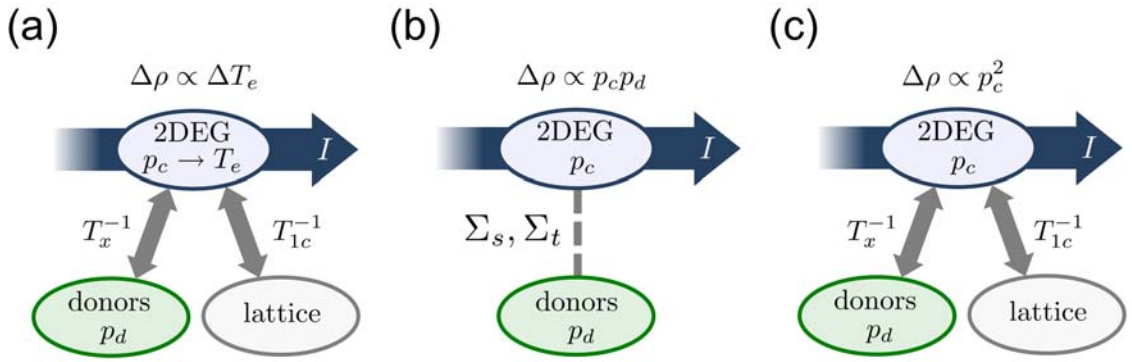

Figure 4.8: Three possible EDMR mechanisms affecting the 2DEG current I (blue arrow) and the expected change in resistivity $\Delta\rho$ associated with each mechanism: (a) bolometric heating, (b) spin-dependent scattering and (c) polarization transfer. The grey arrows represent energy transfer between the systems, while the dashed line in (b) represents elastic scattering.

Bolometric heating of the 2DEG (Fig. 4.8(a)) can occur when the 2DEG orbital electron temperature T_e rises as a result of an increase of the 2DEG spin temperature (i.e. a decrease in the 2DEG spin density polarization p_c) via spin-orbit interaction [128]. The energy transfer from the 2DEG spins to the lattice occurs through conduction electron spin relaxation processes T_{1c} and from donor spins through flip-flop T_x process via exchange scattering with the 2DEG. This effect is expected to be enhanced at higher magnetic fields as the absorbed Zeeman energy on resonance is increased.

Spin-dependent scattering arises from a difference in the scattering cross sections Σ_s and Σ_t when the 2DEG and donor electrons form singlet (s) and triplet (t) pairs, respectively (Fig. 4.8(b)). The number of singlet pairs is increased when either the donor or 2DEG spins are resonantly excited. This leads to a change in sample resistivity of $\Delta\rho/\rho_0 \propto p_c p_d$ under full

power saturation, where ρ_0 is the resistivity in thermal equilibrium, and p_d the spin density polarization for the donor electrons. For an ideal 2DEG, $p_c \propto g\mu_B B$, where g is the Landé g-factor, μ_B the Bohr magneton and B the magnetic field. For donors, $p_d = \tanh(g\mu_B B/k_B T)$, with k_B the Boltzmann constant and T the temperature. This implies that the 2DEG and donor resonance signals should have the same magnetic field dependence, as the product of the polarizations is measured under this mechanism.

The third mechanism we consider results from the polarization dependence of the 2DEG resistivity [129, 130, 131], as was found to be the case for EDMR of high mobility silicon 2DEGs [111, 132]. Donor electrons can contribute to a resonant change in 2DEG resistivity as the donor polarization is transferred to the 2DEG spin system via exchange scattering (Fig. 4.8(c)). The observation of this effect is only possible if spin-orbit coupling is weak and T_e is not perturbed excessively, as the bolometric response will dominate otherwise. These three mechanisms form the basis for the detailed discussion of our results below.

4.3.1 Bolometric detection

In order to assess the possible contribution of bolometric heating of the 2DEG to the EDMR signal, we measured the device resistivity over the temperature range $T = 5 - 12\,\mathrm{K}$ as shown in Fig. 4.9. At these temperatures, acoustic phonon scattering does not contribute to the overall carrier mobility significantly. Hence any temperature dependence of the resistivity is a result of changes in T_e only and independent of the lattice temperature T_l. We observe that carrier transport can be separated into two regimes: (i) $\partial\rho_0/\partial T < 0$ for $V_g < 0.3\,\mathrm{V}$, the activated transport regime, and (ii) $\partial\rho_0/\partial T > 0$ for $V_g > 0.3\,\mathrm{V}$, the metallic regime. For bolometric heating one would expect the sign of $\Delta\rho$ to follow the sign of $\partial\rho_0/\partial T$. The sign of the EDMR signal should thus change at around $V_g = 0.3\,\mathrm{V}$. Our EDMR experiments do not reveal any change in sign, and it disagrees with the temperature gradient for $V_g \geq 0.3\,\mathrm{V}$. We thus conclude that bolometric heating does not contribute to the EDMR signal significantly.

4.3.2 Spin-dependent scattering

Previous EDMR measurements of similar donor-doped FETs at X-band have been attributed to spin-dependent neutral donor scattering [99, 121]. De Sousa *et al.* [110] recently calculated the scattering cross sections for such systems and concluded that $\Sigma_s > \Sigma_t$ (i.e. $\Delta\rho/\rho_0 > 0$), which contradicts Ghosh and Silsbee's as well as our results. We note, however, that a refined calculation taking the full anisotropy of the silicon band structure into account might lead to cases where $\Sigma_s < \Sigma_t$ [133]. The neutral donor scattering model also predicts the 2DEG signal intensity to be equal to the sum of the hyperfine-split donor signal intensities, while our results show that the 2DEG signal intensity is much greater than the sum in both low- and high-field measurements. This can only be the case if spin-dependent scattering with other paramagnetic centers, such as P_b centers [134], also contribute to the 2DEG signal. Such resonance signals were, however, not observed in our experiments. Finally, from the

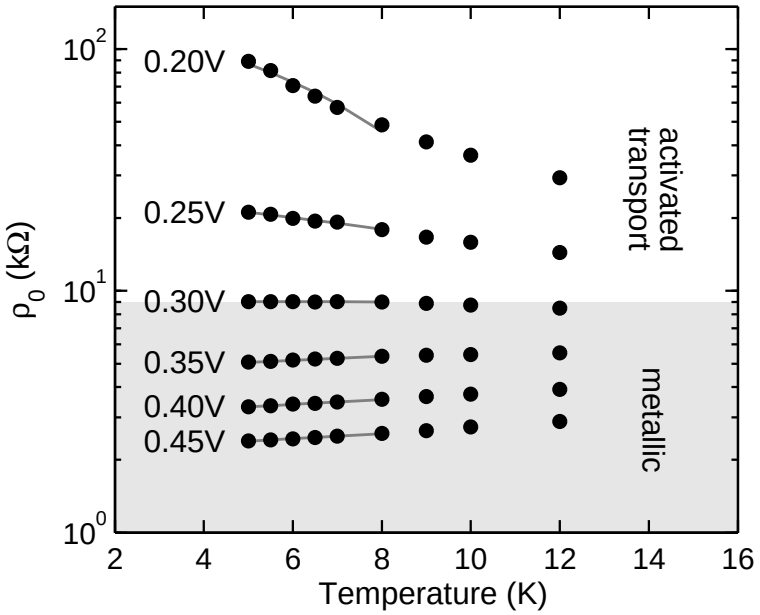

Figure 4.9: Temperature dependence of device resistivity for gate voltages $V_g = 0.20 - 0.45$V. The lines correspond to linear fits to the data for $T \leq 8$ K.

increase in thermal equilibrium polarizations we expect the spin-dependent scattering signal to be enhanced by a factor of 80 at $T = 5$ K from X- to W-band. Over the gate bias range examined, with corresponding 2DEG densities of $5 \times 10^{10} - 1.5 \times 10^{11}/\text{cm}^2$, we have found that the 2DEG enhancement is stronger than expected, while the donor enhancement is substantially smaller. Due to these inconsistencies it is difficult to explain our results by this mechanism alone.

4.3.3 2DEG polarization-dependent resistivity and polarization transfer from donors

We now examine a third EDMR mechanism, which originates from the polarization-dependent resistivity of the 2DEG [111, 132, 135, 136]. We assume the 2DEG resistivity to be approximated by [111]

$$\rho = \rho_1 + \rho_2 p_c^2 \tag{4.4}$$

where ρ_1 and ρ_2 are the polarization-independent and the polarization-dependent components, respectively. Since $\rho_1 \gg \rho_2$ and assuming a complete saturation of the 2DEG spin transition, we have $\Delta\rho/\rho_0 \approx -p_c^2/(\rho_1/\rho_2)$ for the 2DEG. From the positive in-plane magnetoresistances ($\partial\rho/\partial B > 0$), i.e. positive correlation between 2DEG resistivity and p_c

[129, 130, 131], we expect $\rho_2 > 0$. Thus, this model agrees with the negative sign of the EDMR signal observed in our experiments. At X-band, we estimate that $p_c \approx 1\%$ with the 2DEG densities used, and since $\Delta\rho/\rho_0 \approx -10^{-5}$, we have $\rho_1/\rho_2 \approx 10$. Since $p_c \propto B$, the 2DEG signal should increase by 100 times from X- to W-band, which is indeed observed. The signal intensities of the donors depend on the effectiveness of the donor-to-2DEG polarization transfer, which is determined by (i) the spin relaxation rate of the 2DEG T_{1c}^{-1}, and (ii) the spin exchange scattering rate T_x^{-1}, which varies from donor to donor depending on their distance to the oxide interface [110] [3] (we assume the spin relaxation rate of donors T_{1d} to be much smaller than that of the 2DEG [127, 76, 24]). When $T_x^{-1} \ll T_{1c}^{-1}$, p_c returns to its thermal equilibrium rapidly, and hence the change in p_d has little effect on p_c. Therefore, no donor resonance signal should be observed. In the opposite limit where $T_x^{-1} \gg T_{1c}^{-1}$, p_c and p_d are strongly coupled and indistinguishable. In this case one would expect the 2DEG and donor signal intensities to be equal, which was not observed. Since T_x^{-1} does not change much with magnetic field in the temperature range of our experiments [4], the different 2DEG and donor signal intensity ratios at X- and W-band can therefore be explained if T_{1c}^{-1} becomes larger at higher magnetic fields: Donors with $T_x^{-1} \gtrsim T_{1c}^{-1}$ at X-band will be less effective in influencing p_c in W-band as now $T_x^{-1} < T_{1c}^{-1}$. This implies that a reduced number of donors can contribute to the donor resonance signal in the high field measurements, and is consistent with the observed increase in the 2DEG-to-donor signal intensity ratio in W-band vs. X-band. However, we are unaware of any experimental measurements of the magnetic field dependence of T_{1c}^{-1} in the metallic limit of a disordered 2DEG.

We can use a scattering rate model of polarization transfer to verify this intuitive picture. In the simplified model, all 2DEG electrons have one characteristic spin relaxation time and all donors are characterized by a single exchange scattering rate, equivalent to having a delta-doped layer. The goal is to develop a model describing the spin polarizations of the 2DEG interacting with donor electrons in the system. When the 2DEG and donor electrons are not interacting with each other, their polarizations are given by their thermal equilibrium values [137, 99, 110]:

$$p_{c0,eq} = \frac{g\mu_B B}{2(\epsilon_f - \epsilon_0)} \tag{4.5}$$

and

[3] The total 2DEG spin relaxation rate for an ideal 2DEG reads $n_c p_c T_{1c}^{-1} = (n_\uparrow - n_\downarrow)T_{1c}^{-1}$, where n_c is the number of 2DEG electrons, as only unpaired electrons can absorb microwave. The total spin exchange scattering rate in the system should read $n_d T_x^{-1}$, where n_d is the total number of donors present. We abbreviate the total spin relaxation and exchange scattering rates as T_{1c}^{-1} and T_x^{-1} respectively in the main text for simplicity.

[4] See equation (11) of Ref. [110], where the donor T_1^{-1} corresponds to the donor spin-flip exchange rate T_x^{-1} discussed here.

$$p_{d0,eq} = \tanh\left(\frac{g\mu_B B}{k_B T}\right) \tag{4.6}$$

for the 2DEG and donor electrons, respectively.

However, when conduction electrons and donor electrons begin to scatter off each other their polarizations will become interdependent. The rate for donor electrons to flip $\uparrow\rightarrow\downarrow$ (and conduction electrons $\downarrow\rightarrow\uparrow$) is given by:

$$\Gamma_{\uparrow\downarrow} = \gamma \int f(\epsilon - \epsilon_{f\downarrow})(1 - f(\epsilon - \epsilon_{f\uparrow} - g\mu_B B))d\epsilon \tag{4.7}$$

and for the opposite process (donors flip $\downarrow\rightarrow\uparrow$ and conduction electrons flip $\uparrow\rightarrow\downarrow$):

$$\Gamma_{\downarrow\uparrow} = \gamma \int f(\epsilon - \epsilon_{f\uparrow})(1 - f(\epsilon - \epsilon_{f\downarrow} + g\mu_B B))d\epsilon \tag{4.8}$$

where $\epsilon_{f\sigma}$ refers to the Fermi level of the conduction electrons in spin state σ, $f(\epsilon) = 1/(1 + e^{(\epsilon-\epsilon_f)/k_B T})$ is the Fermi function, and $\gamma = \frac{2\pi}{\hbar}|J|^2\rho_{2DEG}^2$ characterizes the exchange scattering rate [110]. The continuity equations for the $\uparrow$-state donor and conduction electron populations become:

$$\frac{\partial}{\partial t}\left(\frac{n_{d\uparrow}}{n_d}\right) = \frac{\partial}{\partial t}p_{d\uparrow} = -\Gamma_{\uparrow\downarrow}p_{d\uparrow} + \Gamma_{\downarrow\uparrow}p_{d\downarrow} + \frac{p_{d0\uparrow,eq} - p_{d_\uparrow}}{T_{1d}} \tag{4.9}$$

$$\frac{\partial}{\partial t}\left(\frac{n_{c\uparrow}}{n_c}\right) = \frac{\partial}{\partial t}p_{c\uparrow} = \frac{n_d}{n_c}(+\Gamma_{\uparrow\downarrow}p_{d\uparrow} - \Gamma_{\downarrow\uparrow}p_{d\downarrow}) + \frac{p_{c0,eq\uparrow} - p_{c_\uparrow}}{T_{1c}} \tag{4.10}$$

where $p = p_\uparrow - p_\downarrow$. The steady-state donor and conduction electron polarizations can then be found from the above equations by solving them simultaneously and assuming $\partial p/\partial t = 0$. This will give the thermal equilibrium polarizations p_{d0} and p_{c0} with 2DEG-donor interaction. For the sample resistivity taking the form of Eq. 4.4: $\rho = \rho_1 + \rho_2 p_c^2$, under complete spin saturation of the 2DEG electrons the 2DEG EDMR signal intensity becomes:

$$\left.\frac{\Delta\rho}{\rho_0}\right|_{2DEG} = \frac{-p_{c0}^2}{\left(\frac{\rho_1}{\rho_2}\right) + p_{c0}^2} \approx \frac{-p_{c0}^2}{\left(\frac{\rho_1}{\rho_2}\right)} \tag{4.11}$$

For the donor resonance signals, we would need to find the conduction electron polarization when the donor electrons are on spin resonance. This value $p_{c,donor}$ is found by solving the continuity equation for the conduction electrons assuming the donor spin transition is saturated ($p_d = 0$, or equivalently $p_{d\uparrow} = p_{d\downarrow}$). The donor EDMR signal intensity becomes:

$$\left.\frac{\Delta\rho}{\rho_0}\right|_{donor} = \frac{p_{c,donor}^2 - p_{c0}^2}{\left(\frac{\rho_1}{\rho_2}\right) + p_{c0}^2} \approx \frac{p_{c,donor}^2 - p_{c0}^2}{\left(\frac{\rho_1}{\rho_2}\right)} \tag{4.12}$$

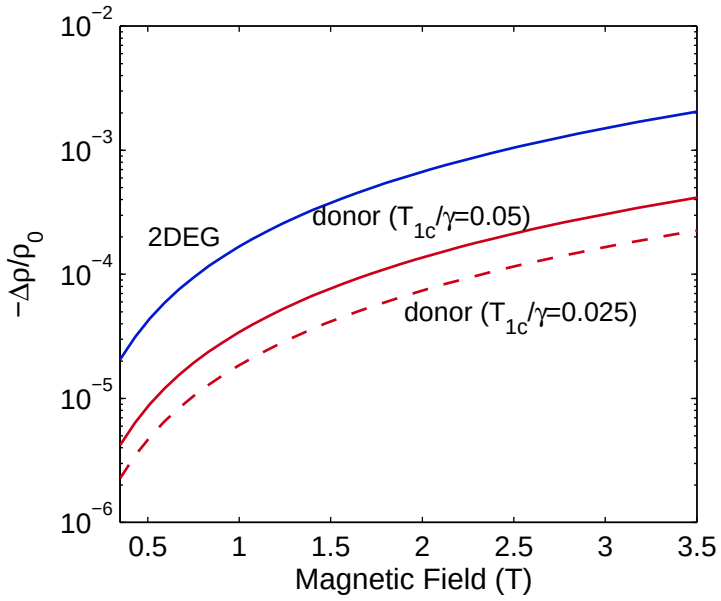

Figure 4.10: Calculated EDMR signal intensities versus the resonance Zeeman field for the 2DEG (solid blue trace) and donors (solid red trace). If the 2DEG T_{1c} is reduced by 1/2, the corresponding donor signal (dashed red trace) is also reduced.

Again, the amplitude of ρ_1 and ρ_2 are estimated from the actual 2DEG signal intensity mentioned above, and we have $\rho_1/\rho_2 \approx 10$, justifying the approximations used in the above expressions. The results of the calculations are shown in Fig. 4.10, where all relevant relaxation times are expressed in terms of γ. T_{1d} was chosen to be long and hence its contribution negligible, since the natural donor relaxation rate is expected to be much longer than any other contributions. T_{1c} was chosen such that the 2DEG-donor signal intensities agree approximately with the experimental observations. A variation of T_{1c} by a factor of 2 was used in this calculation, and the numerical results agree with our intuitive understanding: as the conduction electron spin relaxation is reduced, the contribution from donor resonance signals becomes weaker. X-band donor EDMR measurements would correspond to the solid traces, while W-band measurements would correspond to the dotted line with lower donor signal intensities.

4.4 Conclusions

In conclusion, we have measured EDMR in micron-scale donor-doped silicon MOSFETs in order to understand the spin-dependent transport mechanism in such devices. We have seen

that EDMR is a sensitive technique for characterizing the microscopic environment in such MOSFETs as different resonance signals are observed when different dopants are present in the channel. We also examined changes in the EDMR signal intensities with Zeeman field scaling . To summarize our key findings related to the origin of spin-dependent transport in donor-doped silicon MOSFETs, the main experimental observations are:

1. Negative sign of EDMR signal ($\Delta\rho < 0$ on resonance).

2. Much larger 2DEG signal intensity than donor signal intensities.

3. Stronger 2DEG signal intensity scaling with Zeeman field than donor signals.

Of the three different EDMR mechanisms examined, only a polarization-dependent mobility of 2DEG (and subsequent polarization transfer from donor electrons) can satisfactorily explain all three observations. While spin-dependent scattering has been attributed as the origin of the EDMR signal in donor-doped MOSFETs, our data suggests otherwise. It is likely that the difference in scattering cross sections between singlet and triplet 2DEG-donor spin pairs are too small and overshadowed by the more dominant polarization dependence of the 2DEG mobility itself. However, 2DEG-donor scattering is still an integral part of the 2DEG transport process as neutral donors can perturb the 2DEG polarization significantly. One would expect that an undoped MOSFET channel should also give rise to an EDMR signal under such a spin-dependent transport mechanism, as the spin-dependence is intrinsic to the 2DEG itself. This is indeed the case and the study of undoped MOSFETs will be discussed in the next chapter.

Chapter 5

Spin Relaxation in Silicon MOSFETs

In the previous chapter we have found that the dominant spin-dependent transport mechanism in donor-doped silicon MOSFETs is the inherent polarization dependence of the 2DEG mobility itself. In this chapter, we will investigate systematically the effects of varying the donor density, 2DEG density and temperature with X-band EDMR. In addition, we will deduce the spin relaxation times of conduction and donor electrons in these devices, which are important metrics for the realization of a donor-based quantum computer. Lastly, we will demonstrate the measurement of the g-factor anisotropy in the silicon MOS system.

5.1 EDMR spectra

In the previous chapter, we have seen that different donor species in the MOSFET channel give rise to different EDMR spectra, as the resonance conditions are characteristic to the particular hyperfine coupling of different donors. In this section, we will investigate the EDMR spectra and lineshape in greater detail. All data presented in this chapter are from devices with channel length $l = 160\,\mu$m and width $w = 10\,\mu$m (aFET6). For devices with shorter channel lengths, the spectroscopic features of the EDMR spectra remains the same; however, the signal amplitudes are reduced. This issue will be addressed in the next chapter when we take spin drift and spin diffusion effects into account. Most measurements were performed with the Zeeman field aligned in-plane of the 2DEG ($\hat{n} \perp B$, with $\hat{n}$ being the normal of the silicon surface, or equivalently $\theta = 90°$). Cases where θ was changed will be specifically noted.

5.1.1 Donor distribution

Two types of dopants were used in this study: ^{121}Sb (implanted with two different dosages Φ_0), and ^{31}P (background doped in the epitaxial 28-Si layers). Table 5.1 lists the different types of devices we will examine in this section. The dopant distributions in the channel

Device name	Channel dopant
FZ-Si:intrinsic	None
FZ-Si:^{121}Sb	^{121}Sb ($E = 60\,\mathrm{keV}$, $\Phi_0 = 2 \times 10^{11}/\mathrm{cm}^2$)
FZ-Si:^{121}Sb$^+$	^{121}Sb ($E = 60\,\mathrm{keV}$, $\Phi_0 = 6 \times 10^{11}/\mathrm{cm}^2$)
28-Si:^{31}P	^{31}P ($\approx 3 \times 10^{16}/\mathrm{cm}^3$)
28-Si:^{31}P+^{121}Sb	^{31}P ($\approx 3 \times 10^{16}/\mathrm{cm}^3$), ^{121}Sb ($E = 60\,\mathrm{keV}$, $\Phi_0 = 2 \times 10^{11}/\mathrm{cm}^2$)

Table 5.1: Designations of devices and donors present in the MOSFETs studied. The ion implantation energy E and dose Φ_0 are included for the ^{121}Sb donors.

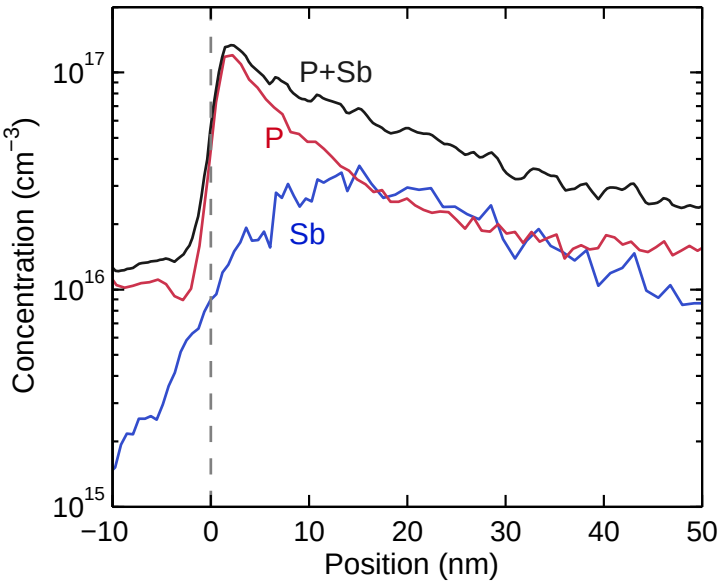

Figure 5.1: SIMS profiles of ^{31}P and ^{121}Sb donor distributions in the 28-Si:^{31}P+^{121}Sb MOSFET channel.

of the 28-Si:^{31}P+^{121}Sb device, which contained both types of dopants, were determined by secondary ion mass spectroscopy (SIMS) [138]. The results are shown in Fig. 5.1. The polycrystalline silicon gate was removed prior to SIMS analysis, but a ≈ 15 nm thick gate oxide remained. In order to determine the position of the Si-SiO_2 interface, the oxygen and ^{28}Si signals were also measured. We set a 50% threshold for these two traces to demarcate the location of the interface, labelled as position 0nm in the figure. The results show a strong pile up of ^{31}P towards the interface, due to segregation during the epitaxial layer growth step and oxidation enhanced diffusion during the gate oxidation step. On the other hand, the implanted ^{121}Sb ($\Phi_0 = 2 \times 10^{11}/\mathrm{cm}^2$) profile remained mostly undistorted. The total

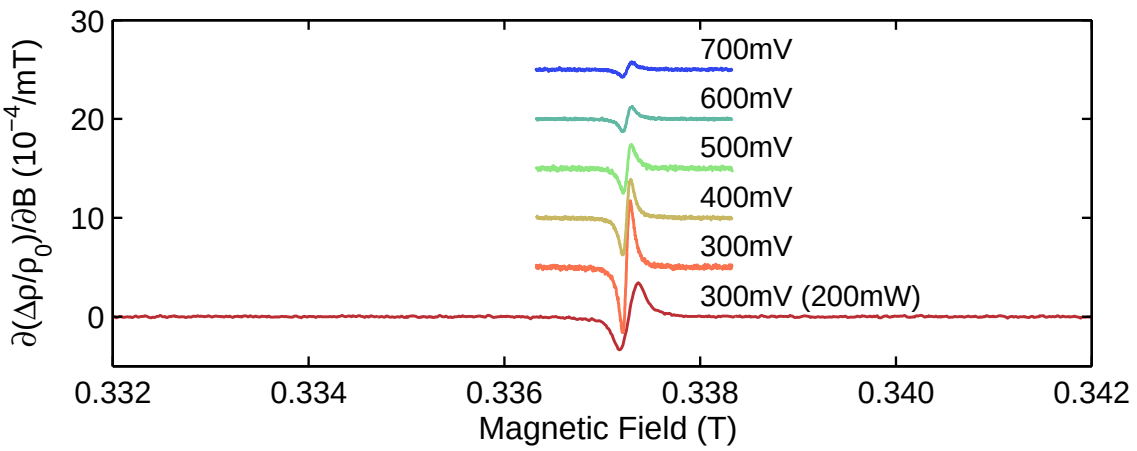

Figure 5.2: EDMR spectra of undoped FZ-Si:intrinsic device measured at $T = 5\,\mathrm{K}$ and $\theta = 90°$. $P_{\mu w} = 12.7\,\mathrm{mW}$ except the lowest trace (red), measured at 200 mW. $V_d = 20\,\mathrm{mV}$ and V_g are indicated next to the traces (offset for clarity).

donor concentration ($[^{31}\mathrm{P}]+[^{121}\mathrm{Sb}]$) is also plotted, showing a nearly monotonic decrease in dopant concentration away from the oxide interface. The thermal budgets used during the fabrication processes are identical for all devices, hence the ^{121}Sb donor profile in the FZ-Si:^{121}Sb device and the ^{31}P donor profile in the 28-Si:^{31}P device are expected to be similar to the profiles shown in Fig. 5.1 (the dopant concentrations are low enough such that concentration-dependent diffusion is not a concern). The wafer FZ-Si:$^{121}\mathrm{Sb}^+$ received three times the ^{121}Sb implantation dosage ($\Phi_0 = 6 \times 10^{11}/\mathrm{cm}^2$) as compared to the other wafers. From SRIM [139] and TCAD [140] simulations, the donor distribution profile is expected to be similar to the lower dosed FZ-Si:^{121}Sb wafer but with the concentrations increased by a factor of three throughout.

The motivation for studying spin-dependent transport in donor-doped MOSFETs is due to the potential for utilizing such devices for performing donor qubit spin-state readout operations. However, from the polarization transfer model discussed in the previous chapter, it is clear that an undoped (intrinsic) MOSFET should also exhibit a strong spin-dependent transport signal. The FZ-Si device without channel implant has background dopant concentrations $< 5 \times 10^{12}\ /\mathrm{cm}^3$ (or equivalently, the mean donor-donor separation is $\approx 800\,\mathrm{nm}$); therefore background dopants are not expected to play any major role in contributing to the 2DEG mobility.

Fig. 5.2 shows the X-band EDMR spectra of the undoped device (FZ-Si:intrinsic) measured at $T = 5\,\mathrm{K}$ under various gate voltage biases. All measurements were performed at a low microwave power of $P_{\mu w} = 12.7\,\mathrm{mW}$, with the exception of the bottom trace measured at $P_{\mu w} = 200\,\mathrm{mW}$ and over a broad region to ensure that no additional spectroscopic fea-

tures are present. The center resonance signal corresponds to that of the 2DEG electrons as discussed in the previous chapter. No evidence of neutral donors or paramagnetic defects are observed in the EDMR spectra. The spectra are similar to the EDMR signals observed in nominally undoped high mobility SiGe heterostructure quantum wells (SiGe 2DEG) reported in literature [111, 132]. This further supports an inherent polarization dependent mobility of the 2DEG, as bounded paramagnetic scattering centers (e.g. neutral donors and paramagnetic defects) are not necessary for the creation of the 2DEG EDMR signal.

The EDMR spectra from a device built on the same FZ-Si substrate but received the low dosage ^{121}Sb implantation (FZ-Si:^{121}Sb) are shown in Fig. 5.3. Only the $m_I = \pm 1/2$ ^{121}Sb lines are shown, separated by 6.7 mT as expected (Table 4.1) [72]. In addition to the presence of the donor resonance lines, the 2DEG signal is also substantially broadened compared with the spectra obtained from the FZ-Si:intrinsic device.

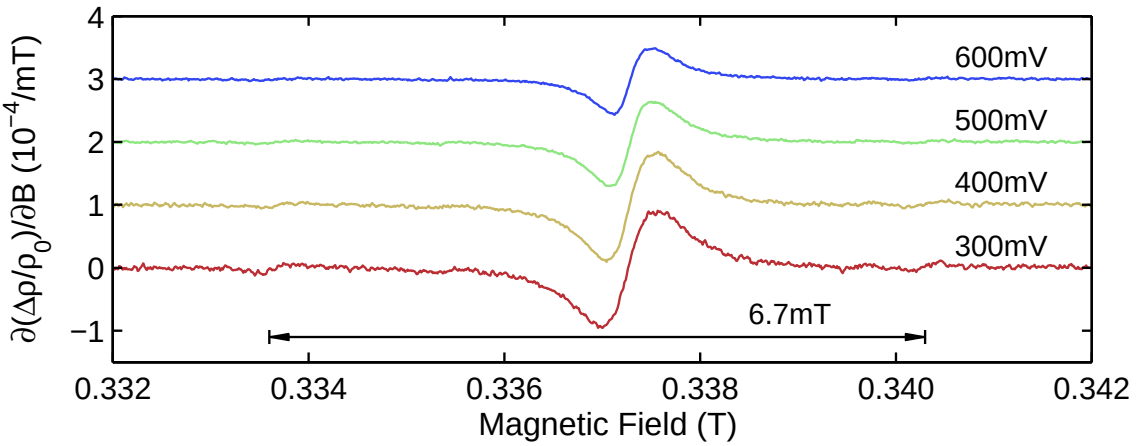

Figure 5.3: EDMR spectra of FZ-Si:^{121}Sb device measured at $T = 5$ K, $\theta = 90°$ and $P_{\mu w} = 200$ mW. $V_d = 20$ mV and V_g are indicated next to the traces (offset for clarity). The $m_I = \pm 1/2$ ^{121}Sb donor resonances are separated by 6.7 mT as indicated.

Fig. 5.4 shows the EDMR spectra from the device that received three times higher implantation dosage of ^{121}Sb (FZ-Si:^{121}Sb$^+$). In addition to smaller donor resonance signals, the central feature consists of two components which are better resolved at higher gate voltages. Two Lorentzian lineshapes are used to fit the observed signal, as shown for the case of $V_g = 700$ mV in Fig. 5.4. The broader component has a peak-to-peak linewidth of $\Delta B_{pp} \approx 0.8$ mT, and is assigned to that of the 2DEG. The narrower component has a linewidth of $\Delta B_{pp} \approx 0.2$ mT, and can be associated with dimers and clusters of donors in the system, similar to EPR measurements in moderately bulk doped silicon [141, 142].

EDMR spectra from the 28-Si:^{31}P device are shown in Fig. 5.5, and that of the 28-

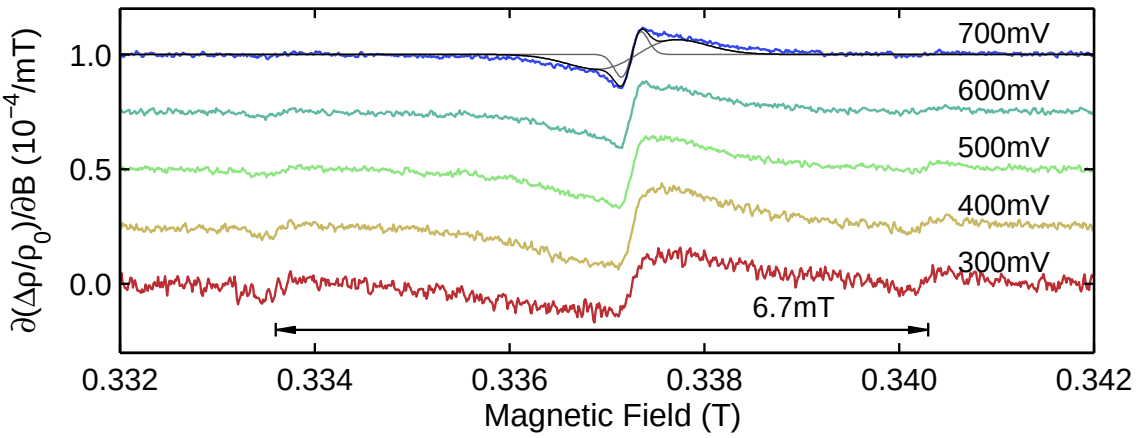

Figure 5.4: EDMR spectra of FZ-Si:^{121}Sb^{+} device measured at $T = 5$ K, $\theta = 90°$ and $P_{\mu w} = 200$ mW. $V_d = 20$ mV and V_g are indicated next to the traces (offset for clarity). The fit to two superimposed Lorentzian lineshapes is shown for $V_g = 700$ mV, with the individual Lorentzian lineshapes illustrated in grey and the summation shown in black.

Si:^{31}P+^{121}Sb device are shown in Fig. 5.6. As before, all donors present in the channel can be identified by the hyperfine splittings. From Fig. 5.1, the total number of ^{31}P donors within 10 nm from the interface is $1.6 \times 10^{11}/\text{cm}^2$, while for ^{121}Sb it is $4.2 \times 10^{10}/\text{cm}^2$. Due to the different nuclear spins, ^{31}P has $8 \times 10^{10}/\text{cm}^2$ donors per hyperfine line, while ^{121}Sb has $7 \times 10^{9}/\text{cm}^2$. However, the hyperfine-split ^{31}P EDMR signal intensities are only ≈ 4 times bigger than the ^{121}Sb signals, instead of the expected factor of ≈ 10. This discrepancy is due to the fact that the large number of ^{31}P donors close to the interface (< 3 nm) are ineffective in contributing to spin-dependent transport, as doubly-occupied D^- states can form [99, 143, 144, 145]. These D^- states are not paramagnetic, and hence not EPR active.

It is interesting to compare the EDMR spectra of the FZ-Si:^{121}Sb^{+} and the 28-Si:^{31}P+^{121}Sb devices, as the peak donor concentrations are in excess of 10^{17} /cm^3 in both cases. While the dimers/clusters signal is clearly observed for the FZ-Si:^{121}Sb^{+} device, the center signal in the 28-Si:^{31}P+^{121}Sb device is well described by a single Lorentzian. This difference is a result of the differences in positions where the peak concentrations occur — where dimers/clusters are most likely to form: for the 28-Si:^{31}P+^{121}Sb device, the peak occurs very close to the Si-SiO$_2$ interface, and the dimers/clusters are hence mostly submerged in the 2DEG. Therefore, they are not EPR active while they degrade the sample mobility (Table 5.2). On the other hand, the peak donor concentration for the FZ-Si:^{121}Sb^{+} device occurs further away from the interface. Dimers and clusters formed in this region are then EPR active and can perturb the 2DEG polarization again through exchange scattering.

Fig. 5.7 shows the microwave power dependence of the EDMR signal intensities of four

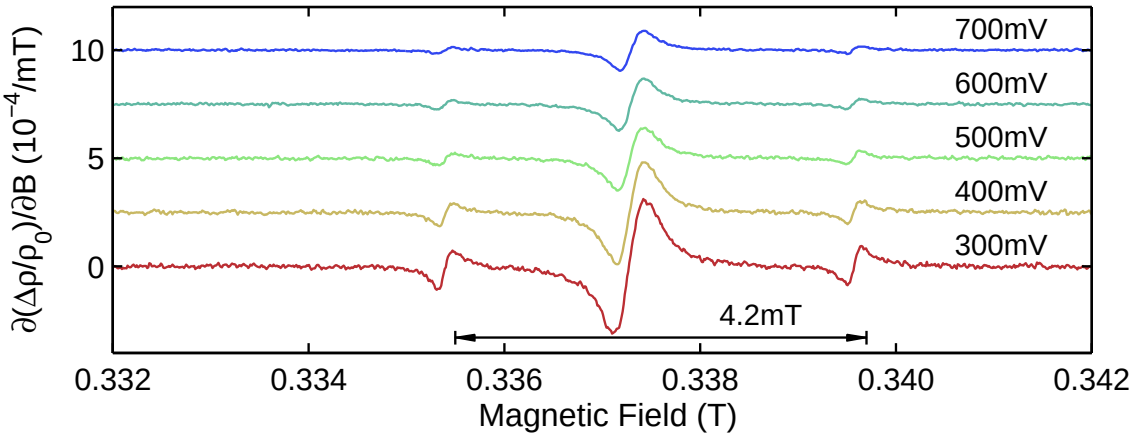

Figure 5.5: EDMR spectra of 28-Si:^{31}P device measured at $T = 5$ K, $\theta = 90°$ and $P_{\mu w} = 200$ mW. $V_d = 20$ mV and V_g are indicated next to the traces (offset for clarity). The $m_I = \pm 1/2$ ^{31}P donor resonances are separated by 4.2 mT as indicated.

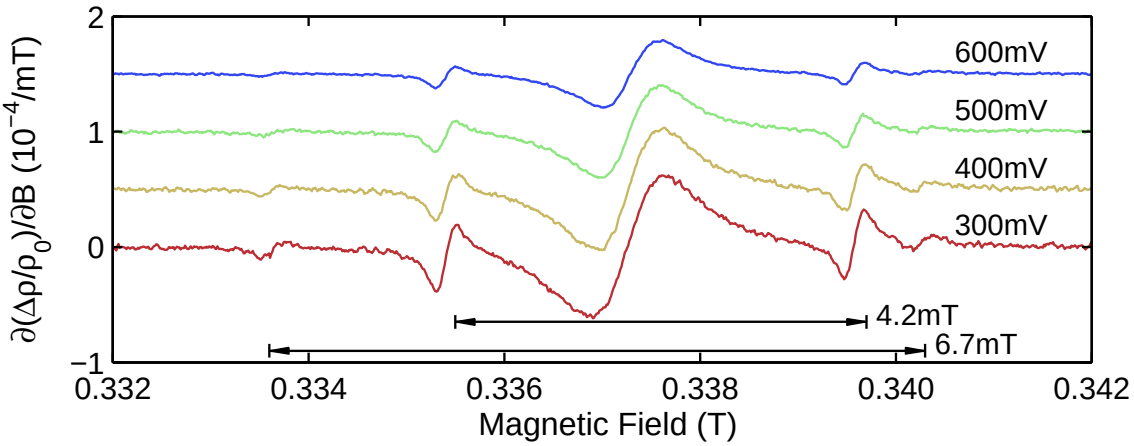

Figure 5.6: EDMR spectra of 28-Si:^{31}P+^{121}Sb device measured at $T = 5$K, $\theta = 90°$ and $P_{\mu w} = 200$ mW. $V_d = 20$ mV and V_g are indicated next to the traces (offset for clarity). The $m_I = \pm 1/2$ ^{31}P and ^{121}Sb donor resonances are separated by 4.2 mT and 6.7 mT, respectively, as indicated.

of the devices: FZ-Si, FZ-Si:^{121}Sb, 28-Si:^{31}P and 28-Si:^{31}P+^{121}Sb. The solid traces for each data set is a fit to the microwave power dependence:

$$\frac{\Delta\rho}{\rho_0} = \alpha\left[\left(\frac{1}{1+\beta P_{\mu w}}\right)^2 - 1\right] \tag{5.1}$$

where the fitting parameters are the saturated signal intensity $\alpha = -(\Delta\rho/\rho_0)_{sat}$ and β. This expression is a direct consequence of Eq. 4.4 when comparing the sample resistivity on and off resonance (see also Eq. 5.7 below). Upon complete spin saturation, $\Delta\rho/\rho_0$ approaches $(\Delta\rho/\rho_0)_{sat}$. In some cases, the microwave power available is not sufficient to completely saturate the spins. Hence, the extrapolated saturation level, $(\Delta\rho/\rho_0)_{sat}$, are used for comparison of signal intensities. The figure reveals that the 2DEG signals converge toward $(\Delta\rho/\rho_0)_{sat} \approx 1.2\times10^{-4}$ for all devices. The ^{121}Sb signal intensities also converge to $(\Delta\rho/\rho_0)_{sat} \approx 2.5\times10^{-6}$. On the other hand, for identical ^{31}P donor profiles, the device without ^{121}Sb in the channel show much stronger resonance signals. This is a consequence of the longer 2DEG T_1 in the 28-Si:^{31}P device compared with the 28-Si:^{31}P+^{121}Sb device as we will examine later in the chapter.

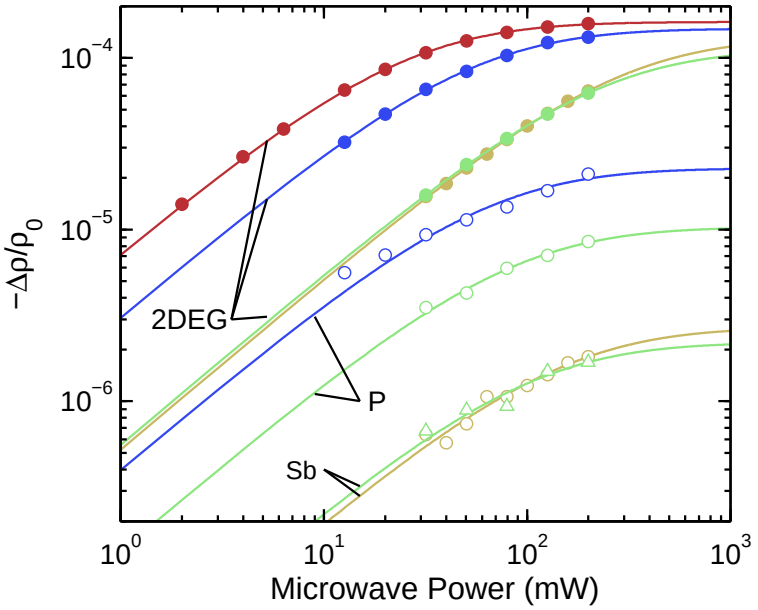

Figure 5.7: Microwave power dependence of EDMR signal intensities for FZ-Si:intrinsic (red), FZ-Si:^{121}Sb (yellow), 28-Si:^{31}P (blue), and 28-Si:^{31}P+^{121}Sb (green) devices. All measurements were made at $V_g = 300$ mV, $V_d = 20$ mV and $T = 5$ K.

5.1.2 Electron density

We now turn our attention to changes in the EDMR signal intensity as the gate voltage, and hence 2DEG density, is varied. When the gate voltage V_g is above the threshold voltage V_t, the 2DEG density n_c is approximated by:

$$n_c = \frac{C_{ox}}{q}(V_g - V_t) \tag{5.2}$$

where C_{ox} is the oxide capacitance calculated based on the thickness of the gate oxide, which is 20 nm for these devices. Fig. 5.8 shows the dependence of the EDMR signal intensities on the 2DEG densities from the 28-Si:^{31}P+^{121}Sb device. When $V_g < V_t$, the EDMR signal intensity decreases rapidly (not shown). Thus, both the 2DEG and donor resonance signals reach a maximum just above the threshold voltage V_t, and decreases as V_g is either increased or decreased. Measurements on the other devices reveal similar characteristics.

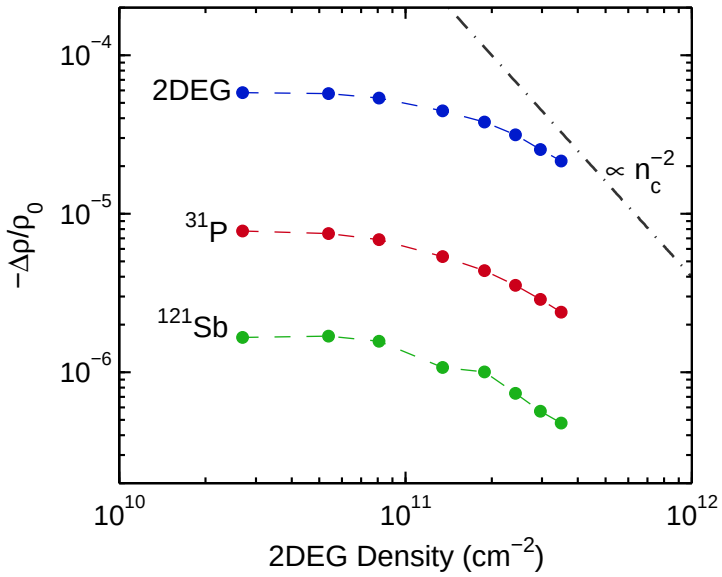

Figure 5.8: 2DEG and donor EDMR signal intensities of 28-Si:^{31}P+^{121}Sb device as a function of 2DEG density. The dashed line represents the expected signal intensity scaling corresponding to $p_c^2 \propto 1/n_c^2$. Measurements were performed at $T = 5$ K, $\theta = 90°$ and $V_d = 20$ mV.

Since the 2DEG polarization $p_c \propto n_c^{-1}$, from the polarization dependence of resistivity (Eq. 4.4) we expect:

$$\frac{\Delta\rho}{\rho_0} \approx -\frac{\Delta p_c^2}{\rho_1/\rho_2} \propto \frac{1}{n_c^2} \tag{5.3}$$

The EDMR signal intensities tend towards a n_c^{-2} dependence only at higher 2DEG densities, as shown by the trend line in Fig.5.8, while the signal intensities vary much less rapidly at lower carrier concentrations. This is similar to previous measurements with high mobility SiGe 2DEG systems [111], which also exhibited a n_c^{-2} dependence in the 2DEG EDMR signal intensity (no donors were present in those systems) at high carrier densities. This dependence was used to support the interpretation that the dominant spin-dependent transport mechanism in the high mobility samples is due to 2DEG electron-electron spin-dependent scattering. However, deviation from the n_c^{-2} dependence was also observed in their case when $n_c < 5 \times 10^{11}/\text{cm}^2$. We note that the 2DEG density dependence of the EDMR signal can be much more complicated than a simple n_c scaling interpretation: the resistivity parameters ρ_1 and ρ_2 also have strong gate voltage dependences due to changes in the dominant scattering mechanisms with carrier density [146, 130, 131, 147]. At lower carrier concentrations electron-electron scattering play a much less significant role than other scattering mechanisms, and hence it seems reasonable that a n_c^{-2} dependence becomes more prominent only at higher gate voltages.

5.1.3 Temperature dependence

Fig. 5.9 shows the temperature dependence of the EDMR signals from the 28-Si:^{31}P device. Both 2DEG and donor signals decrease with increasing temperature, with the former decreasing at a more rapid pace. This is shown more clearly in Fig. 5.10, where the saturated EDMR signal intensities are plotted. The dashed lines correspond to linear fits to:

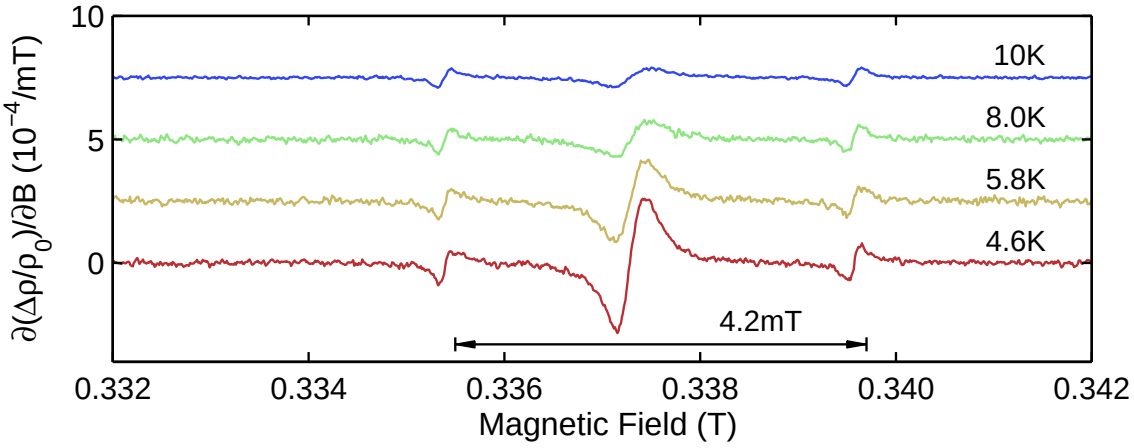

Figure 5.9: Temperature dependence of EDMR spectra from the 28-Si:^{31}P device. The measurements were performed with $V_g = 375\,\text{mV}$, $V_d = 20\,\text{mV}$, $\theta = 90°$ and $P_{\mu w} = 200\,\text{mW}$.

$$\frac{\Delta\rho}{\rho_0} = \frac{a}{T} + b \tag{5.4}$$

where a and b are fitting parameters. The donor exchange scattering rate with the 2DEG has temperature dependence [110]:

$$\frac{1}{T_x} \propto g\mu_B B \coth\left(\frac{g\mu_B B}{2k_B T}\right) \tag{5.5}$$

At X-band, $B \approx 0.35\,\mathrm{T}$ and hence $T_x^{-1} \propto k_B T$. Therefore, the 2DEG-donor signal intensity ratio will reduce if the 2DEG T_1^{-1} does not increase as rapidly as T_x^{-1} with temperature. The measurement of T_1 of the 2DEG at different temperatures will be discussed in the next section.

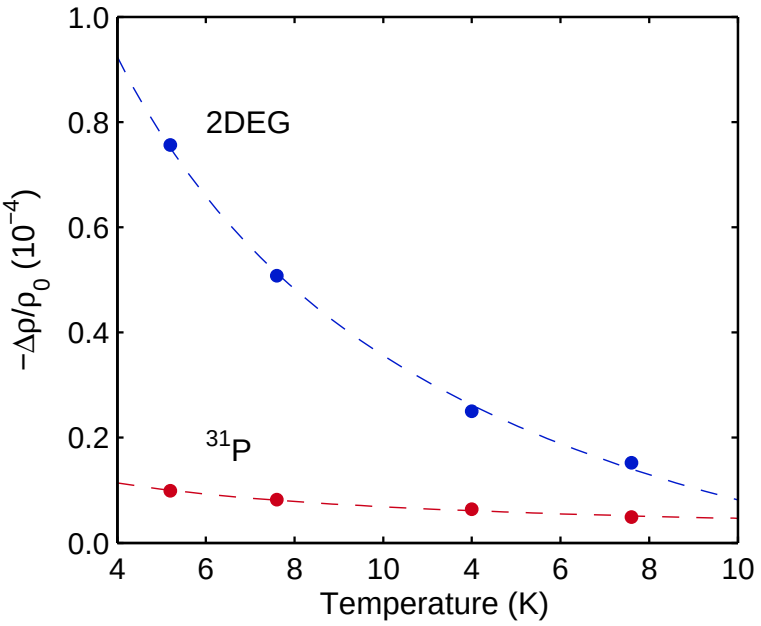

Figure 5.10: Temperature dependence of EDMR signal intensities for 28-Si:^{31}P. $V_g = 375\,\mathrm{mV}$ and $V_d = 20\,\mathrm{mV}$ in all cases.

5.2 Spin relaxation times

In addition to information about the paramagnetic species involved in the spin transitions as discussed in the previous section, the EDMR lineshapes also contain information regarding the spin relaxation times of the paramagnetic species [81, 148]. When the paramagnetic

species are inhomogeneouslly broadened, the cw-EPR linewidth provides information of T_2^* only, and the lineshapes are usually described by Gaussian functions. On the other hand, if the intrinsic homogeneous line broadening is dominant, in which case the EPR lineshapes are described by Lorentzian functions, the natural linewidth yields T_2 directly. In this section, we will study the EDMR lineshapes and extract the spin relaxation times of electrons in silicon MOSFETs.

5.2.1 Transverse spin relaxation time T_2

Fig. 5.11 shows the measured peak-to-peak linewidths ΔB_{pp} of the 28-Si:^{31}P device as a function of microwave power. We focus on the 28-Si:^{31}P device as the relatively large donor signals enable measurements at low microwave powers and small modulation amplitudes in a reasonable timeframe. The EDMR signals are broadened with increasing microwave power as would be expected. At the lowest microwave power used, the EDMR resonance lines are not power broadened and reveals the natural linewidths of the resonance signals.

Fig. 5.12 shows the fits of the EDMR signals to derivative Lorentzian and Gaussian lineshapes measured at the low microwave power of $P_{\mu w} = 12.6$ mW. It is found that the resonance signals are better described by Lorentzian lineshapes for both the 2DEG and

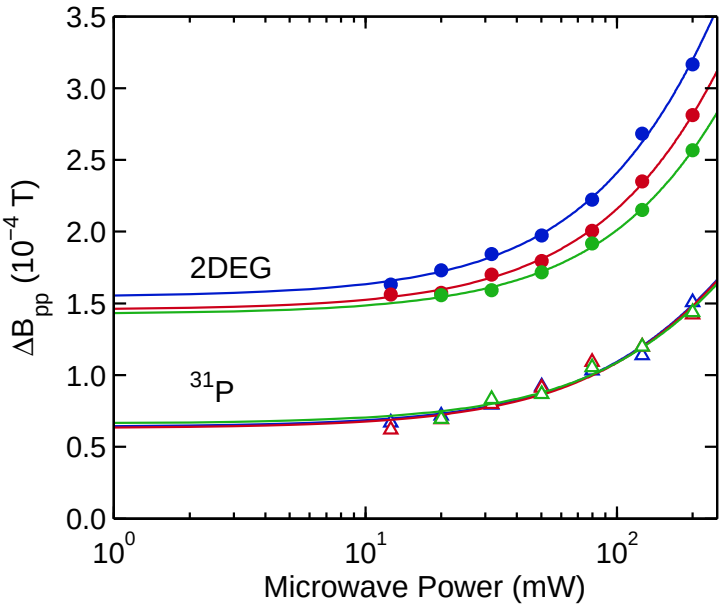

Figure 5.11: Power dependence of the peak-to-peak linewidths ΔB_{pp} of the 2DEG (solid circles) and ^{31}P (open triangles) of the 28-Si:^{31}P device. $V_d = 20$mV, $\theta = 90°$ and $T = 5$ K. $V_g = 275$ (blue), 375 (red) and 475 mV (green).

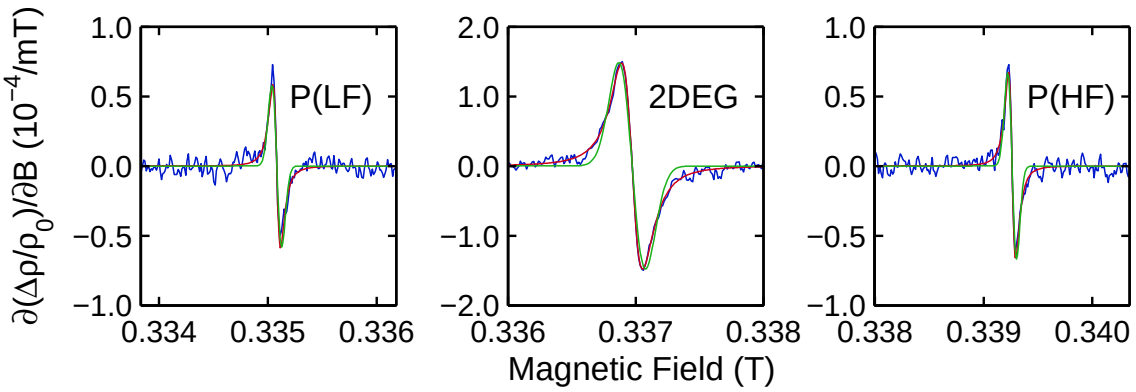

Figure 5.12: EDMR lineshape of the 28-Si:^{31}P device at a low microwave power of $P_{\mu w} = 12.6$ mW (blue). Left panel: low-field ^{31}P signal. Center panel: 2DEG signal. Right panel: High-field ^{31}P signal. Lorentzian (red) and Gaussian (green) fits are also shown. $V_d = 20$ mV and $V_g = 275$ mV.

donor resonance lines in all our EDMR measurements. This suggests that the electrons are homogeneously broadened, and hence, an extraction of the linewidth will provide us with the transverse spin relaxation time T_2 directly. We should note that the EDMR lineshapes are slightly different from the EPR lineshapes and hence care must be taken to relate ΔB_{pp} to T_2, as we will discuss below.

We will now derive the relationship between the EDMR linewidth and spin coherence time T_2. From the Bloch equations (Chapter 2), the polarization is given by [148]:

$$\frac{p}{p_0} = \frac{M_z}{M_0} = \frac{[1+\gamma^2 T_2^2 (B_0 - B)^2]}{1+\gamma^2 T_2^2 (B_0 - B)^2 + \gamma^2 B_1^2 T_1 T_2} \tag{5.6}$$

This expression, combined with Eq.4.4, gives the basic EDMR signal lineshape in MOSFETs:

$$\frac{\Delta\rho}{\rho_0} = \frac{\rho_{res} - \rho_0}{\rho_0} = \frac{\rho_2 p_{c0}^2}{\rho_0} \left[\left(\frac{1+\gamma^2 T_2^2 (B_0 - B)^2}{1+\gamma^2 T_2^2 (B_0 - B)^2 + \gamma^2 B_1^2 T_1 T_2} \right)^2 - 1 \right] \tag{5.7}$$

where the derivative of this expression with respect to B gives the measured EDMR signal lineshape. In the range of experimental conditions used in our measurements, this derivative lineshape is virtually indistinguishable from the derivative Lorentzian lineshape. From Eq.5.7 we can derive the expression for the peak-to-peak linewidth as:

$$\Delta B_{pp} = \frac{1}{3}\frac{1}{\gamma T_2} \left[-12 + 18\gamma^2 B_1^2 T_1 T_2 + 6\sqrt{16 + (3\gamma^2 B_1^2 T_1 T_2)^2} \right]^{1/2} \tag{5.8}$$

In the limit of zero microwave power ($B_1 \to 0$), we have:

$$\Delta B_{pp} = \sqrt{\frac{4}{3}}\frac{1}{\gamma T_2} \tag{5.9}$$

The above equation was used for extracting the T_2 times of our samples. Care was taken to ensure that the modulation amplitudes were smaller than the intrinsic linewidths in order to obtain accurate measurements. The device with EDMR data shown in Figs. 5.11 and 5.12 thus has $T_2 \approx 40$ ns for the 2DEG and $T_2 \approx 100$ ns for the ^{31}P donors.

5.2.2 Longitudinal spin relaxation time T_1

At higher microwave power when power broadening occurs, we can deduce information with regard to the longitudinal spin relaxation time T_1, as we can see from Eq. 5.8:

$$\Delta B_{pp} \propto \sqrt{\frac{T_1}{T_2}} P_{\mu w} \tag{5.10}$$

where the microwave power is related to the microwave field amplitude by $P_{\mu w} = kB_1^2$, and k is a constant depending on the resonator type, Q-factor, and sample material characteristics. It is difficult to determine k, and hence B_1 accurately experimentally, due to changes in the field distributions with different samples inside the resonator. A rough estimate for the rectangular resonator used gives $B_1 \approx 1 \times 10^{-2}$ mT at the maximum power of $P_{\mu w} = 200$ mW [149]. Other groups have reported estimates of $B_1 \approx 9 \times 10^{-2}$ mT for a near identical setup [136]. We can estimate B_1 with our devices by assuming:

1. The EDMR signals are homogeneously broadened, so the true T_2 can be extracted as explained in the previous section.

2. When the magnetic field is aligned perpendicular to the plane of the 2DEG ($\theta = 0°$, $\hat{n}||B$), $T_1 \approx T_2$ for mobile electrons. This has been found to be the case based on pulsed EPR measurements of both silicon MOSFETs [150] and high mobility modulation-doped SiGe 2DEGs [151].

Therefore, we can determine B_1 by examining the microwave power dependence of the linewidth for the 2DEG measured at $\theta = 0°$. This is shown in Fig. 5.13, where we fit the observed linewidth change and find $k \approx 10^7$ W/T. This value corresponds to having $B_1 = 4 \times 10^{-2}$ mT at $P_{\mu w} = 200$ mW, in reasonable agreement with the value expected. We also show the same measurements with $\theta = 90°$ under the same bias conditions, where the steeper slope in the increase of the linewidth corresponds to having T_1/T_2 greater than unity, in this case $T_1 \approx 3T_2$. Using this approximate value for B_1, we can estimate T_1 from the 2DEG and donor signals from the EDMR measurements. The extracted T_1 and T_2 times for the 2DEG and donor electrons in the different MOSFET devices are listed in Tables 5.2,

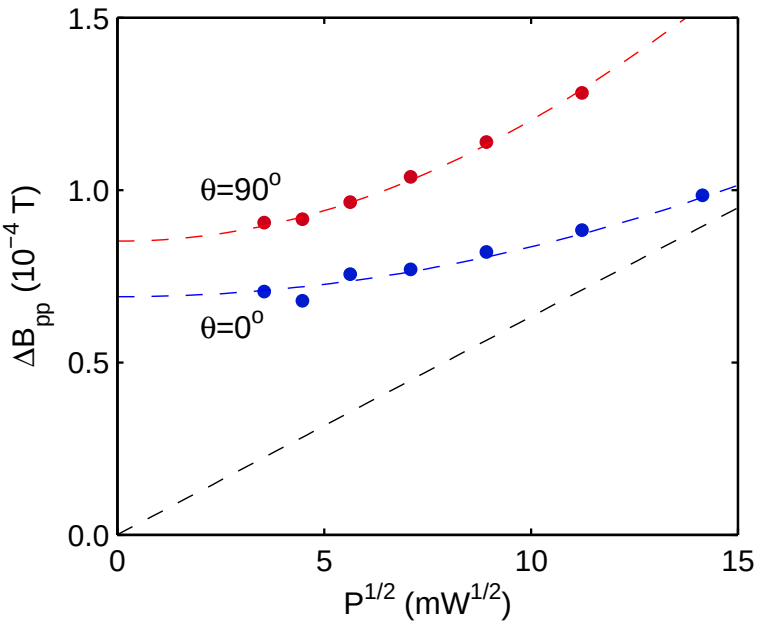

Figure 5.13: Microwave power dependence of the 2DEG EDMR linewidth in a FZ-Si:intrinsic device, measured at the high gate voltage of $V_g = 700\,\mathrm{mV}$ to ensure all conduction electrons are mobile. Two magnetic field orientations are shown: $\theta = 90°$ (red) and $\theta = 0°$ (blue). When $\theta = 0°$, $T_1 \approx T_2$, and the data is used for extracting B_1. Black dashed line corresponds to the limit of no intrinsic line broadening, $T_2 \to \infty$.

5.3 and 5.4. We will relate these experimental observations to the spin relaxation mechanisms in the next section. Even though the extracted T_1 are in reasonable agreement with pulsed EPR studies of large-area MOSFETs [76, 150], we should emphasize, however, that since they are not independently determined in our experiments, they only serve as rough estimates.

5.3 Spin relaxation mechanisms in MOSFETs

5.3.1 2DEG electrons

The spin relaxation of mobile electrons is usually described by spin-orbit coupling [83]. There are two types of such spin relaxation processes: the Elliot-Yafet, and Dyakonov-Perel mechanisms. In the Elliot-Yafet mechanism, spin relaxes due to momentum scattering events [152]. This is because the spin quantum numbers $\mathbf{S}$ are no longer good quantum numbers for describing the spins of individual Bloch states $\mathbf{k}$ in the presence of spin-orbit coupling,

2DEG Device	μ^{peak} (m^2/Vs)	$\Delta\rho/\rho_0\|_{sat}$ (10^{-4})	2DEG T_1 (ns)	2DEG T_2 (ns)
$n_c \approx 6 \times 10^{10}$ cm^{-2}				
28-Si:^{31}P	1.6 ± 0.1	1.48 ± 0.04	572 ± 43	42 ± 2
28-Si:^{31}P+^{121}Sb	1.5 ± 0.1	1.10 ± 0.06	437 ± 230	11 ± 1
FZ-Si:^{121}Sb	2.0 ± 0.1	1.30 ± 0.05	482 ± 34	15 ± 1
FZ-Si	2.1 ± 0.1	1.60 ± 0.02	434 ± 23	97 ± 23
FZ-Si ($\theta = 0°$)	2.1 ± 0.1	1.55 ± 0.07	247 ± 49	146 ± 17
$n_c \approx 3 \times 10^{11}$ cm^{-2}				
FZ-Si	2.1 ± 0.1	0.91 ± 0.02	282 ± 9	88 ± 1
FZ-Si ($\theta = 0°$)	2.1 ± 0.1	0.73 ± 0.05	182 ± 44	125 ± 14
$n_c \approx 5 \times 10^{11}$ cm^{-2}				
FZ-Si	2.1 ± 0.1	0.41 ± 0.01	224 ± 9	76 ± 1
FZ-Si ($\theta = 0°$)	2.1 ± 0.1	0.37 ± 0.03	102 ± 21	96 ± 4

Table 5.2: Summary of peak carrier mobility, 2DEG EDMR signal intensity and spin relaxation times for different devices with three different 2DEG concentrations measured at $T = 4.6 - 4.8$ K.

28-Si:^{31}P	μ^{peak} (m^2/Vs)	$\Delta\rho/\rho_0\|_{sat}$ (10^{-4})	2DEG T_1 (ns)	2DEG T_2 (ns)
$n_c \approx 1 \times 10^{11}$ cm^{-2}				
4.6K	1.6 ± 0.1	1.13 ± 0.03	443 ± 34	44 ± 1
10K	1.4 ± 0.1	0.23 ± 0.03	534 ± 63	32 ± 2

Table 5.3: Temperature dependence of EDMR spin relaxation times for 2DEG electrons.

^{31}P Device	μ^{peak} (m^2/Vs)	$\Delta\rho/\rho_0\|_{sat}$ (10^{-4})	^{31}P T_1 (ns)	^{31}P T_2 (ns)
$n_c \approx 6 \times 10^{10}$ cm^{-2}				
28-Si:^{31}P	1.6 ± 0.1	0.23 ± 0.05	316 ± 66	105 ± 12
28-Si:^{31}P+^{121}Sb	1.5 ± 0.1	0.10 ± 0.02	313 ± 126	74 ± 16

Table 5.4: Summary of peak carrier mobility, donor EDMR signal intensity, and spin relaxation times for the different devices measured at $T = 4.6 - 4.8$ K.

i.e. each $\mathbf{k}$ state consists of an admixture of spin states. After momentum scattering event $\mathbf{k} \rightarrow \mathbf{k}'$, the spin states associated with the electron will also change. As such, if the Elliot-Yafet mechanism is the dominant spin relaxation mechanism, there will be a direct correlation between the momentum scattering time τ_m and the spin relaxation time:

$$\frac{1}{T_1^{EY}} = \alpha_{EY} \frac{1}{\tau_m} \tag{5.11}$$

Where α is the Elliot-Yafet coefficient and depends on the the strength of spin-orbit coupling in the system. We can estimate τ_m from the 2DEG mobility:

$$\mu = \frac{q\tau_m}{m^*} \tag{5.12}$$

where the conductivity effective mass for the $\langle 100 \rangle$ surface is $m^* = 0.19m_0$ [112]. Our samples typically have mobilities $\mu \approx 1 - 2\ \mathrm{m}^2/\mathrm{V\text{-}s}$, and the corresponding momentum scattering times are $\tau_m \approx 1 - 2$ ps. Recent theoretical work by Cheng, Wu and Fabian [153] showed that the Elliot-Yafet spin relaxation mechanism describes the spin relaxation of conduction electrons in bulk silicon well for $T > 60$ K. However, a theoretical description of the Elliot-Yafet mechanism for the MOS 2DEG is still lacking. An order-of-magnitude estimate of the spin relaxation time due to the Elliot-Yafet mechanism is given by [83]:

$$\frac{1}{T_1^{EY}} = \alpha_{EY} \frac{1}{\tau_m} \approx (g - g_0)^2 \frac{1}{\tau_m} \tag{5.13}$$

where $g_0 = 2.0023$ is the free electron g-factor. For the 2DEG electrons in silicon, $g \approx 2$ and hence $\alpha_{EY} \approx 5 \times 10^{-6}$. Wilamowski and Jantsch estimated an upper bound of $\alpha_{EY} \approx 2.4 \times 10^{-6}$ for SiGe 2DEG samples with similar mobilities as our MOSFETs, which is in reasonable agreement with the expected value [136]. We will return to the issue of the 2DEG g-factor at the end of this chapter. Assuming the spin-orbit coupling of the same order in the SiGe and MOS 2DEGs, we have $T_1 \approx (2 \times 10^{-6})^{-1}(1 \times 10^{-12}) = 500$ ns, which is in the range of our extracted T_1. As can be observed from Table 5.2, $T_1 \approx 400 - 500$ ns (for $\theta = 90^\circ$) regardless of sample mobility. In fact, when the sample mobility is degraded by raising the temperature, T_1 also increases as shown in Table 5.3. This is in direct contradiction of Eq. 5.11. In addition, a strong angular dependence is found for T_1 and T_2, while the mobility were identical regardless of θ (the lack of magnetic field orientation dependence is due to the relatively low mobility of the devices). Therefore the Elliot-Yafet mechanism does not seem to be the main contributer to the overall spin relaxation of the 2DEG electrons.

The Dyakonov-Perel mechanism arises from effective magnetic fields due to spin-orbit coupling [83]. These effective fields arise from systems that lack inversion symmetry, and are classified as two types: (i) Dresselhaus [84], and (ii) Bychkov-Rashba fields [85]. Dresselhaus fields arise from bulk systems that lack inversion symmetry, such as III-V semiconductors, and is also known as bulk inversion asymmetry. Since silicon has inversion symmetry in the crystal lattice, Dresselhaus fields are negligible. Bychkov-Rashba fields, sometimes simply

referred to as Rashba fields, arise from systems that have a strong asymmetry due to the potential landscape, i.e. when strong fields are present, and is also known as structural inversion asymmetry. Such is the case for 2DEGs where a large electric field is present in the $\hat{z}$ direction. This results in an effective in-plane magnetic field, and is hence strongly anisotropic as the in-plane electric fields are negligible compared to the out-of-plane electric fields.

We can consider both longitudinal and transverse spin relaxations as being due to these fluctuating effective magnetic fields $\overline{\delta B_i^2}$, where i indicates the direction of the fluctuating field. If the Zeeman field is aligned to the $\hat{z}$ direction [151]:

$$\frac{1}{T_1} = \gamma^2 \left(\overline{\delta B_x^2} + \overline{\delta B_y^2}\right) \frac{\tau_c}{1+\omega_0^2\tau_c^2} \tag{5.14}$$

$$\frac{1}{T_2} = \gamma^2 \overline{\delta B_z^2}\tau_c + \frac{1}{2T_1} = \gamma^2 \overline{\delta B_z^2}\tau_c + \frac{\gamma^2}{2}\left(\overline{\delta B_x^2} + \overline{\delta B_y^2}\right) \frac{\tau_c}{1+\omega_0^2\tau_c^2} \tag{5.15}$$

where τ_c is the correlation time between scattering events, hence $\tau_c \approx \tau_m$, and $\omega_0 = 2\pi f_{\mu w}$ the microwave frequency. Note that when the fluctuating fields are isotropic: $\overline{\delta B_x^2} = \overline{\delta B_y^2} = \overline{\delta B_z^2}$, then $T_1 \geq T_2$. For a 2DEG confined in the $\hat{z}$ direction, the in-plane fluctuating fields are greater than the out-of-plane component due to Rashba fields: $\overline{\delta B_x^2}, \overline{\delta B_y^2} > \overline{\delta B_z^2}$. As the Zeeman field is rotated from pointing along $\hat{z}$ to perpendicular to $\hat{z}$, the fluctuating Rashba fields begin to contribute more to the T_2 relaxation process, hence, T_2 decreases while T_1 increases from this mechanism. This effect is illustrated in Fig. 5.14, where we use the typical sample momentum relaxation time of $\tau_m \approx 2\,\text{ps}$, and $\overline{\delta B_i^2}$ are chosen to give T_1 and T_2 values in the correct range. Note that for the large anisotropy of $\overline{\delta B_i^2}$ used, $T_2 > T_1$ for $\theta = 0°$, which is indeed observed in high mobility SiGe 2DEG samples [151]. We have assumed $T_1 \approx T_2$ in our estimation of B_1 initially, and hence $T_1 \geq T_2$ in our extracted values of T_1.

If the Bychkov-Rashba effect dominates the spin relaxation in the system, degrading the carrier mobility should in effect improve the spin relaxation times. This effect is opposite to that of the Elliot-Yafet mechanism discussed above. This is because the less the carrier scatters, the more time the spin-states will precess about the effective Rashba field associated with the the given momentum state, and hence the spin relaxes. On the other hand, frequent scattering events will create a situation analogous to exchange narrowing and the spins do not have much time to precess before the random field changes direction. The results from Table 5.3 support longer T_1 for lower carrier mobility.

While our results suggest that Rashba fields play a central role in the spin relaxation of mobile electrons in MOSFETs, this finding might be a bit surprising due to the relatively low mobility of the electrons, in which case the Elliot-Yafet mechanism usually dominates. The large uncertainties in the spin relaxation times, in particular the T_1 time make it difficult to quantify the individual contributions of the Elliot-Yafet and Rashba fields to spin relaxation of mobile electrons. Direct measurements performed with pulsed EDMR, where T_1 can

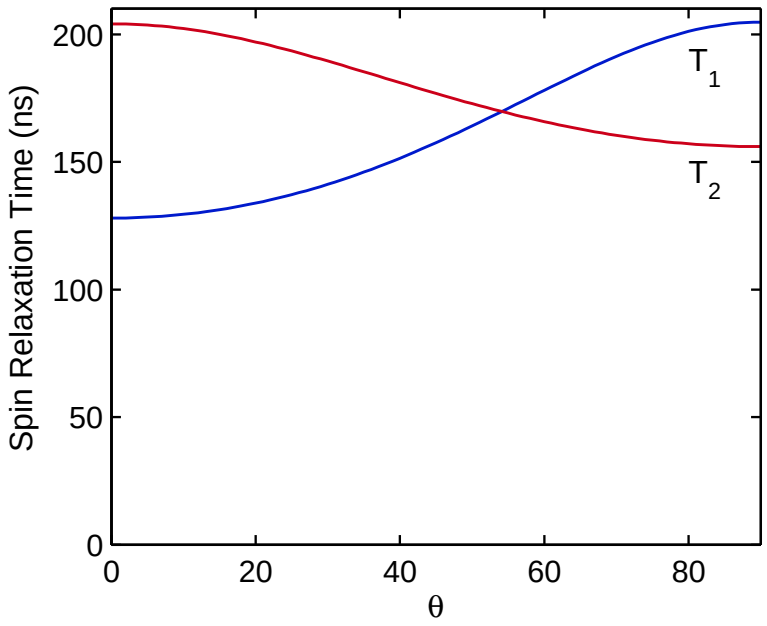

Figure 5.14: Calculated angular dependence of T_1 and T_2 due to Rashba fields. $\omega_0 = 2\pi 10\,\mathrm{GHz/rad}$, $\tau_c = 2\,\mathrm{ps}$, $\overline{\delta B_x^2} = \overline{\delta B_y^2} = 8\,\mathrm{mT}$, $\overline{\delta B_z^2} = 4\,\mathrm{mT}$.

be obtained by modified inversion recovery pulse sequence and T_2 by modified Hahn echo measurements schemes, should yield more accurate measurements.

5.3.2 Donor electrons

The mechanisms limiting T_1 of isolated donor electrons in silicon are due to phonon-related processes, as the spin-orbit coupling fields experienced by the donors are perturbed [154, 155]. A single-phonon spin relaxation process is observed at very low temperatures only ($T \lesssim 1\,\mathrm{K}$) [155]. At slightly higher temperatures, the donor spin relaxation is described by a Raman process, where phonons scatter inelastically with the donor electrons [156]. The Orbach process dominates when phonons can excite the donors to the valley-split excited states, and this process is observed for $T \gtrsim 5\,\mathrm{K}$ as shallow donors have valley-splittings $\Delta \approx 10\,\mathrm{meV}$ in silicon [157, 158]. The temperature dependence and the approximate ranges where these different mechanisms dominate are shown in Fig. 5.15. The spin coherence time T_2, on the other hand, is limited by the Orbach T_1 process for $T \gtrsim 10\,\mathrm{K}$. At lower temperatures, it is limited by spectral diffusion [159, 160]. At cryogenic temperatures, these mechanisms give rise to extremely long T_1 and T_2 times in bulk silicon. The measurement of T_2 in excess 10 s has also been reported at $T = 2\,\mathrm{K}$ using isotopically purified ^{28}Si substrates with low dopant concentrations [77]. However, for donors interacting with a 2DEG, the situation is very

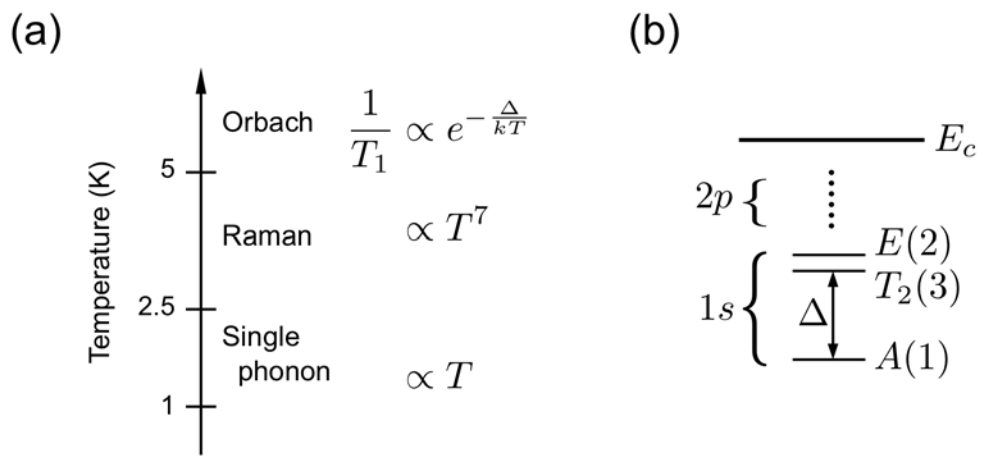

Figure 5.15: Relaxation mechanisms of isolated donors in silicon. (a) Temperature dependence and the dominant spin-lattice relaxation mechanisms. (b) Energy level diagram of shallow donors in silicon. The spin-orbit interaction creates a splitting Δ in the $1s$ manifold of the donor electron ground state. The Orbach process involves the excitation of the donor electron to valley-split excited states.

different. The extracted donor spin relaxation times are summarized in Table 5.4. Only ^{31}P donor EDMR signals are recorded here due to their relatively strong signal intensities. In the two devices examined, both T_1 and T_2 times are similar, with $T_1 \approx 300$ ns and $T_2 \approx 100$ ns. Schenkel *et al* measured the spin relaxation times for shallow implanted ^{121}Sb donors, and found $T_1 > 10$ ms and $T_2 > 100\,\mu$s [24], both orders of magnitude greater than the case of MOSFETs. However, those samples were not gated, and the short donor T_1 and T_2 times in the MOSFETs are due to scattering with conduction electrons.

The EDMR scheme for performing donor nuclear spin-state readout requires the nuclear spin relaxation time T_{1n} to be longer than the EDMR measurement time. Since the anisotropic hyperfine interaction for shallow donors is weak, the effect of the electron spin relaxation times on T_{1n} is expected to be small. Experimentally, it has been found that $T_{1n} \approx 300\,T_1$ for shallow donors in bulk silicon in the Orbach-dominated regime [161], when the hyperfine interaction is perturbed due to excitation into excited states (Fig. 5.15(b)). In the case of MOSFETs, since the limitation to donor electron T_1 is due to electron scattering events instead, it is unclear how this will affect T_{1n}. If we still assume that $T_{1n} \approx 300\,T_1$ as a lower bound, then we anticipate a measurement time of $T_{1n} \approx 100\,\mu$s for shallow donors embedded in MOSFETs.

While the ^{121}Sb EDMR signals are too weak to allow extraction of the donor T_1 and T_2 times, we note that all samples with ^{121}Sb seem to have much shorter T_2 for the 2DEG (Table 5.2). The 2DEG mobilities, on the other hand, do not seem to be affected by the

implanted ^{121}Sb donors (the gate oxide was grown after channel implantation, and hence residual damage from the ion implantation process is expected to be negligible). At this point, it is not clear what is the origin of the shorter 2DEG T_2 for ^{121}Sb doped channels versus ^{31}P doped channels, as they both behave similarly from bulk EPR measurements.

5.4 g-factor anisotropy

The relatively narrow 2DEG signal linewidths in the undoped FZ-Si device allow an accurate determination of the angular dependence of the conduction electron g-factor in the silicon MOSFETs. Fig. 5.16 shows the EDMR spectra for $\theta = 0°$ and $\theta = 90°$. The modulation amplitude was chosen to be between $20-40\,\mu$T to avoid modulation broadening and preserving the natural linewidths of the resonance signals. The microwave power was also carefully chosen too avoid power broadening of the resonance signals. It is clear from Fig. 5.16 that an anisotropy of the resonance signal g-factor is present. Slight variations in microwave frequencies were taken into account when comparing the resonance spectra for different θ, and the data have been adjusted to a reference microwave frequency of 9.44 GHz.

The conduction band edges of the Γ valleys are anisotropic, characterized by the longitu-

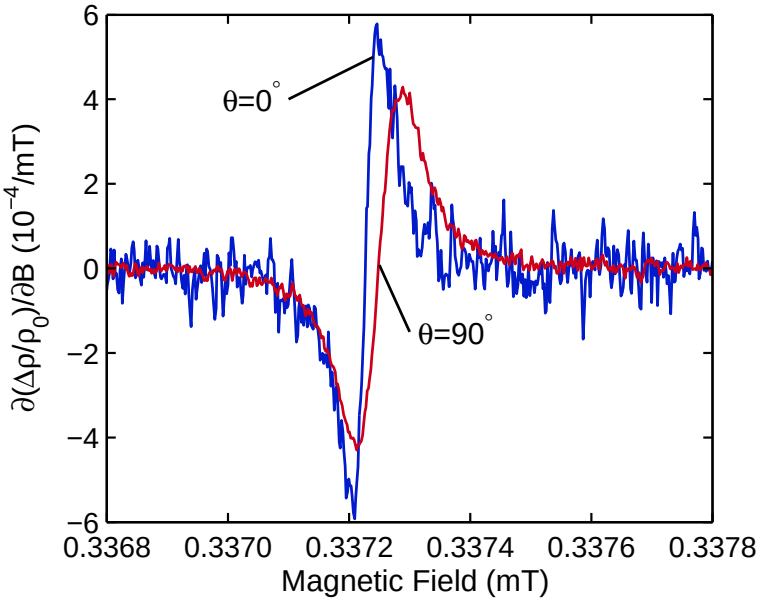

Figure 5.16: EDMR spectra of an undoped FZ-Si MOSFET measured at $T = 4.8$ K, $P_{\mu w} = 6.3$ mW, with $\theta = 0°$ (blue) and $\theta = 90°$ (red). The microwave frequencies are adjusted to a reference of 9.44 GHz for comparison of the line positions.

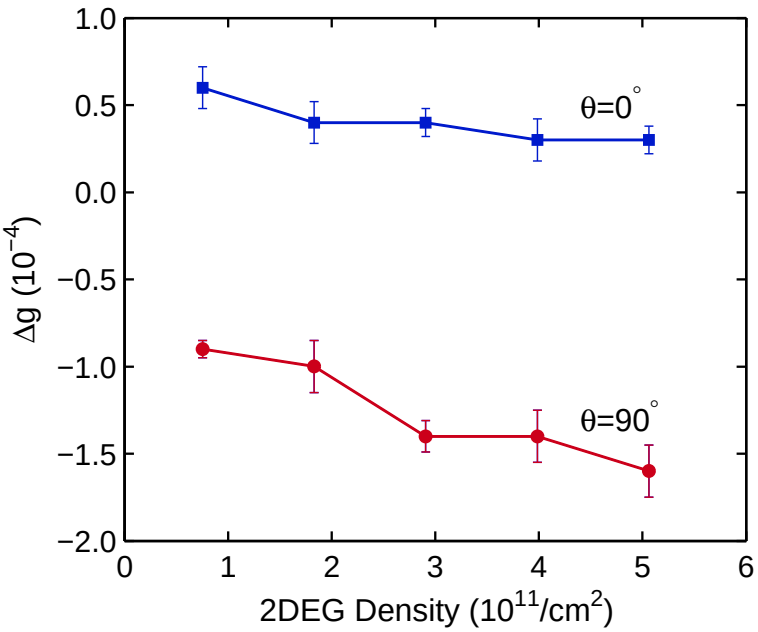

Figure 5.17: Variations of the 2DEG g-factor for different electron densities. $\Delta g = g_{measured} - 2$.

dinal and transverse effective masses. Since the Landé g-factor is a consequence of spin-orbit interaction, the difference in effective masses in different directions results in different values of g-factors within a single valley:

$$g^2(\theta) = g_{\parallel}^2 \cos\theta + g_{\perp}^2 \sin\theta \tag{5.16}$$

In bulk silicon, the six-fold valleys are completely degenerate, and the conduction electrons see an average of the g-factors of the valleys, and no anisotropy in the g-factor is expected (this holds true only in the absence of strain, otherwise valley repopulation will result). However, for conduction electrons of the MOS 2DEG at low temperatures, only the two lowest subbands with the larger longitudinal effective mass are occupied. Since the conduction electrons now average between two valleys that have their principal axis aligned with each other, the anisotropy of the g-factor of this valley will alter the resonance condition, as the Hamiltonian taking the anisotropy into account is:

$$\mathcal{H} = \left(\frac{\mu_B}{\hbar}\right) \mathbf{S} \cdot \mathbf{g} \cdot \mathbf{B} \tag{5.17}$$

Our measured anisotropy is $g_{\parallel} - g_{\perp} = 2.0 \pm 0.5 \times 10^{-4}$, and varies slightly with 2DEG density as shown in Fig. 5.17. This anisotropy is smaller than the values reported from measurements of highly strained silicon 2DEGs in silicon-germanium heterostructures ($g_{\parallel} -$

$g_\perp = 8 \times 10^{-4}$) [48], and that extrapolated from bulk measurements in strained silicon ($g_\parallel - g_\perp = 11 \times 10^{-4}$) [162]. However, it is consistent with EPR measurements of large-area silicon MOSFETs [150]. The reason for the discrepancy with the two former cases is unclear. The 2DEG density dependence might be a consequence of multi-electron effects; however, we are unaware of theoretical calculations that address this issue. Nevertheless, this anisotropy further confirms that the resonance signal originates from a two-dimensional system within silicon.

5.5 Conclusions

In this chapter we have systematically examined the EDMR spectra of donor-doped MOSFETs in X-band. The strong resonance peak observed for intrinsic devices further supports the polarization model described in the previous chapter. For donor-doped devices, we have shown that the donor concentration has a very strong effect on the 2DEG linewidths. We have also examined the linewidths of the EDMR signals in detail, and extracted the relevant spin relaxation and spin coherence times. The spin relaxation and coherence times for the 2DEG in undoped samples are found to be consistent with the values measured by pulsed EPR from large-area samples, with $T_1 \approx 400$ ns and $T_2 \approx 100$ ns, depending on the 2DEG density. From the angular dependence of the relaxation times and by comparing samples with different mobilities, both Elliot-Yafet and Dyakonov-Perel mechanisms seem to play important roles in the 2DEG spin relaxation process. The spin relaxation and coherence times of donor electrons are found to be similar to that of the 2DEG electrons, and are more than 5 orders of magnitude shorter than would be expected from bulk EPR measurements. This dramatic reduction in spin relaxation times is attributed to the scattering with conduction electrons; however, its effect on the nuclear spin relaxation time T_{1n} is unclear. Finally, we have observed g-factor anisotropy in the 2DEG EDMR signal, again confirming the origin of this resonance signal.

Chapter 6

Spin Drift and Spin Diffusion in Silicon MOS Systems

The ability to perform computation with spins in silicon has received significant attention in the past decade for quantum information processing and the emerging field of spintronics. While the focus of this research is for the former, in this chapter we will demonstrate that the technique of EDMR can also be extremely useful for studying issues associated with the latter: namely, the detection of spin drift and spin diffusion effects in silicon. In this chapter, we will first examine the issues associated with spin injection and spin detection in silicon. We will then describe how EDMR experiments with simple three-terminal MOSFETs can be used to extract the spin diffusion and spin drift lengths in the silicon MOS system. Spin drift and spin diffusion are actually both detrimental to the spin-state readout of donor qubits with MOS structures. To circumvent this problem, a novel device structure, the triple-gate MOSFET, is developed and its EDMR results will be presented.

6.1 Spin diffusion and spin drift

6.1.1 Spin injection and spin detection in silicon

Silicon is often regarded as one of the most promising materials for spin-based information processing applications due to the predicted long spin coherence times and spin transport lengths. For spintronic applications (and also the detection channel of a qubit readout MOSFET), the ability to inject polarized electrons is desired. Attempts for spin injection with the simple approach of interfacing semiconductors with ferromagnetic materials have typically shown poor spin injection efficiencies, due to the *conductivity mismatch* problem. One approach to circumvent the issue is to use tunnel junctions to inject highly polarized electrons into the semiconductor. This approach has seen considerable success in recent years [163, 164]. However, an issue that pertains to silicon in particular is the difficulty in

measuring the injected spin polarization. Here we refer to this as the *detection problem* for silicon.

Contrary to GaAs or other optically active semiconductors, carrier recombination is inefficient in silicon. In GaAs, when carriers with different spin states recombine the chirality of the emitted photon is also different. Hence, the spin polarization in GaAs can be probed relatively easily by optical means [83]. Since silicon is not optically active, the carrier spin polarization detection is much more difficult to achieve. In fact, the detection of the injection of spin polarized carriers into silicon has not been demonstrated until recently. Jonker *et al.* used a ferromagnetic tunnel barrier to inject polarized electrons into 10 μm thick undoped silicon film [164]. The electron polarization detection was done by detecting the polarization of the electroluminescence in the p-type substrate. However, the phonon-assisted electron-hole recombination processes in silicon made it difficult to quantify the detected polarization. Instead, similar devices epitaxially grown on top of GaAs/AlGaAs quantum well substrates were used to quantify the resultant polarizations. Appelbaum *et al.* used a spin-valve with tunnel barriers to inject hot polarized electrons into silicon, and the subsequent polarization of the injected carriers was inferred from another spin-selective hot-electron ferromagnetic contact layer [163]. In both cases, elaborate device fabrication schemes were used to create the spin injector and detector. In Chapters 4 and 5, we have shown that the MOSFET resistivity is sensitive to the polarization of the 2DEG electrons. Hence, a measure of the EDMR signal intensity can be used to detect variations in the spin polarizations in the MOSFET channel itself. Therefore, we can use EDMR as a technique to circumvent the detection problem in fairly conventional device architectures built with silicon.

6.1.2 Spin transport model

While we have shown that the EDMR signal intensity of MOSFETs is sensitive to the 2DEG electron polarization in the channel (Chapter 4), we have assumed that the 2DEG polarization remains constant throughout the device. While this can be justified when the device length l is much longer than the spin transport lengths L_s[1], spatial inhomogeneity of electron polarization must be taken into account in order to understand the EDMR results of devices with shorter channel lengths. One cause of the spatial inhomogeneity of the carrier polarization p_c can be due to boundary conditions such as spin injection or depletion at the contacting interfaces, as illustrated in Fig. 6.1. This leads to variations in p_c from its thermal equilibrium value p_{c0} ($p_{c0} \neq 0$ for silicon when a magnetic field is present). A second source of local perturbations of carrier polarization is due to external excitations (e.g. spin resonance), as we will demonstrate at the end of the chapter with triple-gate MOSFETs. However, we will first put these concepts in a more concrete footing with a theoretical model.

[1] L_s refers to the characteristic length scale carriers travel before spin flips occur. A quantitative definition will be given later in the section.

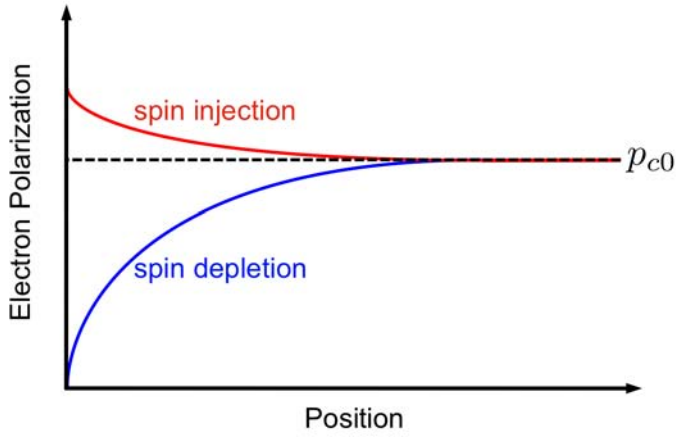

Figure 6.1: Variations of electron polarization p_c from its thermal equilibrium value p_{c0}. Spin injection at the interface results in higher polarizations injected into the device (red). Spin depletion results from contacts with low polarization (blue).

A spin transport equation can be derived in analogy to the continuity equation for charged carrier transport in order to take the spatial variations of p_c into account. Essentially, the charged based continuity equation can be separated into two components corresponding to the spin up and down electron populations. The two equations are then related by the spin relaxation term described by the spin flip time T_1, which is analogous to an effective carrier recombination term in bi-polar carrier transport. The coupled equation for electrons then reads [165, 166]:

$$D\nabla^2 p_c(\mathbf{r}) + \mu E \nabla p_c(\mathbf{r}) - \frac{p_c(\mathbf{r})}{T_1} = 0 \tag{6.1}$$

where we have expressed the spin up and down electron populations in terms of the electron polarization p_c. E is the electric (drift) field, and D and μ are the weighted average electron diffusivity and mobility, respectively. In silicon, it is expected that $D_\uparrow \approx D_\downarrow$ and $\mu_\uparrow \approx \mu_\downarrow$. Thus D and μ are the same as those used in charge transport calculations, as we are assuming that the spatial fluctuation of electron polarization is a direct consequence of carrier diffusion and carrier drift. Electron spin-spin diffusion effects, on the other hand, are neglected. In the one dimensional case along the $\hat{x}$ direction, Eq. 6.1 has a general solution of the form:

$$p_c(x) = A_1 e^{-\frac{x}{L_s^+}} + A_2 e^{\frac{x}{L_s^-}} + p_{c0} \tag{6.2}$$

where A_1 and A_2 are constants subject to boundary conditions. L_s^+ and L_s^- are the down- and up-stream spin transport lengths, respectively, and describe the characteristic length

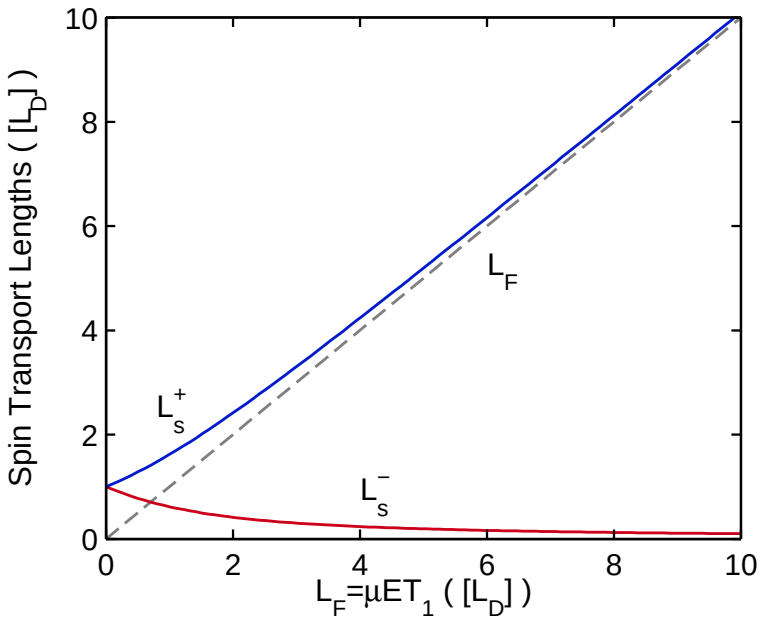

Figure 6.2: Up- and down-stream spin transport lengths as a function of spin drift length L_F (Eq. 6.5). All length scales are in units of the intrinsic spin diffusion length L_D.

scales of variations in p_c. The term down-stream refers to the direction of electron flow due to carrier drift, while up-stream is in the opposite direction. These spin transport lengths are given by:

$$\frac{1}{L_s^{\pm}} = \mp\frac{|q\mu E|}{2D} + \sqrt{\left(\frac{|q\mu E|}{2D}\right)^2 + \frac{1}{L_D^2}} \tag{6.3}$$

where the spin diffusion length is defined as:

$$L_D = \sqrt{DT_1} \tag{6.4}$$

At low fields, $L_s^{\pm} \approx L_D$, and the intrinsic diffusion length dominates the variation in carrier polarization across the interface. We define the spin drift length due to electric field as:

$$L_F = \mu E T_1 \tag{6.5}$$

which is the distance electrons travel due to the bias field before spin flip occurs. The spin transport lengths are plotted in Fig. 6.2 as a function of the spin drift length (which is the same as plotting against electric field), in units normalized to the intrinsic spin diffusion

length L_D. The down-stream spin transport length approaches the spin drift length under high electric fields as one would expect.

The spin transport lengths are sometimes expressed in the literature as [167]:

$$\frac{1}{L_s^{\pm}} = \pm\frac{1}{L'_F} + \sqrt{\frac{1}{4L'_F} + \frac{1}{L_D^2}} \tag{6.6}$$

where L_D has the same definition as above, but with $L'_F = D/\mu E$ referred to as the spin drift length. However, we find this definition to be confusing as it implies that the spin drift length becomes shorter with increasing electric field. While these expressions for the spin transport lengths are identical to Eq. 6.3 given earlier, we will retain the definition given in Eq. 6.5 as the spin drift length.

6.1.3 Spin drift and spin diffusion effects in MOSFETs

In this section, we will demonstrate the use of EDMR as a probe of the variations of the 2DEG polarization in donor-doped silicon MOSFETs. From such measurements, spin drift and spin diffusion effects discussed above can be demonstrated. In order to exploit the technique of EDMR as a probe for the 2DEG polarization, we focus on the donor resonance signals. This is because donors can be locally implanted into specific locations in the device to probe variations in the *local* spin polarization, while the 2DEG resonance has contributions arising from the entire device where the 2DEG is present.

For the silicon MOSFETs described in Chapters 4 and 5, the 2DEG thermal equilibrium polarization under the influence of external magnetic field is given by [137, 99, 110]:

$$p_c = \frac{g\mu_B B}{2(\epsilon_f - \epsilon_0)} \tag{6.7}$$

where $\epsilon_f - \epsilon_0 = n_c/\rho_{2DEG}$. p_c is typically in the range of $5 - 10$ % at X-band for the 2DEG densities of $n_c = 0.5 - 1 \times 10^{11}/\mathrm{cm}^2$. On the other hand, the degenerately doped $n+$ contact regions have significantly lower electron polarizations. These $n+$ contact regions can be thought of as a three dimensional electron gas, which polarization is given by the Pauli paramagnetism [117, 168]:

$$p_{n+} = \frac{g\mu_B B}{2E_F} \tag{6.8}$$

where E_F is the Fermi energy given by the concentration of dopants in the $n+$ regions. The electron concentration in the $n+$ regions formed by the PSG diffusion process is approximately $2 \times 10^{19}/\mathrm{cm}^3$ as determined by SIMS analysis [138]. At X-band with Zeeman fields of $B \approx 0.35$ T, we thus have $p_{n+} \approx 0.01\%$, much lower than the 2DEG thermal equilibrium polarization.

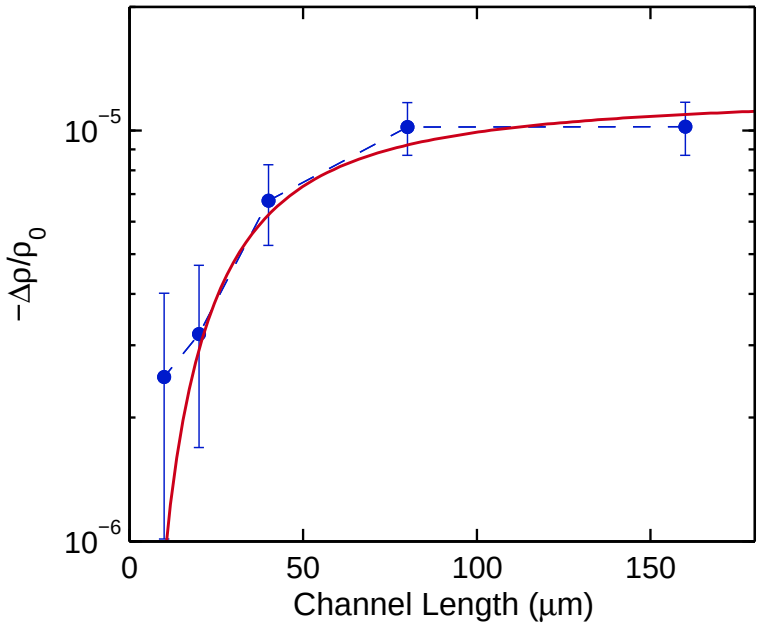

Figure 6.3: ^{31}P EDMR signal intensity for 28-Si:^{31}P+^{121}Sb devices with different channel lengths. The drain bias field was kept below 2.5 V/cm, and $V_g \approx V_t$. $T = 5$K for all measurements. The red trace corresponds to the calculated averaged channel polarization taking the $n+$ contacts and spin drift and spin diffusion effects into account.

Fig. 6.3 shows the ^{31}P donor EDMR signal intensity of 28-Si:^{31}P+^{121}Sb devices with different channel lengths under spin saturation. The drain bias field was 2.5 V/cm in all cases, and V_g was set to just above V_t where the EDMR signal was maximized, as discussed in Chapter 5. The EDMR signal intensity decreases rapidly with decreasing channel lengths. This is in fact what we would expect if we take spin drift and spin diffusion effects from the low polarization of the $n+$ source-drain regions into consideration.

We can validate this intuitive picture by estimating the 2DEG polarization in the channel of the MOSFET. We assume the 2DEG resistivity is given by Eq. 4.4: $\rho = \rho_1 + \rho_2 p_c^2$. Since p_c varies with position in the channel according to Eq. 6.2, the resultant sample resistivity is given by the average polarization $\overline{p_c}$ in the channel: $\rho = \rho_1 + \rho_2 \overline{p_c^2}$. The red trace in Fig. 6.3 shows the calculated average channel 2DEG polarization as $\Delta\rho/\rho_0 \propto \overline{p_c^2}$, and gives reasonable agreement with the experimental data. The diffusivity is calculated from Einstein's relation for a 2DEG [166]: $D = q\mu/\epsilon_f$, and we use $T_1 = 25$ ns. These values give $L_D = 3.4\,\mu$m and $L_F = 1.2\,\mu$m, and up- and down-stream spin transport lengths of 1 and 8 μm, respectively.

Spin drift effects should be more pronounced for shorter devices as the device channel length approaches that of the spin drift length. Fig. 6.4 shows the donor EDMR signal

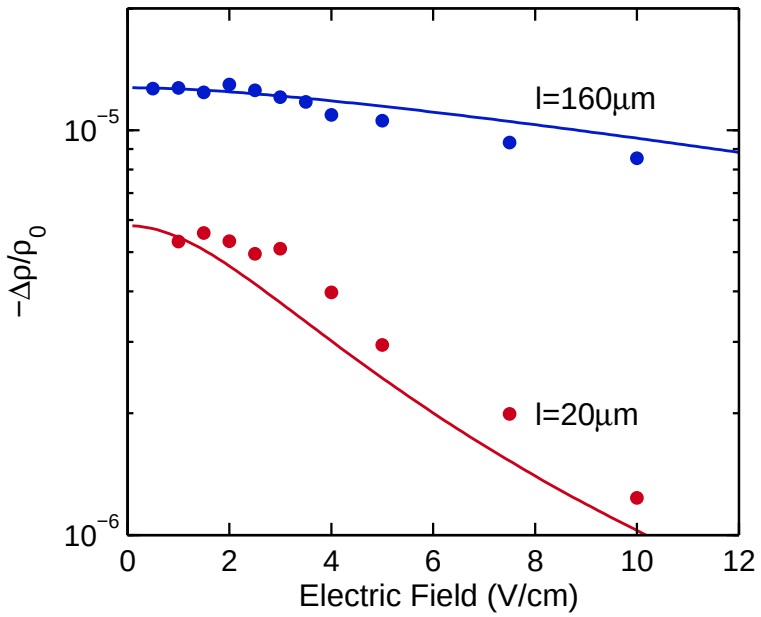

Figure 6.4: Bias-field dependence of the ^{31}P EDMR signal intensity for devices with $l = 160\,\mu$m (blue) and $l = 20\,\mu$m (red). The solid traces correspond to the calculated average channel polarizations taking the $n+$ contacts, spin drift and spin diffusion effects into account. $V_g = 375$ mV and $T = 5$ K for all measurements.

intensities for two devices with channel lengths $l = 20\,\mu$m and $160\,\mu$m as the source-drain electric fields are varied. While the signal intensities are fairly constant for both devices up to 3 V/cm, it declines gradually for the $160\,\mu$m long device while it drops drastically for the $20\,\mu$m device when the electric fields are further increased. Again, the average 2DEG polarization in the channel of the devices can be estimated within the framework of spin drift and spin diffusion. The solid traces in Fig. 6.4 show the estimated average 2DEG polarization in the two devices calculated with $T_1 = 20$ ns, showing reasonable agreement to the experimental data.

The T_1 times extracted here are shorter than the ones estimated from using saturation methods in Chapter 5. When solving the spin transport equations, we assume the boundary conditions are simply given by imposing the polarizations at the contacts to reach p_{n+}. The rigorous boundary conditions are given by imposing spin-resolved current continuity across the interface instead, i.e. $j^{\pm}|_{x^-} = j^{\pm}|_{x^+}$. This would, however, require a more detailed knowledge of the carrier density distribution (for the spin diffusion component). In addition, as mentioned above, electron-electron spin exchange interaction is ignored in this simple calculation. The extracted T_1 times can therefore be refined by including the above considerations; however, here we only seek a qualitative picture for understanding the

phenomena.

By examining the changes in the EDMR signal intensities in donor-doped MOSFETs of different channel lengths and different bias electric fields, we have been able to observe spin drift and spin diffusion with fairly conventional silicon MOSFETs, and a spin diffusion length of $L_D \approx 3\ \mu$m is extracted at $T = 5$ K. The reduction in donor signal intensity with channel length due to spin diffusion from lowly polarized $n+$ source-drain regions is of particular concern for constructing a qubit readout device in a scaled MOS structure. This scaling behavior is rather different from spin-dependent recombination EDMR experiments in donor-doped silicon *resistors*, in which the donor signal intensities are constant with smaller device sizes down to ≈ 50 nm length scales [122]. In fact, a constant scaling was also expected for the MOSFETs when this project began. However, the crucial difference in these two types of EDMR experiments is that in spin-dependent recombination, electron-hole pairs are created in the channel of the device from photoexcitation. The electrons quickly relax and settle on empty donor states, and it is the spin-dependent recombination between spin pairs of the donors and surface defects that determines the spin-dependent current change (Chapter 2). In effect, the polarization of conduction electrons does not matter as much. We will look at a modified MOS architecture to circumvent this scaling problem in the next section.

6.2 Triple-gate MOSFETs

As we have discussed in the previous section, the $n+$ source-drain regions of the MOSFET have much lower electron polarizations compared with the channel. These essentially unpolarized contacts reduce the average 2DEG polarizations in the channel from spin drift and spin diffusion effects. On the other hand, the polarizations of 2DEG electrons itself are gate-tunable by controlling the 2DEG density, as seen from Eq. 6.7. Therefore, a strategy for enhancing the 2DEG polarization in the donor-doped channel is to replace the $n+$ regions with gated regions instead, hence creating an effective spin injector. We will discuss the design and fabrication process of these devices in this section.

6.2.1 Sample design

Fig. 6.5 shows the schematic of the modified MOSFET structure with enhanced spin injection into the donor-doped regions of the device. The device is similar to a conventional MOSFET, but with the gate region divided into three parts in series, and we will refer to this structure as the *triple-gate* MOSFET. Donors are only implanted under the center gate (cg) region, while the two side-gates (dg and sg) act as buffer regions to reduce the detrimental spin drift and spin diffusion effects from the $n+$ source-drain contacts. The side-gates are designed to be 60 μm long, more than 10 times the spin diffusion length L_D. They are also designed to have a wide width of 40 μm in order to reduce series resistance from these side gated

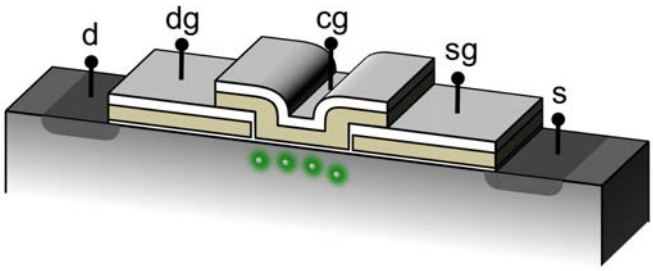

Figure 6.5: Schematic of the triple-gate MOSFET. The drain (d), source (s), drain gate (dg), center gate (cg) and source gate (sg) contacts are labeled. Donors are only implanted under the center gate region of the channel.

regions. Since the side-gate buffer regions are designed to be sufficiently long, unpolarized electrons injected from the source will have plenty of travel distance to attain a higher spin polarization, controllable by the side-gate voltages, before interacting with donors under the center gate.

6.2.2 Device fabrication

An outline of the process flow used for fabricating the triple-gate MOSFETs is described in this section. A detailed step-by-step process flow can be found in Appendix B (aFET8).

1. **Field oxide growth and active area definition**
   Field oxide was grown on 4" wafers with a wet oxidation process. The active regions (MOSFET channel and source-drain regions) were subsequently exposed with a wet etch in diluted HF solution.

2. **Side-gate formation**
   20 nm dry oxide was grown as the gate oxide for the side gates. *In situ* phosphorus doped polycrystalline silicon and low temperature oxide (LTO) hardmask was then deposited. Both layers were then patterned and etched forming the side-gates.

3. **Donor implantation and gate stack**
   The wafers then received a shallow donor implantation (^{75}As) to dope the exposed center channel regions. The remaining oxide was then removed by a dilute HF etch, and another dry oxidation step was carried out to grow the 20 nm thick center gate oxide. In the process, the exposed side-gates walls were also oxidized, creating insulation between the side and center gates. *In situ* phosphorus doped polycrystalline silicon was then deposited and patterned to form the center gate electrode.

4. **Source-drain dopant diffusion**
   Another HF dip was used to remove the oxide over the source-drain regions. Phosphosilicate glass (PSG) was then deposited over the wafer. A high temperature anneal step was then carried out to drive-in the phosphorous from the PSG layer into the silicon to form the heavily doped n+ regions.

5. **Metallization and shunt layers**
   After opening of contact windows through the PSG layer, aluminum was sputter deposited and subsequently patterned. Forming gas anneal was then carried out to form ohmic contacts to the $n+$ source-drain regions and passivate dangling bonds at the Si-SiO_2 interface. Silicon dioxide was then deposited by plasma-enhanced chemical vapor deposition, then followed by the sputter deposition of aluminum to form the capacitive shunt. The wafers were then diced into elongated chips for EDMR measurements as described in Chapter 3.

6.3 EDMR results of triple-gate MOSFETs

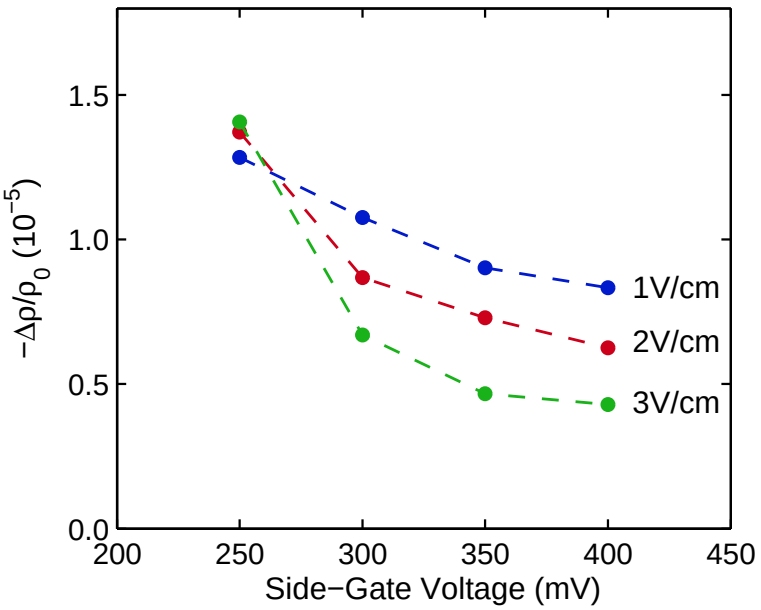

Figure 6.6: Donor EDMR signal intensity from a triple-gate MOSFET with center gate region of $l = 40\mu$m and $w = 40\mu$m. The two side-gates were biased together in these measurements, and the measurements were performed under three different bias (drift) field conditions as indicated.

We will now show that with the triple-gate devices, gate-tunable spin injection into the center region can be achieved. Since donor atoms are located only under the center gate, the donor EDMR signal amplitude reflects the average conduction electron polarization under that region only. Fig. 6.6 shows the measured donor EDMR signal intensities for fixed center gate voltage (and hence fixed center channel resistance), while the side-gate voltages and bias (drift) field were varied. The center gate region of this device had dimensions of $l = 40\,\mu$m and $w = 40\,\mu$m. The side-gate (and hence polarization of injected carriers) clearly influences the EDMR signal amplitude: for small side-gate biases, conduction electrons attain a higher steady-state polarization before being injected into the center region. For side-gate biases greater than that of the center gate bias, the injected electrons now have a lower spin polarization when injected into the channel.

A low bias field (top trace in Fig. 6.6) leads to a smaller L_F, hence electrons from the $n+$ source can reach the thermal equilibrium polarization as demanded by the side-gate biases before reaching the center gate region. On the other hand, at larger bias fields the 60 μm long side-gate regions become less effective and the injected electrons have lower polarization (bottom trace in Fig. 6.6), and hence the signals are suppressed. This result shows that the side-gates are effective in improving the donor signal intensities of the center channel of the device. This strategy can therefore be used to explore devices with shorter channel lengths as we will discuss in the next chapter.

6.4 Conclusions

In this chapter, we have discussed the issue of spatial inhomogeneity of carrier polarizations and its affect on EDMR, i.e. spin drift and spin diffusion effects. Since donors can be locally implanted into the channels of the devices, the donor resonance signal intensities reveal the local 2DEG polarization. This effect is examined with three experiments. First, we have shown that the EDMR signal intensities decrease with shorter channel lengths, a consequence of the relatively low electron polarization of the contacting $n+$ regions. Second, spin drift effects were demonstrated by examining the bias field effect in devices with different channel lengths. Third, we showed that the implementation of side-gates to the MOSFET channel can effectively increase the injected 2DEG carrier polarization before interactions with the donors occur. Thus, EDMR can be used as a tool to probe local 2DEG polarizations to address the *detection problem* of silicon spintronic devices.

Chapter 7

EDMR and Transport Spectroscopy of FinFETs

The silicon MOS devices discussed in the previous chapters are relatively large, containing tens of thousands of donors in the channel regions. While they are suitable for proof-of-principle experiments, nano-scale FET devices need to be studied for few or single-dopant effects. In addition, we seek a device architecture and fabrication scheme that is compatible with the electrical detection of single-ion implantation process. In this scheme the current carried through the nanoscopic FET device can be used to detect single-ion implant events. Mesa-etched silicon-on-insulator (SOI) nano-scale devices, in particular finFET architectures, provide an interesting platform for implementing such few-donor FET devices. In this chapter, we will investigate two types of finFETs toward the realization of donor qubit readout devices.

7.1 Strategy for donor nuclear spin-state readout

Before we describe the finFETs, we shall first discuss the strategy towards the realization of donor nuclear spin-state readout. In the EDMR measurements of micron-scale devices, all hyperfine-split resonance lines are present, as illustrated in Fig. 7.1(a). This is due to the fact that the nuclear spin polarization was close to zero at the temperatures and magnetic fields in which we conducted our experiments. However, it should be remembered that each donor resonance line corresponds to the excitation of electrons residing at a donor atom with a specific nuclear spin. Thus, as the MOSFETs are scaled and the single-donor regime is reached, the EDMR spectrum expected should contain only a single resonance line as illustrated in Fig. 7.1(b). This would thus constitute a nuclear spin-state readout [57]. This readout scheme is only possible if the nuclear spin relaxation time T_{1n} is longer than the electrical detection time.

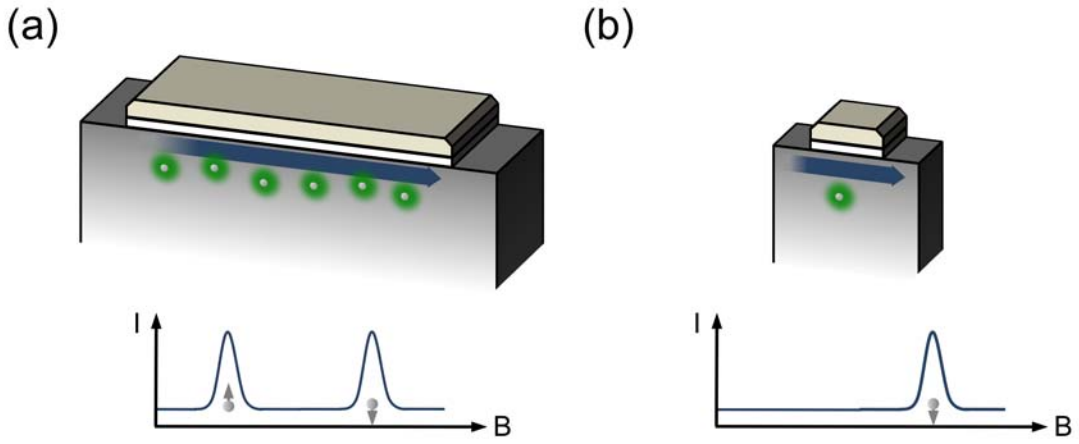

Figure 7.1: Strategy for donor nuclear spin-state readout with EDMR of MOSFETs for $I = 1/2$ donors. (a) In large-area devices with an ensemble of donors, the EDMR spectra have resonance features corresponding to different nuclear spin-state projections. (b) In a single-donor doped device, only one resonance peak corresponding to that of the single nuclear spin should be observed, constituting the nuclear spin-state readout. The 2DEG resonance signals are omitted in the illustrations for clarity.

7.2 FinFETs

FinFETs were originally designed for reducing short channel effects and minimizing the subthreshold swing for scaled MOS devices [169]. One distinguishing feature is the non-planer geometry of the devices. A schematic of the conventional finFET architecture is shown in Fig. 7.2(a): the tall silicon "fin" is made by patterning a silicon-on-insulator (SOI) layer, and the main conduction channels are along the sidewalls as the gate wraps around the three exposed sides of the fin. Variations on this basic fin structure have been introduced in the past few years, with names such as the Ω-FET, Π-FET, Tri-gate FET, MuGFET (Multi-gate FET), to name a few. In this work we will retain the term finFET to describe our non-planer SOI devices.

Two types of finFETs are studied in this work. The first type has a traditional finFET structure but built on isotopically purified ^{28}Si-SOI layer. We will refer to these as the 28SOI-finFETs, and the structure is shown schematically in Fig. 7.2(b). The second type, the triple-gate (TG) finFET, was built on natural silicon SOI substrates, and we will refer to them as TG-finFETs. The use of the triple-gate structure is for enhancing the spin polarization of carriers injected into the center fin of the device as discussed in the previous chapter. In addition, the inclusion of the side-gates prevent accidental doping of the channel

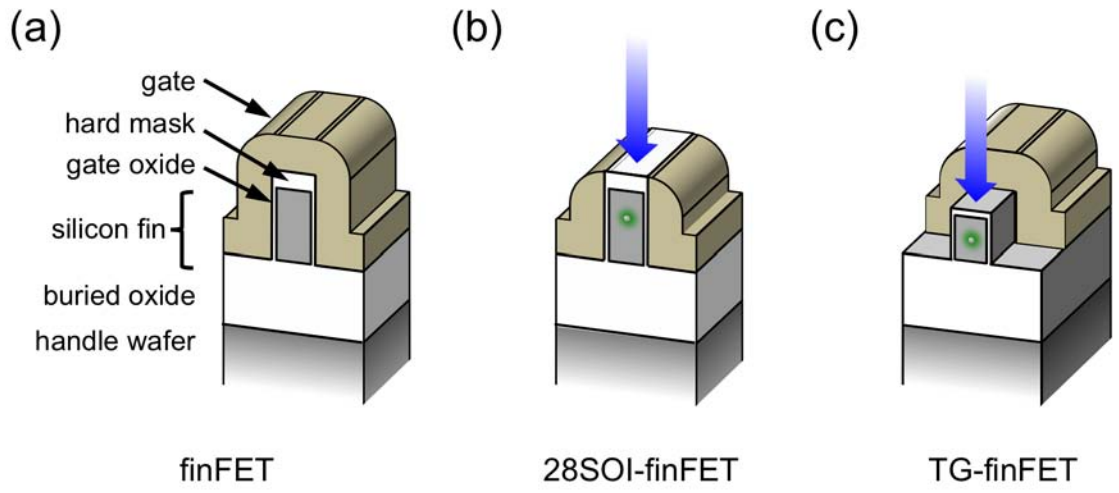

Figure 7.2: Schematics of finFETs and single-ion implantation compatibility. (a) Conventional finFET structure, (b) 28SOI-finFET with split-gates for ion implantation through the hard mask, and the (c) Triple-gate TG-finFET structure, where single-ion implantation can be achieved by implanting into a gap formed between the side-gates.

region as the $n+$ source-drain regions are far away from the center fin. This structure is shown schematically in Fig. 7.2(c). In the following sections, we will discuss sample design considerations, outline the process flows used for fabrication of these devices and discuss their current-voltage (I-V) characteristics. We will also present some EDMR results of these finFETs as well as transport spectroscopy measurements performed at cryogenic temperatures.

7.3 28SOI-finFETs

7.3.1 Design and fabrication

The first batch of finFETs — the 28SOI-finFETs — are designed to have a similar structure as conventional finFETs but with slightly larger dimensions in all aspects. Single-ion implantation compatibility can be achieved by the removal of the top polycrystalline silicon gate over the top of the fin, and donor atoms can be implanted through the hard mask as shown in Fig. 7.2(b). The gates over the side-walls will be left intact during this process and can be used for inducing conduction electrons along the side-walls of the device.

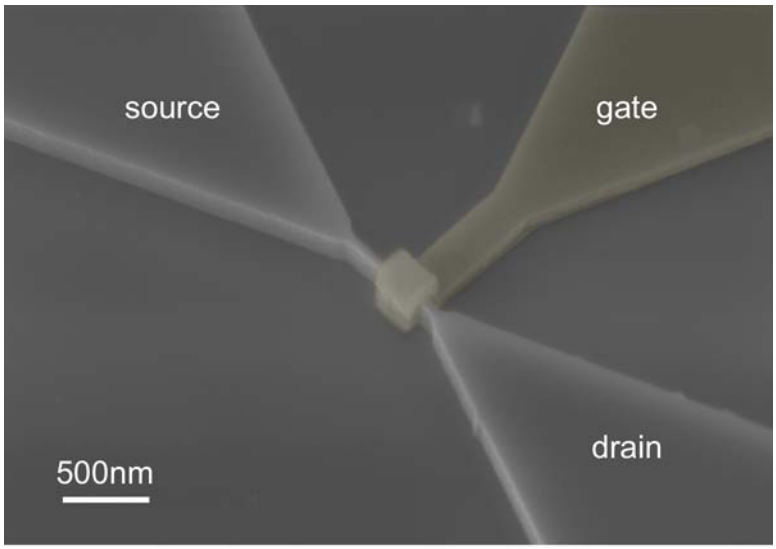

Figure 7.3: False-color SEM micrograph of fabricated 28SOI-finFET, imaged prior to the RTA step. The active region of the fin has dimensions $l = 280$ nm and $w = 80$ nm. The SOI layer is 200 nm thick.

Since a nuclear spin-free environment is desired for the donor qubits, isotopically purified ^{28}Si SOI substrates should be used. However, due to the lack of commercially available ^{28}Si SOI material, a hybrid approach was adopted: starting with commercially available 50 nm natural silicon SOI substrates [170], 150 nm of ^{28}Si was grown epitaxially on top [171]. This relatively thick SOI layer (200 nm total) was needed to ensure implanted donors will reside in the top ^{28}Si layer and far away from the natural silicon to avoid spectral diffusion. The width of the fins were limited to 40 nm for the smallest devices to avoid having donors too close to the oxide interfaces (25 nm wide fins were also drawn but did not survive the fin etch process due to the high aspect ratio required). The gate lengths were limited to 300 nm to avoid excessive in-diffusion from the $n+$ source and drain leads into the center channel region. The fins were also aligned along the $\langle 110 \rangle$ crystallographic axis for maximal electron mobility. A SEM micrograph of a fabricated device is shown in Fig. 7.3. Details of the fabrication process can be found in Appendix B (aFET5). Here we present an outline of the process flow:

1. **Oxide hard mask and SiGe alignment marks**
   Starting wafers were cleaned and a 5 nm dry oxide was grown before sending the wafer for ^{121}Sb channel implantation. After this implantation step, the sacrificial oxide was removed and 100 nm low temperature oxide (LTO) was deposited to serve as the hard mask for the fins. Then 600 nm of $Si_{0.5}Ge_{0.5}$ and an additional 200 nm of LTO

were deposited. These two layers were patterned by standard optical lithography and dry etched to form e-beam alignment markers. We use SiGe to form e-beam alignment markers instead of high Z metal layers in order to ensure complete CMOS compatibility.

2. **Fin definition and etch**
   A bi-layer e-beam resist process consisting of 100 nm AZPN and 50 nm HSQ was used for defining the fins. The top HSQ layer was first exposed by e-beam lithography and developed. The exposed patterns were then transferred to the underlying AZPN layer with a cryogenic etch step carried out at -100 °C to ensure anisotropic side-walls. After the resist pattern transfer, the LTO hardmask and SOI fins were dry etched, and then the residual resist removed.

3. **Gate stack and etch**
   After the fin etch, 3 nm sacrificial oxide was grown and subsequently removed in dilute hydrofluoric acid (HF) to reduce surface roughness of the side walls. Then 10 nm dry oxide was grown, and *in situ* phosphorus-doped polycrystalline-silicon was deposited as the gate electrode material. It was then patterned with e-beam lithography using 300 nm thick MaN-2403 negative e-beam resist. After e-beam exposure and development, the polycrystalline silicon was dry etched. Due to the relatively tall heights of the fins (and hardmask on top), a long overetch step was used to remove stringers around the side-walls of the fins.

4. **Source-drain implant and activation anneal**
   Source-drain ion implantation for $n+$ region formation was done prior to stripping the MaN-2403 resist to reduce unintended gate penetration by the heavy dose implant. A different donor species from the channel implant (^{75}As) was used to avoid any confusion over the origin of possible donor signals. After implantation and resist removal, the wafer was cleaned and dopant activation was achieved with rapid thermal anneal (RTA) at 900 °C for 10 s.

5. **Metallization**
   After the source-drain activation step, an inter-layer dielectric LTO layer was deposited. Contact holes to the source-drain and gate pads were patterned with optical lithography. After the contact holes were etched and photoresist removed, aluminum/tungsten was deposited and patterned to complete the metallization steps.

7.3.2 Device *I-V* characteristics

With the exception of the 25 nm wide fins, the yield of the process was very high. Typical *I-V* characteristics of the 28SOI-finFETs are shown in Fig. 7.4. At room temperature they behave like regular MOSFETs as shown in Fig. 7.4(a), with the drain current correlating

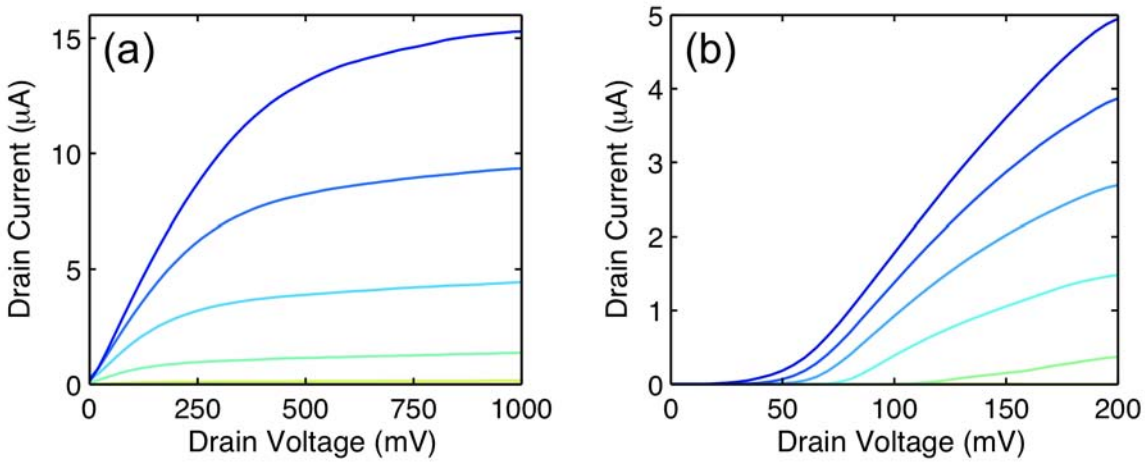

Figure 7.4: Representative *I-V* characteristics of fabricated 28SOI-finFETs. This device has dimensions $l = 280$ nm and $w = 130$ nm. (a) Room temperature measurement with V_g stepped from 0.4 V to −0.2 V in −0.2 V steps from top to bottom. (b) Liquid helium temperature (4.2K) measurement with V_g stepped from 0.3 V to 0 V in −0.1 V steps from top to bottom.

directly with fin width. However, at cryogenic temperatures all devices measured exhibit Schottky-like behavior, as shown in Fig. 7.4(b).

7.3.3 EDMR of 28SOI-finFETs

EDMR was attempted on the 28SOI-finFETs; however, due to poor contact quality the devices exhibited highly non-linear *I-V* characteristics as discussed in the previous section. When the devices were measured in the microwave resonator for EDMR, excessive noise was generated, even though shunt layers were implemented on some of the devices. This rectifying noise completely overwhelmed the possibility of measuring donor resonances in these devices.

7.3.4 Transport spectroscopy

Transport spectroscopy was carried out on a device channel-implanted with ^{121}Sb at 80 keV with a dose of 6×10^{11} cm^{-2}. The post-processing Sb profile peak is expected to be located at 35 nm from the top of the SOI layer, with a peak concentration of 10^{17} cm^{-3} from TCAD simulations [140]. The fin width of the measured device is $w = 80$nm, gate length $l = 280$nm

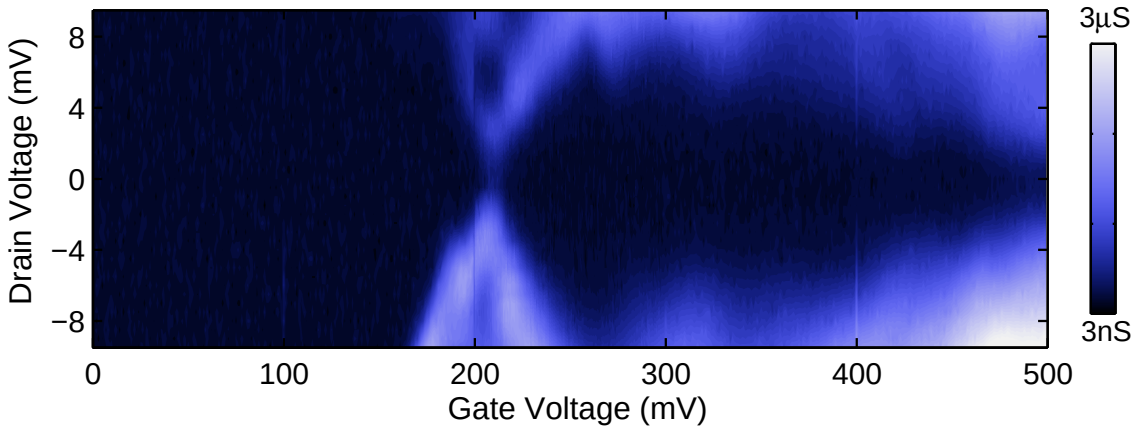

Figure 7.5: Stability diagram of a 28SOI-finFET with dimensions $l = 280$ nm, $w = 80$nm and $h = 200$nm measured at $T = 320$mK. Several overlapping Coulomb diamond features are visible, indicating multiple Coulomb blockade sources in the device.

and height $h = 200$ nm. Approximately 130 donor atoms reside in the fin under the gate for the given device dimensions. Low temperature transport measurements were performed with the device mounted in the Helium-3 cryostat with a base temperature of 320 mK (Chapter3). Low-frequency lock-in measurements at 100 Hz and modulation amplitude of 500 μV were applied to the drain to measure the device conductance. The stability diagram of the device at the base temperature is shown in Fig. 7.5, with several overlapping Coulomb blockade diamonds visible. The Coulomb blockade structures might be caused by local defects at the Si-SiO_2 interface or by surface roughness along the channel. It does not appear to be related to quantum confinement under the entire gate length due to the relatively large dimensions of the device. The overlapping diamonds in the stability diagram also indicate independent charge trapping/blockade centers along the conduction path in the device [172]. Fig. 7.6 shows individual traces of the conductance-gate voltage ($g_d - V_g$) measurements close to the low-voltage corner of the first Coulomb diamond. In the case where the drain voltage is positive, periodic oscillations are observed on the curves. When the drain voltage is biased in the negative regime, a sharp conductance peak is observed at the edge of the diamond edge. The reason for the asymmetry in the transport response is unclear.

7.3.5 Single trap state response

The device performance was extremely stable [173] over ≈ 10 hours of measurement time at low temperature (< 1 K), and random telegraphic noise was only observable at higher temperatures. Fig. 7.7 shows such measurements at $T \approx 10$ K, revealing the sensitivity of

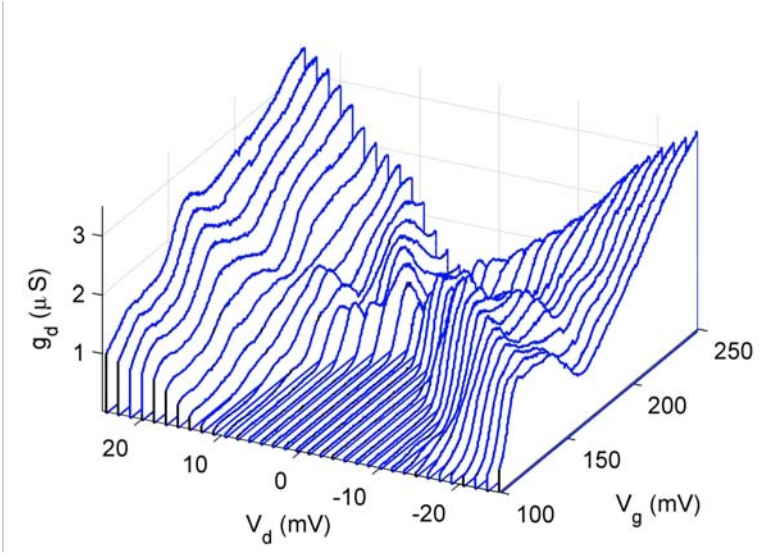

Figure 7.6: Traces of $g_d - V_g$ around the first Coulomb peak at $T = 320$ mK, revealing oscillatory patterns for $V_d > 0$ V and a strong resonant feature for $V_d < 0$ V.

the 28SOI-finFETs to a single Coulomb scattering center caused by an interface trap. The spin state readout of a similar trap state was previously reported using deep sub-micron planer silicon FETs [105]. A trap state created by the formation of a doubly-occupied donor D^- center also perturbs the device current as a Coulomb scattering center. Such D^- centers should then be observable under high magnetic fields and at low temperature [88], which is a promising candidate as a donor spin-state readout mechanism [174].

7.4 Triple-gate finFETs

7.4.1 Design and fabrication

The second generation of finFETs incorporated the idea of using undoped side-gated regions to enhance carrier polarization (Chapter 6), and hence are called the triple-gate finFETs (TG-finFETs). The devices were fabricated on initially 100 nm thick natural silicon SOI wafers, which were subsequently thinned down to 50 nm thick by thermal oxidation. The fins were drawn along the $\langle 110 \rangle$ direction, similar to the 28SOI-finFETs. The two side-gates were patterned with a narrow gap ($50 - 100$ nm) in between, where the fin was located. The wafers were then exposed to low-dose ion implantation, and the smallest fins received five donor atoms on average. These wafers did not have an oxide hardmask on top, and is more akin to tri-gate FETs reported in literature. The height of the fins after all the oxidation

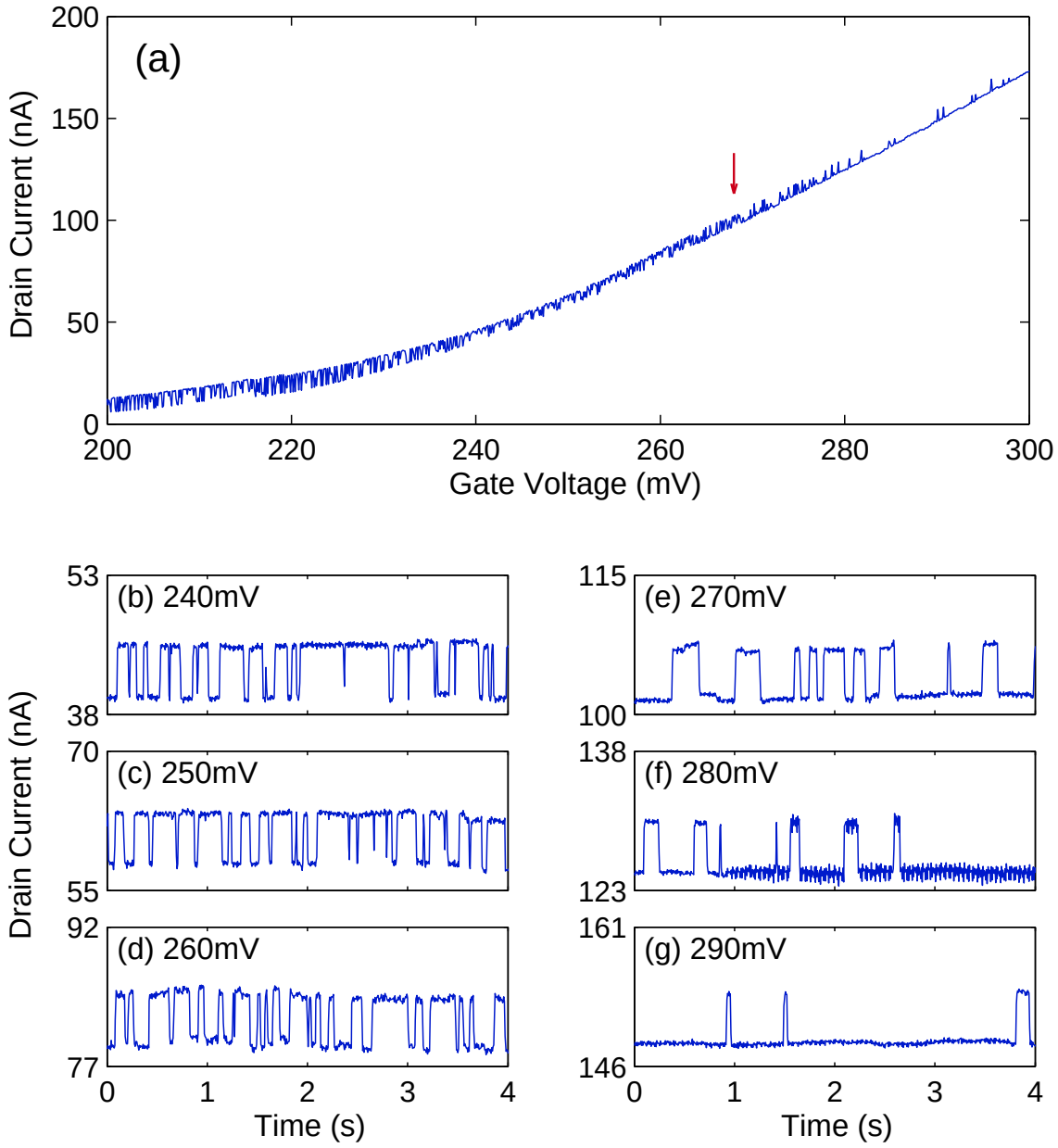

Figure 7.7: Single trap state measurement of 28SOI-finFET. (a) Gate transfer characteristic measured at $T \approx 10$ K with $V_d = 50$ mV. The trap state shifts from mostly unoccupied to mostly occupied at around $V_g = 0.27$ V. (b-g) Random telegraph noise measured at different gate voltages with $V_d = 10$ mV. Device dimensions are $l = 280$ nm and $w = 120$ nm.

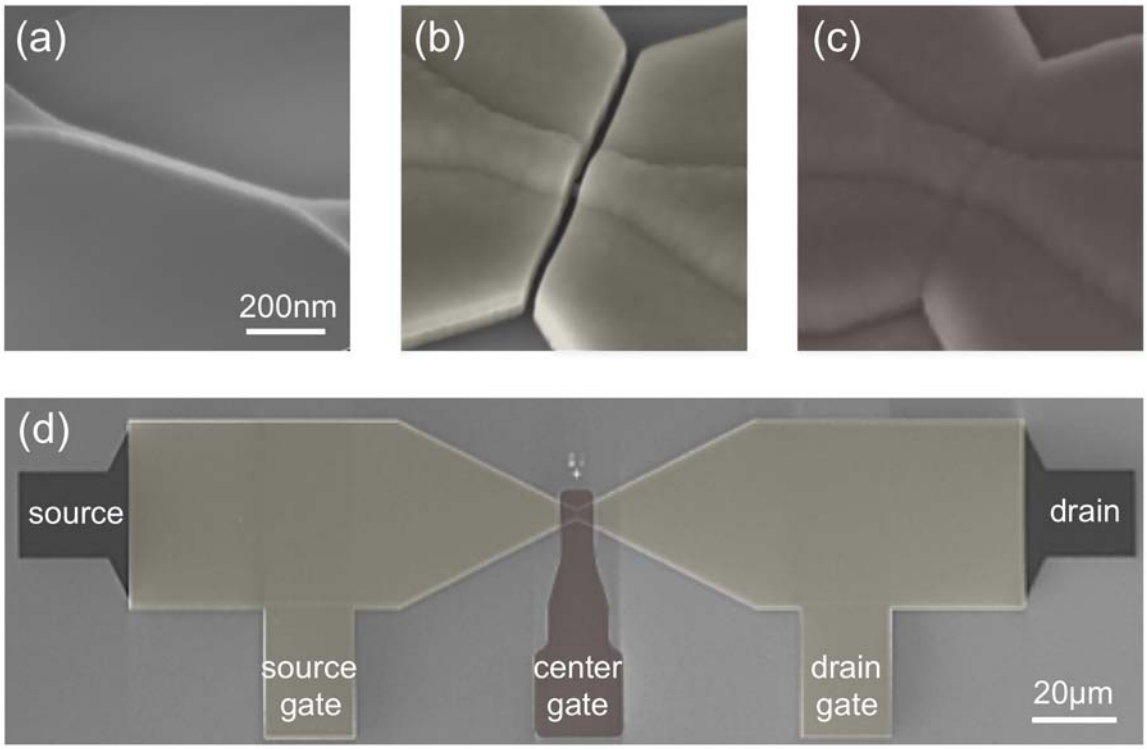

Figure 7.8: False-color SEM micrographs of triple-gate TG-finFETs. (a) After SOI etch and fin patterning, (b) side-gate deposition and patterning (yellow), and (c) center gate deposition (red). (d) Top-view of TG-finFET near completion.

steps is about $h \approx 35$ nm. The SEM micrographs of the devices are shown in Fig. 7.8. The detailed process flow can be found in Appendix B (aFET9), and is outlined here:

1. **SiGe alignment marks**
   100 nm LTO layer was deposited on the SOI wafers to serve as a protective layer for the underlying silicon surface. Then 600 nm of $Si_{0.5}Ge_{0.5}$ and 200 nm LTO were deposited for e-beam alignment marks. The alignment mark patterns were formed using optical lithography and then dry etched. The initial protective LTO layer was then removed by a dilute HF etch to expose the SOI layer.

2. **Fin definition and etch**
   E-beam lithography with the negative MaN-2403 resist was used for the fin and source-drain region definition. After resist development, the fin patterns were transferred to the SOI layer by an anisotropic dry etch process.

3. **Side-gate stack and etch**
   After the fin etch, 14 nm dry oxide was grown on the SOI layer forming the side-gate gate oxide, and then *in situ* phosphorus doped polycrystalline silicon and LTO hardmask were deposited. A second e-beam lithography step was carried out to define the side-gates, with $50 - 100$ nm gap between the gates above the fins. After resist development, the polycrystalline silicon gate was patterned by dry etching, forming the side-gate structures.

4. **Channel implant and center gate stack**
   The fins then received a broad-beam donor implant. The side-gates blocked ions from entering the side-gated SOI regions, and only the exposed fin regions in the gap received ions. After implantation, the remaining oxide on top of the fin was removed by wet etching, and 8nm dry oxide was grown as the channel/fin gate oxide. *In situ* phosphorus doped polycrystalline silicon was again deposited, patterned by optical lithography and etched to form the channel gate structure.

5. **Source-drain implant and activation anneal**
   A wet etch was carried out to remove residual oxide on top of the source-drain regions. Phosphosilicate glass (PSG) was then deposited and annealed to drive in phosphorus dopants into the source-drain SOI regions.

6. **Metallization and shunt layers**
   Contact vias were etched through the PSG layer, and then a thin layer of titanium followed by aluminum was sputter deposited for metallization. The metalic layers were then patterned by dry etching. A thick silicon dioxide layer followed by a thin aluminium layer were then deposited and patterned to form the capacitive shunt on top of the devices.

7.4.2 Device *I-V* characteristics

Fig. 7.9 shows representative *I-V* characteristics of the TG-finFETs. Measurements were performed both at room temperature and liquid helium temperature ($T = 4.2$ K). We refer to the side-gate on the source-end of the device as the source-gate (sg) and the one on the drain-end the drain-gate (dg). The center (fin) gate is simply referred as the gate (g). In these measurements, the two side-gates were biased together, i.e. $V_{sg} = V_{dg}$. The room temperature measurements show *I-V* characteristics consistent with a short channel MOSFET with velocity overshoot. In addition, the side-gated regions add substantial series resistance (≈ 100 kΩ at side-gate voltages of $V_{sg} = V_{dg} = 1$ V) (Fig. 7.9(a)). As the side-gate voltages are reduced, the series resistance is further increased, as seen in the transfer characteristics (Fig. 7.9(b)).

Once the sample was cooled to liquid helium temperatures, the *I-V* characteristics change profoundly. The *I-V* behavior shows substantial injection barrier ($V_d < 200$ mV region in

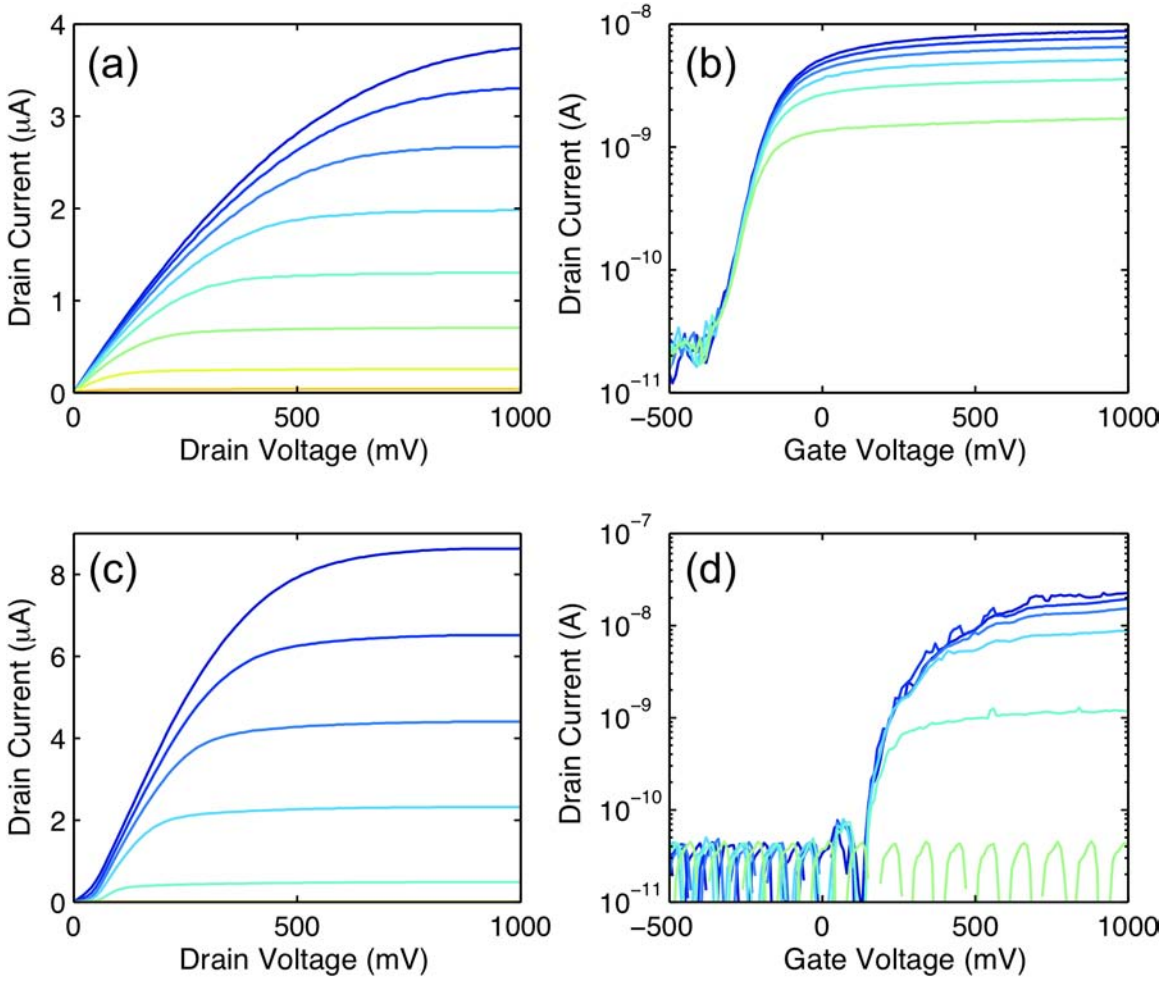

Figure 7.9: I-V characteristics of TG-finFET with lithographic dimensions l = 76 nm and w = 100 nm. Room temperature measurements of (a) I_d-V_d, and (b) I_d-V_g. Liquid helium temperature measurements of (c) I_d-V_d, and (d) I_d-V_g. The I_d-V_d traces were taken with V_g = 0.5 to −0.5 V in −0.1 V steps from top to bottom. Both side-gates biased were at $V_{sg} = V_{dg}$ = 1 V. I_d-V_g traces were taken with $V_{sg} = V_{dg}$ = 1 to 0 V in −0.2 V steps, with V_d = 1 mV.

Fig. 7.9(c)), similar to that observed in Schottky junction MOSFETs. However, the barrier reduces at higher gate voltages. This barrier is not due to poor metal-silicon contact quality as control devices without the fin exhibited normal ohmic-like I-V characteristics at low temperatures. Instead, these kinks are due to the oxide barrier region between the fin and side-gates. The barrier is smaller than the thermal energy k_BT at room temperature, and is

hence only observable at low temperature when k_BT becomes less than or comparable to the barrier height. The gate transfer characteristics are not smooth in liquid helium temperature either (Fig. 7.9(d)), which are due to quantum mechanical effects and will be investigated thoroughly in the next sections with transport spectroscopy techniques.

7.4.3 EDMR of TG-finFETs

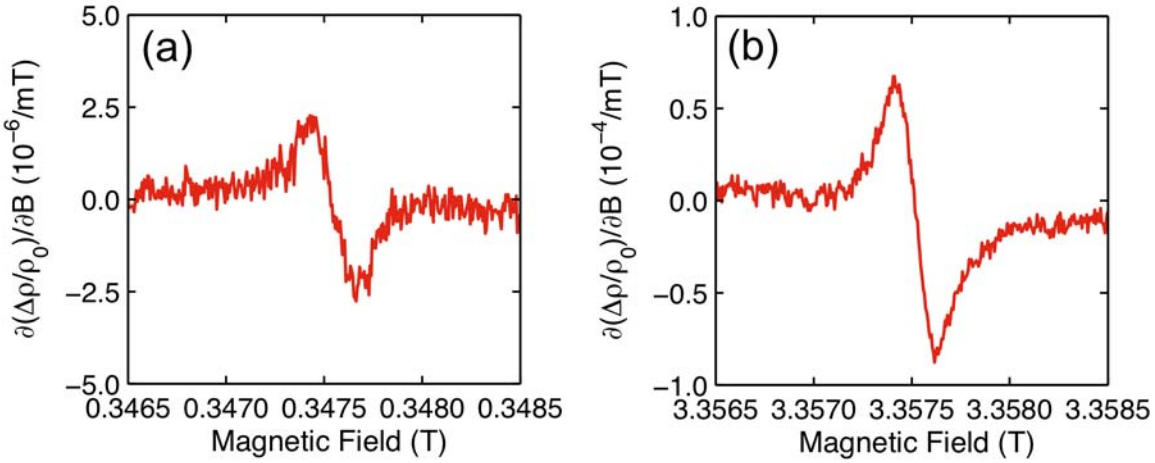

Figure 7.10: EDMR spectra of TG-finFET measured in (a) X- and (b) W-band at $T = 5$ K. The side-gates and center gate were all biased at 0.4 V in both measurements.

Both X- and W-band EDMR measurements were performed on the TG-finFETs and typical results are shown in Fig. 7.10. In all the measurements attempted — under different gate biases and current densities — only a single resonance signal corresponding to conduction electrons was observed. However, in these triple-gate devices, the 2DEG signal can originate from both the center fin region and from the side-gated regions, as we have shown in Chapter 5 that undoped MOSFETs give rise to very large resonance signals as well.

The difficulty in measuring donor resonances with the TG-finFETs biased in the drift-diffusion regime can be estimated from the donor EDMR signal intensities of micron-scale devices. Implanted donor signals with concentrations similar to those in the TG-finFETs typically have $\Delta\rho/\rho_0 \approx 10^{-6}$ at X-band. For 1 mV bias across the fin (corresponding to an electric field of 100 V/cm for a 100 nm long fin), the expected change in voltage on donor resonance is approximately 1 nV. The noise level we can detect is about 100 nV/scan for samples with resistance $\lesssim 100\,\mathrm{k}\Omega$ with our typical measurement settings. Since the signal increases linearly with data acquisition time τ and noise increases by $\sqrt{\tau}$, 10^4 longer data

acquisition time will be needed in order to resolve the donor resonance signals. As a typical measurement takes approximate 60 s to complete, the long data acquisition time required to resolve the donors signals in the TG-finFETs would be beyond practical experimental constraints.

We have seen that in W-band, the donor EDMR signals increase by approximately 20 times. This means 20^2 longer data acquisition time is needed, which is, however, still substantial. In addition, the superconducting magnet coils tend to drift with each measurement due to hysteresis effects. This adds uncertainty in the field position from scan to scan.

The estimate given above neglects the fact that at 100 V/cm the conduction electrons will heat up substantially [112]. This effect will further reduce the observable signals as we have found that the EDMR signal intensities are very sensitive to temperature (Chapter 5). Much lower biases should be used to avoid overheating the device, which means that even longer data acquisition times would be needed.

In order to resolve donor resonance signals in these few dopant devices, a substantial improvement in the signal-to-noise ratio in the measurement scheme must be implemented. One approach would be to implement a double modulation scheme, in which the sample conductivity and magnetic field are modulated at the same time. A second approach is to increase the bandwidth of the measurement by implementing a RLC tank circuit approach, in which the TG-finFET forms the resistive element in the resonant circuit. This approach allows the measurements to be carried out at high frequency (limited by the quality factor of the tank circuit), which was shown to increase the signal-to-noise ratio by a factor 30 when compared with standard single modulation measurements [175].

7.4.4 Transport spectroscopy

In order to better determine the presence of donors in these nano-scale devices and to seek better biasing regimes beyond diffusive transport for EDMR measurements, transport spectroscopy was performed on a large number of the TG-finFETs. Most measurements were carried out at 4.2 K, while selected devices were also measured in the He-3 dilution refrigerator.

It has been reported that tunneling through individual donor states gives rise to strong resonance peaks in the sub-threshold regime of nano-scale MOSFETs. We found that most TG-finFETs exhibited quantum interferences and Coulomb blockade oscillations in transport measurements below threshold at 4.2K. These usually consisted of overlapping features which indicated a high degree of disorderedness in the samples. However, these structures became much better resolved in lower temperature. Fig. 7.11 shows the stability diagrams of a 76 nm long and 70 nm wide device measured at 400 mK. In the measurements the center (fin) gate and drain voltages were scanned as the device conductivity was monitored. The side-gates of the TG-finFETs were shorted together and held constant. Coulomb diamonds are clearly visible but their sizes reduce with increasing side-gate voltages (Fig. 7.11(a)-(d)). Eventually the Coulomb diamonds disappear at the high side-gate voltage of 5V (Fig. 7.11(e)), where

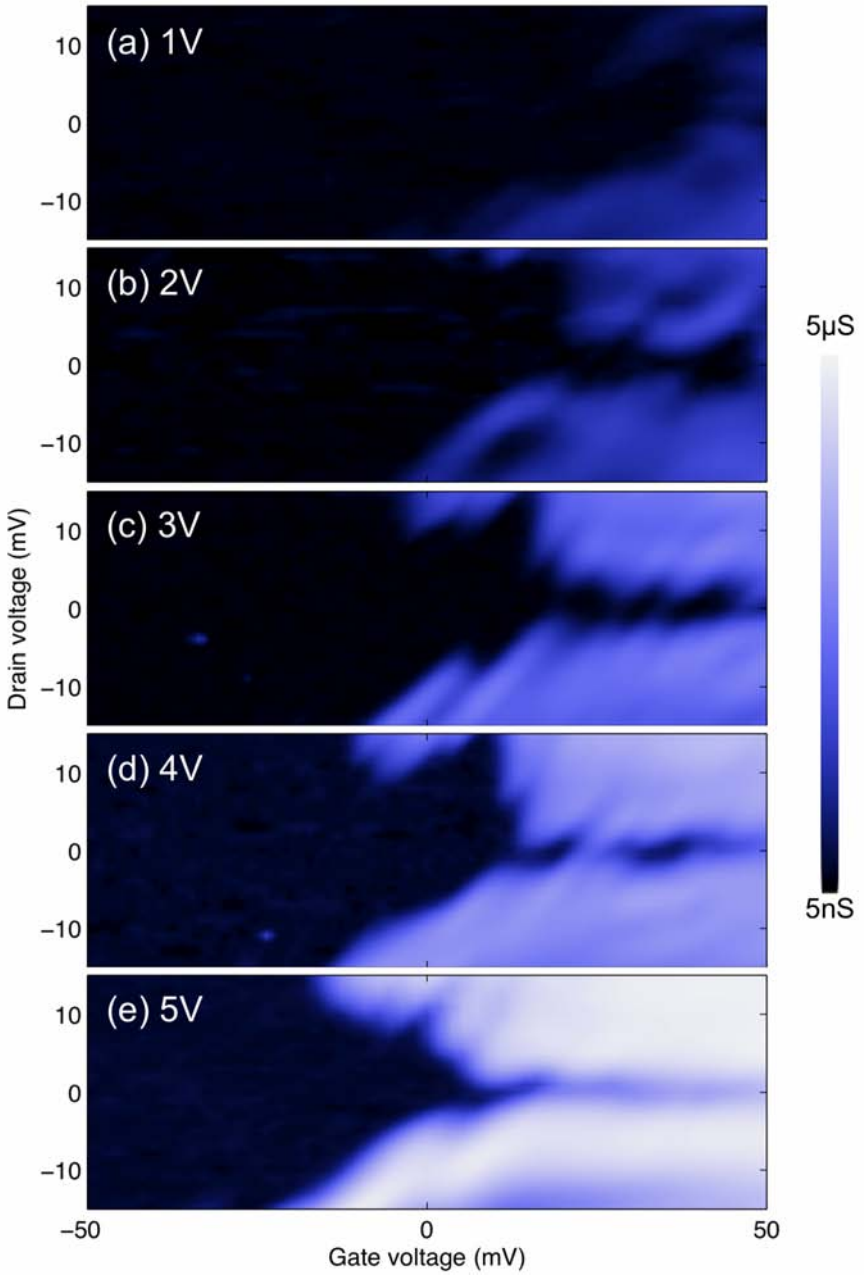

Figure 7.11: Transport spectroscopy of TG-finFET with $l = 76\,\mathrm{nm}$ and $w = 70\,\mathrm{nm}$ measured at $T = 400\,\mathrm{mK}$ under various side-gate voltages. (a)-(e) The x-axis refers to the center (fin) gate voltage, while the two side-gates were connected together and the applied voltages are indicated.

the transport characteristics resembles that of a regular MOSFET.

We can understand this behavior by examining the changes in the potential landscape in the TG-finFETs as the side-gate voltages are varied. This is illustrated in Fig. 7.12, where the conduction band profile is simulated [140]. At low side gate voltages (Fig. 7.12(a)), the regions under the insulating oxide between the center and side-gates create an effective spacer with large potential barriers. Thus, a quantum dot region is formed and Coulomb blockade can occur [176, 177]. When the side-gate voltages are increased (Fig. 7.12(b)), the barriers seen by the quantum dot are lowered and the confinement potential becomes shallower. This effect reduces the charging energy of the dot, and hence the Coulomb blockade diamonds reduce in size. Finally, at very large side-gate biases (Fig.7.12(c)), the barriers are completely removed and the conduction band profile looks like that of a regular MOS device.

The measurements so far only confirm that the resonance features observed in the sub-threshold regime are associated with quantum confinement in the fin, which can be adjusted by tuning the bias conditions of the side-gates. Tunneling through single donor states should give strong resonances which are not periodic Coulomb oscillations. In fact, the observation of transport through single donor states are usually attributed to the occurrence to two resonance peaks: one corresponding to the neutral D^0 donor state, and the second one corresponding to the doubly occupied D^- at higher gate voltages [177, 46, 178, 37]. Of the dozen of devices measured, two showed strong and isolated resonance features. The trans-

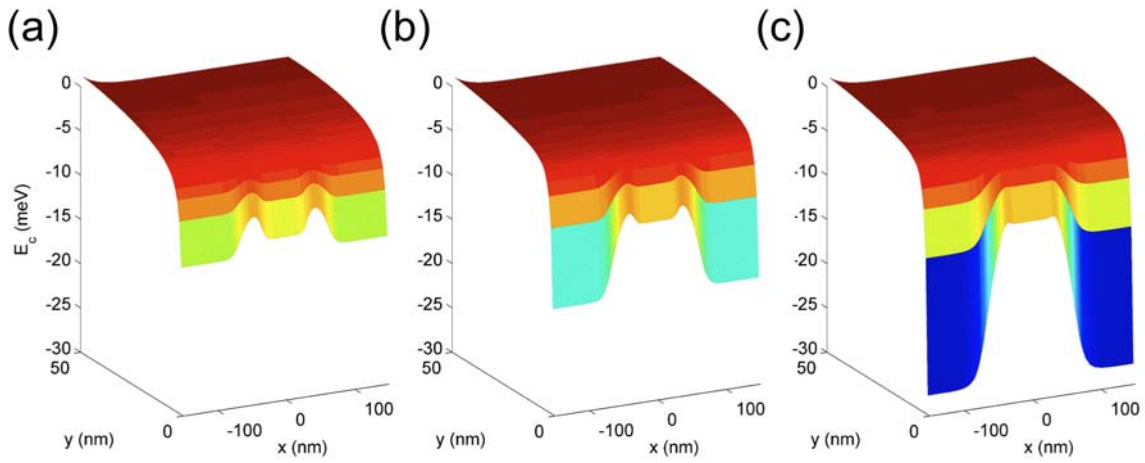

Figure 7.12: Simulated conduction band landscape in TG-finFETs. (a) Low side-gate voltages create a double-barrier quantum dot in the fin, (b) Moderate side-gate voltages creates shallower quantum dot potential in the fin, and (c) High side-gate voltages remove the barriers and the device operates like a regular three-terminal MOSFET.

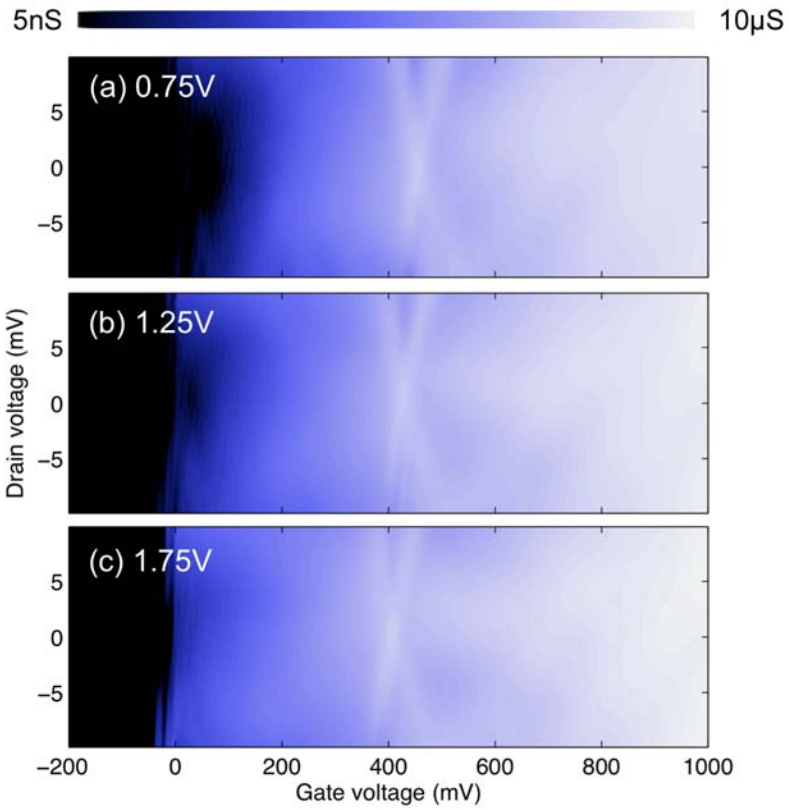

Figure 7.13: Transport spectroscopy of TG-finFET with $l = 100$nm and $w = 50$nm measured at $T = 4.2$ K showing strong isolated resonance feature.

port spectroscopy measurements of one of them with center fin length 100 nm and width 50 nm are shown in Fig. 7.13.

In these devices, Coulomb blockade effects are still observed in the subthreshold regime ($V_g \approx 0\,\mathrm{V}$). At higher gate voltages ($V_g \approx 400\,\mathrm{mV}$ in Fig. 7.13), strong resonance features are observed with its excited state spectrum weakly visible as well. Since these strong resonances are only observed in a small fraction of the devices and appear as isolated resonance features, they are not related to quantum confinement in the silicon fin. One possible origin can be due to the channel-implanted donors in the fin. However, the background currents associated with the turn-on of the devices reduces the visibilities of these resonance features. The fact that the resonance features appear after the device channel has turned on (as opposed to sub-threshold resonance peaks reported in literature) can be attributed to the location of the donor in the fin. In the non-planer geometry of the TG-finFET, the corners of the fin would conduct electrons first due to enhanced electric fields. If the donor is closer to the center of

the fin, then electrons would transport through the corners of the fin first before transport closer to the center of the fin can occur. However, a positive identification of the origin of the resonance features would require further supporting evidence such as magnetoresistance data to observe shifts in the resonance positions, and eventually EDMR experiments.

7.4.5 Magnetotransport of finFETs in the Coulomb blockaded regime

Magnetotransport measurements were carried out for two TG-finFETs at the National High Magnetic Field Laboratory (NHMFL) at Tallahassee, Florida. The cryostat used consists of a dilution refrigerator with base temperature of 20 mK and equipped with a superconducting magnet that can ramp up to 18 T. Fig. 7.14 shows the conductance plots with 0 V dc bias and ac excitation voltage of 20 μV applied to the drain. The data shown in Fig. 7.14(a) is from a device with lithographic dimensions of $l \times w = 100 \times 50\,\mathrm{nm}^2$, while that for Fig. 7.14(b) has dimensions $l \times w = 75 \times 100\,\mathrm{nm}^2$. These two devices did not exhibit the strong resonance features discussed in the previous section.

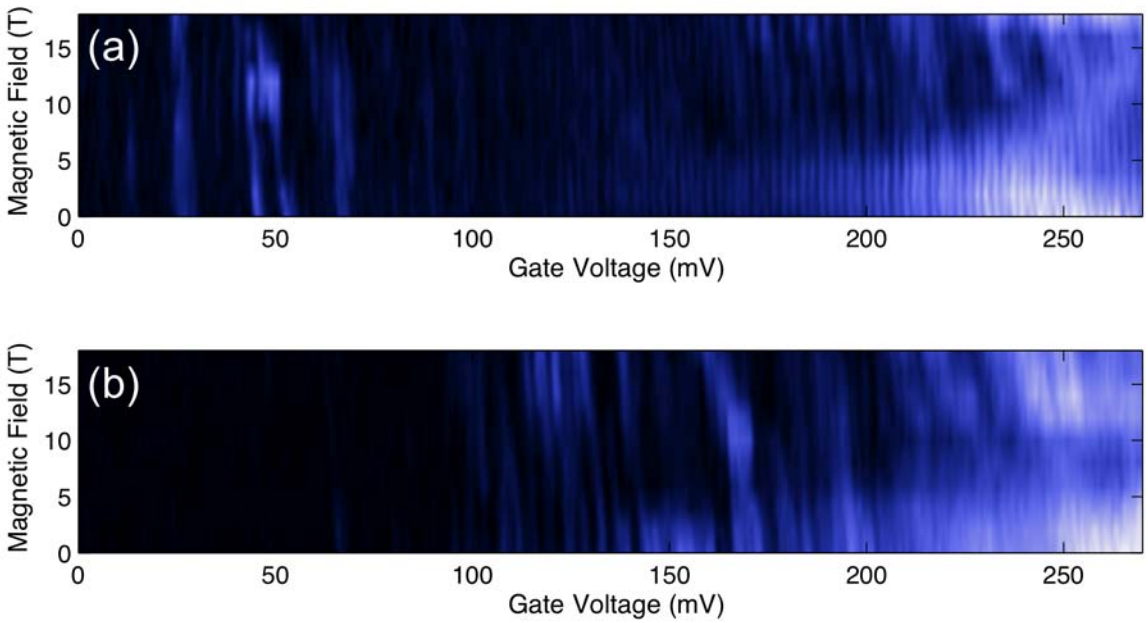

Figure 7.14: Magnetotransport measurements at 0V dc bias measured at a base temperature of $T = 20$ mK. The side gates are biased at 0.8 V in both cases. The fin sizes are: (a) $l = 100$ nm and $w = 50$ nm, and (b) $l = 75$ nm and $w = 100$ nm.

It is interesting to note that a few of the resonance features shift with magnetic field.

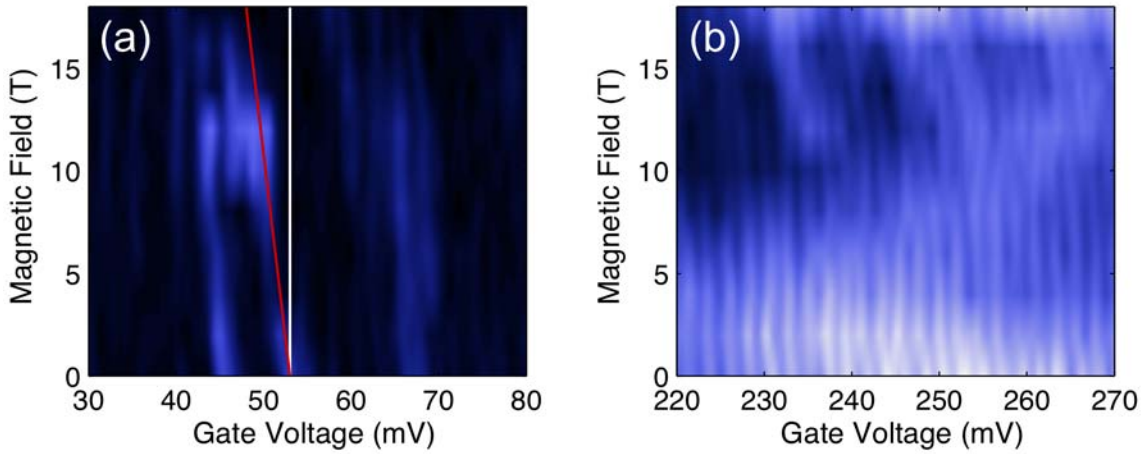

Figure 7.15: Detailed view of the magnetotransport data of the $l = 100$ nm and $w = 50$ nm TG-finFET. (a) Shows the subthreshold regime where isolated resonance features are observed. Certain features show a strong magnetic field dependence, corresponding to the Zeeman shift of paramagnetic states (indicated by dashed red line). (b) Same bias window at higher gate voltage. The Coulomb oscillations of the multi-electron quantum dot do not exhibit strong magnetic field dependence at all.

This is most evident in Fig. 7.14(b) for $V_g \approx 100 - 150$ mV, where some features split with increasing magnetic field and others converge with magnetic field. The splitting of the resonance lines can be understood as a manifestation of the Zeeman shifts for resonance features associated with paramagnetic states. The convergence of the resonance features, on the other hand, is related to the increased probabilities for two-electron co-tunneling events that occur [176].

The oscillations at higher gate voltages ($V_g > 150$ mV) are periodic and reproducible for the smaller device, indicating carrier transport in the Coulomb blockaded regime in a multi-electron quantum dot. Fig. 7.15 shows the zoomed in view of this device for low gate bias (Fig. 7.15(a)) and higher gate bias (Fig. 7.15(b)). The periodicity of the Coulomb oscillations are determined by Fourier transform, and we obtain $\Delta V_g = 2.2$ mV. To estimate the gate capacitance to the quantum confined region, we use:

$$\Delta V_g = \frac{q}{C_g} \tag{7.1}$$

where C_g is the total (fin) gate capacitance associated with the quantum dot, and is found

to be 73 aF. We can also roughly estimate the expected gate capacitance assuming a planer geometry using:

$$C_g \approx \frac{\epsilon_{ox}\epsilon_0}{t_{ox}} A \tag{7.2}$$

where A is the total area of the side walls of the fin, and $t_{ox} = 8$ nm is the gate oxide thickness. From this expression we obtain $C_{ox} = 52$ aF, in reasonably good agreement with the extracted value, hence further confirming that the observed Coulomb oscillations are associated with the quantum confinement from the fin.

The sub-threshold resonance signal highlighted in red in Fig. 7.15(a) shifts to lower gate voltage, as would be expected if the ground state of that resonance feature is associated with singular spins that shift lower in energy with magnetic field [177]. On the other hand, the resonance features at higher gate voltages remain mostly stable with increasing magnetic field in such multi-electron systems. Assuming that the shift in Fig. 7.15(a) arises from Zeeman interaction, and $g \approx 2$, at 18 T, we expect a Zeeman shift of $\Delta E/\Delta B = 0.12$ meV/T. From the slope of the shift of the resonance peak we can then extract the level-arm parameter $\alpha = 0.42$.

7.5 Conclusions

Two types of single-ion implantation compatible finFETs were examined in this chapter. The 28SOI-finFETs exhibited poor contact quality at cryogenic temperatures and appeared to be highly disordered. The poor contact quality prevented meaningful EDMR measurements. The second type of finFETs, the TG-finFETs incorporated the use of side-gates in the design, and the number of channel dopants is expected to be an order of magnitude smaller than the 28SOI-finFETs. EDMR measurements were attempted in the drift-diffusion regime, however, no donor signals were observed. It is expected that the data acquisition time required to resolve donor resonance signals would be prohibitive owing to the small donor EDMR signals. A more promising measurement scheme is to measure in the near-subthreshold conduction regime and seek resonances in transport features that are associated with donor states. Our measurements of over two dozen of devices showed two devices which exhibited anomalous transport resonance features which do not seem to be associated with quantum confinement of the volume of the fin. However, more detailed measurements need to be carried out to identify the origin of those resonance peaks.

Chapter 8

Summary and Future Directions

In this work we have examined the spin-dependent transport of silicon MOSFETs in detail. We have developed a robust design and processing flow for fabricating devices compatible with resonant microwave cavity-based EDMR measurements. EDMR measurements in both X- and W-band resonant microwave cavities were successfully implemented, with the latter being the first such measurements reported in literature. The main results from our systematic studies of micron-scale donor-doped MOSFETs includes:

1. The spin-dependent transport mechanism of silicon MOSFETs is dominated by a polarization-dependent mobility of the 2DEG. Direct spin-dependent scattering with donors plays a much smaller role.

2. The 2DEG spin relaxation times are in the order of 100 ns in silicon MOSFETs at cryogenic temperatures.

3. The spin relaxation times of donor electrons interacting with 2DEG electrons in MOSFETs are also in the order of 100 ns, orders of magnitude smaller than bulk values.

4. Donor signal intensities decrease with MOSFET length instead of the constant scaling originally anticipated. This is due to spin drift and spin diffusion effects from the $n+$ leads. A triple-gate structure is proposed to alleviate this problem, and preliminary EDMR results seem to support this hypothesis.

5. A spin diffusion length of $L_D \approx 3\,\mu$m for conduction electrons is extracted in silicon MOS systems at 5 K using EDMR as an in situ probe of conduction electron polarization.

We also developed and examined single-ion implantation compatible nano-scale donor-doped MOS devices. EDMR was attempted; however, no donor resonance signals were

observed. Transport spectroscopy was carried out and showed promising devices with possible signatures of donor resonances. However, further investigation is required for a definitive identification of the origin of these resonance structures.

Donor nuclear spin readout with EDMR requires the donor nuclear spin relaxation time T_{1n} to be sufficiently long — longer than the measurement time itself. While the donor electron relaxation time T_1 seems to be limited by electron scattering and is relatively short, its correlations to T_{1n} is unclear. Performing pulsed EDMR directly with donor-doped MOSFETs is challenging due to the short T_1. The electrical detection bandwidth is limited by the capacitance of the measurement setup, limiting it to about 100 kHz even for relatively conductive samples. A possible approach is to implement a tank circuit scheme which operates in the MHz range [175]. Pulsed EDMR and electrically detected ENDOR experiments would then allow the direct measurement of T_1 and T_{1n} in such systems. Alternatively, another approach to obtain T_{1n} in donor doped MOSFETs is to perform pulsed EPR/ENDOR experiments with large area MOSFETs (Appendix A (d2D)).

As discussed in Chapter 7, owing to the small donor signals observed, donor resonance detection with few-donor-doped MOSFETs is challenging. One approach to achieve enhanced donor signals is to perform EDMR measurements at even lower temperatures. Extrapolating from the temperature dependence of the donor EDMR signal at X-band (Chapter 5), we estimate that resonance signals of the order $\Delta\rho/\rho_0 \approx 10^{-4}$ can be achieved below 1 K. With a moderate electric field of 10 V/cm applied across a $\approx$ 100 nm long device, the detection sensitivity required is about 10 nV, which seems to be within reach with improvements in the experimental setup. Nevertheless, single-shot measurements of donor nuclear spin-states relying on the polarization transfer mechanism seems prohibitive to realize owing to the relatively small signal amplitudes. Alternative spin-dependent transport mechanisms, such as spin-dependent trapping or spin-dependent tunneling might be more promising.

Recent experiments have shown great promises using the D^- state to trap conduction electrons with shallow donors [60]. Due to the small binding energies of this doubly occupied state, they are usually only observed below $\approx$ 3 K. If the D^- state trapping mechanism is observable in MOSFETs, the donor resonance signals can be substantially increased due to the formation of additional localized Coulomb scattering centers, as observed in the study of trap states in the 28SOI-finFETs. However, the dynamics and stability of the weakly bound D^- states in the presence of the 2DEG remains to be studied.

Spin-dependent tunneling through single-donor states can also be exploited for nuclear spin-state readout with EDMR. In such a scheme, the electron spin ground state of the D^0 electron should be tuned below the source and drain Fermi levels, while the excited state is above. In this scenario, tunneling current through the single dopant is prohibited in the absence of resonant excitation due to spin blockade. When the D^0 electron is resonantly excited, it can then escape to the drain electrode. This scheme would require experimental conditions with Zeeman energy much greater than the thermal energy for high visibility measurements.

From a device architecture perspective, we developed finFETs for single-ion implantation compatibility. FinFETs are attractive as they allow reliable room temperature detection of single-ion implantation events. However, the etched side walls are inevitably prone to disorder. The surface roughness of the fins would also make low temperature transport measurements more complicated, especially since the fins of our triple-gate devices are relatively long. From this point of view, it seems that cleaner planer device structures would be more promising for studying single dopant affects, as single-ion implantation detection has indeed been demonstrated in planar devices as well [30]. In addition, simple statistical implants with small donor ensembles in device channels might suffice for proof-of-principle experimental demonstrations.

Appendix A

Device fabrication

A.1 Summary of devices fabricated

Over the course of this work, nine generations of MOSFETs for EDMR experiments (or ten, depending on the definition "generation") were developed. The different generations of devices are labeled aFET1-9 (aFET stands for accumulation-mode field-effect transistors). We will briefly remark on all these generations of devices, chronicling our effort in developing EDMR-compatible MOSFETs. The detailed process flows for all those devices which results are reported in this thesis (aFET5,6,8 and 9) can be found it Appendix B.

1. **aFET1: Micron-scale bulk-doped natural silicon devices**
   The first generation aFETs were fabricated on bulk-doped natural silicon wafers with either antimony (natural abundance) or phosphorus. The substrate dopings were in the range of $10^{17}/\mathrm{cm}^2$. These devices were fabricated using optical lithography with a stepper, and the diced chips ($\approx 2 \times 5\,\mathrm{mm}^2$) were wirebonded to a quartz supporting substrate with pre-patterened metallic leads. The devices worked well at cryogenic temperatures, and EDMR signals corresponding to donor resonances were observed. However, no 2DEG signals were detected. In addition, the lineshapes of the resonances signals were reminiscent of passage effects in EPR — and it was later determined that the origin of the signals come from a bolometric effect, where background dopants deep in the bulk affected the EDMR signals. Thus, bulk-doped devices should *not* be used for EDMR measurements with microwave resonators.

2. **aFET2: Micron-scale channel-implanted ^{28}Si devices**
   The second generation devices were built on 99.92 % isotopically purified epitaxial ^{28}Si wafers. The channels were implanted with ^{123}Sb. The elongated chip layout was also adopted (Chapter 3) to reduce microwave absorption by the wirebonds. However, there were problems with obtaining good ohmic contacts with the metal layer. The contact resistance were improved by electrical stressing of the contacts through the substrate at

room temperature. In stressed devices, 2DEG and P_b centers were observed in EDMR; however, there were no signs of donors. The P_b signal is attributed to the relatively poor oxide quality of these devices.

3. **aFET3: Micron-scale channel-implanted ^{28}Si devices**
   The third generation devices were also built on 99.92 % isotopically purified epitaxial ^{28}Si wafers. The channels were implanted with ^{121}Sb. The layout of the EDMR chips were modified so that the source-drain direction is perpendicular to the electric-field distribution in the microwave cavity. These devices also had issues with contact quality with the metal layer, and again electrical stressing was needed to reduce the resistance for cryogenic measurements (The issue with metal contact qualities was later found to be due to a poor vacuum and inaccurate vacuum gauge reading in the metal sputter chamber). EDMR was attempted on a large number of aFET3 devices, and resonance signals from both 2DEG and donors were observed in one lucky device. Microwave-induced rectification effects were also examined, and shunts were subsequently implemented on these devices (Chapter 3) yielding significant improvement in noise reduction.

4. **aFET4: Micron-scale channel-implanted natural silicon SOI devices**
   The forth generation devices were built on 50 nm thick natural silicon SOI and channel implanted with ^{121}Sb. The starting wafers were 200 mm in diameter, and were sent for laser dicing to 100 mm to conform to the Berkeley microlab capabilities. Unfortunately, the diced wafer surfaces were severely damaged during this process. Nevertheless, the fabrication process was carried out. A PSG diffusion process was used for source-drain formation for the first time, and the devices exhibited excellent contact quality at cryogenic temperatures (although the oxide quality was poor). Attempts with EDMR did not reveal any donor signals.

5. **aFET5: 28SOI-finFETs**
   The fifth generation devices were built on specially ordered ^{28}Si-SOI substrates. The channels were implanted with ^{121}Sb. The e-beam lithography steps required considerable effort to develop: while the bi-layer process of AZPN/HSQ provided excellent feature sizes and anisotropic side-walls, it became problematic when attempting the gate-pattern etch with this same bi-layer stack. The topology of the SOI fins consisting of 200 nm thick SOI layer and $\approx$ 50 nm LTO hardmask made the AZPN and HSQ layers highly non-uniform. Subsequently, the cryogenic pattern transfer process was not successful. A solution was found by switching to the Microchem MaN 2403 resist, and significant effort was put into testing this new resist and etch compatibility with our process. The silicon fin and gate etch process also required significant effort as different etchers, process conditions and etch chemistry needed to be tested and optimized to achieve high sidewall quality and Si/SiO_2 selectivity. Two wafers were completed at the end (a few others failed during processing): one with aluminum metallization and

the other with tungsten metallization — which was designed to be compatible with the single-ion implantation process. However, contact issues persisted with this generation of devices. EDMR attempts and transport measurements are reported in Chapter 7. A detailed process flow is included in Appendix B (aFET5).

6. **aFET5p: Planer nano-scale FETs on natural silicon**
   Planer nano-scale MOSFETs were also developed using the (then) new CRESTEC e-beam writer at the microlab. The devices were built on high-resistivity natural silicon wafers. The process flow was relatively straightforward: after (poly-silicon) gate patterning with MaN 2403 and etch, a self-aligned source-drain implant was used. 420 nm of the positive e-beam resist ZEP-520A was used as the implant mask for this source-drain definition step. The freeze-out of the silicon substrate was relied upon for providing isolation as in the micron-scale MOSFETs. Subsequently, a shunt capacitor was added on top. Since the shunt layer materials were not optimized at that point, silicon nitride was used as it was believed the higher capacitance with using nitride would further improve the shunt effectiveness. However, it was later found that the silicon nitride induced carriers throughout the silicon chip underneath due to the high fixed charges in the material.

7. **aFET6: Micron-scale channel-implanted natural silicon and ^{28}Si devices**
   The sixth generation devices incorporated the best features of previous devices to improve the EDMR signal. Devices were built on both high resistivity natural silicon substrates as well as ^{28}Si epitaxial layers. The channels were implanted with ^{121}Sb or ^{75}As for others. These devices used PSG diffusion for source-drain formation, and exhibited excellent contact qualities at cryogenic temperatures. The microwave shunts were also integrated into the process flow directly (as opposed to adding them on a chip-by-chip basis in previous generations). The metal layout was also changed to allow an easy PCB mechanical contact scheme for EDMR measurements (thus the unreliable silver epoxy was no longer needed to wire up the devices). These devices exhibited low noise in EDMR and reliable 2DEG and donor resonance signals were observed. These results are the basis of the data shown in Chapters 3-5. A detailed process flow is included in Appendix B (aFET6).

8. **aFET7: Nano-scale quantum dot devices**
   The seventh generation devices was an attempt in creating MOS-compatible quantum dot structures on SOI wafers. The CRESTEC e-beam writer was used and the process mostly developed. However, they were not completed due to priorities with other device fabrication efforts.

9. **aFET8: Micron-scale triple-gate devices**
   The eighth generation devices incorporated the use of triple-gate structures for enhancing the EDMR signal. These side gates were designed to be 60 μm long, much longer

than the expected spin diffusion lengths. Most of the fabrication process and design were similar to the successful aFET6 devices. These results are reported in Chapter 6. A detailed process flow is included in Appendix B (aFET8).

10. **aFET9: Nano-scale triple-gate finFETs (TG-finFETs)**
The ninth generation of devices combined the triple-gate structure with nano-scale few-dopant finFETs. MaN 2403 was used for all the e-beam steps. Special care was taken to further improve the silicon etch processes due to the formation of (very big) stringers for the second gate layer. The measurement results from these devices are reported in Chapter 7. A detailed process flow is included in Appendix B (aFET9).

Other fabrication processes not included in the aFET series include:

11. **d2D: Large-area MOSFETs for EPR**
The spin coherence limitations of donors interacting with a 2DEG can also be studied with EPR if the MOSFET can be made large enough (at least $\approx 1 \times 1\,\mathrm{cm}^2$ for sufficient EPR signal). The measurement of the spin coherence of 2DEG electrons in MOSFETs in EPR was successfully performed by the Princeton group recently. This motivated the work on large-area donor-doped MOSFETs. However, special care is needed when designing the donor implant and thermal budget allowed: Since EPR detects all donors present in the sample, the implanted donors need to stay very close to the interface in order for them to interact with the 2DEG. Otherwise the EPR signal will come from donors not interacting with the 2DEG at all. Thus, these devices were designed to have a minimized thermal budget once the channel donors are implanted in order to reduce dopant diffusion. On the other hand, a high quality oxide interface with low leakage current are desirable. Thus, an hybrid approach was used: 10 nm high quality thermal oxide was first grown, the ^{121}Sb donors were then implanted. After implantation, a RTA step was used to activate the donors. 300 nm LTO was then deposited as the remainder of the gate dielectric. Finally, aluminum was deposited to complete the gate electrode. Initial EPR measurements have been carried out by Alexei Tyryshkin, with preliminary results indicating 100 ns T_1 times for donors. This is consistent with our estimates from EDMR.

12. **FinResistors**
These are patterned SOI silicon fins without the gate — essentially acting as a donor-doped resistor. They were fabricated with Christoph Weis to test spin-dependent recombination in small ensembles of spins in SOI material. The measurement of these devices are in progress at the time of the writing of this thesis.

13. **SDR-1: Shallow donor - Double-donor recombination systems**
The most successful p-EDMR experiments to date use the shallow donor - point defect recombination process. However, interface point defects such as P_b are difficult

to control and create. An alternative is to use a deep double donor to replace the interface defect in the recombination processes. Samples were fabricated with ^{75}As and ^{33}S implanted 100 nm deep into the silicon surface. This depth avoids shallow donor (^{75}As)-interface defect interaction. The ^{33}S double donor was chosen (instead of the more naturally abundant ^{32}S) due to its non-zero nuclear spin, which would allow easy identification in the EDMR spectra. Two samples with two different thermal activation strategies were used. In EDMR, both showed the strong ^{75}As signals. However, signatures for ^{33}S were unclear: no hyperfine-split ^{33}S signals were observed. Instead, a group of complex signals arose. The complex signals might be due to cluster formation during the activation steps, and further experiments are needed to clarify the situation.

14. **SiCQED: Local accumulation gate quantum dots and superconducting resonator**
    This is a collaboration with the QUEST project, in which the fabrication of MOS quantum dots is incorporated with the the design of superconducting resonators for quantum communication with semiconductor qubits. The first device fabrications are near completion at the time of the writing of this thesis.

A.2 Fabrication tips

Here are some (hopefully) useful fabrication tips when working in the UC Berkeley nanofabrication laboratory, most learnt the hard way:

1. **Wet etching**
   Three keys should be remembered for any critical wet etching steps: (i) use a proper sink, (ii) agitate, and (iii) calibrate. The etch rates using large sinks are much more uniform and reproducible than using small dishes. Agitation during the etch process helps uniformity. Always calibrate the etch rate for the etchant and target material; the tables/charts only give ballpark values. Use BHF if etching with PR mask. Use HF only if the etches are dilute and etch times are short.

2. **Dry etching**
   Always calibrate any dry etch process. This means using dummy wafers and carefully checking the etch rates and uniformities of the etch. This is especially critical for silicon etch processes as the etch rate is rather sensitive to the chamber condition, i.e. what crap the previous user put in the chamber. Prepare sufficient dummies with the EXACT same target material as on the real device wafers. When using pocket wafers, generally I avoid using cool-grease as they are tricky to handle (and quite dirty). Etch times then need to be well controlled to avoid burning the photoresist. Always inspect the completed etch process with SEM: microscopic residuals are difficult to spot by

optical inspection. Always do a dilute HF dip to removal silicon etch by-products (they cannot be removed by O_2 plasma or piranha clean).

3. **Thin film growth and deposition**
   The key here is again calibration. Be consistent with wafer orientation, flat orientation, boat used, *etc.* to obtain consistent results. Monitor gas flows and alarms carefully during deposition, and always check the alarm log of the tystar furnaces to make sure the process has completed without problems. For gate oxidation with tystar1, always check the N2 CARR alarm in the back panels after TCA clean to ensure proper gas flow. For SiGe deposition with tystar19, the standard layer used for e-beam alignment marks is highly stressed. Thus, the back side SiGe layer needs to be etched away before any high temperature steps — otherwise wafers can crack easily under stress.

4. **Photoresist coating**
   Standard i-line photoresist is pretty straightforward to handle and generally adheres pretty well on wafers. HMDS can often be skipped, unless a wet-etch step is intended. For wet-etching, always hardbake using UV bake instead of conventional baking on a hotplate, as the photoresist becomes much more robust when prepared using UV bake. Applying the e-beam resist MaN 2403 is often difficult due to poor adhesion on to silicon and silicon dioxide. If the wafer is fresh out of a furnace, usually adhesion is not a problem. If the wafer is out of a sink or the resist has to be reworked, bake the wafer on a hotplate at 180° C for *at least* 30 minutes before doing the HMDS step — this is critical for obtaining good MaN 2403 coverage.

5. **Wirebonding**
   Always ground all connecting leads of the bond pads before wirebonding. The order of the bonds should always be first on the bond pads, then on the device pad. This procedure helps reduce issues with electrostatic discharge of the devices. Always use anti-electrostatic foam boxes to carry devices for wirebonding. Check that the bond pad surfaces are clean, and inspect the bonds carefully to ensure the integrity of the bonds. Also avoid bonds that loop too high. When wirebonding on PCB metal lines, it is usually a good idea to scratch away the solder layer first (using a flat-tip tweezer works best) and expose the underlying copper lines. Make sure the copper surface is freshly scratched for good wirebond contacts.

Other general remarks:

1. **Plan ahead**
   Always prepare multiple wafers as backup. *Anything* can go wrong in the cleanroom, and the extra wafers will let you recover lost time as soon as possible. Both lithography masks and the fabrication process should be well thought out, and with sufficient test structures included. Always check with others to review the fabrication process and

lithography masks. Process and device simulations are also helpful for optimizing process and design considerations. Also prepare sufficient dummy wafers for general calibration and test purposes. Always make sure the cleanroom work for each day is well planned. A single mistake made in the cleanroom can result in months of lost work. Most mistakes I've made (admittedly many) occur late at night after long hours of work. Plan cleanroom work carefully and never overdo it (unless there's a deadline!).

2. **Documentation**
   With multiple device wafers and many test wafers, detailed documentation during every single processing step for each wafer is very important. Never be lazy in doing documentation properly.

3. **Inspect, inspect, inspect!**
   This might get tedious, but the importance of inspection cannot be overemphasized. Inspection includes visual (optical microscopes, ellipsometry, SEM, etc.), electrical (probe station, four-point probe) and topological (step heights). Every processing step needs to be properly inspected to ensure a successful fabrication run.

Appendix B

Fabrication process flows

B.1 Micron-scale planer MOSFETs (aFET6)

Table B.1: Detailed fabrication process flow for micron-scale planer MOSFETs (aFET6).

Step	Step details
	FIELD OXIDE (FOX) GROWTH AND ACTIVE DEFINITION
1	Wafer clean (sink6: piranha 10min, 25:1 HF 1min)
2	FOX growth (tystar2: 2wetoxa, 1000°C, 90min, target=5000Å)
3	HMDS (primeoven: process=0)
4	I-line photoresist (svgcoat: coat=1, bake=1)
5	Active region lithography (ksaligner: low vacuum contact)
6	Develop photoresist (svgdev: develop=1, bake=1)
7	Hardbake photoresist (uvbake: process=A)
8	FOX etch (sink7: MOS, 5:1 BHF)
9	Photoresist ashing (matrix: time = 2min 30s)
10	Wafer pre-clean (sink8: piranha 10min, QDR, SRD)
	CHANNEL IMPLANTATION A
11	Wafer clean (sink6: piranha 10min, 25:1 HF 10s)
12	Sacrificial oxide (tystar2: 2dryoxa, 900°C, 15min, anneal 900°C, 1s, target=90Å)
13	HMDS (primeoven: process=0)
14	I-line photoresist (svgcoat: coat=1, bake=1)
15	Channel A implant lithography (ksaligner: low vacuum contact)
16	Develop photoresist (svgdev: develop=1, bake=1)
17	Hardbake photoresist (uvbake: process=A)
18	Channel implantation
19	Photoresist ashing (matrix: time = 2min 30s)

Continued on next page...

Table B.1 – aFET6 process flow continued

Step	Step details
20	Wafer pre-clean (sink8: piranha 10min, QDR, SRD)
	CHANNEL IMPLANTATION B
21	HMDS (primeoven: process=0)
22	I-line photoresist (svgcoat: coat=1, bake=1)
23	Channel B implant lithography (ksaligner: low vacuum contact)
24	Develop photoresist (svgdev: develop=1, bake=1)
25	Hardbake photoresist (uvbake: process=A)
26	Channel implantation
27	Photoresist ashing (matrix: time = 2min 30s)
28	Wafer pre-clean (sink8: piranha 10min, QDR, SRD)
	GATE STACK
29	Sacrificial oxide removal (sink7: 25:1 HF 120s)
30	Wafer clean (sink6: piranha 10min, 25:1 HF 15s)
31	Furnace TCA clean (tystar1: 1TCA, overnight)
32	Gate oxide (tystar1: 1gateoxa, OX: 900°C, 60min, N2: 950°C,20min, target=200Å)
33	Polysilicon deposition (tystar10:10sdplya, time=90min, target=2200Å)
34	HMDS (primeoven: process=0)
35	I-line photoresist (svgcoat: coat=1, bake=1)
36	Gate lithography (ksaligner: low vacuum contact)
37	Develop photoresist (svgdev: develop=1, bake=1)
38	Descum (technics-c: 50W,1min)
39	Hardbake photoresist (uvbake: process=A)
40	Backside poly-Si etch (lam5)
41	Frontside poly-Si etch (lam5)
42	Photoresist ashing (matrix: time = 2min 30s)
43	Wafer pre-clean (sink8: piranha 10min, QDR, SRD)
	SOURCE-DRAIN FORMATION
44	Oxide removal (sink7: 10:1 HF, 2min)
45	Wafer clean (sink6: piranha 10min, 25:1 HF 60s)
46	Polysilicate glass deposition (tystar11: 11sdltoa, 15min, targer=2400Å)
47	Phosphorus diffusion (tystar2: 2n2annala, 900°C, 20min)
	CONTACTS
48	HMDS (primeoven: process=0)
49	I-line photoresist (svgcoat: coat=1, bake=1)
50	Contacts lithography (ksaligner: low vacuum contact)
51	Develop photoresist (svgdev: develop=1, bake=1)

Continued on next page...

Table B.1 – aFET6 process flow continued

Step	Step details
52	Hardbake photoresist (uvbake: process=A)
53	Contact etch (sink7: 10:1 BHF, 3min)
54	Photoresist ashing (matrix: time = 2min 30s)
55	Wafer pre-clean (sink8: piranha 10min, QDR, SRD)
	METALLIZATION
56	Native oxide removal (sink6: piranha, 25:1 HF 10s)
57	Metal 1 (cpa: Al, 4kW, 22.5cm/min, 1pass, 6mTorr, target=3000Å)
58	Metal 2 (cpa: W, 2kW, 40cm/min, 1pass, 9mTorr, target=850Å)
59	HMDS (primeoven: process=0)
60	I-line photoresist (svgcoat: coat=1, bake=1)
61	Metal lithography (ksaligner: low vacuum contact)
62	Develop photoresist (svgdev: develop=1, bake=1)
63	Hardbake photoresist (uvbake: process=A)
64	W etch (lam3: monitor, reactor=10s, air-lock=60s)
65	Al etch (lam3: monitor, reactor=45s, air-lock=60s)
66	Al residue etch (sink7: Al etchant, 30s)
67	Photoresist strip (sink432c: PRS3000, 85°C, 20 min)
68	Wafer pre-clean (sink8: piranha 10min, QDR, SRD)
69	Forming gas anneal (tystar18: H2SINT4A.018, 400°C,20min)
	MICROWAVE SHUNT
70	Metal clean (sink5: SVC-14, 15min, QDR)
71	Dielectric deposition (oxford2: oxide1, 20min)
72	DI rinse (sink8: QDR, SRD)
73	Shunt metal deposition (cpa: Al, 4kW, 40cm/min, 6mT, 1pass)
74	HMDS (primeoven: process=0)
75	I-line photoresist (svgcoat: coat=1, bake=1)
76	Shunt lithography (ksaligner: low vacuum contact)
77	Develop photoresist (svgdev: develop=1, bake=1)
78	Hardbake photoresist (uvbake: process=A)
79	Al etch (sink7: Al etchant, 1min)
80	Photoresist ashing (matrix: time = 2min 30s)
81	HMDS (primeoven: process=0)
82	I-line photoresist (svgcoat: coat=1, bake=1)
83	Shunt contacts lithography (ksaligner: low vacuum contact)
84	Develop photoresist (svgdev: develop=1, bake=1)
85	Hardbake photoresist (uvbake: process=A)

Continued on next page...

Table B.1 – aFET6 process flow continued

Step	Step details
86	Contact etch (sink7: 5:1 BHF, 3.5min)
87	Photoresist ashing (matrix: time = 2min 30s)
	DICING
88	I-line photoresist (svgcoat2: coat=1, bake=1)
89	Hardbake (oven-vwr: 120°C, 5min)
90	Dice (wafersaw: feedrate=3, z=70)
91	Photoresist strip (sink432c: acetone + IPA rinse)

B.2 Micron-scale planer triple-gate MOSFETs (aFET8)

Table B.2: Detailed fabrication process flow for micron-scale planer triple-gate MOSFETs (aFET8).

Step	Step details
	FIELD OXIDE AND ACTIVE DEFINITION
1	Wafer clean (sink6: piranha 10min, 25:1 HF 60s)
2	Field oxide growth (tystar2: 2wetoxa, 1000°C, 60min, target=3300Å)
3	HMDS (primeoven: process=0)
4	I-line photoresist (svgcoat: coat=1, bake=1)
5	Active region lithography (ksaligner: soft contact)
6	Develop photoresist (svgdev: develop=1, bake=1)
7	Hardbake photoresist (uvbake: process=A)
8	Field oxide etch (sink7: 5:1 BHF, total=3.5min)
9	Dehydrate (oven-vwr: 120°C, 10min)
10	Photoresist ashing (matrix: 2min 30sec)
11	Wafer pre-clean (sink8: piranha 10min, QDR, SRD)
	SIDE-GATE STACK
12	RCA clean (sink6: 25:1 HF tank, RCA1 3.5 hr, RCA2 overnight)
13	TCA clean (tystar1: 1TCA, overnight)
14	Wafer clean (sink6: piranha 10min, 25:1 HF 60s)
15	Gate oxide (tystar1: 1gateoxa, OX: 950°C, 28min, N2: 1000°C, 20min, target=200Å)
16	Polysilicon deposition (tystar10: 10sdplya, time=50min, target=1200Å)
17	LTO deposition (tystar11: 11sultoa, 9min, target=1600Å)
18	LTO densification (tystar2: 2n2annl, 900C, 30min)
19	Dehydrate (oven-vwr: 120°C, 10min)
20	HMDS (primeoven: process=0)
21	I-line photoresist (svgcoat: coat=1, bake=1)
22	Side-gate lithography (ksaligner: soft contact)
23	Develop photoresist (svgdev: develop=1, bake=1)
24	Hardbake photoresist (uvbake: process=A)
25	Hard mask etch (sink7: 10:1 BHF, total 3min 30sec)
26	Polysilicon etch (lam5)
27	Dehydrate (oven-vwr: 120°C, 10min)
28	Oxide etch (sink7: 25:1 HF, 60s)
29	Photoresist ashing (matrix: 2min 30sec)
30	Wafer pre-clean (sink8: piranha 10min, QDR, SRD)

Continued on next page...

Table B.2 – aFET8 process flow continued

Step	Step details
	CHANNEL IMPLANT
31	Wafer clean (sink6: piranha 10min, 25:1 HF 60s)
32	Sacrificial oxide (tystar2: 2dryoxa, 900°C, 5min, annl 900°C,1s, target=50Å)
33	Channel implant (As, 50keV, 2E11)
34	Wafer pre-clean (sink8: piranha 10min, QDR, SRD)
	GATE STACK
35	TCA clean (tystar1: 1TCA, overnight)
36	Wafer clean (sink6: piranha 10min, 25:1 HF 80s)
37	Gate oxide (tystar1: 1gateoxa, OX: 950°C, 28min, N2: 1000°C,20min, target=200Å)
38	Polysilicon deposition (tystar10: 10sdplya, time=50min, target=1200Å)
39	LTO deposition (tystar11: 11sultoa, 9min, target=1600Å)
40	HMDS (primeoven: process=0)
41	I-line photoresist (svgcoat: coat=1, bake=1)
42	Gate lithography (ksaligner: soft contact)
43	Develop photoresist (svgdev: develop=1, bake=1)
44	Hardbake photoresist (uvbake: process=A)
45	Hard mask etch (lam5)
46	LTO wet etch (sink7: 10:1 BHF, 80s, target=2200Å)
47	Photoresist ashing (matrix: 2min 30sec)
48	Wafer pre-clean (sink8: piranha 10min, QDR, SRD)
49	Polysilicon etch (lam5)
50	Wafer pre-clean (sink8: piranha 10min, QDR, SRD)
	SOURCE-DRAIN FORMATION
51	Wafer clean (sink6: piranha 10min, 25:1 HF 10s)
52	LTO deposition (tystar11: 11sultoa, 15min, target=2400Å)
53	HMDS (primeoven: process=0)
54	I-line photoresist (svgcoat: coat=1, bake=1)
55	PSG mask lithography (ksaligner: soft contact)
56	Develop photoresist (svgdev: develop=1, bake=1)
57	Hardbake photoresist (uvbake: process=A)
58	LTO etch (sink432c: 10:1 BHF, total=2.5min)
59	Photoresist ashing (matrix: 2min 30sec)
60	Wafer pre-clean (sink8: piranha 10min, QDR, SRD)
61	Wafer clean (sink6: piranha 10min, 25:1 HF 20s)
62	PSG deposition (tystar11: 11sdltoa, 15min, targer=2300Å)
63	PSG diffusion (tystar2: 2n2annala, 900°C, 20min)

Continued on next page...

Table B.2 – aFET8 process flow continued

Step	Step details
	CONTACT ETCH
64	HMDS (primeoven: process=0)
65	I-line photoresist (svgcoat: coat=1, bake=1)
66	Contacts lithography (ksaligner: soft contact)
67	Develop photoresist (svgdev: develop=1, bake=1)
68	Hardbake photoresist (uvbake: process=A)
69	LTO etch (sink432c: 5:1 BHF, total=5.5min)
	BACKSIDE ETCH
70	I-line photoresist (svgcoat: coat=1, bake=1)
71	Hardbake photoresist (uvbake: process=A)
72	Back side poly and LTO etch (lam5)
73	Photoresist ashing (matrix: 2min 30sec)
74	Wafer pre-clean (sink8: piranha 10min, QDR, SRD)
	METALLIZATION
75	Wafer clean (sink6: piranha 10min, 25:1 HF 20s)
76	Aluminum (cpa: Al, 4kW, 22.5cm/min, 1pass, 6mTorr, target=3000Å)
77	Tungsten (cpa: W, 2kW, 40cm/min, 1pass, 9mTorr, target=850Å)
78	HMDS (primeoven: process=0)
79	I-line photoresist (svgcoat: coat=1, bake=1)
80	Metal lithography (ksaligner: soft contact)
81	Develop photoresist (svgdev: develop=1, bake=1)
82	Hardbake photoresist (uvbake: process=A)
83	Metal etch (lam3: MONITOR, reactor total 80s,air-lock=1min)
84	Al etch (sink8: Al etchant, total 90s)
85	Photoresist ashing (matrix: 2min 30sec)
86	Wafer rinse (sink8: QDR, SRD)
87	Photoresist strip (sink432c: PRS3000, 85°C, 60min, DI rinse)
	FORMING GAS
88	Metal clean (sink432c: PRS3000, 85°C, 60min, DI rinse)
89	Forming gas (tystar18: H2SINT4A.018, 400°C,20min)
	MICROWAVE SHUNT
90	Dielectric deposition (oxford2: oxide1, 20min, C1=9, C2=29)
91	Wafer rinse (sink8: QDR, SRD)
92	Shunt metal deposition (CPA: Al, 4kW, 40cm/min, 6mT, 1pass)
93	Dehydrate (Y2 hotplate: 150°C, 5min)
94	HMDS (sink4: hmds 10min)

Continued on next page...

Table B.2 – aFET8 process flow continued

Step	Step details
95	I-line photoresist (svgcoat: coat=1, bake=1)
96	Shunt metal lithography (ksaligner: soft contact)
97	Develop photoresist (svgdev: develop=1, bake=1)
98	Hardbake photoresist (uvbake: process=A)
99	Al etch (sink8: QDR, Al etch=45s, QDR)
100	Photoresist ashing (matrix: 2min 30sec)
101	HMDS (primeoven: process=0)
102	Shunt electric lithography (ksaligner: soft contact)
103	Develop photoresist (svgdev: develop=1, bake=1)
104	Hardbake photoresist (uvbake: process=A)
105	Dielectric etch (sink7: non-mos, 5:1 BHF, total 5.5min)
106	Photoresist strip (sink432c: PRS3000, not heated, 60min)
107	Photoresist ashing (matrix: 2min 30sec)
	DICING
108	I-line photoresist (svgcoat2: coat=1, bake=1)
109	Hardbake (oven-vwr: 120°C, 5min)
110	Dice (wafersaw: feedrate=3, z=70)
111	Photoresist strip (sink432c: acetone + IPA rinse)

B.3 28SOI-finFETs (aFET5)

Table B.3: Detailed fabrication process flow for 28SOI-finFETs (aFET5).

Step	Step details
	WAFER CUT
1	Photoresist coating 8" 28-SOI wafers
2	Wafer laser cut to 4" and edge rounded (American Precision)
3	Photiresist strip and clean (sink432c: PRS3000, sonnication, DI rinse)
4	Wafer pre-clean (sink8: piranha 10min, QDR, SRD)
	CHANNEL IMPLANT
5	Wafer clean (sink6: piranha 10min, 25:1 HF 5min)
6	Sacrificial oxide(tystar2: 2dryoxa, 900°C ,5min, anneal 900°C,1s)
7	Channel implant
8	Wafer pre-clean (sink8: piranha 10min, QDR, SRD)
9	Wafer clean (sink6: piranha 10min, 25:1 HF 1.2min)
10	tystar2 (2dryoxa: 900°C,5min)
	SiGe STACK
11	LTO (tystar11: 11sultoa, 5min, target=1000Å)
12	SiGe deposition (tystar19: NSGDEP.019, 1hr, target=6000Å)
13	LTO (tystar11: 10min, target=2000Å)
	BACK SIDE ETCH
14	HMDS (primeoven: process=0)
15	I-line photoresist (svgcoat: coat=1, bake=1)
16	Hardbake (oven-vwr: 20min)
17	Back side LTO etch (lam2: SIO2MON, adjust CHF_3=20,CF_4=90, total 2min)
18	Back side SiGe etch (lam4: recipe 440 (std, no BT, ME=Cl_2 only), time=1min)
19	Back side LTO etch (lam2: SIO2MON, 30sec)
20	Photoresist ashing (matrix: time = 2min 30s)
21	Wafer pre-clean (sink8: piranha 10min, QDR, SRD)
	ALIGNMENT MARK PATTERNING
22	HMDS (primeoven: process=0)
23	I-line photoresist (svgcoat: coat=1, bake=1)
24	E-beam alignment mask (ksaligner: low vacuum cont)
25	Develop photoresist (svgdev: develop=1, bake=1)
26	Descum (technics-c: 50W, 1min)
27	Hardbake photoresist (uvbake: process=A)
28	LTO etch (lam2: SIO2MON, total = 2min, CHF_3=0, CF_4=90)

Continued on next page...

Table B.3 – aFET5 process flow continued

Step	Step details
29	Photoresist ashing (technics-c: 300W, 7min)
30	Wafer pre-clean (sink8: piranha 10min, QDR, SRD)
31	SiGe etch (lam4: recipe440, total=70sec, no BT, ME: Cl_2=180)
32	Wafer pre-clean (sink8: piranha 10min, QDR, SRD)
	FIN PATTERN AND ETCH
33	E-beam bilayer photoresist coating (AZPN and HSQ)
34	E-beam lithography (Molecular Foundry)
35	HSQ-AZPN cryogenic pattern transfer
36	Hard mask etch (lam5: pocket wafer)
37	Photoresist ashing (matrix: time = 1min 30s)
38	Wafer pre-clean (sink8: piranha 10min, QDR, SRD)
39	FIN etch (lam5)
	GATE STACK
40	Wafer pre-clean (sink8: piranha 10min, QDR, SRD)
41	Wafer clean (sink6: piranha 10min, 25:1 HF 10s)
42	Sacrificial oxide (tystar2: 2dryoxa,900°C, 3min, anneal=1s)
43	Wafer clean (sink6: piranha 10min, 25:1 HF 30s)
44	TCA clean (tystar1: 1TCA, overnight)
45	Gate oxide (tystar1:1gateoxa, OX: 900°C, 20min, N2:950°C, 25min)
46	Polysilicon deposition (tystar10: 10sdplya, 20min, target=500Å)
47	Gate hard mask (tystar11: 11sultoa, 5min, target=1000Å)
48	LTO densification (tystar2: 2n2annla, 900°C, 20min)
49	E-beam photoresist (coat: HMDS + MaN 2403)
50	E-beam lithography (Molecular Foundry)
51	Gate etch (lam5)
52	Etch by-product removal (sink7: 100:1 HF, 30s)
	SOURCE-DRAIN FORMATION
53	Source-drain implantation (As, $2 \times 15/cm^2$, 15keV, 7° tilt)
54	Back side etch (lam5)
55	HF dip (sink432A: 30:1 HF, 10s)
56	Photoresist ashing (technics-c: 300W, 3min)
57	Wafer pre-clean (sink8: piranha 10min, QDR, SRD)
58	Wafer clean (sink6: piranha 10min)
59	Rapd thermal anneal (heatpulse2: N2, 900°C, 10s)
60	Wafer pre-clean (sink8: piranha 10min, QDR, SRD)
	INTERLAYER DIELECTRIC

Continued on next page...

Table B.3 – aFET5 process flow continued

Step	Step details
61	Wafer clean (sink6: piranha 10min)
62	LTO (tystar12: 12sultoa, 5min, target=1000Å)
63	HMDS (primeoven: process=0)
64	I-line photoresist (svgcoat: coat=1, bake=1)
65	Contacts lithography (ksaligner: low vacuum cont)
66	Develop photoresist (svgdev: develop=1, bake=1)
67	Descum (technics-c: 50W, 1min)
68	Hardbake photoresist (uvbake: process=A)
69	Contact etch (sink7: 10:1 BHF, 70s)
70	Photoresist ashing (matrix: 2min 30s)
71	Wafer pre-clean (sink8: piranha 10min, QDR, SRD)
	METALLIZATION
72	Wafer clean (sink6: piranha 10min, 25:1 HF 20s)
73	Metal (cpa, Al, 4kW, 22.5cm/min, 1pass, 6mTorr, target=3000Å)
74	HMDS (primeoven: process=0)
75	I-line photoresist (svgcoat: coat=1, bake=1)
76	Metal lithography (ksaligner: low vac cont)
77	Develop photoresist (svgdev: develop=1, bake=1)
78	Hardbake photoresist (uvbake: process=A)
79	Aluminum etch (sink7: Al etchant, 2min 20s)
80	Photoresist ashing (matrix: 2min 30s)
81	Photoresist cleaning (sink432c: sonicate in acetone 10min, IPA, DI rinse)
82	Photoresist strip (sink432c: PRS3000)
	FORMING GAS ANNEAL
83	Wafer rinse (sink8: QDR, SRD)
84	Forming gas anneal (tystar18: H2SINT4A.018, 400°C,20min)
	SHUNT
85	Wafer clean (sink432c: sonicate acetone, ISP)
86	DI rinse (sink8: QDR, SRD)
87	Nitride deposition (oxford2: nitride2, 1hour, target= 1 μm)
88	I-line photoresist (svgcoat: coat=1, bake=1)
89	Shunt lithography (ksaligner: low vacuum cont)
90	Develop photoresist (svgdev: develop=1, bake=1)
91	Shunt deposition (edwardseb3: Cr=270Å, Pd=3000Å)
92	Lift-off (sink432c: acetone soak, IPA, DI)
	DICING

Continued on next page...

Table B.3 – aFET5 process flow continued

Step	Step details
93	I-line photoresist (svgcoat: coat=1, bake=1)
94	Dice (wafersaw)
95	Photoresist striping (acetone soak + ISP rinse)

B.4 Triple-gate TG-finFETs (aFET9)

Table B.4: Detailed fabrication process flow for Triple-gate TG-finFETs (aFET9).

Step	Step details
	SOI THINNING
1	Wafer clean (sink6: piranha 10min, 25:1 HF 1min)
2	SOI thinning (tystar2: 2wetoxa,850°C,1hr20min, target=950Å ox, 400Å Si consumed)
	SiGe STACK
3	Wafer clean (sink6: piranha 10min, 25:1 HF 12min)
4	LTO (tystar11: 11sultoa, 5min, target=1000Å)
5	SiGe (tystar19:NSGDEP.019, 1hr, target=6000Å)
6	LTO (tystar11: 11sultoa, 2min, target=500Å)
7	I-line photoresist (svgcoat: coat=1, bake=1)
8	Hardbake photoresist (uvbake: process=A)
9	Back-side SiGe etch (lam5)
10	Photoresist ashing (matrix: time = 2min 30s)
11	Wafer pre-clean (sink8: piranha 10min, QDR, SRD)
12	HMDS (svgcoat6: prime=1, coat=9, bake=9)
13	I-line photoresist (svgcoat: coat=1, bake=1)
14	Alignment marks lithography (ksaligner: soft contact)
15	Develop photoresist (svgdev6: develop=3, bake=9)
16	Hardbake photoresist (uvbake: process=A)
17	SiGe etch (lam5)
18	LTO etch (sink7: mos-clean, 10:1 BHF, 40s, QDR)
19	LTO etch (sink7: mos-clean, 25:1 HF, 60s, QDR)
20	Photoresist ashing (matrix: time = 2min 30s)
21	Wafer pre-clean (sink8: piranha 10min, QDR, SRD)
	FIN DEFINITION AND FIN ETCH
22	Dehydration (hotplate: 180°C, 30min)
23	HMDS (svgcoat6: prime=1, coat=9, bake=9)
24	Photoresist coating (spinner1: Ma-N 2403, 3000rpm, 45s)
25	Pre-exposure bake (hotplate: 90°C hotplate, 60s)
26	Fin pattern e-beam lithography (Molecular Foundry)
27	Develop photoresist (TMAH 25%:DI=1:9, 60s, DI rinse)
28	Fin etch (lam5)
29	Polymer removal (sink7: mos-clean, 100:1 HF, 10s)
30	Photoresist ashing (matrix: time = 2min 30s)

Continued on next page...

Table B.4 – aFET9 process flow continued

Step	Step details
31	Wafer pre-clean (sink8: piranha 10min, QDR, SRD)
	SIDE-GATES
32	TCA clean (tystar1: 1TCA)
33	RCA clean (sink6: 25:1 HF, RCA 1 3hr and RCA 2 overnight)
34	Wafer clean (sink6: piranha 10min, 25:1 HF 15s)
35	Gate oxide (tystar1: 1dryoxa, O2: 900°C, 35min, N2: 950°C, 20min, target ox=150Å)
36	Polysilicon deposition (tystar10, 10sdplya, 60min, target=1000Å)
37	LTO deposition (tystar11: 11sultoa, 8min, target=1000Å)
38	Hardmask densification (tystar2: 2n2annla, 850°C, 20min)
39	HMDS (svgcoat6: prime=1, coat=9, bake=9)
40	Photoresist coating (spinner1: Ma-N 2403, 3000rpm, 45s)
41	Pre-exposure bake (hotplate: 90°C hotplate, 60s)
42	Side-gate e-beam lithography (Molecular Foundry)
43	Develop photoresist (TMAH 25%:DI=1:9, 60s, DI rinse)
44	Hardmask etch (centura-mxp)
45	Polymer removal (sink7: mos-clean, 100:1 HF, 10s)
46	Photoresist ashing (matrix: time = 2min 30s)
47	Wafer pre-clean (sink8: piranha 10min, QDR, SRD)
48	Polysilicon etch (lam5)
49	Wafer pre-clean (sink8: piranha 10min, QDR, SRD)
50	Polymer removal (sink7: mos-clean, 100:1 HF, 10s)
	CHANNEL IMPLANT
51	HMDS (svgcoat6: prime=1, coat=9, bake=9)
52	I-line photoresist (svgcoat: coat=1, bake=1)
53	Channel implant lithography (ksaligner: soft contact)
54	Develop photoresist (svgdev6: develop=3, bake=9)
55	Hardbake photoresist (uvbake: process=A)
56	Channel implant
57	HF dip (sink7: mos-clean, 25:1 HF, 40s)
58	Photoresist ashing (matrix: time = 2min 30s)
59	Wafer pre-clean (sink8: piranha 10min, QDR, SRD)
	CENTER GATE STACK
60	TCA clean (tystar1: 1TCA)
61	RCA clean (sink6: 25:1 HF, RCA 1 3hr and RCA 2 overnight)
62	Wafer clean (sink6: piranha 10min, 25:1 HF 15s)
63	Gate oxide (tystar1: 1dryoxa, O2:900°C, 12min, N2: 950°C, 10min, target ox=80)

Continued on next page...

Table B.4 – aFET9 process flow continued

Step	Step details
64	Polysilicon deposition (tystar10, 10sdplya, 60min, target=1000Å)
65	LTO deposition (tystar11: 11sultoa, 8min, target=1000Å)
66	HMDS (svgcoat6: prime=1, coat=9, bake=9)
67	I-line photoresist (svgcoat: coat=1, bake=1)
68	Center gate lithography (ksaligner: soft contact)
69	Develop photoresist (svgdev6: develop=3, bake=9)
70	Hardbake photoresist (uvbake: process=A)
71	Hardmask etch (sink7: mos-clean 10:1 BHF, 60s)
72	Photoresist ashing (matrix: time = 2min 30s)
73	Wafer pre-clean (sink8: piranha 10min, QDR, SRD)
74	Polysilicon etch (lam5)
75	Polymer removal (sink7: mos-clean, 100:1 HF, 10s)
76	Wafer pre-clean (sink8: piranha 10min, QDR, SRD)
	PSG Doping
77	Oxide removal (sink7: 25:1HF, 60s)
78	Wafer clean (sink6: piranha 10min, 25:1 HF 60s)
79	PSG deposition (tystar11: 11sdltoa, 20 min, target=2500)
80	Phosphorus diffusion (tystar2: 2n2annla, 900°C, 20 min)
	CONTACT ETCH
81	HMDS (svgcoat6: prime=1, coat=9, bake=9)
82	I-line photoresist (svgcoat: coat=1, bake=1)
83	Contact lithography (ksaligner: soft contact)
84	Develop photoresist (svgdev6: develop=3, bake=9)
85	Hardbake photoresist (uvbake: process=A)
86	Contact etch (sink7: 10:1 BHF, 3min 15s)
	BACK SIDE CLEAN
87	HMDS (svgcoat6: prime=1, coat=9, bake=9)
88	I-line photoresist (svgcoat: coat=1, bake=1)
89	Back side clean (sink432c: acetone, IPA wipe)
90	Back side poly etch (lam5)
91	Photoresist ashing (matrix: time = 2min 30s)
92	Wafer pre-clean (sink8: piranha 10min, QDR, SRD)
	METALLIZATION
93	Wafer clean (sink6: piranha 10min, 25:1 HF 20s)
94	Metallization (novellus: Ti)
95	Metallization (cpa: Al 3000Å)

Continued on next page...

Table B.4 – aFET9 process flow continued

Step	Step details
96	HMDS (svgcoat6: prime=1, coat=9, bake=9)
97	I-line photoresist (svgcoat: coat=1, bake=1)
98	Metal lithography (ksaligner: soft contact)
99	Develop photoresist (svgdev6: develop=3, bake=9)
100	Hardbake photoresist (uvbake: process=A)
101	Metal etch (lam3)
102	Post-metal clean (sonication, sink 8 QDR)
103	Forming gas (tystar18: H2N2SINT4A, 20min)
	SHUNT
104	Rinse clean (sink8: qdr, srd)
105	Shunt dielectric (oxford2: oxide1, 20minute, target=1 μm)
106	Rinse clean (sink8, qdr, srd)
107	Al deposition (CPA: Al2%Si, 4kW, 40cm/min, 6mT, 1 pass, target = 1000Å)
108	HMDS (svgcoat6: prime=1, coat=9, bake=9)
109	I-line photoresist (svgcoat: coat=1, bake=1)
110	Shunt lithography (ksaligner: soft contact)
111	Develop photoresist (svgdev6: develop=3, bake=9)
112	Hardbake photoresist (uvbake: process=A)
113	Al etch (sink8: Al etchant, 1minute)
114	Photoresist ashing (matrix: time = 2min 30s)
115	HMDS (svgcoat6: prime=1, coat=9, bake=9)
116	I-line photoresist (svgcoat: coat=1, bake=1)
117	Shunt contact lithography (ksaligner: soft contact)
118	Develop photoresist (svgdev6: develop=3, bake=9)
119	Hardbake photoresist (uvbake: process=A)
120	Dielectric etch (lam2: SIO2MON, total=180s)
	DICING
121	HMDS (svgcoat6: prime=1, coat=9, bake=9)
122	I-line photoresist (svgcoat: coat=1, bake=1)
123	Hardbake (oven-vwr: 5min)
124	Dice (wafersaw: feedrate=2, z=70 μm)
125	Photoresist striping (acetone soak + IPA rinse)

Appendix C

Sample preparation for W-band EDMR measurements

The samples for W-band EDMR measurements require special attention due to the small sample volume allowed in the resonant microwave cavity. Below is the procedure used for retrofitting aFET6 and aFET8 X-band samples for W-band measurements. There are three main steps: (i) removal of X-band microwave shunt layers to expose underlying metallic lines (for wirebonding), and (ii) dicing the X-band samples to smaller dimensions and (iii) substrate thinning for fitting into the W-band cavity. aFET9 wafers have specially designed W-band-compatible samples in the layout, and hence only substrate thinning is needed.

Microwave shunt removal

1. *I-V* test to identify good devices.

2. Microwave shunt metal aluminum etch: apply photoresist with cue-tip to center $\approx 0.5 - 1$ cm region of X-band chips. Bake the resist at 95° C for 10 minutes on a hot plate. Rinse the chips with sink7 DI hose, dip in Al etchant for ≈ 40 s (until aluminum is gone), re-rinse. Aceton and IPA clean.

3. Oxide (shunt dielectric) etch: Pre-bake the sample to dehydrate at 125° C for 15 minutes on a hotplate. Apply photoresist with cue-tip to lower 1 cm region of chips. Bake at 95° C for 10 minutes on a hot plate. Do not use any higher temperature or add additional photoresist mid-way! Hardened resist tends to crack and will peel off in HF. Newly added PR will bubble. Use cue-tip to make sure resist cover all edges completely — otherwise HF will creep in. Etch in 5:1 BHF for approximately 3.5 minutes (will see underlying W turn pale. Etches 1 μm oxford2 oxide and 500nm wet oxide. DI rinse, acetone and IPA clean.

4. *I-V* test to check devices have survived the multiple etch steps.

Dicing

1. Apply photoresist to lower 1.5 cm of chip using cue-tip (avoid having the resist layer too thick, which would make alignment in wafersaw difficult), spread out resist to as thin as possible.

2. Wafersaw: Use feed rate=3. At most can do 6 chips in one run. Dice chips to 15 mm in length, and then as narrow as possible (close to outer metal lines). Acetone soak + IPA rinse.

Substrate thinning

1. Sample mounting: use 6 substrate with very thick oxide (> 500 nm). Use droppler from i-line resist to draw a line, filled with photoresist. Draw different lines for different chips to avoid chips drifting in a large pool. Place chips face down into photoresist line, resist should creep up to edge of surface. Bake on hot plate at 95°C on hot plate for 30 minutes. Do not user higher temperature; otherwise resist will bubble.

2. Substrate thinning: STS with receipt HEXA250. aFET6/8: starting substrate $\approx$ 520 μm. Do 1 hour STS only; otherwise chips get too thin and breaks easily. aFET9: starting substrate ≈ 640 μm. Do 1 hour 40 minutes etch in STS, thickness reduces to ≈ 330 μm.

3. Sample removal: scrub away residual side walls while the chips are still mounted on handle wafer! Submerge wafer in acetone. Remove chips, IPA rinse.

4. *I-V* test.

After the EDMR chips are prepared, they have to be carefully mounted on specially designed PCB pieces which fit inside the W-band EDMR probe. This assembly is shown in Fig. C.1. An additional PCB support piece is used to attach the EDMR chip to the main PCB board. All PCB material are approximately 100 μm thick. Both GE varnish and Dow Cyclotene were tested as the adhesive for mounting the EDMR chips, and it was found that Cyclotene survives thermal cycles much better than varnish when cured properly. Aluminum wirebonds were used in all instances and were found to be reliable against repeated thermal cycles.

Figure C.1: Mounted W-band EDMR sample. (a) Wirebonded EDMR chip on PCB support piece. (b) Sample inserted into extractable W-band probe tip.

Appendix D

EPR/EDMR at BIERLab

D.1 Cryogenic EDMR experiments with Bruker ESP300E

The Bruker ESP300E with Oxford ESR900 cryostat was designed for small-volume sample EPR measurements. The modification for reliable low temperature EDMR measurements requires special attention as only ≈ 10 cm separates the (cold) sample and ambient temperature along the EPR sample tube. Hence, the addition of electrical leads in the sample tube for EDMR measurements makes efficient cooling of the sample difficult. We discovered this problem since the MOSFET substrate did not freeze out even when the thermal couple reads liquid helium temperature, indicating the sample temperature was significantly higher. Three strategies were used to circumvent this problem:

1. Use of low-thermal conductivity stainless steel co-axial cables for electrical contacts (Lakeshore Cryogenics CC-SS).

2. Exposing the EDMR samples directly to helium flow by mounting the device extending out of the conventional EPR quartz tube.

3. The addition of a second (outer) quartz tube which forces helium flow to return at a higher position so that even the PCB pieces are efficiently cooled.

The working design is shown schematically in Fig. D.1. The actual sample insert including a mounted EDMR chip is shown in Fig. D.2. With the modified thermal isolation of the insert assembly, base temperature can easily be reached at the sample position. The EDMR MOSFET devices can also be used as a sensitive temperature probe to check the thermal stability of the modified insert space. Fig. D.3 shows the measured I-V characteristics of a device with its position inside the cavity varied. The 0 mm position corresponds to extending the device all the way down until it reaches the position of the thermal couple. The measurements show that good thermal stability is achieved over the entire resonator space with this modified sample insert as the I-V characteristics look practically identical.

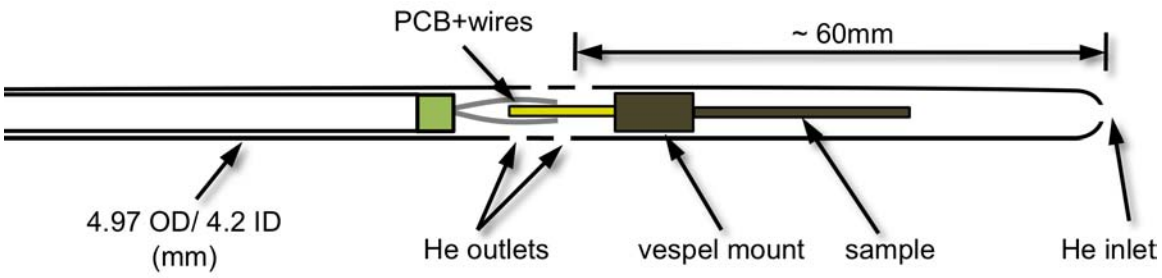

Figure D.1: Sample insert design for Bruker ESP300E for cryogenic EDMR measurements. The outer quartz tube forces cold helium gas to flow higher up along the sample.

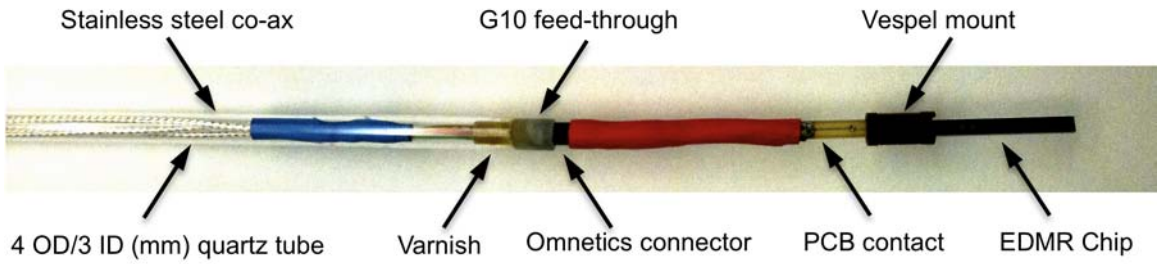

Figure D.2: Modified sample mount for Bruker ESP300E for cryogenic EDMR measurements.

D.2 Bruker ESP300E EPR/EDMR measurement procedure

D.2.1 Oxford ESR900 cryostat cool-down procedure

1. If the cryostat has not been used for a prolonged period of time (weeks), first purge the cryostat by flowing warm Helium gas for about an hour, also make sure the transfer line outer jacket has good vacuum (low 10^{-2} bar).

2. Refill liquid nitrogen to the reference junction of the thermocouple, turn on the Oxford temperature controller.

3. Open the needle valve on the transfer line by 3 turns, insert it into the liquid helium dewar slowly. Once helium gas begins to flow out of the transfer line nozzle, insert the nozzle into the cryostat helium input port. Turn the connecting nut by a few turns (it

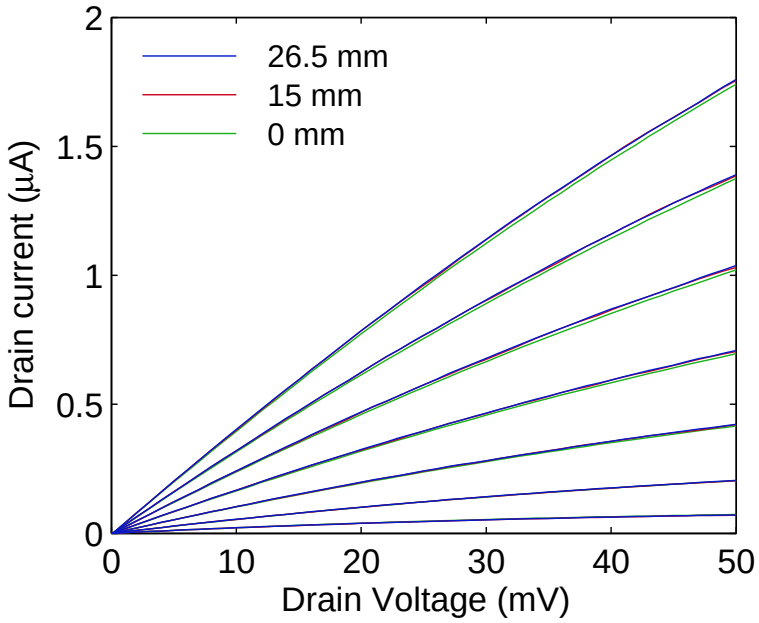

Figure D.3: MOSFET *I-V* characteristics versus sample position in the Oxford ESR900 cryostat.

should not be turned tight at this point), and make sure that the transfer nozzle can still wiggle a bit.

4. Connect the return line of the transfer line to the helium flow meter, set the helium flow to maximum by turning the knob counter clockwise. Turn on the diaphragm pump to begin pumping on the return line. The pressure will soon drop to approximately 200 mbar. Let it pump for a few more minutes, then the flow meter should begin to vibrate. After another few minutes, helium should begin to flow. Tighten the nut connecting the transfer line to the cryostat until secure.

5. If the transfer line is already connected to the cryostat (e.g. left connected from previous measurements), turn on the diaphragm pump, loosen the cryostat-transfer line connection nut until only a few turns are left, pull the transfer line slightly out and let it pump for ≈ 15 minutes. Then open the needle valve to 3 turns open, after a few minutes the helium flow meter should begin to vibrate, after another few minutes helium should begin to flow and the flow meter will reach greater than 1.5L/hr. At that point tighten the cryostat-transfer line connection nut.

6. The temperature should begin to drop and should read approximately $3.4 - 3.7$ K in about 15 to 20 minutes — wait an additional 15 minutes so that everything is stabilized.

7. Close the needle valve of the transfer line to about 0.5 turns, check that the temperature has not increased dramatically while doing so. Then reduce the helium flow to the pump first to 2 L/hr, gradually go down in 0.5 L/hr steps until reaching a steady flow of 0.5L/hr. Wait for half a minute or so between each adjustment to make sure the temperature is stable.

8. At this setting (0.5 turn open on the needle valve and 0.5L/Hr helium flow), the temperature should be stable at about $4.5 - 5$ K. A 60 L liquid helium dewar would last for about 30 hours of total service time.

D.2.2 Setting up for EDMR measurements

1. Check device *I-V* characteristics with parameter analyzer.

2. Bias up the device with the battery boxes.

3. Tune the microwave cavity in regular EPR mode.

4. Carry out regular EPR to find center of resonance line.

5. Under the desired conditions for EDMR (e.g. microwave power, modulation amplitude, *etc.*), check that the device signal is within the tolerance of the spectrometer lock-in ($\pm$1V).

6. Tune the microwave power down to 40 dB (microwave bridge output voltage can be pretty high when the microwave power is high).

7. Toggle EPR/EDMR switch box to EDMR position.

8. Set to desired microwave power and set all other measurement parameters.

9. Run EDMR measurement!

D.2.3 Shut-down procedure

1. **Microwave bridge**
   Set the microwave power to 40 dB, then send to *Standby* mode.

2. **Magnetic field**
   Using the field controller local control, set the sweep width to 0 G and center field to 100 G (LOC - 0 - SW - 100 -CF). Then turn the magnetic field coil power supply off.

3. **Cryostat warm-up**
   Close the needle valve of the transfer line completely. If a new dewar is needed for the next day, take the transfer line out to warm up and dry overnight.

D.2.4 File transfer

1. Ensure that the PC is connected to Bruker ESP300E: COM1 serial port to *t1*, COM2 serial port to terminal.
2. Open HyperTerminals *Bruker_Transfer* and *Bruker_TERM* on the PC.
3. In the *Bruker_Transfer* terminal, select *transfer*, then *Receive File*. Select destination folder and the transfer protocol should be *kermit*.
4. In the *Bruker_TERM* terminal, hit *return*, and a prompt symbol *$* should appear. Type in order:
   - deiniz t1
   - xmode /t1 nopause baud=9600 cs=8 stop=1 par=none
   - iniz t1
5. In the *Bruker_TERM* terminal, go into the directory where the files are saved (*chd* command), then type:
   - kermit s8il /t1 filename.ext

   to initiate file transfer.
6. The spectrum files **.spc* are binary files (4-byte signed integers), use the *MatLab* script *sca2ascii* to convert them to ascii files. Note that the parameter files **.par* must also be present in the same directory to establish values for the field axis.

D.3 EDMR signal optimization

The following are a few rules of thumbs for optimizing the cw-EDMR signals:

1. **Modulation frequency (f_{mod})**
   The modulation frequency should be chosen such that it is much slower than any transient effect expected from the device. On the other hand, a higher frequency in principle will give lower noise measurements due to the decrease of $1/f$ noise of the device. The RC delay of the sample probe and the device, with a cut-off frequency typically in the $5 - 10$ kHz range, poses an upper bound on the highest modulation frequency that can be used. The Bruker ESP300E has a set of fixed allowable modulation frequencies; in general, the lowest frequency option of 1.56 kHz is used. For the newer Elexsys systems, any frequency from $0.5 - 100$ kHz can be used. We generally use around 1 kHz.

It is imperative to avoid choosing a modulation frequency that is an exact higher harmonic of the main power line (60 Hz in the U.S., 50 Hz in Europe). Main power pick-up noise can be further minimized by choosing a modulation frequency and conversion time such that

$$f_{mod} \times \tau_{conversion} = integer \tag{D.1}$$

The reason is that it is desired to have the signal sampled at the exact same point in the main power phase cycle in order to minimize extra noise from the main lines. A spectrum analyzer becomes handy when deciding which frequency to attempt the measurements at.

2. **Modulation phase (θ_{mod})**
   Due to RC delays in the measurement set-up, the phase of the measurements needs to be optimized in order to ensure that the recorded EDMR amplitude is not artificially attenuated due to incorrect phase settings, as

$$V_{out}^{recorded} = V_{out} \cos(\theta_{sig} - \theta_{ref}) \tag{D.2}$$

   When two measurements are made with amplitudes y_1 at $\theta_{sig} = 0°$ and y_2 at $\theta_{sig} = 90°$, the optimal phase is simply:

$$\theta_{opt} = \arctan\left(\frac{y_2}{y_1}\right) \times \frac{180°}{\pi} \tag{D.3}$$

   Note that the signs of y_2 and y_1 need to be taken into account as well. A check can be performed by recording the data at $\theta_{opt} + 90°$, where there should be *no* EDMR signal at all.

3. **Modulation amplitude (A_{mod})**
   The optimal modulation amplitude is one that closely matches the signal linewidth. A larger modulation amplitude results in over-modulated lineshapes (smaller signal amplitudes, and non-derivative lineshapes), and a smaller modulation amplitude leads to a smaller signal as

$$y_{pp} \propto A_{mod} \tag{D.4}$$

4. **Magnetic field step (δB)**
   To ensure sufficient sampling steps, the magnetic field step should be chosen to be at least smaller than 1/10 of the measured linewidth.

5. **Microwave power ($P_{\mu w}$)**
   The choice of microwave power depends on what quantity is desired. To obtain intrinsic linewidths, the smallest possible microwave power where the signal is still observable should be used. For general EDMR experiments, the signal intensities saturate at

higher microwave power, hence the maximum microwave power available should be used. However, rectification issues should always be checked when adjusting the microwave power.

Appendix E

List of publications

1. **Suppression of microwave rectification effects in electrically detected magnetic resonance measurements**
   C.C. Lo, A.M. Tyryshkin, F. Bradbury, C.D. Weis, J. Bokor, T. Schenkel, and S.A. Lyon
   In preparation (2011)

2. **Electrically detected magnetic resonance of neutral donors interacting with a two-dimensional electron gas**
   C.C. Lo, V. Lang, J. Bokor, R.E. George, J.J.L. Morton, A.M. Tyryshkin, S.A. Lyon and T. Schenkel
   Accepted by Physical Review Letters, available at http://arxiv.org/abs/1012.3811 (2011)

3. **Electrically detected magnetic resonance in a W-band microwave cavity**
   V. Lang, **C.C. Lo**, R.E. George, S.A. Lyon, J. Bokor, T. Schenkel, A. Ardaven and J.J.L. Morton
   Review of Scientific Instruments, **82**(3), 034794 (2011)

4. **Device fabrication and transport measurements of FinFETs built with ^{28}Si SOI wafers towards donor qubits in silicon**
   C.C. Lo, A. Persaud, S. Dhuey, D. Olynick, F. Borondics, M. C. Martin, H. A. Bechtel, J. Bokor and T. Schenkel
   Semiconductor Science and Technology **24**, 105022 (2009)

5. **Spin-dependent scattering in a silicon transistor**
   R. de Sousa, **C.C. Lo** and J. Bokor
   Physical Review B, **80**(4), 045320 (2009)

6. **Critical issues in the formation of quantum computer test structures by ion implantation**

T. Schenkel, **C.C. Lo**, C. D. Weis, A. Schuh, A. Persaud and J. Bokor
Nuclear Instruments and Methods in Physics Research Section B **267**(8-9), 2563 (2009)

7. **Mapping of ion beam induced current changes in FinFETs**
C. D. Weis, A. Schuh, A. Batra, A. Persaud, I. W. Rangelow, J. Bokor, **C.C. Lo**, S. Cabrini, D. Olynick, S. Duhey and T. Schenkel
Nuclear Instruments and Methods in Physics Research Section B (IBMM 2008 conference proceedings) **267**(8-9), 1222 (2009)

8. **Single atom doping for quantum device development in diamond and silicon**
C.D Weis, A. Schuh, A. Batra, A. Persaud, I.W. Rangelow, J. Bokor, **C.C. Lo**, S. Cabrini, E. Sideras-Haddad, G.D. Fuchs, R. Hanson, D.D. Awschalom and T. Schenkel
Journal of Vacuum Science and Technology B, **26**(6), 2596 (2008)
Featured in *Virtual Journal of Quantum Information*, **8**(12) and *Virtual Journal of Nanoscale Science & Technology*, **18**(24)

9. **Detection of low energy single ion impacts in micron scale transistors at room temperature**
A. Batra, C.D. Weis, J. Reijonen, A. Persaud, T. Schenkel, S. Cabrini, **C.C. Lo** and J. Bokor
Applied Physics Letters, **91**(19), 193502 (2008)

10. **Spin-dependent scattering off neutral antimony donors in ^{28}Si field-effect transistors**
C.C. Lo, J. Bokor, T. Schenkel, J. He, A.M. Tyrhsykin and S.A. Lyon
Applied Physics Letters, **91** (24), 242106 (2007)
Featured in *Virtual Journal of Quantum Information*, **7**(12) and *Virtual Journal of Nanoscale Science & Technology*, **16**(26)

11. **Strategies for integration of donor electron spin qubits in silicon**
T. Schenkel, J.A. Liddle, J. Bokor, A. Persaud, S.J. Park, J. Shangkuan, **C.C. Lo**, S. Kwon, S.A. Lyon, A.M. Tyryshkin, I.W. Rangelow, Y. Sarov, D.H. Schneider, J. Ager and R. de Sousa
Microelectronics Engineering, **83**(4-9), 1814 (2006)

Bibliography

[1] International Technology Roadmap for Semiconductors. *http://www.itrs.net*, 2009.

[2] S. A. Wolf, D. D. Awschalom, R. A. Buhrman, J. M. Daughton, S. von Molnar, M. L. Roukes, A. Y. Chtchelkanova, and D. M. Treger. Spintronics: A spin-based electronics vision for the future. *Science*, 294:1488, 2001.

[3] D. Loss and D. P. DiVincenzo. Quantum computation with quantum dots. *Physical Review A*, 57(1):120, 1998.

[4] S. Bandyopadhyay, B. Das, and A. E. Miller. Superconducting with spin-polarized single electrons in a quantum coupled architecture. *Nanotechnology*, 5:113, 1994.

[5] R. P. Cowburn and M. E. Welland. Room temperature magnetic quantum cellular automata. *Science*, 287:1466, 2000.

[6] P. Sharma. How to create a spin current. *Science*, 307:531, 2005.

[7] S. Datta and B. Das. Electronic analog of the electro-optic modulator. *Applied Physics Letters*, 56(7):665, 1990.

[8] S. Bandyopadhyay and M. Cahay. Reexamination of some spintronic field-effect device concepts. *Applied Physics Letters*, 85(8):1433, 2004.

[9] K. C. Hall and M. E. Flatté. Performance of a spin-based insulated gate field effect transistor. *Applied Physics Letters*, 88:162503, 2006.

[10] S. Bandyopadhyay and M. Cahay. Electron spin for classical information processing: a brief survey of spin-based logic devices, gates and circuits. *Nanotechnology*, 20:412001, 2009.

[11] G. Schmidt, D. Ferrand, L. W. Molenkamp, A. T. Filip, and B. J. van Wees. Fundamental obstacle for electrical spin injection from a ferromagnetic metal into a diffusive semiconductor. *Physical Review B*, 62(8):R4790, 2000.

[12] G. Schmidt and L. W. Molenkamp. Spin injection into semiconductors, physics and experiments. *Semiconductor Science and Technology*, 17:310, 2002.

[13] G. Schmidt. Concepts for spin injection into semiconductors — a review. *Journal of Physics D: Applied Physics*, 38:R107, 2005.

[14] M. A. Nielsen and I. L. Chuang. *Quantum computation and quantum information*. Cambridge University Press, Cambridge, United Kingdom, 2000.

[15] G. Benenti, G. Casati, and G. Strini. *Principles of Quantum Computation and Information*. World Scientific, Singapore, 2004.

[16] R. P. Feynman. Simulating physics with computers. *International Journal of Theoretical Physics*, 21:467, 1982.

[17] P. Shor. Algorithms for quantum computation: discrete logarithms and factoring. *Proceedings, 35^{th} annual symposium on foundations of computer science*, 1994.

[18] D. P. DiVincenzo. The physical implementation of quantum computation. *arXiv:quant-ph/0002077v3*, 2000.

[19] B. Kane. A silicon-based nuclear spin quantum computer. *Nature*, 393:133, 1998.

[20] A. J. Skinner, M. E. Davenport, and B. E. Kane. Hydrogenic spin quantum computing in silicon: a digital approach. *Physical Review Letters*, 90(8), 2003.

[21] T. Shinada, Y. Kumura, J. Okabe, T. Matsukawa, and I. Ohdomari. Current status of single ion implantation. *Journal of Vacuum Science & Technology B: Microelectronics and Nanometer Structures*, 16:2489, 1998.

[22] T. Schenkel, A. Persaud, S. J. Park, J. Meijer, J. R. Kingsley, J. W. McDonald, J. P. Holder, J. Bokor, and D. H. Schneider. Single ion implantation for solid state quantum computer development. *Journal of Vacuum Science and Technology B*, 20(6):2819, 2002.

[23] T. Schenkel, A. Persaud, S. J. Park, J. Nilsson, J. Bokor, J. A. Liddle, R. Keller, D. H. Schneider, D. W. Cheng, and D. E. Humphries. Solid state quantum computer development in silicon with single ion implantation. *Journal of Applied Physics*, 94(11):7017, 2003.

[24] T. Schenkel, J. A. Liddle, A. Persaud, A. M. Tyryshkin, S. A. Lyon, R. de Sousa, K. B. Whaley, J. Bokor, J. Shangkuan, and I. Chakarov. Electrical activation and electron spin coherence of ultralow dose antimony implants in silicon. *Applied Physics Letters*, 88(11):112101, 2006.

[25] T. Hopf, D. N. Jamieson, S. M. Hearne, C. Yang, C. I. Pakes, A. S. Dzurak, E. Gauja, and R. G. Clark. Ion beam induced charge and numerical modeling study of novel detector devices for single ion implantation. *Nuclear Instruments and Methods in Physics Research B*, 231:463, 2005.

[26] D. N. Jamieson, C. Yang, T. Hopf, S. M. Hearne, C. I. Pakes, S. Prawer, M. Mitic, E. Gauja, S. E. Andresen, F. E. Hudson, A. S. Dzurak, and R. G. Clark. Controlled shallow single-ion implantation in silicon using an active substrate for sub-20-keV ions. *Applied Physics Letters*, 86(20):202101, 2005.

[27] D. N. Jamieson, V. Chan, F. E. Hudson, Se. E. Andresen, C. Yang, T. Hopf, S. M. Hearne, C. I. Pakes, S. Prawer, E. Gauja, A. S. Dzurak, and R. G. Clark. Quantum effects in ion implanted devices. *Nuclear Instruments and Methods in Physics Research B*, 249:221, 2006.

[28] J. A. Seamons, E. Bielejec, M. S. Carroll, and K. D. Childs. Room temperature single ion detection with geiger mode avalanche diode detectors. *Applied Physics Letters*, 93(4):043124, 2008.

[29] E. Bielejec, J. A. Seamons, and M. S. Carroll. Single ion implantation for single donor devices using geiger mode detectors. *Nanotechnology*, 21:085201, 2010.

[30] A. Batra, C. D. Weis, J. Reijonen, A. Persaud, T. Schenkel, S. Cabrini, C. C. Lo, and J. Bokor. Detection of low energy single ion impacts in micron scale transistors at room temperature. *Applied Physics Letters*, 91(19):193502, 2007.

[31] T. Shinada, T. Kurosawa, H. Nakayama, Y. Zhu, M. Hori, and I. Ohdomari. A reliable method for the counting and control of single ions for single-dopant controlled devices. *Nanotechnology*, 19(34):345202, 2008.

[32] T. Schenkel, C. C. Lo, C. D. Weis, A. Schuh, A. Persaud, and J. Bokor. Critical issues in the formation of quantum computer test structures by ion implantation. *Nuclear Instruments and Methods in Physics Research B*, 267:2563, 2009.

[33] B. C. Johnson, G. C. Tettamanzi, A. D. C. Alves, S. Thompson, C. Yang, J. Verduijn, J. A. Mol, R. Wacquez, M. Vinet, M. Sanquer, S. Rogge, and D. N. Jamieson. Drain current modulation in a nanoscale field-effect-transistor channel by single dopant implantation. *Appled Physics Letters*, 96(26):264102, 2010.

[34] T. M. Buehler, V. Chan, A. J. ferguson, A. S. Dzurak, F. E. Hudson, D. J. Reilly, A. R. Hamilton, and R. G. Clark. Controlled single electron transfer between Si:P dots. *Appled Physics Letters*, 88(19):192101, 2006.

[35] V. C. Chan, T. M. Buehler, A. J. Ferguson, D. R. McCamey, D. J. Reilly, A. S. Dzurak, and R. G. Clark. Ion implanted Si:P double dot with gate tunable interdot coupling. *Journal of Applied Science*, 100:106104, 2006.

[36] F. E. Hudson, A. J. Ferguson, C. C. Escott, C. Yang, D. N. Jamieson, R. G. Clark, and A. S. Dzurak. Gate-controlled charge transfer in Si:P double quantum dots. *Nanotechnology*, 19:195402, 2008.

[37] K. Y. Tan, K. W. Chan, M. Möttönen, A. Morello, C. Yang, J. van Donkelaar, A. Alves, J.-M. Pirkkalainen, D. N. Jamieson, R. G. Clark, and A. S. Dzurak. Transport spectroscopy of single phosphorus donors in a silicon nanoscale transistor. *Nano Letters*, 10:11, 2010.

[38] A. Persaud, F. I. Allen, F. Gicquel, S. J. Park, J. A. Liddle, T. Schenkel, T. Ivanov, K. Ivanova, I. W. Rangelow, and J. Bokor. Single ion implantation with scanning probe alignment. *Journal of Vacuum Science and Technology B*, 22(6):2992, 2004.

[39] A. Persaud, K. Ivanova, Y. Sarov, T. Ivanov, B. E. Volland, I. W. Rangelow, N. Nikolov, T. Schenkel, V. Djakov, D. W. K. Jenkins, J. Meijer, and T. Vogel. Micromachined piezoresistive proximal probe with integrated bimorph actuator for aligned single ion implantation. *Journal of Vacuum Science and Technology B*, 24(6):3148, 2006.

[40] T.-C. Shen, J. Y. Ji, M. A. Zudov, R. R. Du, J. S. Kline, and J. R. Tucker. Ultradense phosphorous delta layers grown into silicon from PH molecular precursors. *Applied Physics Letters*, 80:1580, 2002.

[41] T.-C. Shen, J. S. Kline, T. Schenkel, S. J. Robinson, J.-Y Ji, C. Yang, R.-R. Du, and J. R. Tucker. Nanoscale electronics based on two-dimensional dopant patterns in silicon. *Journal of Vacuum Science and Technology B*, 22(6):3182, 2004.

[42] S. R. Schofield, N. J. Curson, M. Y. Simmons, F. J. Rueß, T. Hallam, L. Oberbeck, and R. G. Clark. Atomically precise placement of single dopants in Si. *Physical Review Letters*, 91(13):136104, 2003.

[43] M. Y. Simmons, F. J. Ruess, K. E. J. Goh, T. Hallam, S. R. Schofield, L. Oberbeck, N. J. Curson, A. R. Hamilton, M. J. Butcher, R. G. Clark, and T. C. G. Reusch. Scanning probe microscopy for silicon device fabrication. *Molecular Simulation*, 31(6-7):505, 2005.

[44] A. Fuhrer, M. Füchsle, T. C. G. Reusch, B. Weber, and M. Y. Simmons. Atomic-scale, all epitaxial in-plane gated donor quantum dot in silicon. *Nano Letters*, 9(2):707, 2009.

[45] F. R. Bradbury, A. M. Tyryshkin, G. Sabouret, J. Bokor, T. Schenkel, and S. A. Lyon. Stark tuning of donor electron spins in silicon. *Physical Review Letters*, 97(17):176404, 2006.

[46] G. P. Lansbergen, R. Rahman, C. J. Wellard, I. Woo, J. Caro, N. Collaert, S. Biesemans, G. Klimeck, L. C. L. Hollenberg, and S. Rogge. Gate-induced quantum-confinement transition of a single dopant atom in a silicon FinFET. *Nature Physics*, 4:656, 2008.

[47] R. Rahman, G. P. Lansbergen, S. H. Park, J. Verduijin, G. Klimeck, S. Rogge, and L. C. L. Hollenberg. Orbital stark effect and quantum confinement transition of donors in silicon. *Physical Review B*, 80(16):165314, 2009.

[48] H. Huebl, A. R. Stegner, M. Stutzmann, M. S. Brandt, G. Vogg, F. Bensch, E. Rauls, and U. Gerstmann. Phosphorus donors in highly strained silicon. *Physical Review Letters*, 97(16):166402, 2006.

[49] L. Dreher, T. A. Hilker, A. Brandlmaier, S. T. B. Goennenwein, H. Huebl, M. Stutzmann, and M. S. Brandt. Electrostatic hyperfine tuning of phosphorus donors in silicon. *Physical Review Letters*, 106(3):037601, 2011.

[50] W. Kohn. *Shallow impurity states in silicon and germanium.* Solid State Physics. Academic Press, New York, 1957.

[51] B. Koiller, R. B. Capaz, X. Hu, and S. D. Sarma. Shallow-donor wave functions and donor-pair exchange in silicon: *Ab initio* theory and floating-phase heitler-london approach. *Physical Review B*, 70(11):115207, 2004.

[52] R. de Sousa. Dangling-bond spin relaxation and magnetic 1/f noise from the amorphous-semiconductor/oxide interface: Theory. *Physical Review B*, 76(24):245306, 2007.

[53] A. D. Greentree, J. H. Cole, A. R. Hamilton, and L. C. L. Hollenberg. Coherent electronic transfer in quantum dot systems using adiabatic passage. *Physical Review B*, 70(23):235317, 2004.

[54] L. C. L. Hollenberg, C. J. Wellard, C. I. Pakes, and A. G. Fowler. Single-spin readout for buried dopant semiconductor qubits. *Physical Review B*, 69(4):233301, 2004.

[55] A. D. Greentree, A. R. Hamilton, L. C. L. Hollenberg, and R. G. Clark. Electrical readout of a spin qubit without double occupancy. *Physical Review B*, 71(11):113310, 2005.

[56] A. R. Stegner, C. Boehme, H. Huebl, M. Stutzmann, K. Lips, and M. S. Brandt. Electrical detection of coherent ^{31}P spin quantum states. *Nature Physics*, 2:835, 2006.

[57] M. Sarovar, K. C. Young, T. Schenkel, and K. B. Whaley. Quantum nondemolition measurements of single donor spins in semiconductors. *Physical Review B*, 78(24):245302, 2008.

[58] A. Morello, C. C. Escott, H. Huebl, L. H. Willems van Beveren, L. C. L. Hollenberg, D. N. Jamieson, A. S. Dzurak, and R. G. Clark. Architecture for high-sensitivity single-shot readout and control of the electron spin of individual donors in silicon. *Physical Review B*, 80(8):081307(R), 2009.

[59] A. Morello, J. J. Pla, F. A. Zwanenburg, K. W. Chan, K. Y. Tan, H. Huebl, M. Möttönen, C. D. Nugroho, C. Yang, J. A. van Donkelaar, A. D. C. Alves, D. N. Jamieson, C. C. Escott, L. C. L. Hollenberg, R. G. Clark, and A. S. Dzurak. Single-shot readout of an electron spin in silicon. *Nature*, 467:687, 2010.

[60] D. R. McCamey, J. van Tol, G. Morley, and C. Boehme. Electronic spin storage in an electrically readable nuclear spin memory with a lifetime >100 seconds. *Science*, 330:1652, 2010.

[61] J. M. Elzerman, R. Hanson, L. H. Willems van Beveren, B. Witkamp, L. M. K. Vandersypen, and L. P. Kouwenhoven. Single-shot read-out of an individual electron spin in a quantum dot. *Nature*, 430:431, 2004.

[62] R. Hanson, L. H. Willems van Beveren, I. T. Vink, J. M. Elzerman, W. J. M. Naber, F. H. L. Koppens, L. P. Kouwenhoven, and L. M. K. Vandersypen. Single-shot readout of electron spin states in a quantum dot using spin-dependent tunnel rates. *Physical Review Letters*, 94(19):196802, 2005.

[63] F. H. L. Koppens, C. Buizert, K. J. Tielrooij, I. T. Vink, K. C. Nowack, T. Meunier, L. P. Kouwenhoven, and L. M. K. Vandersypen. Driven coherent oscillations of a single electron spin in a quantum dot. *Nature*, 442(17):766, 2006.

[64] L. J. Klein, K. A. Slinker, J. L. Truitt, S. Goswami, K. L. M. Lewis, S. N. Coppersmith, D. W. Van Der Weide, M. Friesen, R. H. Blick, D. E. Savage, M. G. Lagally, C. Tahan, R. Joynt, M. A. Eriksson, J. O. Chu, J. A. Ott, and P. M. Mooney. Coulomb blockade in a silicon/silicon-germanium two-dimensional electron gas quantum dot. *Applied Physics Letters*, 84(20):4047, 2004.

[65] K. A. Slinker, K. L. M. Lewis, C. C. Haselby, S. Goswami, L. J. Klein, J. O. Chu, S. N. Coppersmith, R. Joynt, R. H. Blick, M. Friesen, and M. A. Eiriksson. Quantum dots in Si/SiGe 2DEGs with schottky top-gated leads. *New Journal of Physics*, 7:246, 2005.

[66] N. Shaji, C. B. Simmons, M. Thalakulam, L. J. Klein, H. Qin, H. Luo, D. E. Savage, M. G. Lagally, A. J. Rimberg, R. Joynt, M. Friesen, R. H. Blick, S. N. Coppersmith,

and M. A. Eriksson. Spin blockade and lifetime-enhanced transport in a few-electron Si/SiGe double quantum dot. *Nature Physics*, 4:540, 2008.

[67] M. Thalakulam, C. B. Simmons, B. M. Rosemeyer, D. E. Savage, M. G. Lagally, M. Friesen, S. N. Coppersmith, and M. A. Eriksson. Fast tunnel rates in Si/SiGe one-electron single and double quantum dots. *Applied Physics Letters*, 96(18):183104, 2010.

[68] C. B. Simmons, J. R. Prance, B. J. Van Bael, T. S. Koh, Z. Shi, D. E. Savage, M. G. Lagally, R. Joynt, M. Friesen, S. N. Coppersmith, and M. A. Eriksson. Tunable spin loading and T_1 of a silicon spin qubit measured by single-shot readout. *Physical Review Letters*, 106(15):156804, 2011.

[69] M. Xiao, M. G. House, and H. W. Jiang. Measurement of the spin relaxation time of single electrons in a silicon metal-oxide-semiconductor-based quantum dot. *Physical Review Letters*, 104(9):096801, 2010.

[70] E. Nordberg, G. Eyck, H. Stalford, R. Muller, R. Young, K. Eng, L. Tracy, K. Childs, J. Wendt, R. Grubbs, J. Stevens, M. Lilly, M. Eriksson, and M. Carroll. Enhancement-mode double-top-gated metal-oxide-semiconductor nanostructures with tunable lateral geometry. *Physical Review B*, 80(11):115331, 2009.

[71] E. Nordberg, H. Stalford R. Young, G. A. Ten Eyck, K. Eng, L. Tracy, K. D. Childs, J. R. Wendt, R. K. Grubbs, J. Stevens, M. Lilly, M. Eriksson, and M. Carroll. Charge sensing in enhancement mode double-top-gated metal-oxide-semiconductor quantum dots. *Applied Physics Letters*, 95(20):202102, 2009.

[72] G. Feher. Electron spin resonance experiments on donors in silicon. I. Electronic structure of donors by electron nuclear double resonance technique. *Physical Review*, 114(5):1219, 1959.

[73] J. J. L. Morton, A. M. Tyryshkin, R. M. Brown, S. Shankar, B. W. Lovett, A. Ardavan, T. Schenkel, E. E. Haller, J. W. Ager, and S. A. Lyon. Solid-state quantum memory using the ^{31}P nuclear spin. *Nature*, 455(7216):1085, 2008.

[74] R. R. Hayes, A. A. Kiselev, M. G. Borselli, S. S. Bui, E. T. Croke III, P. W. Deelman, B. M. Maune, I. Milosavljevic, J.-S. Moon, R. S. Ross, A. E. Schmitz, M. F. Gyure, and A. T. Hunter. Lifetime measurements (T1) of electron spins in Si/SiGe quantum dots. *arXiv:0909.0173v1*, 2009.

[75] S. Y. Paik, S. Y. Lee, W. J. Baker, D. R. McCamey, and C. Boehme. T_1 and T_2 spin relaxation time limitations of phosphorus donor electron near crystalline silicon to silicon dioxide interface defects. *Physical Review B*, 81(7):075214, 2010.

[76] S. Shankar, A. M. Tyryshkin, J. He, and S. A. Lyon. Spin relaxation and coherence times for electrons at the Si/SiO_2 interface. *Physical Review B*, 82(19):195323, 2010.

[77] S. A. Lyon, A. M. Tyryshkin, S. Tojo, K. M. Itoh, J. J. L. Morton, T. Schenkel, M. L. W. Thewalt, H. Riemann, N. V. Abrosimov, and P. Becker. Ultralong coherence of phosphorus donors in high-purity ^{28}Si silicon. *American Physical Society March Meeting, Dallas*, 2011.

[78] G. E. Pake. *The physical principles of electron paramagnetic resonance*. W. A. Benjamin, Massachusetts, U.S.A., 1973.

[79] A. Schweiger and G. Jeschke. *Principles of pulse electron paramagnetic resonance*. Oxford University Press, Oxford, 2001.

[80] C. P. Slichter. *Principles of Magnetic Resonance*. Springer, New York, U.S.A., 1990.

[81] C. Poole. *Electron spin resonance: a comprehensive treatise on experimental techniques*. John Wiley & Sons, Inc., New York, USA, 1983.

[82] R. de Sousa and J. D. Delgado S. D. Sarma. Silicon quantum computation based on magnetic dipolar coupling. *Physical Review A*, 70(5):052304, 2004.

[83] I. Žutić, J. Fabian, and S. Das Sarma. Spintronics: Fundamentals and applications. *Reviews of Modern Physics*, 76:323, 2004.

[84] G. Dresselhaus. Spin-orbit coupling effects in zinc blende structures. *Physical Review*, 100(2):580, 1955.

[85] Y. A. Bychkov and E. I. Rashba. Oscillatory effects and the magnetic-susceptibility of carriers in inversion-layers. *Journal of Physics C: Solid State Physics*, 17(33):6039, 1984.

[86] R. Maxwell and A. Honig. Neutral-impurity scattering experiments in silicon with highly spin-polarized electrons. *Physical Review Letters*, 17(4):188, 1966.

[87] A. Honig. Neutral-impurity scattering and impurity zeeman spectroscopy in semiconductors using highly spin-polarized carriers. *Physical Review Letters*, 17(4):186, 1966.

[88] D. Thornton and A. Honig. Shallow-donor negative-ions and spin-polarized electron-transport in silicon. *Physical Review Letters*, 30(19):909, 1973.

[89] D. J. Lepine. Spin-dependent transport on silicon surface. *Physical Review B*, 6(2):436, 1972.

[90] G. Mendz and D. Haneman. Spin dependent recombination and photoconductive resonance in silicon. *Journal of Physics C: Solid State Physics*, 11:L197, 1978.

[91] G. Mendz, D. J. Miller, and D. Haneman. Photoconductive resonance in silicon: theory and experiment. *Physical Review B*, 20(12):5246, 1979.

[92] G. Mendz and D. Haneman. A new model of spin-dependent resonance at Si surfaces. *Journal of Physics C - Solid State Physics*, 13:6737, 1980.

[93] L. S. Vlasenko. Photoelectrically detected magnetic resonance spectroscopy of the excited triplet states of point defects in silicon. *Physics of the Solid State*, 41:5, 1999.

[94] I. Solomon, D. Biegelsen, and J. C. Knights. Spin-dependent photoconductivity in *n*-type and *p*-type amorphous silicon. *Solid State Communications*, 22:505, 1977.

[95] M. S. Brandt, M. W. Bayerl, M. Stutzmann, and C. F. O. Graeff. Electrically detected magnetic resonance of a-Si:H at low magnetic fields: the influence of hydrogen on the dangling bond resonance. *Journal of Non-Crystalline Solids*, 227:343, 1998.

[96] I. Solomon. Spin-dependent recombination in a silicon *p-n* junction. *Solid State Communications*, 20:215, 1976.

[97] F. C. Rong, W. R. Buchwald, E. H. Poindexter, W. L. Warren, and D. J. Keeble. Spin-dependent shockley-read recombination of electrons and holes in indirect-band-gap semiconductor *p-n* junction diodes. *Solid-State Electronics*, 34(8):835, 1991.

[98] P. Christmann, W. Stadler, and B. K. Meyer. Temperature dependent electrically detected magnetic resonance studies on silicon *pn* diodes. *Appled Physics Letters*, 66(12):1521, 1995.

[99] R. N. Ghosh and R.H. Silsbee. Spin-spin scattering in a silicon two-dimensional electron gas. *Physical Review B*, 80(4):045320, 1992.

[100] J. H. Stathis. Electrically detected magnetic resonance study of strees-induced leakage current in thin SiO_2. *Applied Physics Letters*, 68(12):1669, 1996.

[101] G. Kawachi, C. F. O. Graeff, M. S. Brandt, and M. Stutzmann. Carrier transport in amorphous silicon-based thin-film transistors studied by spin-depenedent transport. *Physical Review B*, 54(11):7957, 1996.

[102] G. Kawachi, C. F. O. Graeff, M. S. Brandt, and M. Stutzmann. Saturation measurements of electrically detected magnetic resonance in hydrogenated amorphous silicon based thin-film transistors. *Japanese Journal of Applied Physics*, 36:121, 1997.

[103] M. S. Brandt, R. T. Neuberger, and M. Stutzmann. Spin-dependent capacitance of silicon field-effect transistors. *Applied Physics Letters*, 76(11):1467, 2000.

[104] D. Kaplan, I. Solomon, and N. F. Mott. Explanation of the large spin-dependent recombination effect in semiconductors. *Le Journal de Physique*, 39(4):L–51, 1978.

[105] M. Xiao, I. Martin, E. Yablonovitch, and H. W. Jiang. Electrical detection of the spin resonance of a single electron in a silicon field-effect transistor. *Nature*, 430(6998):435, 2004.

[106] J. R. Petta, A. C. Johnson, J. M. Taylor, E. A. Laird, A. Yacoby, M. D. Lukin, C. M. Marcus, M. P. Hanson, and A. C. Gossard. Coherent manipulation of coupled electron spins in semiconductor quantum dots. *Science*, 309:2180, 2005.

[107] D. A. Neamen. *Semiconductor physics and devices.* McGraw-Hill, New York, U.S.A., 2003.

[108] M. S. Brandt, S. T. B. Goennenwein, T. Graf, H. Huebl, S. Lauterbach, and M. Stutzmann. Spin-dependent transport in elemental and compound semiconductors and nanostructures. *Physica Status Solidi (C)*, 1(8):2056, 2004.

[109] F. Hoehne, H. Huebl, B. Galler, M. Stutzmann, and M. S. Brandt. Spin-dependent recombination between phosphorus donors in silicon and Si/SiO_2 interface states investigated with pulsed electrically detected electron double resonance. *Physical Review Letters*, 104(4):046402, 2010.

[110] R. de Sousa, C. C. Lo, and J. Bokor. Spin-dependent scattering in a silicon transistor. *Physical Review B*, 80:045320, 2009.

[111] C. F. O. Graeff, M. S. Brandt, M. Stutzmann, M. Holzmann, G. Abstreiter, and F. Schäffler. Electrically detected magnetic resonance of two-dimensional electron gases in Si/SiGe heterostructures. *Physical Review B*, 59(20):13242, 1999.

[112] T. Ando, A. B. Fowler, and F. Stern. Electronic properties of two-dimensional systems. *Reviews of Modern Physics*, 54(2):437, 1982.

[113] F. F. Fang and W. E. Howard. Negative field-effect mobility on (100) Si surfaces. *Physical Review*, 16(18):797, 1966.

[114] F. Stern and W. E. Howard. Properties of semiconductor surface inversion layers in the electric quantum limit. *Physical Review*, 163(3):816, 1967.

[115] P. Y. Yu and M. Cardona. *Fundamentals of semiconductors - Physics and materials properties, 3^{rd} edition.* Springer-Verlag, Berlin, Germany, 2001.

[116] M. Lundstrom. *Fundamentals of carrier transport, Second edition.* Cambridge University Press, Cambridge, U.K., 2000.

[117] G. Burns. *Solid State Physics*. Academic Press, San Diego, U.S.A., 1990.

[118] J. M. Ziman. *Principles of the theory of solids*. Cambridge University Press, Cambridge, U.K., 1972.

[119] R. T. Weber and A. A. Heiss. *Bruker ESP 300E EPR Spectrometer User's Manual, Version 0.1*. 1992.

[120] P. M. Lenahan and J. F. Conley Jr. What can electron paramagnetic resonance tell us about the Si/SiO_2 system? *Journal of Vacuum Science and Technology B*, 16(4):2134, 1998.

[121] C. C. Lo, J. Bokor, T. Schenkel, A. M. Tyryshkin, and S. A. Lyon. Spin-dependent scattering off neutral antimony donors in ^{2}8Si field-effect transistors. *Applied Physics Letters*, 91(24):242106, 2007.

[122] D. R. McCamey, H. Huebl, M. S. Brandt, W. D. Hutchison, J. C. McCallum, R. G. Clark, and A. R. Hamilton. Electrically detected magnetic resonance in ion-implanted Si:P nanostructures. *Applied Physics Letters*, 78(4):045303, 2008.

[123] G. Ferrari, L. Fumgalli, M. Sampietro, E. Prati, and M. Fanciulli. Cmos fully compatible microwave detector based on mosfet operating in resistive regime. *IEEE Microwave and Wireless Components Letters*, 15(7):1531, 2005.

[124] E. Prati, M. Fanciulli, A. Calderoni, G. Ferrari, and M. Sampietro. Effect of microwave irradiation on the emission and capture dynamics in silicon metal oxide semiconductor field effect transistors. *Applied Physics Letters*, 1033(10):104502, 2008.

[125] J. W. Sidabras, R. R. Mett, and J. S. Hyde. Aqueous flat-cells perpendicular to the electric field for use in electron paramagnetic resonance spectroscopy, II: Design. *Journal of Magnetic Resonance*, 172:333, 2005.

[126] V. Lang, C. C. Lo, R. E. George, S. A. Lyon, J. Bokor, T. Schenkel, A. Ardavan, and J. J. L. Morton. Electrically detected magnetic resonance in a W-band microwave cavity. *Review of Scientific Instruments*, 82(3):034794, 2011.

[127] S. Shankar, A. M. Tyryshkin, S. Avasthi, and S. A. Lyon. Spin resonance of 2D electrons in a large-area silicon MOSFET. *Physica E*, 40:1659, 2007.

[128] K. Morigaki and M. Onda. Spin-dependent conductivity o phosphorus-doped silicon in the intermediate concentration region. *Journal of the Physical Society of Japan*, 36(4):1049, 1974.

[129] E. Abrahams, S. V. Kravchenko, and M. P. Sarachik. Metallic behavior and related phenomena in two dimensions. *Reviews of Modern Physics*, 73(3):251, 2001.

[130] V. M. Pudalov, G. Brunthaler, A. Prinz, and G. Bauer. Weak anisotropy and disorder dependence of the in-plane magnetoresistance in high-mobility (100) Si-inversion layers. *Physical Review Letters*, 88:076401, 2002.

[131] T. Okamoto, M. Ooya, K. Hosoya, and S. Kawaji. Spin polarization and metallic behavior in a silicon two-dimensional electron system. *Physical Review B*, 69(4):041202(R), 2004.

[132] J. Matsunami, M. Ooya, and T. Okamoto. Electrically detected electron spin resonance in a high-mobility silicon quantum well. *Physical Review Letters*, 97(4):066602, 2006.

[133] K. C. Kwong, J. Callaway, N. Y. Du, and R. A. LaViolette. Elastic scattering of electrons by neutral donor impurities in silicon. *Physical Review B*, 43(2):1576, 1991.

[134] Y. Nishi. Study of silicon-silicon dioxide structure by electron spin resonance I. *Japanese Journal of Applied Physics*, 10(1):52, 1971.

[135] Z. Wilamowski and W. Jantsch. Spin resonance properties of the two-dimensional electron gas. *Physica E*, 10:17, 2001.

[136] Z. Wilamowski and W. Jantsch. Suppression of spin relaxation of conduction electrons by cyclotron motion. *Physical Review B*, 69(3):035328, 2004.

[137] R. N. Ghosh. *Spin dependent transport in a silicon two-dimensional electron gas*. PhD thesis, Cornell University, 1991.

[138] Evans Analytical Group. *Santa Clara, CA, USA*.

[139] SRIM simulator. The Stopping and Range of Ions in Matter. *http://www.srim.org/*, 2010.

[140] Taurus Process and Taurus Device simulator. *http://www.synopsys.com/tools/tcad/*, 2008.

[141] H. Kodera. Effect of doping on the electron spin resonance in phosphorus doped silicon. III. Absorption intensity. *Journal of the Physical Society of Japan*, 27(5):1197, 1969.

[142] P. R. Cullis and J. R. Marko. Determination of the donor pair exchange energy in phosphorus-doped silicon. *Physical Review B*, 1(2):632, 1970.

[143] M. Taniguchi and S. Narita. D^- state in silicon. *Solid State Communications*, 20:131, 1976.

[144] H. Kamimura. Electronic states of a negative donor ion in silicon and germanium. *Journal of Non-Crystalline Solids*, 32:187, 1979.

[145] L. E. Oliveira and L. M. Flicov. Effect of compressive uniaxial stress on the binding energies of D^- centers in Si:P and Si:As. *Physical Review B*, 33:6990, 1986.

[146] T. Okamoto, K. Hosoya, S. Kawaji, and A. Yagi. Spin degree of freedom in a two-dimensional electron liquid. *Physical Review Letters*, 82(19):3875, 1999.

[147] J. Matsunami and T. Okamoto. Electrical detection of electron-spin resonance in two-dimensional systems. *Electron Spin Resonance and Related Phenomena in Low-Dimensional Structures, Topics Appl. Physics*, page 129, 2009.

[148] C. Poole and H. A. Farach. *Handbook of electron spin resonance*. Springer-Verlag New York, Inc., New York, USA, 1999.

[149] A. M. Tyryshkin and S. A. Lyon. Private communication.

[150] S. Shankar. *Electron spin coherence in bulk silicon and silicon heterostructures*. PhD thesis, Princeton University, 2010.

[151] A. M. Tyryshkin, S. A. Lyon, W. Jantsch, and F. Schäffler. Spin manipulation of free two-dimensional electrons in Si/SiGe quantum wells. *Physical Review Letters*, 94(12):126802, 2005.

[152] Y. Yafet. *Solid State Physics*, volume 14. Academic Press, New York, 1963.

[153] J. L. Cheng, M. W. Wu, and J. Fabian. Theory of the spin relaxation of conduction electrons in silicon. *Physical Review Letters*, 104(1):016601, 2010.

[154] R. Orbach. On the theory of spin-lattice relaxation in paramagnetic salts. *Proceedings of the Physical Society*, 77(4):821, 1961.

[155] G. Feher and E. Gere. Electron spin resonance experiments on donors in silicon. II. Electron spin relaxation effects. *Physical Review*, 114(5):1245, 1959.

[156] T. G. Castner. Raman spin-lattice relaxation of shallow donors in silicon. *Physical Review*, 130(1):58, 1963.

[157] T. G. Castner. Direct measurement of the valley-orbit splitting of shallow donors in silicon. *Physical Review*, 8(1):13, 1963.

[158] T. G. Castner. Orbach spin-lattice relaxation of shallow donors in silicon. *Physical Review*, 155(3):154, 1967.

[159] R. de Sousa and S. D. Sarma. Theory of nuclear-induced spectral diffusion: Spin coherence of phosphorus donors in Si and GaAs quantum dots. *Physical Review B*, 68(11):115322, 2003.

[160] A. M. Tyryshkin, S. A. Lyon, and A. M. Raitsimring. Electron spin relaxation times of phosphorus donors in silicon. *Physical Review B*, 68(19):193207, 2003.

[161] A. M. Tyryshkin, J. J. L. Morton, A. Ardavan, and S. A. Lyon. Davies electron-nuclear double resonance revisited: Enhanced sensitivity and nuclear spin relaxation. *The Journal of Chemical Physics*, 124(23):234508, 2006.

[162] D. K. Wilson and G. Feher. Electron spin resonance experiments on donors in silicon. III. Investigation of excited states by the application of uniaxial stress and their importance in relaxation processes. *Physical Review*, 124(4):1068, 1961.

[163] I. Appelbaum, B. Huang, and D. J. Monsma. Electronic measurements and control of spin transport in silicon. *Nature*, 447:295, 2007.

[164] B. T. Jonker, G. Kioseoglou, A. T. Hanbicki, C. H. Li, and P. E. Thompson. Electrical spin-injection into silicon from a ferromagnetic metal/tunnel barrier contact. *Nature Physics*, 31:542, 2007.

[165] Z. G. Yu and M. E. Flatté. Electric-field dependent spin diffusion and spin injection into semiconductors. *Physical Review B*, 66:201202(R), 2002.

[166] Z. G. Yu and M. E. Flatté. Spin diffusion and injection in semiconductor structures: Electric field effects. *Physical Review B*, 66:235302, 2002.

[167] C. Józsa. Electrical spin drift in graphene field-effect transistors. *Physical Review Letters*, 100(23):236603, 2008.

[168] C. Kittel. *Introduction to Solid State Physics, 7^{th} edition.* John Weiley& Sons, New York, U.S.A., 1996.

[169] D. Hisamoto, W. C. Lee, J. Kedzierski, H. Takeuchi, K. Asano, C. Kuo, E. Anderson, T. J. King, J. Bokor, and C. M. Hu. FinFET - A self-aligned double-gate MOSFET scalable to 20 nm. *IEEE Transactions on Electron Devices*, 47(12):2320, 2000.

[170] Soitec. *Grenoble, France.*

[171] Lawrence Semiconductor Research Laboratory Inc. *Tempe, AZ, U.S.A.*

[172] L. L. Sohn, L. P. Kouwenhoven, and G. Schoen, editors. *Mesoscopic Electron Transport, NATO ASI Series E.* Kluwer Academic Publishers, Dordrecht, The Netherlands, 1997.

[173] N. M. Zimmerman, B .J. Simonds, A. Fujiwara, Y. Ono, Y. Takahashi, and H. Inokawa. Charge offset stability in tunable-barrier Si single-electron tunneling devices. *Applied Physics Letters*, 90(3):033507, 2007.

[174] D. R. McCamey, G. Morley, H. Seipel, L. Brunel, J. Van Tol, and C. Boehme. Spin-dependent processes at the crystalline Si-SiO_2 interface at high magnetic fields. *Physical Review B*, 89(18):182115, 2006.

[175] H. Huebl, R. P. Starrett, D. R. McCamey, A. J. Ferguson, and L. H. Willems van Beveren. Electrically detected magnetic resonance using radio-frequency reflectometry. *Review of Scientific Instruments*, 80(11):114705, 2009.

[176] M. Hofheinz. *Coulomb blockade in silicon nanowire MOSFETs*. PhD thesis, Université Grenoble I – Joseph Fourier, 2006.

[177] H. Sellier, G. P. Lansbergen, J. Caro, S. Rogge, N. Collaert, I. Ferain, M. Jurczak, and S. Biesemans. Transport spectroscopy of a single dopant in a gated silicon nanowire. *Physical Review Letters*, 97(20):206805, 2006.

[178] G. P. Lansbergen. *Electron transport through single donors in silicon*. PhD thesis, Technische Universiteit Delft, 2010.